DISSERTATION

SUBMITTED TO THE

COMBINED FACULTIES OF THE NATURAL SCIENCES AND MATHEMATICS

OF THE RUPERTO-CAROLA-UNIVERSITY OF HEIDELBERG, GERMANY

FOR THE DEGREE OF

DOCTOR OF NATURAL SCIENCES

PRESENTED BY

MASTER PHYS. SVITLANA ZHUKOVSKA

BORN IN: KYIV (UKRAINE)

ORAL EXAMINATION: DECEMBER 17th, 2008

Dust formation by stars

and

evolution in the interstellar medium

REFEREES: PROF. DR. HANS-PETER GAIL
              PROF. DR. MAX CAMENZIND

Zusammenfassung

Das Hauptziel dieser Arbeit ist das Studium des Ursprungs und der Entwicklung des interstellaren Staubs in der Milchstraße. Wir erarbeiten ein Modell der chemischen Entwicklung der galaktischen Scheibe als Grundlage unseres neuen Staubentwicklungsmodells, das erstmals die individuelle Entwicklung des Sternenstaubs und in Molekülwolken der galaktischen Scheibe kondensierten Staubs berücksichtigt. Die Staubproduktion von AGB-Sternen behandeln wir im Detail, indem wir Berechnungen synthetischer AGB-Modelle mit Modellen zur Staubkondensation in dem von Sternen ausgestoßenen Material kombinieren. Weiterhin schätzen wir die Effizienz der Staubkondensation in Supernovae durch Anpassen der Ergebnisse von Modellrechnungen zur Sonnenumgebung an beobachtete Haufigkeiten von durch Supernova-Explosionen erzeugten präsolaren Staubkörnern. Unsere Ergebnisse legen dar, dass Supernovae überwiegend Staub aus Kohlenstoff mit einem sehr kleinen Anteil von Staub aus Silikaten, Eisen und Siliziumcarbid erzeugen. Wir zeigen, dass interstellarer Staub während der gesamten Entwicklungsgeschichte der galaktischen Scheibe hauptsächlich aus im interstellaren Medium entstandenem Staub besteht. Zudem dominiert die Staub aus AGB-Sternen und Supernovae im interstellaren Medium nur bei Metallizitäten unterhalb des für effizientes Staubwachstum in Molekülwolken nötigen Minimums.

Abstract

The main goal of this thesis is the study of the origin and evolution of interstellar dust in the Milky Way. We develop a model for the chemical evolution of the galactic disk as a basis for our new model of dust evolution, which considers for the first time the individual evolutions of stardust and of dust condensed in molecular clouds of the Galactic disk. We include dust production by AGB stars in detail, using the results of synthetic AGB models combined with models of dust condensation in stellar outflows, and estimate the efficiency of dust condensation in supernovae by matching model results for the Solar neighbourhood with observed abundances of presolar dust grains of supernova origin. Our results indicate that supernovae produce mainly carbon dust, with only small amounts of silicates, iron and silicon carbonate. We show that the interstellar dust population is dominated by dust grown in the interstellar medium across the Galactic history; moreover, dust formed in AGB stars and supernovae is a dominant source of dust only at metallicities lower than the minimal value for efficient dust growth in molecular clouds.

Contents

CONTENTS

List of Figures

LIST OF FIGURES

List of Tables

Publications

Part of the results presented in the thesis has been published in the following papers

1. "Evolution of interstellar dust and stardust in the solar neighbourhood", Zhukovska, S., Gail, H.-P., & Trieloff, M. 2008, Astronomy & Astrophysics, 479, 453

2. "Condensation of MgS in outflows from AGB stars", Zhukovska, S.& Gail, H.-P. 2008, Astronomy & Astrophysics, 486, 229

3. "Stardust from AGB stars", Gail, H.-P., Zhukovska, S., Hoppe,P. & Trieloff, M. 2008, submitted to ApJ

4. "Modeling Dust Evolution in the Interstellar Medium", Zhukovska, S., Gail, H.-P., Proceedings of the Conference "Pathways through an Eclectic Universe", ASP Conference Series, Vol. 390, p. 117

5. "Modeling of dust evolution in the Milky Way", Zhukovska, S., Gail, H.-P., Proceedings of the Spitzer Conference on "The Evolving ISM in the Milky Way and Nearby Galaxies", 2008

6. "Contribution of dust by AGB stars during Galactic evolution", Zhukovska, S., Gail, H.-P., ASP Conference Series, Vol. 378, p. 499, Proceedings of Vienna Conference "Why Galaxies Care about AGB Stars", 2006

7. "Multiphase model of galactic chemical evolution", Zhukovska, S., Gail, H.-P., Proceedings of the CRAL-2007 Conference, EAS Publications Series, Vol. 24, p. 299, 2007

1

Introduction

More than two hundred years ago Hershel (1785) described the dark patches in the sky as 'holes in the heavens'. Only in 1930 it was proven that these dark regions are caused by solid dust particles in space by comparing the photometric and geometric distances to open clusters (Trümpler 1930). Since then the nature of interstellar grains has been a subject of active research advancing by the method of trial and error. The model of the interstellar dust grains have evolved from the metallic iron grains proposed because of abundant iron meteorites, which at that time were believed to be of interstellar origin. Oort & van de Hulst (1946) introduced a "dirty ice" model of interstellar grains composed of hydrogen-rich volatiles (H_2O, CH_4, NH_3) prevailing in the decade 1950-1960. For reviews of the historical evolution of the interstellar dust models we refer to, e.g., Li (2005), Dorschner (2003).

New observational data that become available with the progress in observational technologies put additional constraints on the viability of the dust models. The measurements of the extinction curve extended to UV with the beginning of the satellites' era and the discovery of interstellar polarization notably restricted the range of materials and sizes of interstellar grains, and returned the refractory dust grains into considerations. In particular, it was proven that neither single type nor single size grains are capable to reproduce the observed extinction. In 1977 Mathis, Rumpl & Nordsieck proposed the model of interstellar grains consisting of bare silicate and graphite grains with power law size distribution $dn(a)/da \sim a^{-3.5}$, which together with optical data from Draine & Lee (1984) provides an excellent fit to the average interstellar extinction. This model with some modifications formed the basis for the standard model of the interstellar grains (Zubko et al. 2004, Weingartner & Draine 2001). For many decades the question of the origin of dust in interstellar space that would explain the grain sizes and compositions predicted by the dust models remained the most intriguing one. Two main competing theories of the interstellar dust origin under discussion for more than 70 years are:

growth in the interstellar medium vs. condensation in evolved stars.

In the present work we intend to study the origin and evolution of the dust grain population in the interstellar medium of the Milky Way incorporating recent progress in the theoretical studies of dust production by stars and laboratory investigations of grains of stellar origin as outlined below.

1.1 Dust production by stars

It is known that dust grains are formed in stellar ejecta or stellar winds of highly evolved stars from the refractory elements therein. The resulting gas-dust mixture is ultimately mixed with the general interstellar matter. For the first time, the idea of graphite formation in stellar winds of carbon stars was proposed in Hoyle & Wickramasinghe (1962). Later, these authors also argue that a significant fraction of refractory elements in the metal-rich expanding ejecta of supernovae (SNe) should condense into dust (Hoyle & Wickramasinghe 1970). But generally only some fraction of the refractory elements in the ejecta is really condensed into solid phases; a big mass fraction of the refractory elements returned to the ISM – or sometimes even most of it – stays in the gas phase. Turbulent mixing in the ISM rapidly intermingles the material that is ejected by the many different stellar sources. While all the dust particles from stellar sources, called *stardust* particles, retain their peculiar isotopic compositions of a number of elements indicative of their formation sites, in the gas phase the material from all sources is mixed together and the resulting isotopic composition of the mix is different from that of the stardust particles. The refractory elements in the ISM gas therefore have different isotopic compositions than the same elements found in stardust grains.

1.1.1 Presolar dust grains

Stardust grains are found in the Solar System as a rare fraction of the fine grained matrix material of meteorites (e.g. Bernatowicz & Zinner 1997; Hoppe 2004; Nguyen et al. 2007). They are identified as such by the unusual isotopic composition of at least one element that shows that the grains have condensed from material that contains freshly synthesised nuclei from stellar burning zones. Laboratory studies have found a wide assortment of such stardust grains, also called presolar dust particles, with a variety of chemical compositions that can be associated with a variety of stellar sources. The composition of the grain material indicates two basically different chemical environments of formation, (1) a carbon-rich environment, and (2) an oxygen-rich environment, which yield two completely different groups of mineral compounds:

1. solid graphitic carbon, diamond, silicon carbide, silicon nitride, and

2. corundum, hibonite, spinel, magnesium-iron-silicates.

Besides of these main components, a number of minor components (e.g. titanium oxide, solid solutions of titanium carbide with zirconium and molybdenum carbide, kamacite, and cohenite) have been identified that are so far only known to exist as inclusions in grains of the major dust components. Additional components may exist and await identification, in particular, since some kinds of dust

may not survive all the stages between the stellar source and the final laboratory investigation. The observed isotopic anomalies essentially indicate two different kinds of stellar sources of the presolar dust grains, (1) AGB stars and (2) core-collapse supernovae.

1.2 Dust condensation in the ISM

The idea of dust condensation from the interstellar gas through random accretion of gas atoms was first proposed by Lindblad (1935), but it was abandoned for many decades in favour of stellar origin of dust due to growing evidence of circumstellar dust around evolved stars. From the instant of the formation in stellar ejecta on, stardust grains are subject to destructive processes in the ISM by sputtering and shattering processes induced by SN shocks (cf. Jones et al. 1996, and references therein). They are finally incorporated into newly formed stars and their planetary systems after about 2.5 Gyrs residence in the ISM, which is also the typical timescale for replenishment of the ISM with new stardust. Theoretical studies have shown that typical average lifetimes against destruction by SN shocks are only about 0.5 Gyrs (Jones et al. 1996). This rather short timescale compared to the timescale for replenishment would result in very low dust abundance in the ISM. This, however, is not observed. Instead one observes a high degree of depletion of the refractory elements in the gas phase of the ISM (e.g. Savage & Sembach 1996; Jenkins 2004), and this clearly requires additional growth processes in the interstellar medium that tie up the atoms of the refractory elements in dust. The only possible sites where accretion of gas phase material onto grains may proceed with a reasonably short timescale are the dense molecular clouds of the ISM (Draine 1990). Also, accretion seems to be necessary to explain copious amounts of dust observed in hyperluminous galaxies in the early universe. Their high dust content can be only reproduced if unrealistically high supernova dust production is included, otherwise it also requires an additional growth process in the ISM (Dwek, Gallino & Jones 2007).

1.2.1 MC-grown dust

Any solid phase material grown in molecular clouds, the *MC-grown dust*, has isotopic compositions of the refractory elements that are different from what is found in the stardust particles and may be identified by this property. Such dust material may be found both as coating of stardust grains and as separate grains. Unfortunately, the isotopic composition of the refractory elements in MC-grown dust grains incorporated into the Solar System equals the isotopic composition of the elements in the Solar System, which makes it impossible to distinguish by laboratory investigations of isotopic abundances of refractory elements alone between dust formed in the Solar System and MC-grown dust. There are other indications, however, that point to a presolar origin of some fraction of the interplanetary dust particles, the GEMS (Bradley 2003; Messenger et al. 2003), which shows isotopic abundances of refractory elements corresponding to normal Solar System isotopic abundances and which therefore are likely to be MC-grown dust grains. The category of presolar dust grains therefore also includes

the MC-grown dust species that are isotopically inconspicuous, a property presently making them difficult to be identified as of extrasolar origin.

1.3 Evolution of interstellar dust

If we intend to calculate the abundances for the different components of the interstellar dust mixture in the Milky Way at the solar circle and in particular the composition of the dust mixture from which the Solar System formed, we have to construct a model of the Milky Way's chemical evolution that is coupled with a model for the evolution of the dust component of the interstellar matter. The evolution of the dust component is not independent of the evolution of the element abundances, since the refractory elements forming the dust are only gradually formed during the course of the chemical evolution of the galaxy. The model for the dust evolution needs to consider the injection of stardust into the ISM, the destruction processes of dust in the ISM, and the growth processes in molecular clouds. Very simple models for the evolution of the dust content of galaxies have already been constructed (e.g. Lisenfeld & Ferrara 1998; Hirashita 2000; Edmunds 2001; Morgan & Edmunds 2003; Inoue 2003), but these are too simplistic to allow for a detailed calculation of the composition of the interstellar dust mixture. Only the method developed by Dwek (1998) integrating the chemical evolution of the galactic disk and the dust evolution into a common model is sufficiently general to allow a modelling of the complex interplay between the processes determining the dust evolution and has the potential of being extended to even more complex systems. This model is a one-zone model, i.e., the galactic disk is approximated by a set of independent cylinders with all physical variables within a cylinder averaged over the vertical direction with respect to the disks midplane; and a one-phase model, i.e., one averages the properties of the ISM over its different phases (cold, warm, and hot; cf. Tielens 2005). This type of model allows a successful, and at the same time, rather easy calculation of some important properties of the Milky Way disk, in particular of its chemical evolution (cf. Matteuchi 2003). The price one has to pay for the simplifications is that some processes, in particular those depending critically on the phase structure of the ISM, cannot be treated with sufficient accuracy. Nevertheless, the results obtained by Dwek (1998) show that such a simple model can be used successfully to calculate the evolution of the interstellar dust. We take the concept of Dwek as a basis for constructing a new model that allows a more complex mixture of stardust and MC-grown dust to be treated.

1.3.1 Multicomponent dust model

For the input of stardust from AGB-stars, we use the recent results for the dust production by AGB-stars (Ferrarotti & Gail 2006), which are somewhat extended in this work. These tables present rather detailed information on the amount and composition of stardust formed by AGB-stars. For stardust from SNe, we follow the procedure of Dwek (1998) and use a simple parametrisation for the dust production rate since no other suitable information on dust production is available. Observations are

inconclusive and the theory is only in its infancy (Bianchi & Schneider 2007, Schneider et al. 2004; Nozawa et al. 2003, and references therein). We, in turn, try to gain some insight into the dust production efficiency of supernovae by comparing our model results with the meteoritic abundances of stardust from SNe. The dust growth in molecular clouds is treated in some detail, since we intend to distinguish in the model between stardust and MC-grown dust. In principle it would also be necessary to consider that, according to observations of element depletion in the ISM, the MC-grown dust has a definite core mantle structure with a more resilient core and a more easily destructible mantle. A theoretical treatment of this grain structure would require considering at least a two-phase interstellar medium (cf. Tielens 1998; Inoue 2003) and not a simple one-phase model as in our present calculation.

1.3.2   Modelling of dust in the Galactic disk

The chemical evolution of our own galaxy is best understood due to the wealth of available observational constraints: the star formation profile, density distribution, and composition of neutral and molecular gas, the chemical composition of stars along the galactic radius and so on. There is a number of theoretical studies of the Milky Way in the literature that mostly agree on the main ingredients of its chemical evolution model (e.g., Chiappini et al. 1997, Cescutti et al. 2007, Goswami & Prantzos 2000). Therefore, such kind of model forms a good basis for the application of our multicomponent dust model constructed for the Solar neighborhood to study the dust evolution in the Milky Way disk as a whole. The most important feature of the model is that the chemical evolution of the Milky Way proceeds more rapid in the inner disk than in the outer regions as inferred from the Galactic abundance gradients. This allows us to study the dust production from AGB stars, SNe and condensation in molecular clouds in dependence on the metallicity.

1.4   Plan of the thesis

In Chapter 2 the evolution model for the Milky Way disk is introduced. The basic ingredients of the model and a comparison with the main set of observational constraints for the Solar neighbourhood and the Milky Way disk are presented. Chapter 3 explains the model for dust return by low mass stars and our estimates for the efficiencies of dust production in SNe. Chapter 4 discusses the evolution of dust in the interstellar medium, namely our approach to the modelling of dust destruction processes by SN shocks and dust growth in molecular clouds. Chapter 5 presents the results for the evolution of the interstellar dust abundances in the Solar neighborhood and the whole Milky Way disk. The dust input into the Solar system and our estimates of dust production efficiencies in SNe are presented. We discuss the main consequences of galactic abundance gradients on the composition of interstellar dust mixture. Some concluding remarks and future prospects are given in Chapter 6.

1. INTRODUCTION

2

Chemical evolution as a tool

2.1 Introduction

Chemical evolution (CE) modeling describes how gas is converted into stars and follows the enrichment of the ISM with products of nucleosynthesis frm AGB stars or supernova explosion. Due to this enrichment the initially primordial gas gradually increases its metallicity to the present observed value. The stellar ejecta are efficiently mixed with the ISM and eventually, with a timescale that is of order of 2.5 Gyr in the Solar vicinity, are incorporated into new generations of stars, that bear the unique records of the chemical composition of the ISM at the instant and location of their formation, *the abundance pattern*. The abundance pattern plays a crucial role in understanding the chemical evolution signatures because the chemical elements and isotopes originate from different stellar sites. The analysis of abundance ratios of different elements reveal the relative role of stellar sources that produced them. This analysis is done by means of chemical evolution modeling.

It provides a powerful tool for the interpretation of the vast volume of observed chemical compositions of stars, the interstellar and even of the intergalactic medium, that allows to trace back the history of the chemical and dynamical evolution of the galaxy (for a review see Matteucci 2003). CE modeling relies on the three main ingredients:

1. stellar yields $Y_i(M, Z)$, characterizing the element production in dependence on stellar mass and metallicity;

2. stellar lifetimes $\tau(M, Z)$, providing the timescale of chemical enrichment;

3. Initial Mass Function (IMF) $\phi(M)$, providing the frequency distribution of stars with respect to their initial masses.

The first two items are provided by the stellar evolution theory, while the IFM is inferred from observations of young stellar clusters. New observations (e.g., more accurate abundance patterns or distance determinations, stellar counts etc) provide new constraints for the CE model, so that it is

never complete, but is continuously developing with the progress in stellar evolution theory and the ever growing observational data.

For the Solar neighborhood there is the largest number of observational constraints, that have to be reproduced by the CE model: G-dwarf distribution, age-metallicity relation, stellar abundance ratios, current rates of supernovae of type II and Ia, and gas, stellar and remnant densities. The metallicity distribution of the G-dwarfs, long living stars with an age comparable to the age of galaxy, is particularly important constraint, which together with observed age-metallicity relations allows to trace back the past history of the evolution and to determine the galaxy formation scenario. Presently the chemical evolution models seem to agree on the open model of galactic evolution, in which the Milky Way is formed by the slow infall of primordial gas from the halo or intergalactic space (Boissier & Prantzos 1999, Hou et al. 2000, Chiappini et al. 1997). Although for the Milky Way disk there is no such constraint as the metallicity distribution of long lived stars in the solar neighborhood, recent modeling of the abundance gradients based on new homogeneous set of observations has confirmed the inside-out scenario of the Milky Way formation, i.e., faster formation of the inner parts of the disk relatively to the outer ones (Cescutti et al. 2007). The model of the Milky Way disk should also reproduce the present observed profiles of gas, stars and star formation rate.

To study the evolution of the dust content of our Galaxy we developed a standard open model of galactic chemical evolution. In the one-zone approximation we neglect radial motions in the galactic disk (but cf. Vorobyov & Shchekinov 2006) and consider its evolution in a set of independent rings. In the Sections 2.2 and 2.3 we describe the basic equations and the ingredients of our CE model. The Sect. 2.5 presents the results for the Solar vicinity and the Sect. 2.6 the model of the Milky Way disk.

2.2   Basic equations

Galactic chemical evolution models describe the temporal change of the surface densities or mass fractions of three main Galactic components: gas, stars and stellar remnants. We follow a mathematical formulation of the problem similar to Dwek (1998), who first extended the standard system of equations for the chemical evolution of the galactic disk (cf. Matteucci 2003) to include the evolution of the dust component of the Galaxy. In case of absence of radial flows the total surface density of the disk Σ_{tot} is determined:

$$\frac{d\,\Sigma_{\text{tot}}(r,t)}{d\,t} = \frac{d\,\Sigma^{\text{inf}}(r,t)}{d\,t} - \frac{d\,\Sigma^{\text{out}}(r,t)}{d\,t} \tag{2.1}$$

The first term on the l.h.s. is the infall rate of matter from the halo or intergalactic space; the second term is the outflow rate, i.e. by galactic wind.

The change of the ISM (gas+dust) surface density Σ_i of element i at the galactocentric radius r is determined by the gas in- and outflows, gas consumption by the star formation, and the mass ejected by stars at the end of their life:

$$\frac{d\,\Sigma_i(r,t)}{d\,t} \quad = \quad \frac{d\,\Sigma_i^{\text{inf}}(r,t)}{d\,t} - \frac{d\,\Sigma_i^{\text{out}}(r,t)}{d\,t} - \frac{\Sigma_i(r,t)}{\Sigma_{\text{ISM}}(r,t)}B(r,t) +$$

Table 2.1: Comparison of some observed properties in the solar neighbourhood with model results

Observable	Model	Observed	Reference
Total surface density $\Sigma_{\rm tot}$ [$M_\odot{\rm pc}^{-2}$]	56	$50-62$	(1)
ISM surface density $\Sigma_{\rm ISM}$ [$M_\odot{\rm pc}^{-2}$]	9.7	$7-13$	(2)
		$13-14$	(3)
Gas fraction $\Sigma_{\rm ISM}/\Sigma_{\rm tot}$	0.17	$0.15-0.25$	(4)
Surface density of visible stars Σ_* [$M_\odot{\rm pc}^{-2}$]	38.6	$30-40$	(5)
Surface density of stellar remnants [$M_\odot{\rm pc}^{-2}$]	7.7	$2-4$	(6)
Star formation rate B [$M_\odot{\rm pc}^{-2}{\rm Gyr}^{-1}$]	3.1	$3.5-5$	(7)
SN II rate $R_{\rm SNII}$ [${\rm pc}^{-2}{\rm Gyr}^{-1}$]	0.016	$0.009-0.0326$	(8)
SN Ia rate $R_{\rm SNIa}$ [${\rm pc}^{-2}{\rm Gyr}^{-1}$]	0.0024	$0.0015-0.0109$	(8)
Infall rate [$M_\odot{\rm pc}^{-2}{\rm Gyr}^{-1}$]	1.45	$0.5-5$	(9)

References: (1) Holmberg & Flynn (2004); (2) Dickey (1993); (3) Olling & Merrifield (2001); (4) Boisser & Prantzos (1999); (5) Gilmore et al. (1989); (6) Mera et al. (1998); (7) Rana (1991); (8) Tammann et al. (1994); (9) Braun & Thilker (2004).

$$+ \int_{M_l}^{M_u} B(r,t_{\rm b})\phi(M)\frac{Y_i(M,Z)}{M_{\rm av}}dM\,, \tag{2.2}$$

where $B(r,t)$ is the stellar birthrate, $Y_i(M,Z)$ is the stellar yield of element/isotope, i.e. mass of element/isotope i ejected by a star at the end of its life, $\phi(M)$ is the Initial Mass Function (IMF), and $M_{\rm av}$ is the average stellar mass. The choice of these quantities for the CE model will be described in the next Section. The instant of birth of a star $t_{\rm b}$ dieing at instant t is given by the non-linear equation

$$t_{\rm b} = t - \tau(M,Z_{\rm ISM}(t_{\rm b}))\,, \tag{2.3}$$

where $\tau(M,Z)$ is the lifetime of a star with mass M and metallicity Z. The Eq. (2.3) is solved numerically for each M and t for $Z_{\rm ISM}(t_{\rm b})$ and $t_{\rm b}$. The metallicity of a star born at instant $t_{\rm b}$ is equal to the metallicity of the interstellar gas at this time. The total gas density in the ISM and the metallicity are given by sums over all nuclei:

$$\Sigma_{\rm ISM}(r,t) = \sum_i \Sigma_i(r,t)\,, \quad Z_{\rm ISM}(r,t) = \sum_{i\neq\{\rm H,He\}} \frac{\Sigma_i(r,t)}{\Sigma_{\rm ISM}(r,t)}\,. \tag{2.4}$$

The surface density of living stars Σ_* at instant t can be calculated from the stellar birthrate:

$$\Sigma_*(r,t) = \int_0^t B(r,t')\left[\int_{M_l}^{M_u} \phi(M)H(t-t'-\tau(M,Z(t')))dM\right]dt'\,, \tag{2.5}$$

Table 2.2: Main observed properties of the galactic disk and values used in model calculations

Observable	Model	Observed	Reference
Scale length of thin disk d_{thin} [kpc]	2.5	2.6 ± 0.6	(1)
Scale length of thick disk d_{thick} [kpc]	3.5	3.6 ± 0.7	(1)
		3.0 ± 1.5	(2)
Scale height of thin disk h_{thin} [kpc]	0.3	0.3 ± 0.06	(1)
Scale height of thick disk h_{thick} [kpc]	0.9	0.9 ± 0.18	(1)
		0.91 ± 0.3	(2)
Thick disk density fraction ρ_{thick}/ρ_{thin}	0.1	0.12 ± 0.01	(1)
		0.059 ± 0.03	(2)
Mass of disk [10^{10} M$_\odot$]	5.1	3-6	(6)
Mass of the ISM [10^9 M$_\odot$]	6.8	6-8	(6)
Stellar mass [10^{10} M$_\odot$]	3.3	4-5	(6)
SN Ia per century	0.16	0.1-0.5	(3)
		0.55-2	(4)
SN II per century	1.2	0.8-3	(5)
		0.4-2	(3)
		0.17-0.7	(4)

References: (1) Jurić et al. 2008; (2) Buser et al. 1999; (3) Cappellaro & Turatto 1996; (4) Tammann et al. 1994; (5) Diel et al. 2006; (6) Boissier & Prantzos (1999).

where $H(t)$ is Heaviside step function introduced to account for the dead stars. The current density of stellar remnants can be calculated by subtracting the density of gas, Σ_{ISM} and living stars, Σ_* from the total density in the disk.

2.3 Main ingredients of CE model

2.3.1 Galaxy model

Formation scenario

First models of chemical evolution of the Galaxy were simple "closed-box" models, in which the Galaxy's mass is already fixed at the initial instant of evolution. However, these models failed to reproduce the metallicity distribution of metal-poor stars, one of the most important observational constraints on chemical evolution modelling, a problem known as G-dwarf problem (see Sect. 2.5.3). Open models assume formation of the Galaxy by accretion of primordial or metal-poor gas from

extragalactic sources to solve the G-dwarf problem, as was first suggested by Chiosi (1980) and later discussed by Pagel (1997). Merging with other galaxies seems not to have played a mayor role during most of the lifetime of the Milky Way, except for the very first evolutionary phase for which stellar dynamics (cf. Helmi et al 2006) and elemental abundances (Reddy et al. 2006; Ramírez et al. 2007) indicate that there were major merging events. Therefore merging is not considered in the model. In open models the total surface density of the disk changes by the accretion of gas, outflows, and radial motions within the disk. For the Milky Way, outflows in eq.(2.1) can be neglected due to the strong gravitational potential, and radial motions are neglected in the one-zone approximation. In our model the infall rate entirely defines the evolution of the total surface density.

Several scenarios for gas accretion have been proposed by different authors, suggesting different rates and sequences for formation of the galactic components, see Matteucci (2003) for details. Models assuming an exponentially decreasing infall of the gas are most successful in reproducing most of the observational constraints. Following Chiappini et al. (1997) we adopt a two-infall, exponentially decreasing model that assumes two subsequent episodes of Galaxy formation. Initially, the halo and thick disk are formed during a short period of about $\tau_{\text{thick}} \approx 1$ Gyr, then the thin disk is formed by accretion of material on a much longer timescale of τ_{thin}. We adopt an inside-out scenario of the disk formation, in which the inner disk forms earlier than the outer (Chiappini et al. (1997)). Cescutti et al. 2007 recently have shown that this scenario is able to reproduce well the abundance gradients in the disk, one of the most important observational constraints. The timescale of the thin disk formation in this model is:

$$\tau_{\text{thin}}(r) = \begin{cases} 0.875r - 0.4375 & \text{for } r > 2 \text{ kpc} \\ 1.3125 & \text{for } r < 2 \text{ kpc} \end{cases}, \tag{2.6}$$

The accretion rate is given in this model by the expression:

$$\frac{\mathrm{d}\,\Sigma_i^{\text{inf}}(r,t)}{\mathrm{d}\,t} = \begin{cases} (X_i)_{\text{inf}}A(r)e^{-t/\tau_{\text{thick}}} & \text{for } t < t_0 \\ (X_i)_{\text{inf}}A(r)e^{-t/\tau_{\text{thick}}} + (X_i)'_{\text{inf}}B(r)e^{-(t-t_0)/\tau_{\text{thin}}} & \text{for } t > t_0, \end{cases} \tag{2.7}$$

where $t_0 = 1$ Gyr is the time of onset of accretion onto the thin disk. The formation of the disk is assumed to start $t_{\text{G}} = 13$ Gyrs ago. Both $(X_i)_{\text{inf}}$ and $(X_i)'_{\text{inf}}$ denote element abundances of infalling gas, which we assume to be primordial.

The coefficients $A(r)$ and $B(r)$ are derived so as to reproduce the present-day density distribution of the disk:

$$A(r) \quad = \quad \frac{\Sigma_{\text{thick}}(r,t_{\text{G}})}{\tau_{\text{thick}}\left(1 - e^{-t_{\text{G}}/\tau_{\text{thick}}}\right)}, \tag{2.8}$$

$$B(r) \quad = \quad \frac{\Sigma_{\text{thin}}(r,t_{\text{G}})}{\tau_{\text{thin}}(r)\left(1 - e^{-(t_{\text{G}}-t_0)/\tau_{\text{thin}}(r)}\right)}. \tag{2.9}$$

Present density distribution in the disk

The general disk parameters are determined from kinematics measurements, by star counts together with proper motions, or with colour distribution analysis. The observed characteristics of the Milky Way and the values chosen for the model calculations are summarized in Table 2.2. The present Galactic disk is well fit by the the double exponential density distributions:

$$\Sigma_{\text{thin}}(r, t_G) = \Sigma_{0,\text{thin}} e^{-(r-r_\odot)/d_{\text{thin}}} , \quad M_{\text{thin}}(t_G) = 2\pi\Sigma_{0,\text{thin}} d_{\text{thin}}^2 e^{r_\odot/d_{\text{thin}}} ,$$
$$\Sigma_{\text{thick}}(r, t_G) = \Sigma_{0,thick} e^{-(r-r_\odot)/d_{\text{thick}}} , \quad M_{\text{thick}}(t_G) = 2\pi\Sigma_{\text{thick}}^0 d_{\text{thick}}^2 e^{r_\odot/d_{\text{thick}}} , \tag{2.10}$$

where d_{thin} and d_{thick} are the scale lengths of the thin and thick disk, $\Sigma_{0,\text{thin}}$ and $\Sigma_{0,\text{thin}}$ are the total (gas + stars) local surface densities of the thin and thick disk, respectively, and M_{thin} and M_{thick} denote the total disk masses at present time.

The parameters of the disks as well as the ratio between their masses significantly vary in the literature. We adopt a value of d_{thin} = 2.5 kpc, within range of the recently determined value of 2.6 ± 0.6 kpc from the Milky Way tomography with Sloan Digital Sky Survey (Jurić et al. 2008). The radial scale length of the thick disk varies in the range of 2.5-4.5 kpc in different studies; the most recent determinations found a value of 3.04 ± 0.11 kpc (Cabrera-Lavers et al. 2005) and 3.6 ± 0.7 kpc (Jurić et al. 2008). The value of 3.5 kpc is adopted for d_{thick} for our Milky Way model.

The surface densities of the thin and thick disk can be obtained from the ratio of the volume densities and scale heights of the thin and thick disks known from observations. We adopt the more moderate value of $\rho_{\text{thick}}/\rho_{\text{thin}}$ = 0.06 from Buser et al. (1999), which provides a better fit to the observed galactic abundance gradients. Corresponding values of the surface densities are $\Sigma_{\text{thin}}(r_\odot, t_G)$ = 46 $M_\odot\,\text{pc}^{-2}$ and $\Sigma_{\text{thick}}(r_\odot, t_G)$ = 10 $M_\odot\,\text{pc}^{-2}$ normalized to the total density in the solar neighborhood of 56 $M_\odot\,\text{pc}^{-2}$. The masses of the thin and thick disk from 2.10 are $5.5 \times 10^{10}\,M_\odot$ and $8 \times 10^9\,M_\odot$, respectively.

2.3.2   Star formation rate

The stellar formation rate (SFR) determines how gas is converted into stars. The details of the star formation process are still poorly understood, therefore the models of chemical evolution use heuristic prescriptions for the star formation rate, which depend on the gas density, total surface density, galactic rotation etc.

Observations of the global SFR in spiral galaxies suggest a Schmidt-law type of dependence of the stellar birthrate on some power of the total gas surface density (Kennicutt 1998). However, studies of star formation rate profiles in the galactic disk from different stellar tracers indicate strong radial dependence, which is also one of the most likely mechanisms explaining Galactic abundance gradients (e.g. Matteucci 2003). Although a number of different star formation prescriptions has been proposed in the literature, most of them rest on two main physical assumptions.

- One assumption correlates the star formation efficiency with angular frequency of the gas in the disk in addition to the dependence on the gas density. It is based on the idea that the stars are formed when the ISM, rotating with angular frequency $\Omega(r)$ is periodically compressed by the passage of the spiral pattern, rotating with a frequency $\Omega_p \ll \Omega(r)$. This leads to SFR $\propto (\Omega_{(r)} - \Omega_p) \propto \Omega(r)$, and for the disks with the flat rotational curves, to SFR $\propto r^{-1}$ (Wyse & Silk 1989). Boisser & Prantzos 1999 proposed following stellar birthrate, based on the above considerations:

$$B(r,t) = \nu \Sigma_{\mathrm{g}}(r,t)^{1.5} \left(r/r_\odot \right)^{-1} . \tag{2.11}$$

- Another important star formation rate was suggested in self-regulating star formation theory in Talbot & Arnett 1975, who first introduced an additional dependence of the star formation rate on the total surface density $\Sigma_{\mathrm{tot}}(r,t)$. The idea for this is that the star formation process in the molecular cloud is regulated by self-gravity, that depends on the total local density of the matter. Later Dopita & Ryder (1994) confirmed this by observations and suggested an empirical law of star formation $B(r,t) \propto \Sigma_{\mathrm{tot}}^{n} \Sigma_{\mathrm{g}}^{m}$, with $m = 5/3$ and $n = 1/3$ giving the best fit for the observed relationship between the stellar brightness and the surface brightness in H_α in galactic disks. At the same time they found that a SFR as given by Eq. (2.11) seems to excluded by their observations. Later Alibes et al. 2001 used this SFR in the form:

$$B(r,t) = \nu \frac{\Sigma_{\mathrm{tot}}(r,t)^{n} \Sigma_{\mathrm{g}}(r,t)^{m}}{\Sigma_{\mathrm{tot}}(r_\odot, t_{\mathrm{G}})^{n+m-1}} , \tag{2.12}$$

A more complicated parametrization of the star formation law was proposed in Chiappini et al. 1997:

$$B(r,t) = \nu \left[\frac{\Sigma_{\mathrm{tot}}(r,t)}{\Sigma_{\mathrm{tot}}(r_\odot, t)} \right]^{2(k-1)} \left[\frac{\Sigma_{\mathrm{tot}}(r, t_{\mathrm{G}})}{\Sigma_{\mathrm{tot}}(r,t)} \right]^{k-1} \Sigma_{\mathrm{g}}(r,t)^{k} , \tag{2.13}$$

We tested the different prescriptions for the stellar birthrate described above and obtained the best fit with the SFR from Chiappini 1997 with the power of $k = 5/3$ (Dopita & Ryder 1994). Therefore we adopt the SFR from Eq. (2.13) for the chemical evolution model presented in Sect. 2.5, which will provide the basis for constructing multicomponent dust model. For the Solar neighborhood, $r = r_\odot$, one obtains the following expression for the stellar birthrate:

$$B = \nu \Sigma_\odot^{2/3} \Sigma_{\mathrm{tot}}^{-2/3}(t) \Sigma_{\mathrm{gas}}^{5/3}(t) , \tag{2.14}$$

where $\Sigma_\odot$ is the total surface density at the Solar cylinder at present time; the value of $56\,\mathrm{M_\odot\,pc^{-2}}$ is taken from observations (Table 2.1). ν is star formation efficiency, fitted such that the model reproduces the present-day star formation rate and gas density in the solar neighbourhood. We take $\nu = 1.3\,\mathrm{Gyr^{-1}}$.

The observations point to the existence of a star formation threshold, i.e., a minimum surface density Σ_g required for star formation, which appears to be about 7 $M_\odot\,pc^{-2}$ (Kennicutt 1998). However, recent observations from GALEX UV satellite reveal star formation even in regions with as much lower density, implying that the density threshold should be a function of the physical parameters of the environment. Since the question of the star formation threshold is still an open one, we set the density threshold in our star formation law to the value suggested in Kennicutt 1998. In the numerical calculation, the transition from zero to the threshold value is smoothed to avoid the unphysical numerical oscillations in the solution for the surface density Σ_g close to the threshold that are otherwise produced by some integration methods.

2.3.3 Initial mass function

The initial mass function (IMF) $\Phi(M)$ gives the distribution of masses of stars born in a star formation event. The IMF is one of the most important components of the galactic chemical evolution model as it establishes the frequency of low and high mass stars, and thus their relative role in the chemical evolution. Observations indicate surprising constancy of the IMF for different systems and environments, allowing to use the IMF $\phi(M)$ throughout the evolution. We adopt the IMF consisting of four separate power-law type distributions in four separate intervals of initial masses proposed by Kroupa (2002):

$$
\Phi(M) = A \begin{cases} C_1 M^{-0.3}, & 0.01 \le M/M_\odot < 0.08 \\ C_2 M^{-1.3}, & 0.08 \le M/M_\odot < 0.5 \\ C_3 M^{-2.3}, & 0.5 \le M/M_\odot < 1.0 \\ C_4 M^{-2.7}, & 1.0 \le M/M_\odot < 100, \end{cases}
\tag{2.15}
$$

where the coefficients $C_1 = 2.0158$, $C_2 = 0.1612$, and $C_3 = C_4 = 0.0806$ are derived from the normalization procedure. During the calculation we found that one obtains better model fits, if for high-mass stars, the exponent is changed to 2.55. This somewhat flatter power law ($\Phi \propto M^{-2.6}$) is, for instance, observed for massive stars in the Orion nebula (Preibisch et al. 2002).

The number of stars in the mass range from M_1 to M_2 is:

$$
N(M_1 < M < M_2) = \int_{M_1}^{M_2} \Phi(M)\,dM\,,
\tag{2.16}
$$

and average stellar mass is then given by the integration over the full range of stellar masses:

$$
M_{av} = \int_{0.01}^{100} M\Phi(M)\,dM\,.
\tag{2.17}
$$

For adopted IMF the value of average stellar mass is 0.27 $M_\odot$.

2.3.4 Stellar lifetimes and nucleosynthesis yields

Stellar lifetimes and nucleosynthesis yields result from extensive stellar evolution calculations usually involving state of the art methods and significant computational efforts. Stellar yields $Y_i(M, Z)$ represent the mass of element i ejected by the a star of mass M and metallicity Z. They are usually divided into three groups according to different nucleosynthesis sites: low and intermediate mass stars, Supernovae Ia, and massive stars.

Low and Intermediate mass stars 0.8-8 $M_\odot$

The single low and intermediate mass stars are important for the galactic evolution due to their high frequency relatively to high mass stars. They contribute to the enrichment of the Milky Way with heavy elements due to excessive mass loss during the final stage of their AGB evolution. We adopt the yields for H, ^{4}He, ^{12}C, ^{13}C, ^{14}N, and ^{16}O from van den Hoek & Groenewegen (1997), tabulated for the range $0.8 - 8\ M_\odot$ of initial masses and for metallicities 0.001, 0.004, 0.008, 0.02, and 0.04. Van den Hoek & Groenewegen (1997) computed their yields combining the evolutionary tracks of the Geneva group up to the early asymptotic giant branch with a synthetic thermal pulsing AGB evolution models including first, second and third dredge-up phases and Hot Bottom Burning. For ^{23}Na, ^{24}Mg, ^{25}Mg, ^{26}Mg, ^{26}Al, and ^{27}Al, the yields of Karakas et al. (2003) for the mass-range $1.0 - 6.5\ M_\odot$ and range of metallicities $Z = 0.004,\ 0.008,\ 0.02$ are used. The data are extrapolated outside the range of tables. The authors perform stellar evolution calculations from the pre-main sequence to near the end of the thermally pulsing AGB phase with post-processing nucleosynthesis calculations.

Supernovae Type Ia

SN Ia are important contributors of the iron and the iron peak elements in the late disk evolution. They are commonly believed to originate from deflagration in a C-O White Dwarf in a binary system, which is triggered by accretion of material from a companion (Whelan & Iben 1973), although the nature of the progenitors is still a question under debates. The rate of SN Ia explosions is calculated using the prescription of Matteucci & Greggio (1986) for a model assuming a C-O white dwarf plus red giant:

$$R_{\mathrm{SNIa}}(t) = \beta M_{\mathrm{av}}^{-1} \int_{M_{B\,\mathrm{min}}}^{M_{B\,\mathrm{max}}} \phi(M_B) \left[\int_{\mu_{\mathrm{min}}}^{0.5} f(\mu) B(t - \tau(\mu M_B)) d\mu \right] dM_B \,, \tag{2.18}$$

where $f(\mu) = 24\mu^2$ is the distribution function for the mass fraction of the secondary ($\mu = M_2/M_B$), $\mu_{\mathrm{min}} = \max\left[\frac{M_2(t)}{M_B}, \frac{M_B - 0.5 M_{B\,\mathrm{max}}}{M_B}\right]$. The range of binary masses for this scenario is from $M_{B\,\mathrm{min}} = 3\ M_\odot$, in order to ensure that the accreting white dwarf reaches the Chandrasekhar mass, to $M_{B\,\mathrm{max}} = 16\ M_\odot$ based on the assumption that the C-O white dwarf comes from primaries with a mass up to $8\ M_\odot$. The parameter β describes the fraction of the systems in this mass range that eventually succeeded in evolving to a SN Ia event, which is fixed by reproducing the supernova rate ratio $R_{\mathrm{SNII}}/R_{\mathrm{SNIa}}$ and the
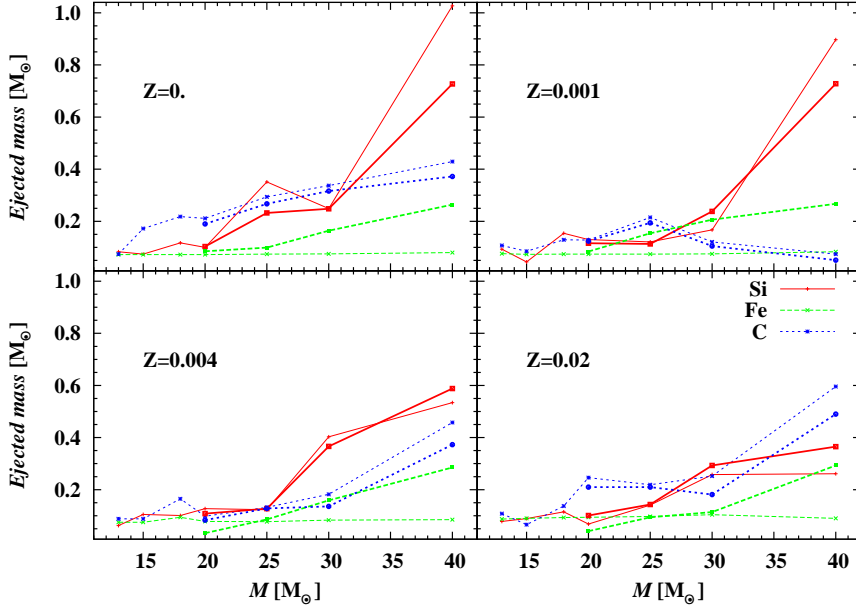
Figure 2.1: Ejected masses of the important dust-forming elements, Si, C and Fe from Supernovae (the thin lines) and Hypernovae (thick lines) as a function of initial stellar mass from Nomoto et al. (2006) yields

iron abundance; a value of $\beta = 2 \cdot 10^{-2}$ gives the best fit of our model to the observations. The mass ejection rate for SN Ia is determined by the similar expression:

$$E_{i,\mathrm{SNIa}}(t) = \beta M_{\mathrm{av}}^{-1} \int_{M_{B\min}}^{M_{B\max}} \phi(M_B) \left[\int_{\mu_{\min}}^{0.5} f(\mu) B(t - \tau(\mu M_B)) Y_{i,\mathrm{SNIa}} d\mu \right] dM_B \,, \qquad (2.19)$$

The SN Ia metallicity dependent yields $Y_{i,\mathrm{SNIa}}$ are taken from W7 models in Iwamoto et al. (1999). Hachisu et al. (1996; 1999) recently propose a new evolutionary model for SN Ia progenitor, that accounts for the essential role played by an optically thick stellar wind from the WD in stabilizing the mass transfer in binaries to a compact object. They have found that SN Ia can only occur for the progenitors with [Fe/H]>-1.1. This restriction is applied in our chemical evolution model.

Within the frame of the generally preferred close binary model, the appearance of SN Ia event is delayed till secondary low or intermediate mass component fills its Roche Lobe and start to transfer matter, this is reflected in the delayed Fe enrichment of the ISM relative to α-elements produced by short lived massive stars. However, recently a new hypothesis for SN Ia progenitor was proposed, according to which a percentage from 35 to 50 per cent of the total Type Ia SNe should occur by systems with lifetimes as short as 10^8 yr (Matteucci et al. 2006).

Massive stars $8\,M_\odot \le M \le 120\,M_\odot$

The massive stars are believed to explode as core collapse supernovae unless the entire star collapses into a black hole with no mass ejection. Nuclei synthesized by massive stars during the pre-supernova phase and in the final explosion ejected into the ISM constitute most of metals in the Universe. The problem of yields from massive stars is complicated by the need to model supernova explosions, many details of which are still unknown. In particular main uncertainties in the SN II yields are introduced by mass loss rate in the pre-supernova phase, the mechanism that initiates explosion, and the mass cut, the surface separating the material falling back onto neutronized core from the ejected shell.

Exhaustive calculations of Woosley & Weaver (1995) made available nucleosynthesis yields for the massive stars for an extensive set of isotopes (from H to Zn), stellar masses (from 11 to 40 $M_\odot$) and metallicities (from Z=0 to Z=$Z_\odot$). For more than a decade they remained the most commonly used yields in chemical evolution modelling, with commonly accepted reduction of iron yield by a factor 2 and an increase by a factor 2 of the yield of Mg. For comparison and analysis of available yields we refer e.g., to Goswami & Prantzos (2000) and Prantzos (2000).

Recently new nucleosynthesis prescriptions became available, based on new theoretical and observational studies of supernovae and extremely metal poor stars in the halo (Nomoto et al. 2006). The yields include two additional classes of SNe: 1) very energetic Hypernovae, whose kinetic energy equals 10 times of that of normal core-collapse supernovae, and 2) very faint and low-energy SNe. The Nomoto et al. 2006 yields for Hypernovae are calculated for the masses 20, 25, 30, 40, 50 $M_\odot$ and explosion energy E_{51}=10, 20, 30, 40, and for normal SNe II of 13 - 50 $M_\odot$, $E_{51} = 1$, and Z=0, 0.001, 0.004, 0.02. We present the ejected masses of important dust-forming elements, Si, C and Fe as a function of initial stellar mass from these yields in Fig. 2.1. It demonstrates that the SNe and HNe eject quite similar amount of carbon; massive stars with $M > 30$ $M_\odot$, which explode as HNe, return larger mass of iron yields, however. As seen in the figure, there is a weak dependence of supernovae dust production on the initial stellar metallicity.

For comparison purposes, we implemented in the chemical model the yields of Woosley & Weaver (1995) and Nomoto et al. 2006 and show that the latter describes better the abundance ratio of dust forming elements in the Solar neighborhood. Therefore it is preferred throughout the calculations.

The rate of explosions of massive stars as SN II is determined by the expression:

$$R_{\mathrm{SNII}}(t) = (1-\beta)M_{\mathrm{av}}^{-1} \int_{M_{\mathrm{wd}}}^{M_{B\max}} \phi(M)B(t-\tau(M,Z))dM + M_{\mathrm{av}}^{-1} \int_{M_{B\max}}^{M_u} \phi(M)B(t-\tau(M,Z))\,dM \quad (2.20)$$

where M_{wd} is the lower mass for the formation of degenerate C-O core, we take the value of $8\,M_\odot$.

The mass ejection of element i rate is:

$$E_{i,\mathrm{SNII}}(t) = (1-\beta)M_{\mathrm{av}}^{-1} \int_{M_{\mathrm{wd}}}^{M_{B\max}} \phi(M)B(t-\tau(M,Z))dM + M_{\mathrm{av}}^{-1} \int_{M_{B\max}}^{M_u} \phi(M)B(t-\tau(M,Z))Y_{i,\mathrm{SNII}}(M,Z)dM$$

$$(2.21)$$

For massive stars with $M > 40$ $M_\odot$, the mass returned by the stars up to the end of carbon burning is taken from the models of Schaller et al. (1993), Schaerer et al. (1993), and Charbonnel

et al. (1993). It is assumed that the remaining mass collapses into a Black Hole. The mass return of nuclei is determined from the models for all those nuclei, whose surface abundances are given in the tables. For all others, we assume that their abundance in the returned mass equals their initial abundance.

Stellar lifetimes

Stellar lifetimes determine the timescale of the enrichment of the ISM gas by stars. They usually result from extensive numerical simulations of the stellar evolution, which can strongly depend on the particular stellar models, prescription for the stellar wind, etc. We implement the stellar lifetimes as a function of stellar mass and metallicity by using an analytical approximation given by Reiteri et al. (1996):

$$\log \tau_*(M, Z) = a_0(Z) + a_1(Z) \log M + a_2(Z)(\log M)^2 \,, \tag{2.22}$$

where lifetime is expressed in years and mass in Solar units. The coefficients are given by the following expressions,

$$
\begin{aligned}
a_0(Z) &= 10.13 + 0.07547 \log Z - 0.008084 (\log Z)^2 \\
a_1(Z) &= -4.424 - 0.7939 \log Z - 0.1187 (\log Z)^2 \\
a_2(Z) &= 1.262 + 0.3385 \log Z + 0.05417 (\log Z)^2
\end{aligned}
$$

This formula is a good fit for the stellar lifetimes computed by the Padova group (Alongi et al. 1993; Bressan et al. 1993, Bertelli et al. 1994) in the metallicity range $7 \cdot 10^{-5} < Z < 3 \cdot 10^{-2}$ and for initial masses between 0.6 and 120 M$_\odot$.

2.3.5   Mixing of ejected material in the ISM

It is assumed that stellar ejecta are perfectly and instantaneously mixed with the general interstellar medium; i.e., the composition of the interstellar medium is assumed to be homogeneous and uniquely defined at each instant. This is justified by the observed low scatter of element abundances in the present ISM and of stellar element abundances in open stellar clusters (see Scalo & Elmegreen 2004, and references therein).

2.4   Numerical implementation

We have written a flexible code in FORTRAN 90 for the evolution of the element abundances in the gas and dust phase in the interstellar medium. For this purpose we numerically solve a system of non-linear integro-differential equations (2.2) together with Eq. (2.3) for the instants of stellar birth to follow the evolution of the surface densities of 69 isotopes from H to Zn and 12 dust species. In the present work the code has been used for study the evolution of the Solar neighborhood and the Milky
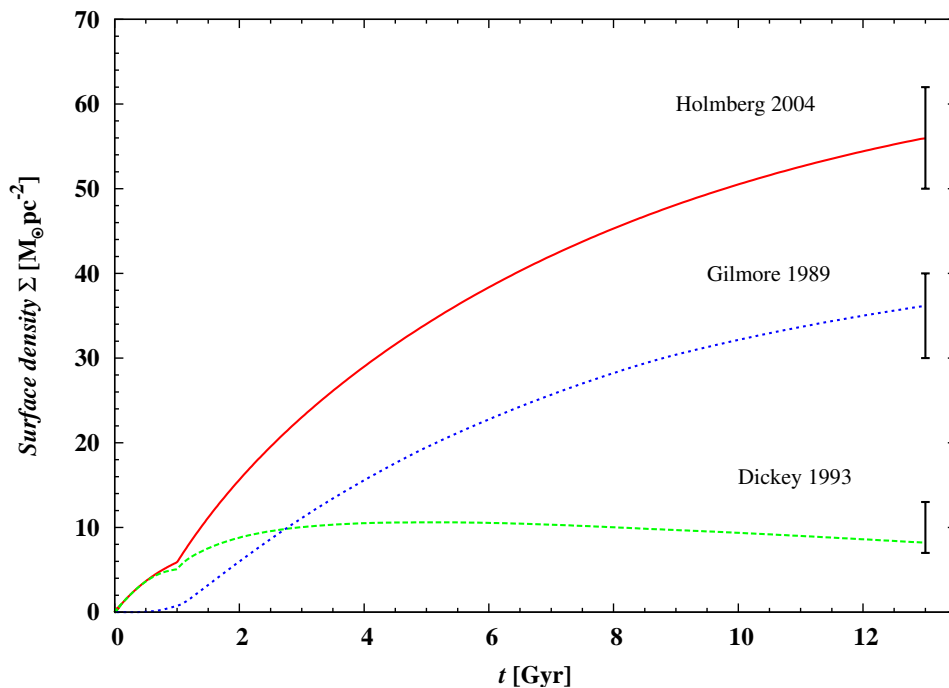
Figure 2.2: Time evolution of the total surface density Σ_{tot} (full line), of the surface density of visible stars (dotted line), and of the interstellar matter surface density Σ_{ISM} (dashed line) of the galactic disk at the solar distance from the galactic centre, and observed values for the present day total surface density in the solar neighbourhood (Holmberg & Flynn 2004), for the surface density of the stellar component (Gilmore et al. 1989), and for the surface density of the interstellar medium (Dickey 1993)

Way disk. The main ingredients of the chemical evolution model used in Eq. (2.2) are discussed in Sect. 2.3, the infall rate is given by Eq. (2.7), the stellar birthrate $B(r, t)$ by Eq. (2.13), the IMF $\phi(M)$ by the Eq. (2.15), the stellar lifetimes $\tau(M, Z)$ by Eqs. (2.22). The outflow term in Eq. (2.2) is neglected, since it is not important for massive galaxy like the Milky Way. The equations for the dust evolution are similar to Eq. (2.2) and discussed in Sect. 3.1. An explicit integration method is used with the 5-th order Runge-Kutta scheme with adaptive time step refinement.

We performed the preliminary tests showed that the code can also be a useful tool in study of the evolution of gas and dust content in different types of galaxies, dwarf galaxies, other spirals, young star bursts. It is easily adjustable for the different ingredients of the chemical evolution model by modification in formation scenario, total density distribution, star formation rate, and the IMF.

2.5 Evolution of the Solar neighborhood

Now we show the results of a numerical calculation of the chemical evolution of the Galactic ring at the position of the Sun. The viability of chemical evolution model for the Solar neighborhood is

usually tested by comparison with some standard set of observational constraints: G-dwarf metallicity distribution, age-metallicity relation, Solar System abundances at the instant of its formation t_{SSF}, present stellar birthrate, SN Ia and SN II rate. The model for the whole galactic disk should additionally reproduce observed gas and stellar density profiles, stellar birthrate along galactic disk, and radial abundance gradients.

We perform calculations with the WW95 yields for massive stars as well as with the most recent yields from Nomoto et al. (2006). In the following we will discuss application of both yields. Since the Nomoto et al. (2006) yields produce results that better fit the abundance ratios of main dust forming elements, we use them in our CE model coupled with the dust evolution.

Figure 2.2 shows the evolution of the total surface mass density $\Sigma_{tot}(r_\odot, t)$ and that of the interstellar medium $\Sigma_{ISM}(r_\odot, t)$ for the galactic disk. In the model it is assumed that the formation of the disk started 13 Gyrs ago. Initially most of the material in the disk was in gaseous interstellar matter, but today and at the time of Solar System formation most of the galactic matter is condensed into stars. A minor fraction is locked up in stellar remnants (White Dwarfs, Neutron Stars, Black Holes).

The evolution of the stellar birthrate is shown in Fig. 2.3a. Star formation commences about 1 Gyr after the onset of matter infall since about 1 Gyr time is required in the two-infall model until the gas density at the galactocentric distance of the sun increases to the threshold value for the star formation of $M_{ISM} = 7\,M_\odot\,pc^{-2}$ (Kennicutt 1998). The stellar birthrate culminated about 2 Gyrs after the onset of star formation, and since then it had gradually declined. Most of the stars born are low and intermediate mass stars. The massive stars mass fraction for the newly born stars is only 3.4% according to the initial mass function Eq. (2.15), but this small fraction is responsible for nearly all of the heavy nuclei synthesised in the Milky Way.

Figure 2.3b shows the evolution of the supernova rates at the solar galactocentric distance $r_\odot$. Because of the short lifetime of massive stars, the supernova rate for type II supernovae closely resembles the birthrate of stars. Supernovae of type Ia appear with a delay of several Gyrs because (i) their progenitors are long-lived intermediate mass stars and (ii) supernova explosions in binaries are suppressed at low metallicities as proposed by Hachisu et al. (1996; 1999). Since supernovae of type Ia are the main sources of Fe, the iron abundance increases in the Milky Way only on a rather long timescale.

2.5.1 Chemical evolution in the Solar neighborhood

For constraining of the chemical evolution model the total gas abundances are usually compared with the stellar abundances inferred from the photospheric spectra of stars. It is generally assumed that the abundances of the stellar photosphere bear record of the initial composition of the original molecular cloud out of a star was formed. Accordingly to the modern stellar evolution theory the products of nucleosynthesis are not usually mixed with the surface layers, expect such known examples as Wolf-Rayett stars, helium stars, AGB stars after dregde-up, etc. This is also confirmed by the close agreement between element abundances from the meteorites representing material of the parent
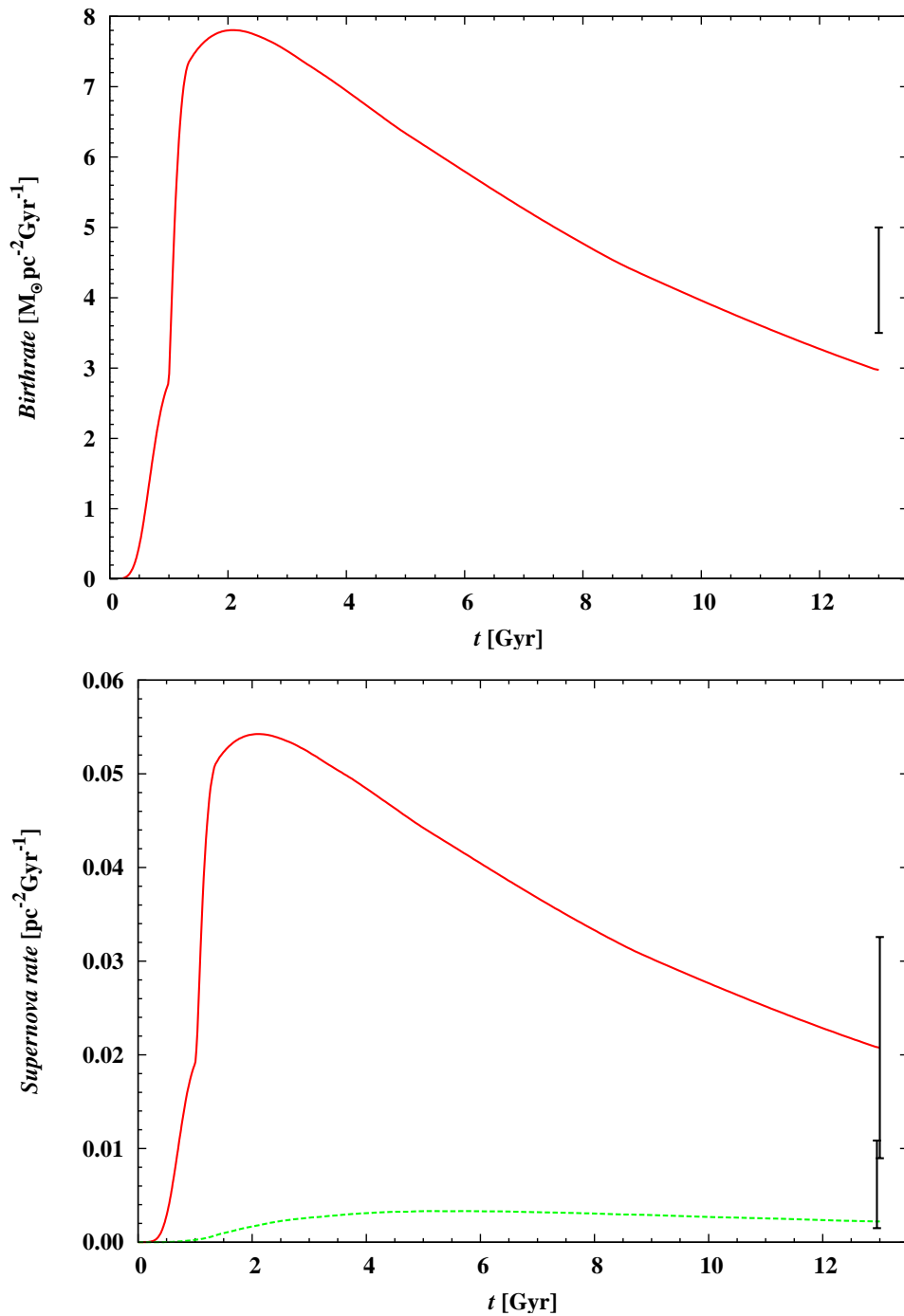
Figure 2.3: (a) Evolution of the stellar birthrate B at the solar galactocentric distance $r_\odot$. The error bar shows the presently observed stellar birthrate (Rana 1991). (b) Evolution of the supernova type II (full line) and type Ia (dashed line) rates at the solar galactocentric distance $r_\odot$ and observed values at the present time from Tammann (1994).
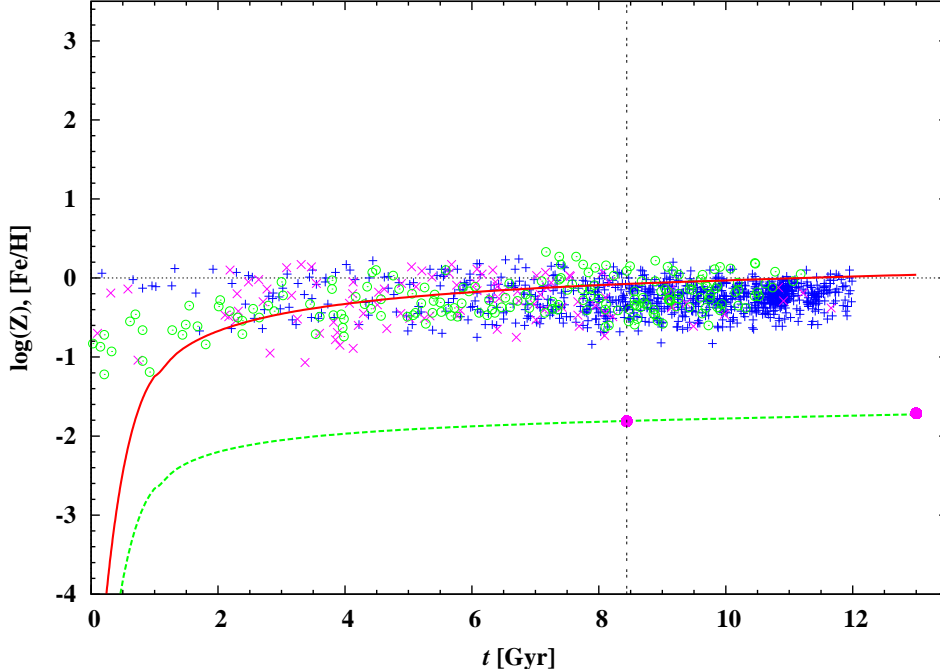
Figure 2.4: Evolution of metallicity Z of the ISM (full line) at the solar galactocentric distance $r_\odot$ and Age-metallicity relation for [Fe/H] (dashed line). The pluses and crosses show the age-metallicity relation from the sample of thin and thick disk stars, respectively from Ibukiyama & Arimoto (2002). The open circles show data from Ramírez et al. (2007). The thin vertical line indicates the Solar System birth time which we assume to be 4.56 Gyr ago, and the two filled circles indicate the observed metallicity of the sun and of the present-day ISM.

clouds formed the Solar System 4.56 Gyr ago and the Solar photospheric abundances. Direct comparison of model results with the present gas abundances is complicated because many elements are "missing" from the gas phase being condensed onto dust grains. Therefore the element abundances measured along different lines of sight in the ISM are used to constrain the dust model.

2.5.2 Evolution of metallicity

Figure 2.4 shows the time evolution of the metallicity Z and the abundance ratio [Fe/H] [1] of the interstellar medium at the solar radius $r_\odot$. The predicted evolution of the [Fe/H] ratio in the ISM is compared with the age-metallicity relation of the solar neighbourhood of late-type dwarfs from the

---

[1] The abundance ratio [X/Y] for two elements X and Y is defined as

$$[X/Y] = \log\left(\frac{\epsilon_X}{\epsilon_Y}\right) - \log\left(\frac{\epsilon_X}{\epsilon_Y}\right)_\odot ,$$

where ϵ_X is the element abundance of element X by number relative to hydrogen.

sample of thin and thick disk stars with distances measured by HIPPARCOS satellite (Ibukiyama & Arimoto 2002); the typical error in [Fe/H] in this data is of 0.15 dex, while it is of 0.1 dex in older data from Edvardsson (1993). The Figure also show the recent set of data from Ramírez et al. (2007).

The age-metallicity relation is reasonably well reproduced for the last about 10 Gyrs, but there is an increasing discrepancy for earlier times. This is a general problem of all such evolution calculations and most likely stems from the unrealistically high stellar ages for many stars due to the rather crude methods of age determination.

All model calculations for the evolution of heavy element abundances with time predict a well-defined relation between metallicity and time-of-birth at a certain location in the galactic disk like the one shown in Fig. 2.4. Observationally determined ages obtained by comparing the position of a star in the Hertzsprung-Russel diagram with evolutionary isochrones, and relating spectroscopically determined metallicities of stars with such age determinations, show a tremendous scattering of metallicities for a given age. It has been concluded that this reflects (i) a true scattering of metallicities of the matter out of which stars are formed at given galactocentric radius and birthtime, and (ii) possibly a mixing of stars from different galactic zones by radial diffusion (Edvardsson et al. 1993). Pont & Eyer (2004) have shown, however, that the tremendous scattering most likely results from the difficulty of obtaining reliable stellar ages from evolutionary isochrones and that any true internal scattering of metallicities at given age is probably less than 0.15 dex. More careful analysis of age-metallicity relations based on such improved methods (da Silva et al. 2006) also seem to support a small intrinsic scatter of metallicities at any given age.

2.5.3   Metallicity distribution of G dwarfs

We compare the observed G-dwarf distribution from the most recent and most complete compilation of Nordström et al. (2004) with what is predicted by the model in Fig. 2.5. The dashed line shows the result of a convolution of the model results with a Gaussian with dispersion of 0.2 dex in order to simulate observational errors in the metallicity determination and intrinsic cosmic scatter in metal abundances. The errors of modern abundance determinations are usually claimed to be 0.1 dex or even less. The true scatter of stellar abundances for stars born at the same instant and location is difficult to determine, since neither the birthplace nor the birthtime of single stars is accurately known. The small scatter of abundances between stars in open stellar clusters indicate, however, that the intrinsic scatter seems to be very small (see Scalo & Elmegreen 2004, and references therein); we arbitrarily assume a contribution of 0.1 dex to the total scatter.

The calculated metallicity distribution reproduces the general trends of the observed distribution, but it does not agree particular well. Some deviations are seen for low and high metallicities. After convolution the discrepancies at the higher metallicity end disappear almost completely. For low metallicities the discrepancies persist and indicate that our model assumptions are not likely to be realistic for the earliest evolutionary phase. Since, for the main application of our model, this phase is not important, we did not try to improve the model in this respect.
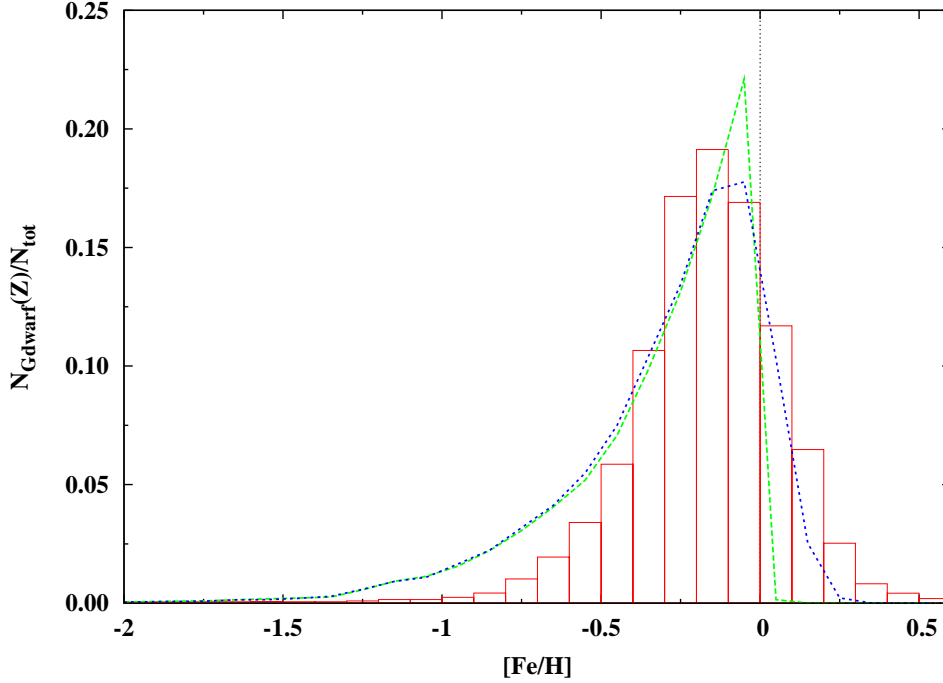
Figure 2.5: G-dwarf metallicity distribution in the solar vicinity predicted by the model and the observed distribution as derived by Nordström (2004). The thin dashed line shows the G-dwarf distribution from direct calculations, while the thick dotted line is the result of a convolution with a Gaussian with half-width 0.2 dex to account for the observational scatter.

2.5.4   Evolution of abundance ratios of individual elements

Abundance ratios [X/Fe] of elements X and their variation with time reflect the synthesis of heavy elements during galactic evolution. Reproducing these variations by the model is one of the most important tests of the model's reliability. For comparing the variation of [X/Fe] with observed variations of stellar abundances, stellar ages would be required that are, however, unknown or of low accuracy. One prefers to compare instead the variation of the abundance ratios [X/Fe] with the abundance ratio [Fe/H], since [Fe/H] is also determined from stellar atmosphere analysis and varies, at least for the Milky Way, monotonously with the age of the galactic disk (cf. Fig. 2.4), i.e., can be taken as a measure of stellar age. In our model we have calculated the evolution of 63 isotopes using nucleosynthesis prescription of Nomoto et al. (2006) and, for comparison, that of Woosley & Weaver (1995). Results are presented in Fig. 2.6 for the elements related to dust formation. We concentrate here on these elements, since we are mainly concerned with problems related to interstellar dust evolution. The model calculations with new yields reproduce well the observed abundance ratios for O, Mg, Ca for all range of metallicities as well as for [Al/Fe] for [Fe/H]<1.5, in contrast to the results with WW95 yields. The general trend of [S/Fe] and [Si/Fe] is better described with new yields. The WW95 yields
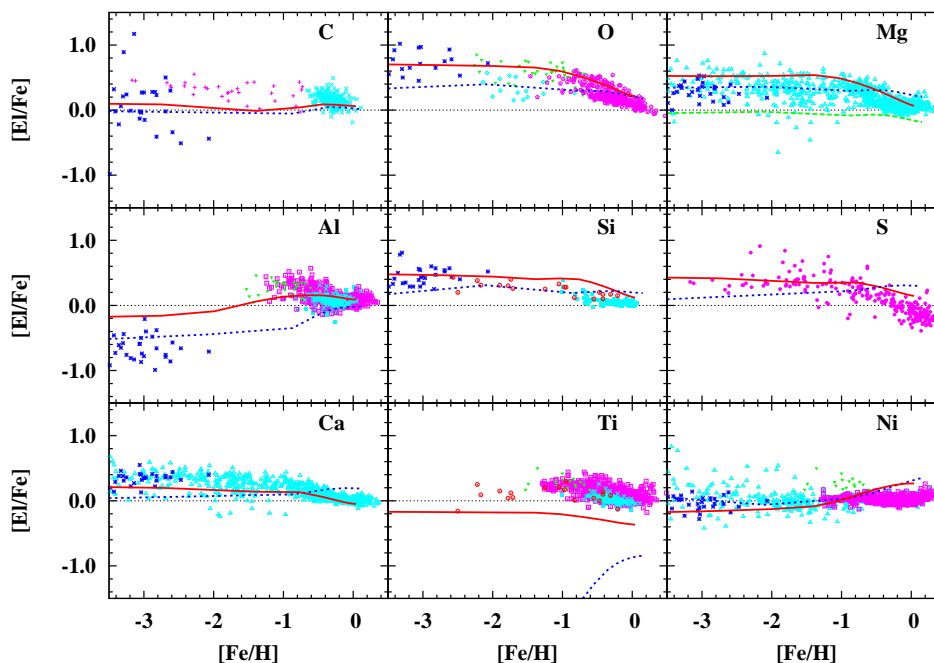
Figure 2.6: Comparison of the predicted abundance ratios of the main dust-forming elements [El/Fe] with observations of stellar abundances. The solid and dashed lines show model calculations with Nomoto (2006) and Woosley & Weaver (1995) SNII yields, respectively. We corrected WW95 yields for Fe and Mg to achieve better fits to observations. For illustrative purposes, a model calculation with uncorrected Mg yields from WW95 is shown with a thin dashed line. The observed stellar element abundances for F and G stars from the solar neighbourhood are shown with different symbols for each of the sources: pluses (Akerman et al. 2004), crosses (Reddy et al. (2003), open squares (Soubiran et al. 2005), open rhombuses (Melendez et al. 2002), solid downwards triangles (Jonsell et al. 2005), open upwards triangles (Venn et al. 2004), solid squares (Chen et al. 2000), open circles (Gratton et al. 1991), solid circles (Caffau et al. 2005), asterisks (Cayrel et al. 2004), open pentagons (Ramírez et al. 2007).

provide too low abundance of Ti relatively to the Solar, while with the new yields the abundance is much higher, although it is still 0.2 dex lower than the observed ratio.

The figure shows the model results if SN II yields from Nomoto et al. (2006) are used, and the corresponding results if yields from Woosley & Weaver (1995) are used. The various dots, crosses etc. show results of stellar abundance analysis for G stars from the solar neighbourhood with the sources of data are given in the figure caption. These data show considerable scatter because of the errors in abundance determinations and possibly some small intrinsic scatter of element abundances of stars of comparable age. Nevertheless there are clear observable correlations between the abundance ratios [X/Fe] and [Fe/H]. For the elements shown, the new results of Nomoto et al. show a better agreement between the calculated abundance evolution and the observed correlations of [X/Fe] with [Fe/H] than the older Woosley & Weaver results; for other elements, however, there are some discrepancies with observations.

There are some substantial problems with the yields of Woosley & Weaver (1995). First, the iron yields of Woosley & Weaver are too high, as already found in Timmes et al. (1995), and we follow their recommendation to reduce the Fe yield. Second, there is another severe problem with the Woosley & Weaver results for magnesium. The calculated abundances based on the original yields are shown in Fig. 2.6 where these abundances are definitely too low, a familiar problem (e.g. Goswami & Prantzos 2000; Francois et al. 2004). A comparison of the model results with the observed evolution of stellar magnesium abundances with metallicity shows that the shape of the [Mg/H]-[Fe/H]-relation is reproduced reasonably well by the model, except that the absolute values of [Mg/H] are systematically too low by a factor of 2.5. We therefore increased the Mg yields of Woosley & Weaver (1995) by this factor in order to reproduce the Mg abundance of the Solar System. The resulting variation in [Mg/H] with [Fe/H] is shown in the figure and reproduces the observations much better. Such a correction would be necessary for calculating dust abundances, since reliable results for dust condensation require that the abundance ratios Si/Mg and Fe/Si of the main dust-forming elements agree with the observed abundance ratios in the Milky Way. Otherwise one would get a deviating dust mixture.

Since the yields of Nomoto et al. (2006) give results for the abundance evolution of the main dust-forming refractory elements much closer to observations than the Woosley & Weaver (1995) yields, and since they do not require to introduce some ad hoc scaling, we prefer to use the Nomoto et al. (2006) yields for the model calculations.

Figure 2.7a compares the calculated abundance ratio Si/Mg with observed abundance ratios in the atmospheres of nearby F and G stars and their correlation with metallicity [Fe/H]. The model results are close to the observed values. From mineralogy the ratio of (Mg+Fe)/Si determines the composition of dust that can be formed if Mg and Si are both completely condensed into dust. Oxygen is, in any case, abundant enough to form any kind of Mg-Si-compound. A ratio of (Mg+Fe)/Si = 1 indicates pyroxene-type stoichiometry ($Mg_xFe_{1-x}SiO_3$), and for ratio of 2 one can form olivine ($Mg_{2x}Fe_{2(1-x)}SiO_4$); for (Mg+Fe)/Si> 2 the silicates and oxides can be formed. The evolution of ratio (Mg+Fe)/Si in the SOlar vinicity as predicted by the model is shown in Figure 2.7b. It indicates
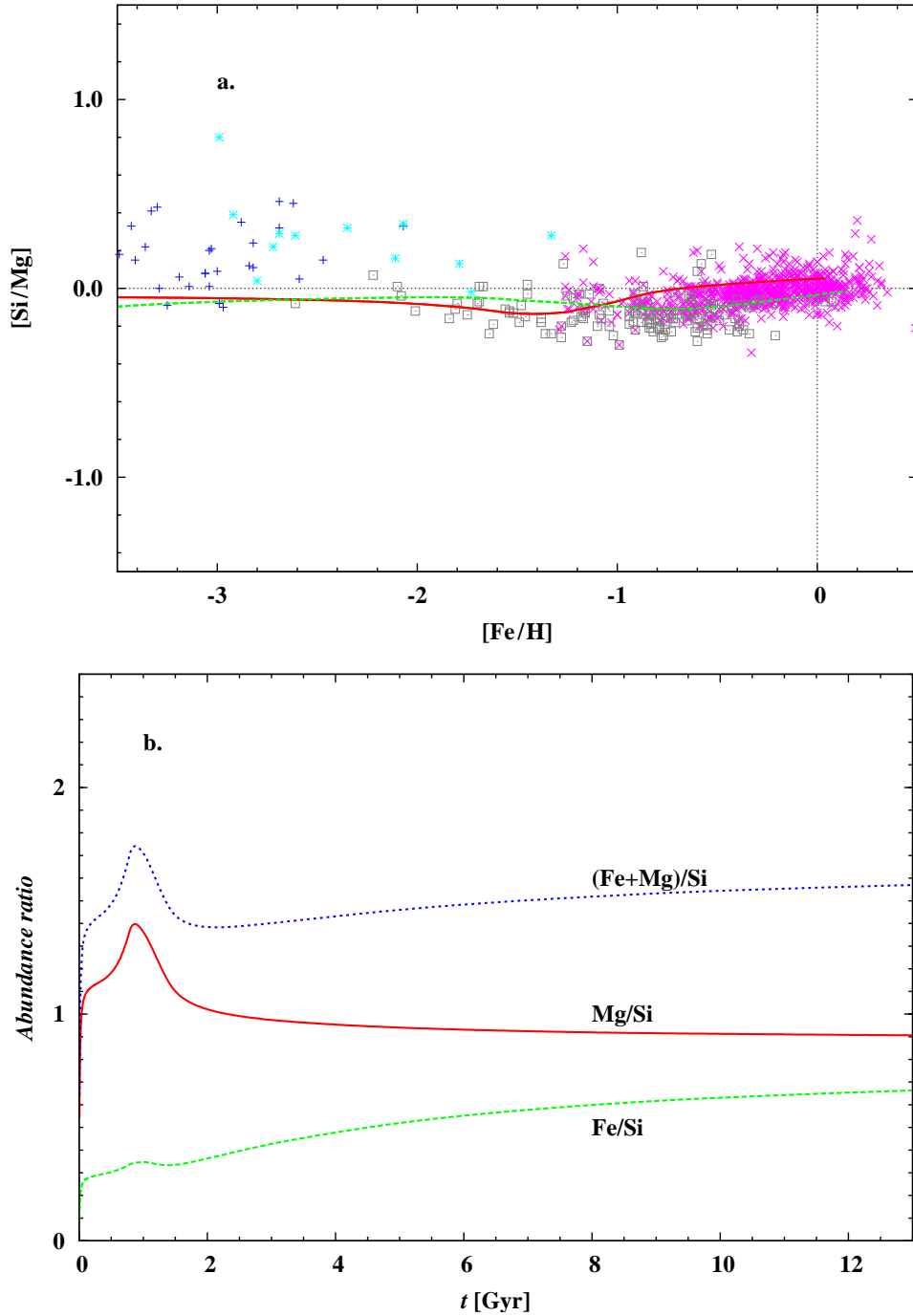
Figure 2.7: a. Abundance ratio Si/Mg of the major silicate dust forming elements relative to Solar abundance as compared to observations of F and G stars. The full line corresponds to a model using SN yields of Nomoto et al. (2006), the dashed line to a model using SN yields from Woosley & Weaver (1995). For the latter the Mg abundance is scaled such that it reproduces the solar Mg abundance at [Fe/H]=0. **b.** Evolution of abundance ratios of Mg and Fe to Si that determine the silicate stochiometry in the Solar neighborhood.

27

that the interstellar gas has the ratio of $\approx$ 1.5 for most of evolution except the early stage, so one except the mixture of Mg-Fe silicates in space.

2.5.5   Stellar abundance constraints

Solar System abundances

Solar abundances are often referred to as Cosmic abundance, Galactic Local abundance or standard abundance due to the fact that the Solar abundances can be measured by different methods: either spectroscopic abundance determinations from the solar photosphere or/and laboratory analysis of primitive meteorites. Therefore the model of the Solar cylinder should also reproduce the element abundances of the Solar System at instant of Solar System formation, i.e., t_{SSF} = 4.56 Gyr ago, which reflects the abundance of the ISM from which the Sun was formed. Table 2.3 shows element abundances in the Solar System in the frequently used logarithmic scale (ϵ is the abundance of an element relative to H by number)

$$a = \log \epsilon + 12 \qquad (2.23)$$

for the elements from H to Zn that can be compared to the results of the model calculation if we use supernova yields from Woosley & Weaver (1995) or Nomoto et al. (2006), since the tables only cover this range of elements.

Abundances for the solar photosphere given in the table are from the compilation of Asplund et al. (2005), except for He where the recommended value for the early sun from Grevesse & Sauval (1998) is given. Abundances for meteorites are from the compilation of Palme & Jones (2003). For C, N, and O abundances from Holweger (2001) are also given. The last column indicates if solar photosphere abundances from Asplund et al. (S), or from Holweger (H), or meteoritic (M) abundances are preferred for comparison with model calculation results; a small letter indicates that the element is not used for a comparison in the present work.

The tabular values for the photosphere consider the recent significant downward revision of the abundances of O, C, and N by Allende Prieto, Lambert & Asplund (2001; 2002) compared to the previous compilations of Grevesse & Sauval (1998) and Anders & Grevesse (1989). The table also gives the abundances for C, N, and O derived by Holweger (2001), who also found a reduction in the solar abundances for these elements to be necessary, but not as reduced as in the papers by Allende Prieto et al. The abundances of Allende Prieto et al. pose serious problems for solar helioseismology (Delahaye & Pinsonneault 2006; Basu et al. 2007) while the abundances of Grevesse & Sauval (1998) give good fits to observations. The incompatibility of the new C, N, O abundances with helioseismological results should be taken seriously and the abundance reductions following from using numerically calculated models for the solar convective flows (Asplund et al. 2000) to determine spectral line profiles seem to result in unrealistically small abundances.

No reliable abundances of the noble gases can be determined for the solar photosphere. For He a photospheric abundance is given in the table, which is the value recommended by Grevesse & Sauval (1998) to be taken as the value of the He abundance of the early sun; the He abundance of the present

Table 2.3: Solar system element abundances *a* and the standard error of the abundance determination σ

Z	Elem.	Sun		Meteorites		used
		a	σ	*a*	σ	
1	H	12.00	–			S
2	He	10.99	0.02	1.92		S
3	Li	1.05	0.10	3.30	0.04	m
4	Be	1.38	0.09	1.41	0.04	m
5	B	2.70	0.20	2.77	0.04	m
6	C	8.39	0.05	7.39	0.04	
		8.59	0.11			H
7	N	7.78	0.06	6.32	0.04	
		7.93	0.11			H
8	O	8.66	0.05	8.43	0.04	
		8.74				H
9	F	4.56	0.30	4.45	0.06	m
10	Ne	8.08	0.07			s
11	Na	6.17	0.04	6.30	0.02	M
12	Mg	7.53	0.09	7.56	0.01	M
13	Al	6.37	0.06	6.46	0.01	M
14	Si	7.51	0.04	7.55	0.01	M
15	P	5.36	0.04	5.44	0.04	S
16	S	7.14	0.05	7.19	0.04	M
17	Cl	5.50	0.30	5.26	0.06	s
18	Ar	6.70	0.06			s
19	K	5.08	0.07	5.11	0.02	M
20	Ca	6.31	0.04	6.33	0.01	M
22	Ti	4.90	0.06	4.95	0.04	M
23	V	4.00	0.02	3.99	0.02	M
24	Cr	5.64	0.10	5.67	0.01	M
25	Mn	5.39	0.03	5.51	0.01	M
26	Fe	7.45	0.05	7.49	0.01	M
27	Co	4.92	0.08	4.90	0.01	M
28	Ni	6.23	0.04	6.23	0.02	M
29	Cu	4.21	0.04	4.28	0.04	M
30	Zn	4.60	0.03	4.66	0.04	M
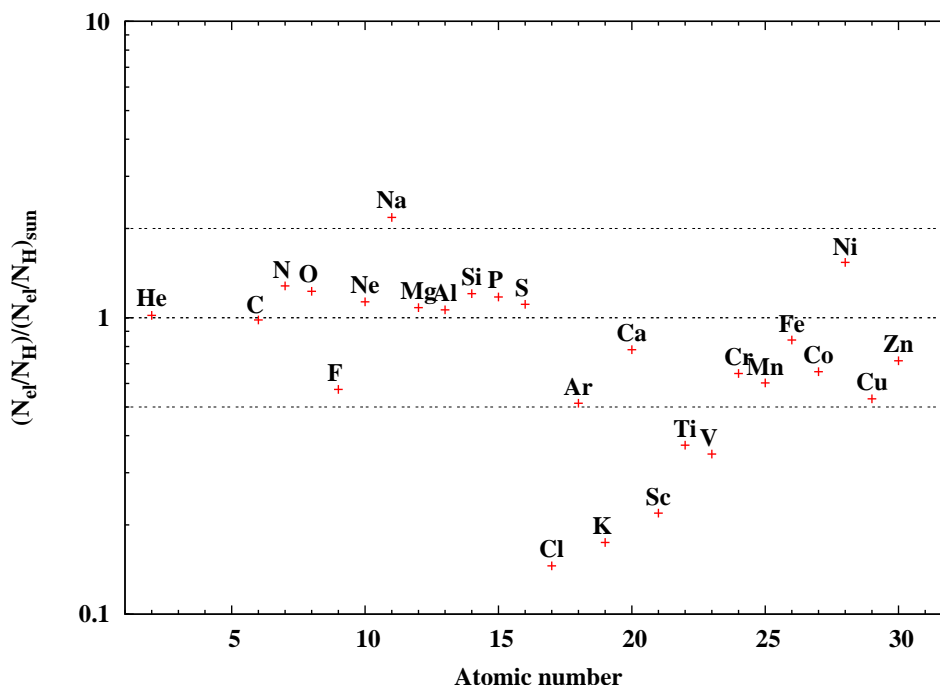
Figure 2.8: Calculated element abundances relative to the solar abundances at the instant of Solar System formation (data according to Table 2.3). Thin dotted lines indicate an as much as twice a deviation from observed values

sun is lower due to segregation effects and cannot be used for a comparison. The abundances for the other noble gases given in the table are determined from the Ne/Mg and Ar/Mg abundance ratios determined from coronal lines as given by Feldman & Widing (2003). It is not sure that they really correspond to the initial solar abundances.

For meteorites the abundance of H and of the noble gases do not reflect their abundance in the material out of which the parent bodies of the meteorites formed since these elements are not incorporated into the bodies of the early Solar System. Therefore no data for meteoritic abundances are given in the table for these elements.

For meteorites the abundances of the volatile elements C, N, and O are also not representative for the abundances in the early Solar System since these elements are not (N) or only to a small fraction (C, O) condensed into solids and incorporated into the parent bodies of the meteorites. Correspondingly, the meteoritic abundances of C, N, and O given in the table are much lower than the photospheric abundances. For these elements the solar photospheric abundances have to be used for comparison purposes. A number of elements are highly volatile (cf., e.g., Palme & Jones 2003) and it is doubtful that these elements are completely condensed in the parent bodies of the meteorites. Besides H, the noble gases, and C, N, and O, these are the elements Cl, Br, I, In, Cs, Hg, Tl, Pb, Bi, from which Cl is one of the elements in the table. For comparison purposes one should therefore use
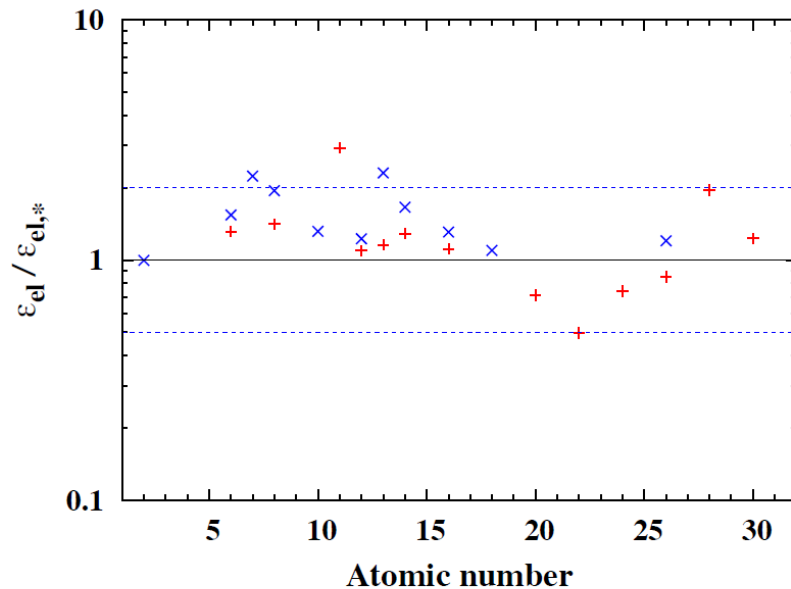
Figure 2.9: Calculated element abundances relative to the abundances of F & G stars from the solar vicinity, with ages less than 1 Gyr (pluses), and of B stars from the range $r_\odot \pm 2$ kpc of the galactocentric distances (crosses) (data according to Table 2.4). Thin dotted lines show the as much as twice a deviation from observed values

the Cl abundance from the photosphere, but since the abundance determination of Cl for the solar photosphere is rather inaccurate, Cl is presently not suited for comparison.

For the remaining elements, the meteoritic and the solar photospheric abundances agree closely, except for a number of heavier elements not contained in our table. For comparison with the results of the chemical evolution calculation, we usually preferred the more accurate meteoritic abundance, whereas the solar photospheric was used when both methods were only moderately accurate (as specified in last column of Table 2.3). Additionally, the elements Li, Be, B, F are excluded from the comparison, since their production mechanisms are not implemented in the model program.

In Fig. 2.8 we present the predicted element abundances of the ISM relative to Solar System abundances at the instant of Solar System formation at $r = r_\odot$. Thin horizontal lines indicate a deviation by a factor of two upward or downward from Solar System abundances. As can be seen, the model fits the observed abundances with good accuracy. Most calculated element abundances reproduce the Solar System element abundances within a factor of about two, many elements even much better. The somewhat worse results for Cl, K, and Sc have also be found by Kobayashi et al. (2006); the rather bad results for these elements are of no importance for our model, since they are not one of the main dust-forming elements.

Table 2.4: Average abundances a of F and G stars with solar metallicity ($|\Delta[\text{Fe/H}]| < 0.05$) and of young stars (age $\leq$ 1 Gyr) from the solar neighbourhood. σ_{abd} is the accuracy of the abundance determinations from stellar spectra, σ_* is the scattering of the stellar abundances around the mean. Z is the metallicity calculated from these abundances

		Nearby F & G stars						B dwarfs		
		solar met.			age < 1 Gyr					
Z	Element	a	σ_{abd}	σ_*	a	σ_*	Source	a	σ_*	Source
2	He							11.02	0.05	3
6	C	8.37	0.06	0.11	8.39	0.11	2	8.32	0.10	4
7	N							7.73	0.28	5
8	O	8.75		0.07	8.77	0.13	1	8.63	0.18	4
10	Ne							8.11	0.04	6
11	Na	6.30	0.03	0.16	6.27	0.10	1			
12	Mg	7.63	0.06	0.32	7.64	0.21	1	7.59	0.15	7
13	Al	6.52	0.05	0.24	6.54	0.22	1	6.24	0.14	5
14	Si	7.60	0.05	0.28	7.61	0.23	1	7.50	0.21	5
16	S	7.17	0.16		7.29	0.10		7.22	0.10	4
18	Ar							6.48	0.04	8
20	Ca	6.42	0.03	0.37	6.48	0.39	1			
22	Ti	4.92	0.03	0.11	4.94	0.14	1			
24	Cr	5.66	0.02	0.13	5.73	0.28	1			
26	Fe	7.55	0.06	0.12	7.61	0.25	1	7.46	0.08	9
28	Ni	6.22	0.02	0.09	6.25	0.07	1			
30	Zn	4.53	0.06	0.27	4.54	0.13	1			
	Z	0.0140			0.0147			0.0121		

Sources: (1) Bensby et al. (2005), (2) Bensby & Feltzing (2006), (3) Lyubimkov et al. (2004), (4) Daflon & Cunha (2004), (5) Rolleston et al. (2000), (6) Cunha et al. (2006), (7) Lyubimkov et al. (2005), (8) Holmgren et al. (1990) (9) Cunha & Lambert (1994).

Abundances of F & G stars

Abundances of the ISM cannot be measured directly because in the ISM the refractory elements are condensed into dust (cf. Savage & Sembach 1996). One possibility to indirectly determine total element abundances in the ISM is to determine atmospheric abundances from some kind of 'young' stars that have not changed their surface abundances since they formed from interstellar matter. Best-suited for this purpose are probably F and G main sequence stars from the galactic neighbourhood, that show the kinematics of thin disk stars and high metallicities, or, if stellar ages have been determined, have an age of no more than a few Gyrs. For such stars one can assume that they formed from interstellar material with essentially the same properties as the present-day ISM of the galactic neighbourhood. Bensby et al. (2005) and Bensby & Feltzing (2006) determined recently abundances for a number of elements for thin and thick disk stars from the solar neighbourhood. From the elements considered in that paper, the following are relevant for our purposes: C, O, Na, Mg, Al, Si, Ca, Ti, Cr, Fe, Ni, and Zn.

First, we consider from this sample the stars with an [Fe/H] ratio within ±0.05 of the solar value. There are 6 stars that satisfy this condition, and Table 2.4 shows the average abundances a of the above elements and the average scattering σ_* of the abundances around the mean value. For comparison the table also shows the random errors of the abundance determinations from stellar spectra as given by the authors. These abundances are surprisingly close to the Solar System abundances, though the general metallicity is somewhat higher. If the range of metallicities is increased to ±0.1 of the solar [Fe/H] ratio, the number of stars increases to 13, but the average values for the abundances are practically unchanged; i.e., the average abundances given for solar like stars in the table do not depend substantially on the precise choice of the limit Δ[Fe/H]. Hence abundances of F & G stars with Solar System metallicity agree rather well with Solar System abundances as given in Table 2.3, which have already been compared in Fig. 2.8 with results of our model calculation. Our model therefore reproduces the observed abundances of solar metallicity stars reasonably well at the solar circle.

Second we choose from the sample of Bensby et al. (2005) and Bensby & Feltzing (2006) the thin disk stars with ages less than 1 Gyrs. Despite the large uncertainties of such age determinations, it seems likely that these stars belong to the most recently born stars in the sample of thin disk stars. Their abundances should therefore sample the abundance of the ISM in the solar vicinity during the last, e.g., 1 - 2 Gyrs or so. The average abundances of the elements determined by Bensby et al. (2005) and Bensby & Feltzing (2006) for these stars are given in Table 2.4. Extending the sample to stars with ages less than 2 Gyrs does not result in significant changes in the average abundances; i.e., the results do not depend on the precise choice of the age limit. The typical metallicity Z of the 'present' ISM determined in this way (the contribution of N and Ne to Z is estimated) is slightly higher than the Solar System metallicity, as one may expect from ongoing element synthesis. Our model results for the present day ISM abundances are compared in Fig. 2.9 with the observed abundances of F & G stars formed within the last Gyr given in Table 2.4. Our model results for the present ISM are also in good agreement with observations.
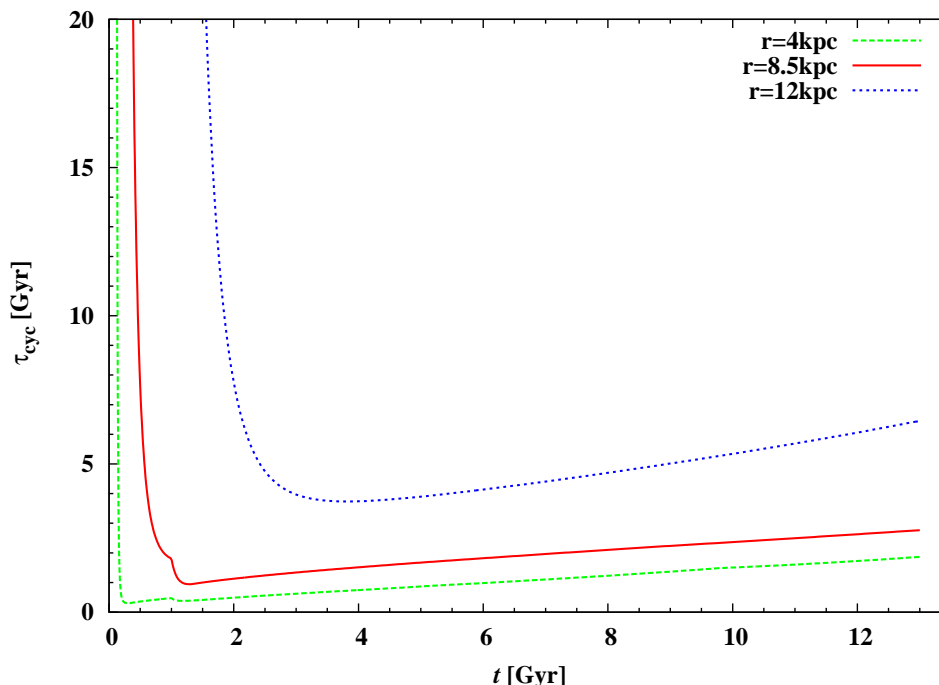
Figure 2.10: Characteristic astration timescale for conversion of interstellar matter into stars at the solar circle (solid curve) as well as at the galactocentric radius $r = 4$ kpc and $r = 12$ kpc (dashed and dotted lines, respectively).

Abundances of B dwarfs

Stars of early spectral type B have short lifetimes, so they sample abundances from the present-day thin disk. Abundances have been determined in particular for B stars in stellar clusters and we show in Table 2.4 average abundances taken from the literature for B dwarfs in stellar cluster with galactocentric distances from a range of ± 2 kpc around

the solar circle. Despite the rather heterogeneous observational material the scattering of observed abundances around the mean is moderate; i.e., element abundances in the ring 8 ± 2 kpc around the galactic centre seem to be quite homogeneous. The average abundances and, thus, the metallicity Z, are typically slightly less than the present-day abundances found from F and G stars (see Fig. 2.9), as also found by Sofia & Meyer (2001). Figure 2.9 compares our calculated abundances for the current ISM with the abundances of a B dwarf; the agreement, again, is reasonable, but compared to the case of F & G stars it is worse since abundances of B dwarfs are less than for F & G stars.
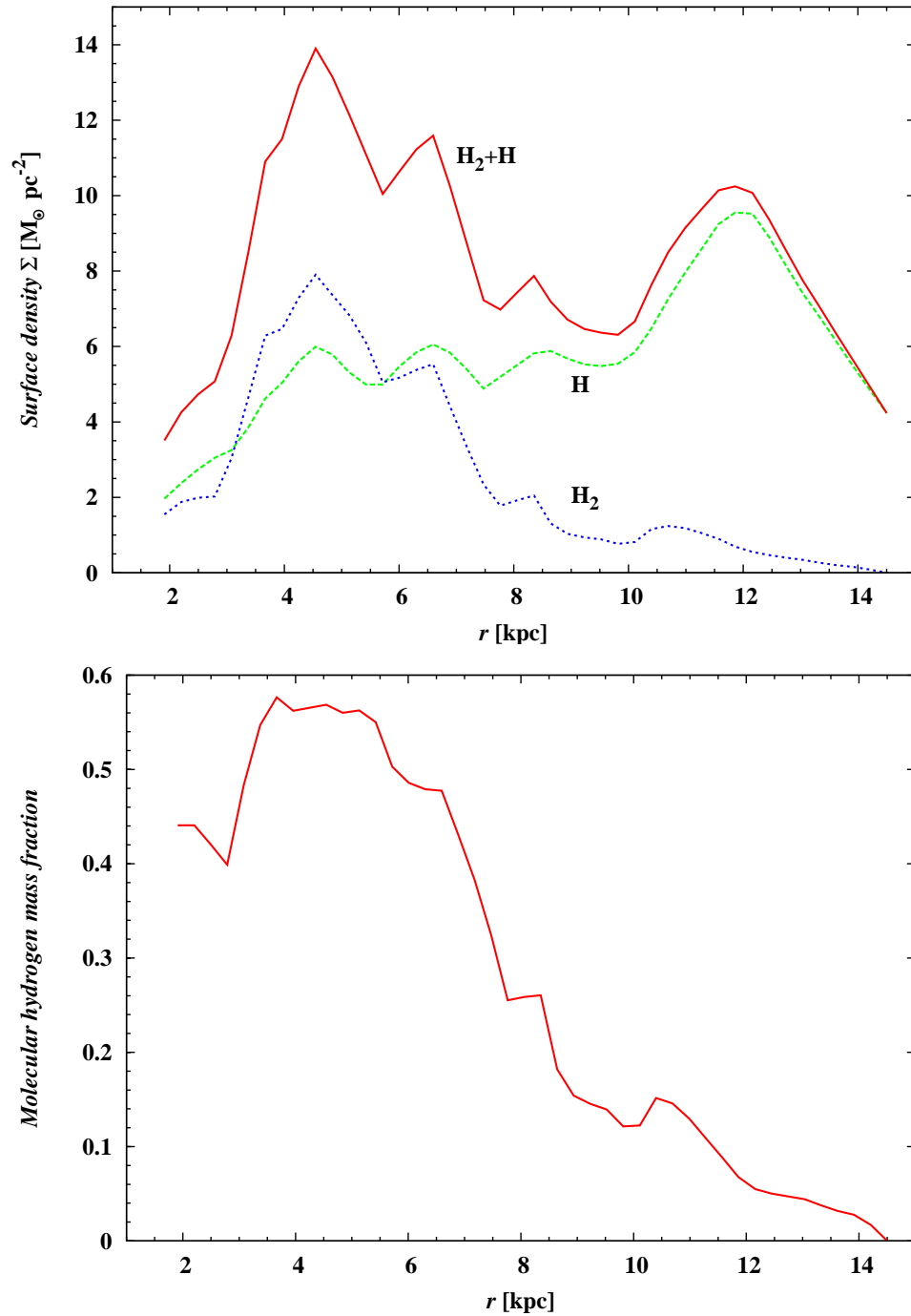
Figure 2.11: *Top.* The radial distribution of the present gas surface densities of molecular and atomic hydrogen and total hydrogen density from Dame (1993). *Bottom.* The radial distribution of mass fraction of molecular hydrogen relatively to total hydrogen density from observations (Dame 1993)
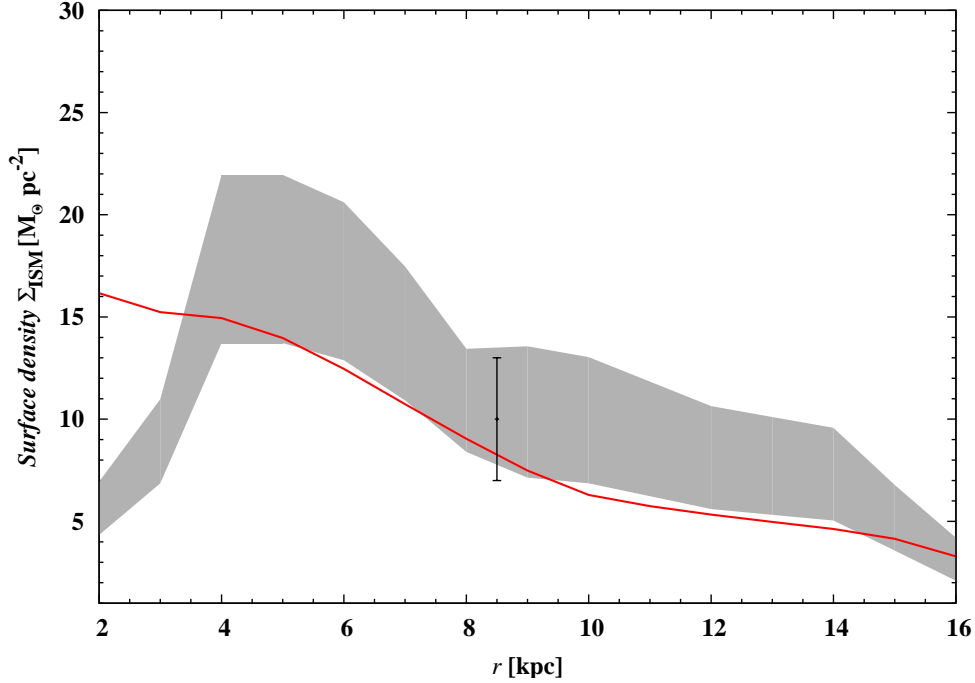
Figure 2.12: Radial distribution of the present gas surface density predicted by the model (solid line) and observed gas density profile (shaded area). The lower border of the observed density profile is the sum of atomic and molecular hydrogen given in Dame (1993), corrected for the contribution of 30% helium. The upper one is obtained by adopting the gas surface density in the solar neighbourhood as 16 $M_\odot$ and scaling the curve of Dame (1993) accordingly to Prantzos & Aubert (1995). The error bar indicates observations of the gas density in the Solar neighborhood (Dickey 1993)

2.5.6 Astration time for the interstellar matter

In the context of dust evolution, an important quantity is the timescale for conversion of interstellar matter into stars, the astration timescale. This is given by

$$\tau_{\mathrm{cyc}} = \frac{\Sigma_{\mathrm{ISM}}}{B} .$$
(2.24)

This quantity is shown for the Solar circle in Fig. 2.10. At the instant of forming of the Solar System, the astration timescale was about 2 Gyrs.

.

2.6 Evolution of the Milky Way disk

In the previous Section we have demonstrated that the model of the Solar neighborhood, which provides a basis for the construction of the multicomponent dust model, reproduces well the main set of
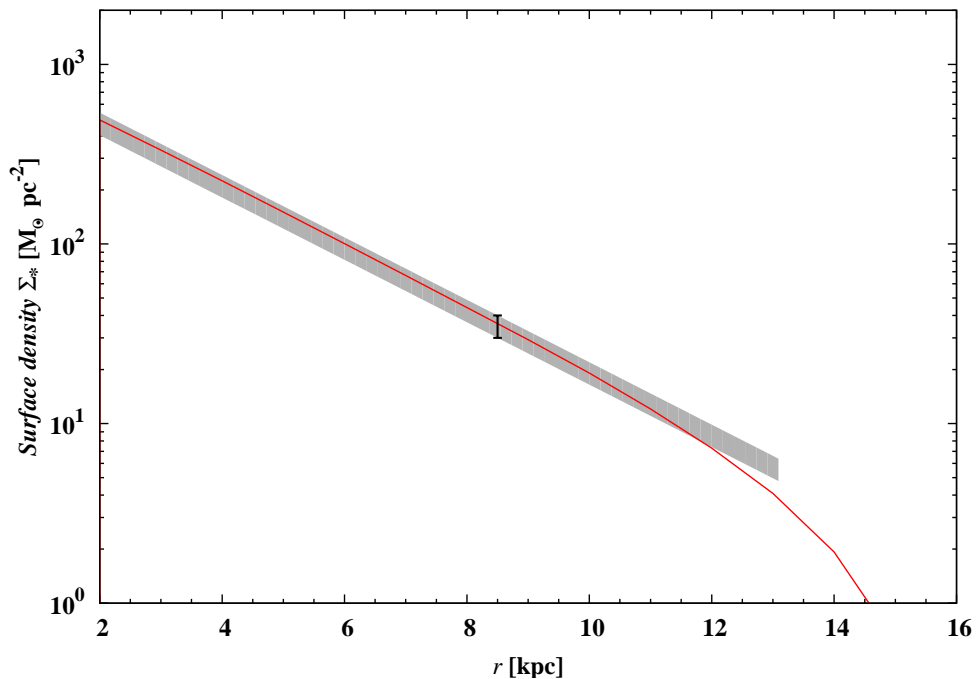
Figure 2.13: The profiles of the present stellar density Σ_* in the Galactic disk as predicted by the model (solid line) and observations (shaded area). The observed stellar density distribution approximated by the exponent profile with scale length 2.5 kpc. The lower and upper limits are normalized for the stellar density in the Solar neighborhood $35 \pm 5\,\mathrm{M_\odot\,pc^{-2}}$ (error bar, from Gilmore et al. 1989).

observational constraints. This dust model can then be applied for studying the dust evolution in the ISM for different objects. Among them, the Milky Way disk appears as an ideal laboratory for testing the applicability of the dust model due to the largest available body of observational and theoretical studies of its chemical evolution.

In the following we present results of the chemical evolution model for the whole galactic disk and compare them with observed profiles of present day surface densities of gas and stars, stellar birthrate and radial metallicity gradients.

Gas distribution

The present gas density profile can be derived from the hydrogen density, taking into account helium contribution, since helium and hydrogen dominate the ISM mass. Observations of the surface densities of atomic and molecular hydrogen in the disk from Dame (1993) are shown in Fig. 2.11. Figure also presents the mass fraction of molecular hydrogen, indicating the fraction of molecular clouds, an important parameter for the dust growth, which will be discussed in Chapt. 4. Figure 2.12 shows the current gas radial profile as predicted by the disk model and the observed distribution
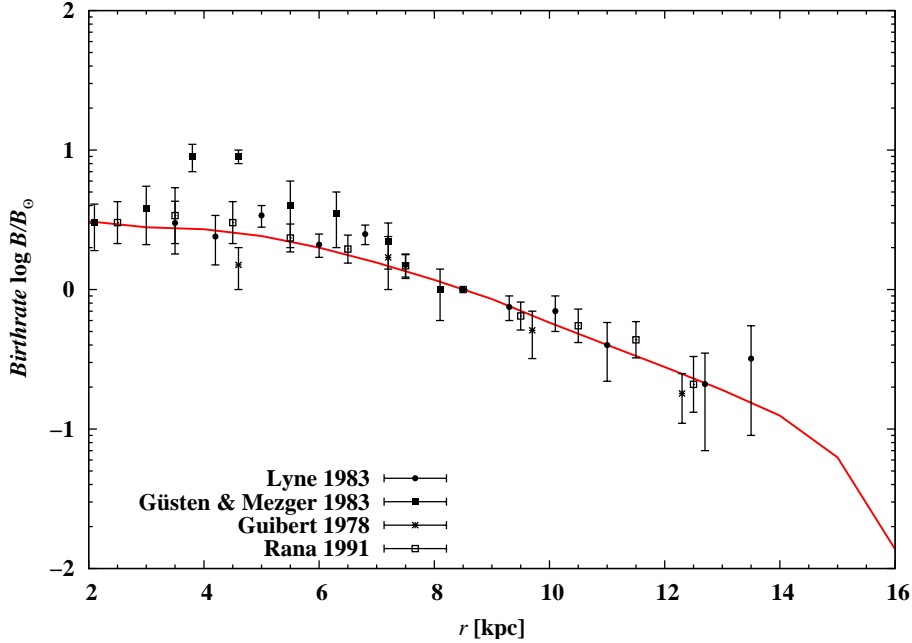
Figure 2.14: Profile of the present star formation rate in the Galactic disk, as predicted by the model calculations (line) and observational data from different tracers of star formation (error bars). It is normalized to present SFR in the Solar neighborhood.

(shaded area). The lower limit of the observed gas distribution is obtained as the sum of atomic and molecular hydrogen from Dame (1993), corrected for the 30% contribution from helium. The upper limit of the gas denisty profile is derived by scaling the curve of Dame (1993) to the 16 $M_\odot$ at the Solar circle accordingly to Prantzos & Aubert (1995). The model fits well the deacrease of the gas density at radial distances larger than 14 kpc. The radial profile of the gas density is the constraint, which is most difficult to reproduce in the model calculations. In present work the shape of the gas distribution at the densities below the threshold value for star formation is influenced by the choice of the cut-off function (see Sect. 2.3.2). We introduced the regime of suppressed star formation for densities $\Sigma < 7$ $M_\odot\,pc^{-2}$ by multiplication of the star formation rate by the smoothing function. The Gaussian function $\sim e^{-(\Sigma_{ISM}-7)^2/2\Delta^2}$ with $\Delta = \sqrt{2.5}$ $M_\odot\,pc^{-2}$ allows to describe particularly well the gas distribution in the outer disk.

Stellar profile

The stellar profile is exponentially decreasing outwards, with a length scale of about $d_* \propto 2.5$ kpc as estimated from the recent Milky Way tomography with Sloan Digital Sky Survey using 48 million stars and photometric parallaxes (Jurić et al. 2008). The COBE observations suggest that the stellar
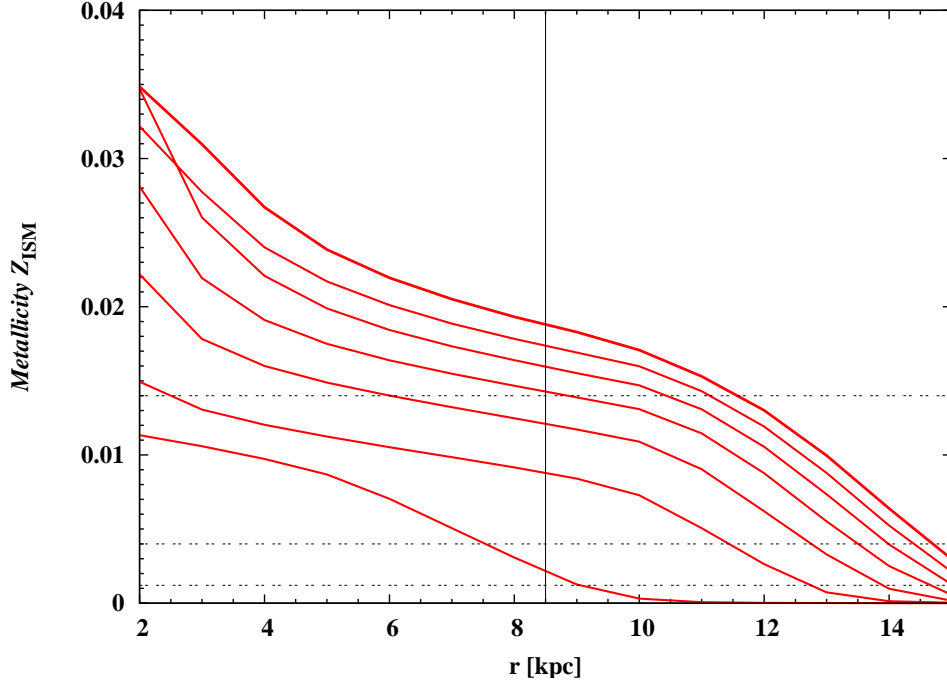
Figure 2.15: Variations of radial metallicity profiles in the Galactic disk at instants from 1 Gyr to 13 Gyr (from bottom to top) with 2 Gyr steps as predicted by the model calculations. Thin vertical line shows Galactocentric radius of the Sun. The horizontal lines show the minimum metallicity for the iron, carbon and silicate dust growth in the molecular clouds (from top to bottom, respectively) from Table 4.1.

disk has an outer edge 4 kpc from the Sun (Freudenreich 1998). Figure 2.13 presents comparison of the current stellar profile with model predictions. The lower and upper limits for the stellar density are obtained by normalization to the values in the Solar neighborhood of $35 \pm 5 \, M_\odot \, pc^{-2}$ (Gilmore et al. 1989). The stellar density deviates from an exponential profile in the outer disk due to suppressed star formation regime as discussed above.

Star formation

Figure 2.14 shows the star formation rate as predicted by the model calculations, compared with observational data. The SFR is normalized to present SFR in the Solar neighborhood. Data are based on several tracers of star formation: Lyman continuum photons from HII regions (Güsten & Mezger 1983), pulsars (Lyne et al. 1985), supernova remnants (Guibert et al. 1978) and compilation from Rana 1991.
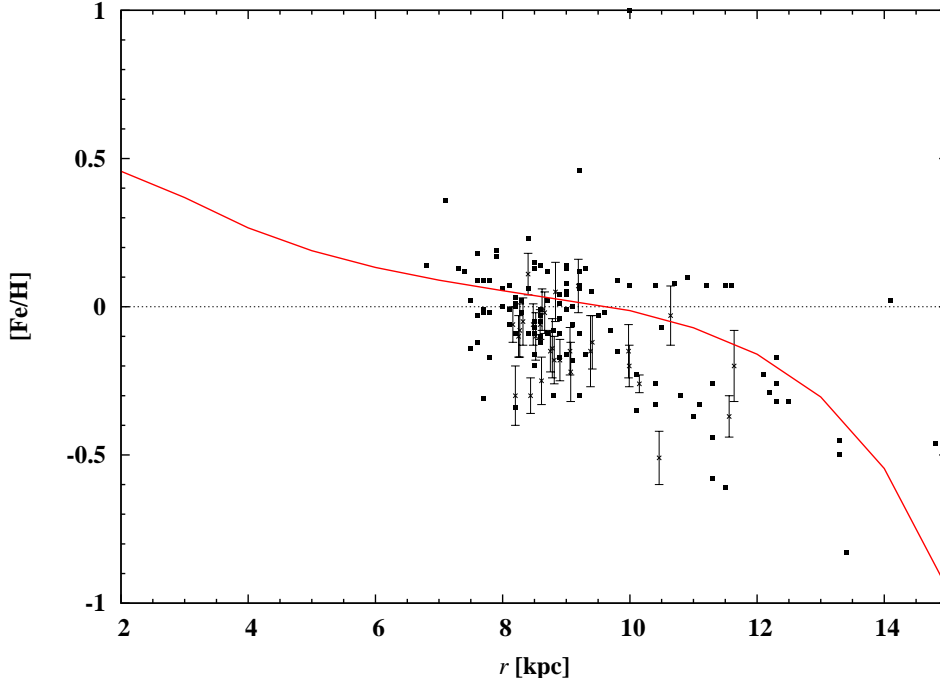
Figure 2.16: Radial variation of iron abundance as predicted by model calculations and found by observations. Filled squares show the determinations from open clusters with typical errors of 0.1 dex kpc^{-1} from Chen et al. (2003); crosses with error bars are the recent data from Lemasle et al. (2007).

2.6.1 Galactic abundance gradients

The existence of galactic radial abundance gradients is now well established through observations, though their magnitudes show large discrepancies. Different objects have been used to estimate abundance gradients, namely H II regions, B stars, Cepheids, open clusters and planetary nebulae, that are relatively young and can be a measure of the present ISM composition (Hou et al. 2000, Chen et al. 2003). In the following we present a comparison of the radial gradients predicted by our model with observed data obtained by different methods to test its viability. For a detailed analysis of the abundance gradients in the Milky Way we refer to a recent study of Cescutti et al. 2007.

Table 2.5: Present radial abundance gradients in the galaxy as predicted by the model. The magnitude of gradient is given in dex kpc^{-1}

r, kpc	[Fe/H]	O	C	Si	Mg	Ca	S
2-13	-0.065	-0.047	-0.053	-0.049	- 0.045	-0.059	-0.054
	±0.005	±0.004	±0.005	±0.004	±0.004	±0.005	±0.005
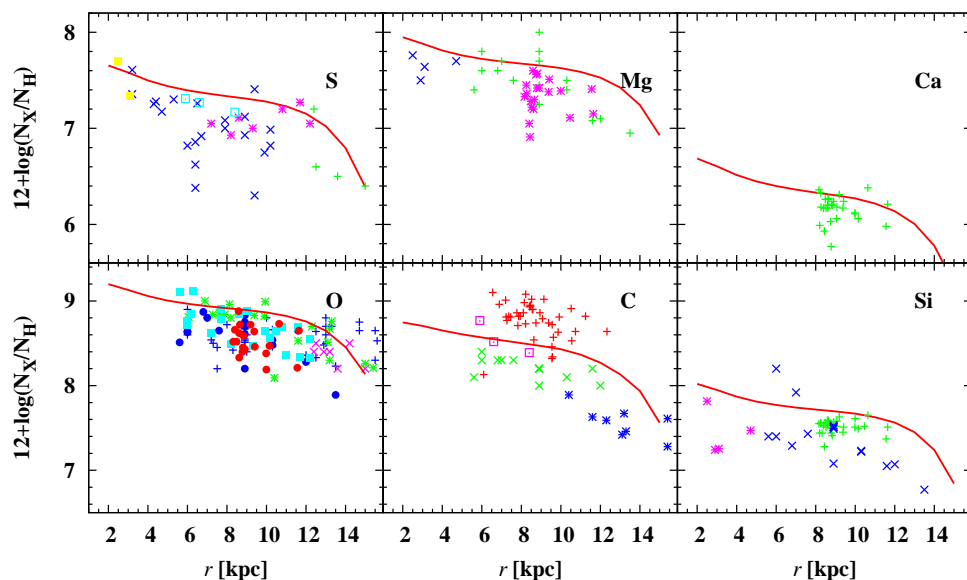
Figure 2.17: Galactic radial profiles for abundances of main dust forming elements, as predicted by model calculations (solid line) and found by observations (different symbols). The observational data are from Shaver et al. (1983), Kaufer et al. (1994), Simpson et al. (1995), Vilchez & Esteban (1996), Smartt & Rolleston (1997), Gummersbach et al. (1998), Lemasle et al. (2007).

Figure 2.15 presents the variations of metallicity profiles in the Galactic disk at instants from 1 Gyr to 13 Gyr. The model predicts shallower gradients in the early epoch of Galaxy formation with the steepest gradient in the inner region at about 9 Gyr.

Iron gradient

Empirical estimates give quite steep gradients d[Fe/H]/dr ranging from -0.05 to -0.07 dex kpc^{-1}, however, much shallower gradients have also been estimated: -0.044 dex kpc^{-1} and even as low values as of -0.003 dex kpc^{-1} have been measured (for a review of different observations see Chen et al.(2003) and references therein). The radial variation of [Fe/H] predicted by the model calculations and the recent abundance determinations from Lemasle et al. (2007) and Chen et al. (2003) are shown in Fig. 2.16. Chen et al. (2003) found an iron gradient of -0.063 ± 0.008 dex kpc^{-1} from a large compilation of abundance determinations from open clusters. More recent determinations of Lemasle et al. (2007) suggest a similar value for the iron radial gradient of -0.061 dex kpc^{-1} and -0.056 if they include 69 Cepheids with homogeneous distance determinations. The model gives a similar value

of the iron gradient of -0.065 dex kpc^{-1}. An exhaustive recent study of the Milky Way abundance gradients in Cescutti et al. (2007) argues that generally accepted iron gradients of -0.07 dex kpc^{-1} are too steep and in fact should be flatter, namely -0.05; the same holds for the slopes of other elements. As was noted in Andrievsky et al. (2002), observed radial variations of [Fe/H] and of other elements have different slopes, depending on the range of the galactocentric distances considered, so a multi-zonal gradient seems to be more appropriate. This can also be seen for the model results in Fig. 2.16. However, in oder to determine whether the difference in the slope estimates is dominated by empirical uncertainties or if they might be intrinsic, a detailed investigation of stellar ages and radial distribution of the different chemical tracers is required (Lemasle et al. 2007).

Radial gradients for other elements

We present the galactic abundance gradients of the main dust forming elements (O, C, Si, Mg, S, Ca), as predicted by the model, in Table 2.5. Comparison with observations of different kinds of objects is shown in Fig. 2.17. The magnitude of radial gradients for different elements is not the same, since they have various production sites characterised by different evolutionary timescales and metallicity dependences.

The data from H II regions and O stars suggest a rather steep radial gradient for oxygen of $\log (O/H) /dr \sim -0.07$ dex kpc^{-1} (see Hou et al. 2000, Cescutti et al. 2007, for a review of observational data). Recent determinations from Cepheids give a similar value of -0.065 dex kpc^{-1} (Lemasle et al. 2007) for $5 < r < 12$ kpc and a smaller slope of -0.041 ± 0.03 for $8 < r < 12$ kpc. Deharveng et al. (2000), after a consistent analysis of the H II data, concluded that the gradient should be -0.039 ± 0.005 dex kpc^{-1}, i.e., considerably less than generally thought. Also, Andrievsky et al. (2002) finds a much flatter slope of -0.022 ± 0.009 dex kpc^{-1}. Our model of the Galactic disk predicts the present gradient d $\log(O/H)/dr \sim -0.05$ dex kpc^{-1}. The abundance of oxygen predicted by the model appears to be higher than the observed one (Fig. 2.17). This is a general feature of chemical evolution models of the disk, because they are tuned to reproduce the present Solar oxygen abundance, which is higher than the abundances determined from HII regions.

The radial gradient for carbon is poorly determined. From the studies of B-stars in the range $6 < r < 12$ kpc Gummersbach et al. (1998) suggest a rather small gradient of -0.045 dex kpc^{-1}, which is close to our result of $-0.047 - 0.050$ dex kpc^{-1}. However, the Rolleston et al. (2000) determinations from B-stars located in open clusters give a value of -0.07 dex kpc^{-1} for the range $6 < r < 18$ kpc.

Our results for Si and Mg are in agreement with the study of abundance gradients in the Milky Way of Cescutti et al. (2007), who compare their results with homogeneous observational data. Their slopes for Si and Mg are -0.039 and -0.045 dex kpc^{-1}, while we find -0.049 and -0.045 dex kpc^{-1}. For Ca Cescutti et al. (2007) find -0.047, while our gradient has a value of -0.059. This agrees with estimates from B stars of -0.06 ± 0.01 dex kpc^{-1} (Rolleston 2000). More recent data from

Lemasle et al. (2007) suggest even shallower gradients for Si and Ca, -0.031 ± 0.029 and -0.014 ± 0.029 dex kpc^{-1}, respectively.

The gradient for sulfur seems to follow the oxygen one, with a recently determined value of -0.047 dex kpc^{-1} (Cescutti et al. 2007), while older determinations give a steeper slope of -0.07 dex kpc^{-1} (Rolleston 2000). Our model provides an intermediate value of -0.054 dex kpc^{-1}.

2.7   Toward the SED calculation

The ISM dust plays a crucial role in the redistribution of the energy from stars from the UV to the IR wavelength range due to absorption, scattering and re-emission of stellar light, so that the emitted spectrum becomes substantially different from the initial stellar radiation. Study of galaxies obscured by dust relies on the understanding of dust properties: spatial distribution of dust in the galaxy, composition, temperatures and size distribution of grains, which are needed for the solution the radiative transfer equation in dusty media. The spectrophotometric evolution of galaxies has been already studied in the literature by a combination of chemical evolution models of the galaxy and stellar population synthesis. The most widely used codes for modeling SED of galaxies are GRASIL (Silva et al. 1998), STARDUST (Devriendt et al 1999), PEGASE (Fioc & Rocca-Volmerange 1997).

These codes differ in prescriptions for the stellar evolution and individual stellar spectra and also the treatment of dust. Dust effects on stellar light are usually accounted for in a simplified ways by its extinction and emissivity properties, but the models do not include a physical model for the dust evolution in the ISM. In a study of Luminous and Ultraluminous Infrared galaxies Vega et al. (2008) match the parameters in their dust model to the local ISM, although the dust properties can differ for objects powered by AGNs or starburst.

The model of dust evolution developed in the present work follows the evolution of dust from stars and molecular clouds, therefore it can become a useful tool for analysis of the spectra from galaxies undergoing various evolutionary stages, in which different sources and processes may dominate the dust mass. Coupling of our model of dust evolution with a radiative transfer code will provide a direct link to observations that allows to verify the model on well studied objects on one hand, and to predict how the evolution of dust amount and composition influences the emergent spectra of the galaxies on the other hand. Such predictions are particularly useful in light of forthcoming PLANCK and HERSHEL missions that are expected to provide much information about the cold dust, which are unavailable from previous missions.

Our model provides the dust, gas and star surface densities, that can be used for radiative transfer calculations with an assumption on the vertical distribution in the disk. In the following we describe our method of calculation of the starlight from the Galaxy that is the first step necessary for the radiative transfer calculations.
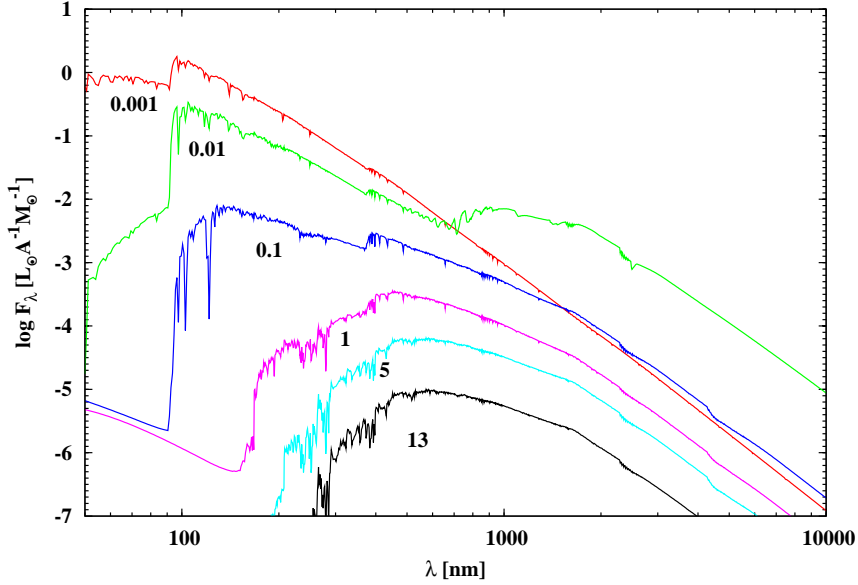
Figure 2.18: Integrated spectra from a single stellar population of Solar metallicity with ages between 0.001 and 13 Gyr (the number below each curve) relative to Solar luminosity $L_\odot = 3.839 \cdot 10^{33}$ erg s^{-1}.

2.7.1 Calculation of the intrinsic galactic stellar flux

The spectral synthesis method is based on an idea of summation of the individual spectra of stars from different stellar generations. The basics of the method are described in detail in, e.g., Fioc & Rocca-Volmerange (1997); a comparative analysis of the ingredients of stellar population synthesis can be found in Bruzual & Charlot (2003).

The calculation of the intrinsic stellar flux density $F_\lambda(r,t)$ per unit area of the Galactic disk consists of 3 main blocks:

1. *Chemical evolution models* provide the star formation history $B(r,t)$ and the ISM metallicity $Z_{ISM}(r,t)$ (or the iron abundance [Fe/H]) for the Milky Way model described above. We calculate $F_\lambda(r,t)$ for the range Galactic disk radii from 1 to 16 kpc with 1 kpc steps.

2. *Single stellar evolution (SSE)* determines the evolutionary stage of each star of mass m of metallicity $Z_* = Z_{ISM}(t)$ and age τ. It provides the stellar parameters radius R_*, effective temperature T_{eff} and luminosity L_*. The surface gravity is obtained by using

$$g = \frac{Gm}{R_*^2}. \tag{2.25}$$

44

3. *Spectral library* returns the flux f'_λ per unit of stellar surface area emitted by a star of mass m in the frequency range $[\nu, \nu + d\nu]$ for a set of stellar parameters $T_{\rm eff}$, $\log g$ provided by the SSE block and iron abundance [Fe/H] from the chemical evolution. The total emergent flux from a star is obtained via

$$F_\nu = f'_\nu \times 4\pi R_*^2, \tag{2.26}$$

where R_* is provided by the single stellar evolution code.

Stellar flux density $\mathcal{F}_\nu(r, t)$ per unit area of the galactic disk is calculated by adding the contribution from all generations of stars weighted by the stellar birthrate at the instant of their birth:

$$\mathcal{F}_\lambda(r, t) = \int_0^t \left[\int_{M_l}^{M_u} F_\lambda(M, t - t', Z_*(r, t'))\Phi(M)dM \right] B(r, t')dt' , \tag{2.27}$$

where $F_\lambda(M, \tau, Z_*(r, t'))$ is the spectrum of a star of mass M, age τ with the metallicity Z_*, which is the metallicity of the ISM at instant of stellar birth $Z_{\rm ISM}(r, t_{\rm birth})$, the stellar birthrate B and the IMF Φ are taken for the model of the Milky Way disk from Sect. 2.3.

Although the principle of spectral synthesis is simple, computational problems and erroneous results may be caused by unoptimized algorithms. We discretize the integrals in eq. (2.27) similarly to the isochrone method of discretization of the integral over time (Fioc & Rocca-Volmerange 1997):

$$\mathcal{F}_\lambda(r, t) = \sum_{i=1}^{p-1} B(r, t - \theta_i)(\theta_{i+1} - \theta_i) \int_{M_l}^{M_u} \Phi(M)F_\lambda(M, t - \theta_i, Z_*)dM , \tag{2.28}$$

where p is the number of time intervals, such that $\theta_{i+1} - \theta_i$ is short enough, so that consecutive isochrones have evolved only a little. The logarithmic mass grid is chosen so that the variation of grid points do not influence the shape of the spectrum.

The total SED from the Galactic disk is obtained by integration of the flux density from eq. (2.27):

$$L_\lambda(t) = 2\pi \int_{r_{\min}}^{r_{\max}} \mathcal{F}_\lambda(r, t)r dr \tag{2.29}$$

where the lower and upper integration limits are $r_{\min} = 1$ kpc and $r_{\max} = 16$ kpc.

Single stellar evolution

We utilize the analytical formulae for the single stellar evolution from Hurley et al. (2000). They provide the stellar luminosity L_*, the radius R_* and temperature $T_{\rm eff}$ of a star from zero-age main sequence up to the remnant stages. The formulae approximate the stellar evolution tracks for the range of metallicity between 0.0001 and 0.03 and masses between 0.5 and 50 $M_\odot$ within accuracy of 5%.
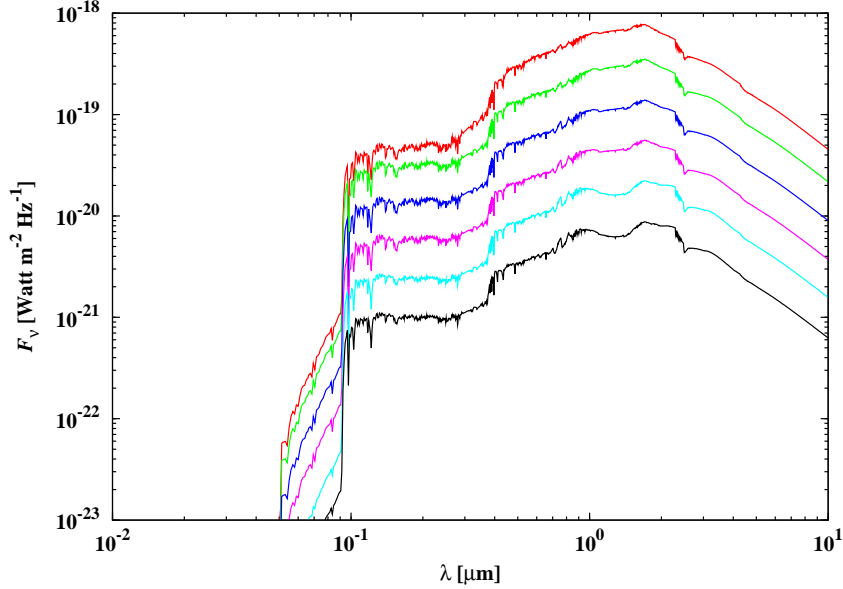
Figure 2.19: Intrinsic galactic luminosity density emitted by stars per unit of disk area for several Galactic radii between 2 and 12 kpc (from top to bottom) with 2 kpc steps at instant 5 Gyr.

During AGB stage low and intermediate mass stars strongly increase their luminosities. Although AGB stage is short compared to the life times of these stars, they make an important contribution to the total luminosity of the stellar population. Therefore the time and mass step in calculations must be chosen carefully to account for this evolutionary phase. The analytical formulae from Hurley et al. (2000) provide the duration of both early and thermally pulsing AGB phase as well as the radius variation during evolution.

Spectral Libraries

For a stellar library we use the BaSeL 3.01 semi-empirical library of stellar spectra for wave length from 9 nm to 160 μm. We prefer an application-oriented version of the BaSeL library "Padova 2000", which was calibrated to reproduce color-magnitude diagrams of globular clusters at all levels of metallicity and is better suited to model collective stellar properties (Westera et al. 2002, Lejeune et al. 1997, 1998). It is organized on the grid of parameter space [Fe/H], T_{eff} and $\log g$ for a wide range of stellar parameters. The spectra are given for 6 values the metallicity [Fe/H] -2, -1.5, -1, -0.5, 0, and +0.5. The stellar temperature range is $2000 \leq T_{\text{eff}} \leq 50000$ K. Wolf-Rayet stars and central stars of planetary nebulae can reach temperatures beyond this range, whose emission in the ultravio-

46
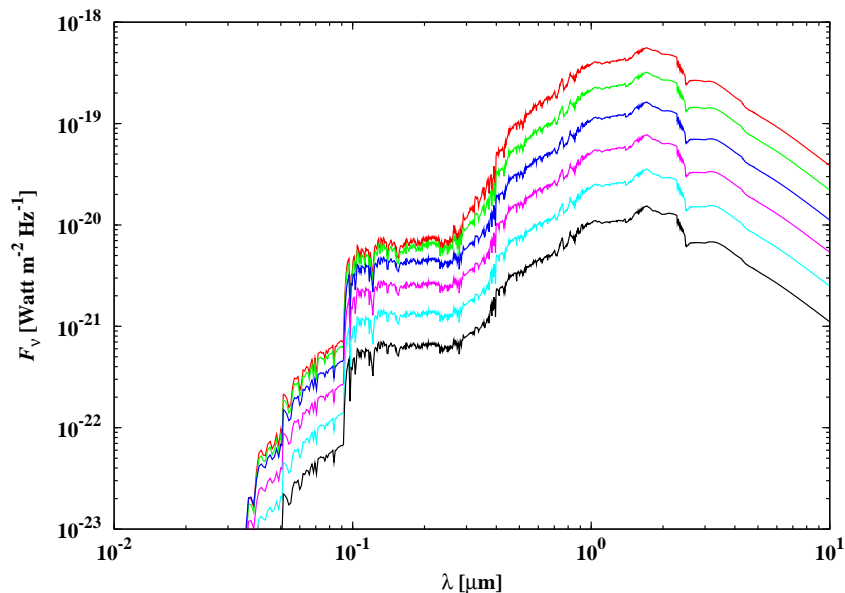
Figure 2.20: Intrinsic galactic luminosity density emitted by stars per unit of disk area for Galactic radii between 2 and 12 kpc (from top to bottom) with 2 kpc steps at instant 13 Gyr (present time).

let becomes important on late stages of galactic evolution. We approximate the spectra of stars with parameters beyond the grid of BaSeL library by pure blackbody radiation.

2.7.2 Results of spectral synthesis

Single Stellar Population

For test purposes we calculate the integrated fluxes of the single stellar population (SSP) that is a building block for the stellar population synthesis. SSP is a model of an instantaneous burst of star formation useful for the analysis of the contribution of different types of stars to the integrated spectrum at various epochs. Such tests have already been performed with existing codes for SSP in, for example, Bruzual & Charlot (2003). The calculated fluxes from the SSP of mass 1 $M_\odot$ and Solar metallicity with ages between 1 Myr and 13 Gyr are presented in Fig. 2.18.

Luminosity density in the Galactic disk

Figure 2.19 shows the intrinsic galactic flux density emitted by all stars per unit of disk area for several Galactic radii between 1 and 12 kpc at instant 5 Gyr calculated from eq. (2.27). Figure 2.20 depicts
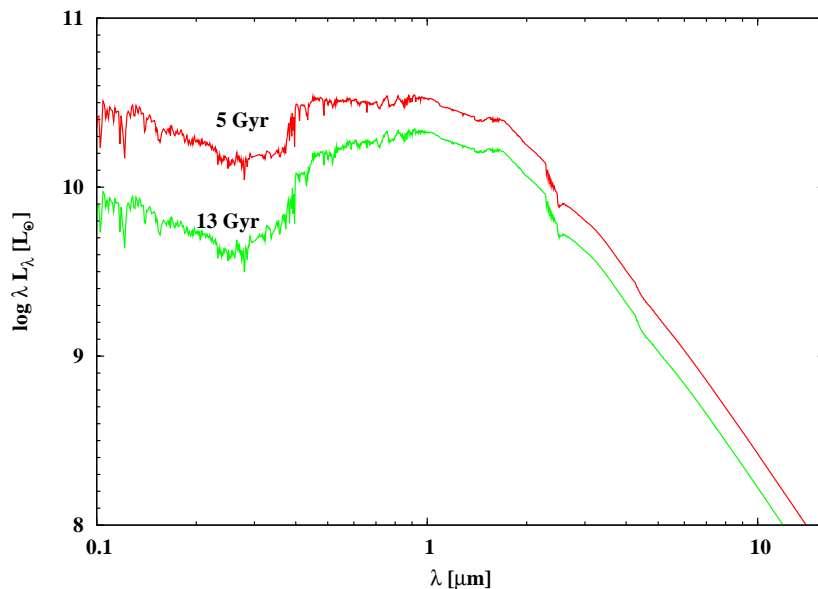
Figure 2.21: Integrated stellar SED from the Galactic disk as a function of wavelength at instants 5 and 13 Gyr in Solar luminosity units ($L_{\odot} = 3.8 \times 10^{33}$ erg s^{-1}).

the same for the present time t_G=13 Gyr. These data, together with distribution of dust and gas from our model of the galactic disk will provide the input for the radiative transfer calculations to be done in the future.

Total stellar SED in the Galactic disk

The total stellar SED from the Galactic disk surface obtained from eq. (2.29) for ages 5 and 13 Gyr is presented in Fig. 2.21. This is the basis for the calculations of the interstellar radiation field heating the dust grains. Our model spectrum of the Milky Way disk is in a good agreement with the stellar SEDs of normal spiral galaxies presented in the literature, for example, in Silva et al. (1998).

3

Multicomponent dust model

In the following we present the components of our model of evolution of the interstellar dust in the Milky Way disk. The model is based on the simple one-zone approximation for the galactic disk evolution described above. It follows the principles of the Dwek (1998) model, which was the first one that coupled dust evolution consistently with a full model for the chemical evolution of the Milky Way. The present model calculation concentrates on the following dust species

- silicates

- carbon

- silicon carbide

- iron

The silicate and carbon grains are the most abundant components of the interstellar dust that are responsible for most of its mass. They are also efficiently formed in stellar outflows of AGB stars and identified as stardust in meteorites and Interplanetary Dust Particles (IDPs). Another dust species of stellar origin found in meteorites is the silicon carbide (SiC), which is also a widespread stardust component. The model also considers iron dust, though it has not yet been identified as a presolar dust species. For theoretical reasons it should, however, be an abundant dust species produced in stellar outflows.

3.1 Evolution model for the interstellar dust

In our model we differentiate between dust coming from different types of parent stars. Even if the chemical composition of a certain dust species formed in outflows or ejecta of different stellar types is the same, the individual grains of this dust species are carriers of the isotopic anomalies corresponding
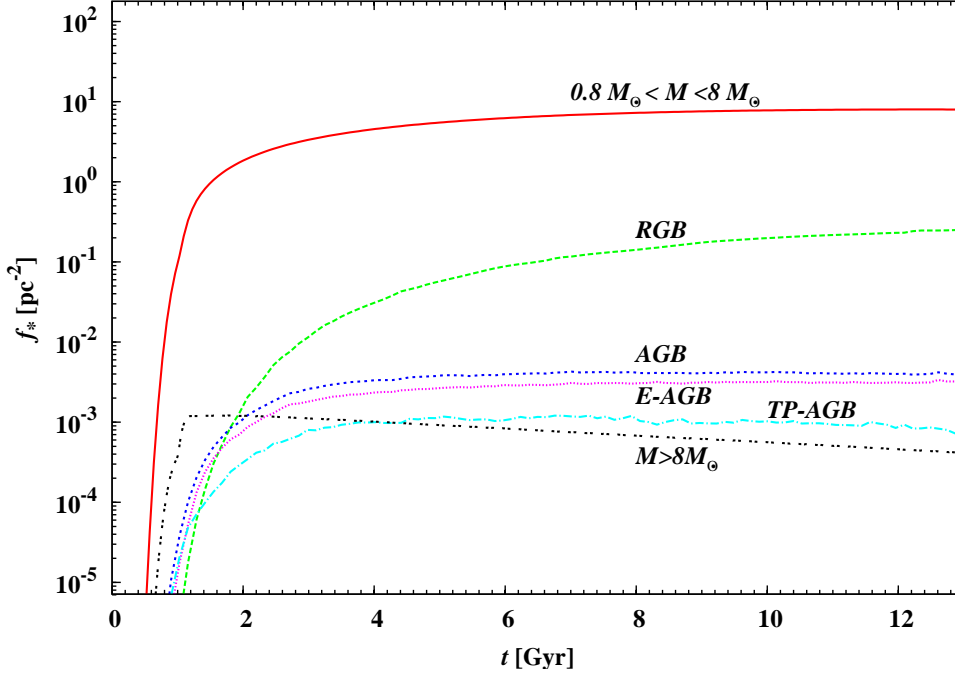
Figure 3.1: Number densities of low mass stars at various evolutionary stages in the solar circle. E-AGB and TP-AGB denote the number of stars at early AGB and thermally-pulsing AGB, respectively; the total number of AGB stars is also shown. The number density of high mass stars is presented for comparison.

to the particular nuclear processes operating in their parent stars. If they are investigated in the laboratory as presolar dust grains, one can, at least in principle, identify the formation site for every grain. This makes it desirable to count dust species from different types of stars with the same overall chemical composition but with different types of isotopic anomalies as different species denoted by j.

First, we include dust species of stellar origin. The important dust factories are low and intermediate mass stars at the final stages of their evolution. Efficient dust formation in stellar winds of these stars starts only when they experiences the strong mass-loss at the thermally pulsing AGB (TP-AGB). Although this phase is short in comparison with the lifetimes of low mass stars and the fraction of TP-AGB stars is only 10^{-4} of the total number of low and intermediate stars, the TP-AGB stars are responsible for majority of the stardust in the ISM. For illustration purposes, Fig. 3.1 demonstrates the evolution of the total surface number density of low and intermediate stars, and the surface number densities of these stars on the Red Giant Branch (RGB), the early AGB and the TP-AGB. The analysis of various evolutionary stages of stars is done by coupling our code for the galactic chemical evolution modeling with the analytical approximation for the stellar evolution of Hurley et al. (2000). As seen from Fig. 3.1, the number of red giant stars exceeds the number of TP-AGB stars in the solar vicinity by a factor of 100. In some studies of presolar dust grains in meteorites RGB stars are

Table 3.1: Dust species considered in the model calculation

	silicates	carbon	SiC	iron
AGB stars	√	√	√	√
SN II	√	√	√	√
SN Ia	—	—	—	√
ISM	√	√	—	√

identified as their progenitors. Our recent study of dust condensation during RGB (Gail et al. 2008) showed that only negligible amount of dust is formed in stellar winds of RGB stars. Thus, the low and intermediate stars become important dust contributors only in the TP-AGB stage. In the following the dust produced during this stage is denoted as AGB dust.

From the analysis of isotopic anomalies of presolar dust grains it is known that SN II also form dust, although its amount is very uncertain. Therefore we include the SN II as possible dust sources in the ISM and estimate their contribution to the stardust content in Sect. 3.4. Supernovae of type II and AGB stars can form all of the four chemically different types of dust considered in our model. The contribution from Supernovae of type Ia is even more uncertain. In principle, some iron can condense in Fe-rich adiabatically expanding ejecta, although most of this dust is likely to be destroyed by radioactive heating as the ejecta are reheated to the temperatures around 10^4 K (Wang 2006). For this reason only iron dust from SN Ia is included in the model. Hence we consider in our model nine different kinds of stardust coming from three different types of parent stars.

Second, we consider dust formed in the interstellar medium itself. From the element abundances in the interstellar medium, one expects that silicate dust can be formed. Observations of the interstellar dust indicate that carbon dust can also be formed in certain regions of the interstellar medium. It seems unlikely, however, that SiC dust can be formed, since this requires a carbon-rich environment, which is not encountered in interstellar space. Iron dust may also be formed in the ISM, though this element is probably consumed mainly by silicate formation. Hence we consider in our model three kinds of dust formed in the interstellar medium: silicate, iron, and carbon dust. In all, our model considers the twelve different kinds of dust from stellar sources and the interstellar medium given in Table 3.1.

We describe the abundance of each dust component j in the interstellar medium by its surface mass density $\Sigma_{j,\mathrm{d}}$. The evolution of the surface density is determined by the equation

$$\frac{\mathrm{d}\,\Sigma_{j,\mathrm{d}}}{\mathrm{d}\,t} = -\frac{\Sigma_{j,\mathrm{d}}}{\Sigma_{\mathrm{ISM}}}\,B + \sum_l R_{j,l,\mathrm{d}} - L_{j,\mathrm{d}} + G_{j,\mathrm{d}}\,. \tag{3.1}$$

The first term on the r.h.s. describes the loss of dust from the interstellar medium by star formation. It is assumed that only the dust content of the matter that is converted into stars is destroyed and

that no additional dust is destroyed during this process. Also no return of freshly-formed dust from protostellar disks by winds or jets is assumed to occur, though this has been speculated possibly to be important (Tielens 2003). The second term on the r.h.s. describes the amount of dust of kind j injected by stars of type l into the interstellar medium. The third term on the r.h.s. describes the losses, the destruction of dust of kind j in the interstellar medium, mainly by supernova shocks, and the last term describes the gain, the formation of dust of kind j in the interstellar medium by growth processes in molecular clouds. We assume no contribution of dust from the infall in our model.

From equations (3.1), one calculates the surface mass density of the different dust species j. Additionally, one has the set of equations for the total surface densities Σ_i of each element i in the ISM. The surface density $\Sigma_{i,\mathrm{g}}$ of each element in the gas phase of the ISM then follows as the difference between its total surface density Σ_i and the sum of the contributions of all dust species containing that element,

$$\Sigma_{i,\mathrm{g}} = \Sigma_i - \sum_j \nu_{ij} \frac{A_i}{A_{j,\mathrm{d}}} \Sigma_{j,\mathrm{d}} \,. \tag{3.2}$$

Here ν_{ij} is the number of atoms of element i in one formula unit[1] of dust species j, A_i and $A_{j,\mathrm{d}}$ are the atomic weights of element i and of one formula unit of dust species j, respectively, and the summation is over all dust species containing element i.

In the following we describe some details of dust production by stars related to the modeling of dust evolution in the interstellar medium.

3.2 Dust return by AGB stars

The main stardust factories are low and intermediate mass stars at the end of their evolution. These are stars with initial masses between about $0.8\,\mathrm{M}_\odot$ and about $8\,\mathrm{M}_\odot$, which end their life as White Dwarfs. The lower mass limit corresponds to that initial mass, for which the lifetime of a star corresponds to the age of the Milky Way. The upper mass limit corresponds to stars that finally explode as supernovae and do not evolve through an AGB phase[2].

The initial element mixture of all stars is oxygen rich in the sense that the abundance ϵ_O of oxygen exceeds the abundance ϵ_C of carbon. This does not change during their whole evolution up to the TP-AGB, despite some abundance changes during the first and second dredge-ups on the Red Giant Branch and the early AGB, respectively. If the third dredge-up process starts operating, the ashes of He burning are mixed to the convective envelope of the star after each thermal pulse, increasing the carbon abundance of the convective envelope stepwise, but only marginally changes its oxygen

---

[1]The formula unit is the fictitious molecular group in the solid corresponding to the chemical formula of the condensed phase

[2]Presently we neglect the possibility that stars from the region of initial masses $8 < M < 12\,\mathrm{M}_\odot$ may become super-AGB stars (e.g. Gil-Pons & García-Berro 2002)
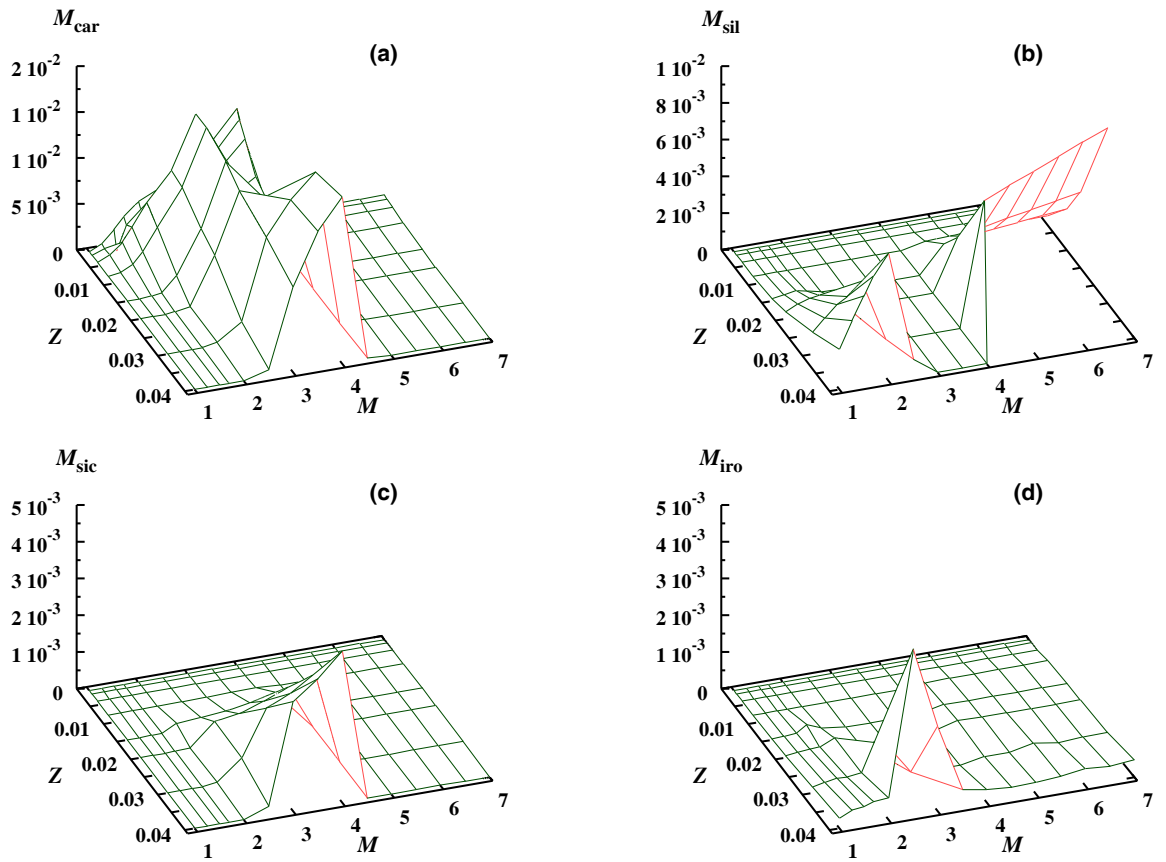
Figure 3.2: Dependence of the dust masses returned by single AGB stars for the four main kinds of dust species (silicates, carbon, silicon carbide, and iron) on metallicity Z and initial stellar mass M_*. All masses are in units of $M_\odot$. Data from Ferrarotti & Gail (2006) with some additional models.

abundance. The resulting evolution of the carbon-to-oxygen ratio ϵ_C/ϵ_O on the TP-AGB depends on the initial mass of the stars:

(1) Low mass stars with initial masses less than about $M = 1.5\,M_\odot$ lose their envelope by a stellar wind before the carbon abundance exceeds the oxygen abundance. Only for low metallicities does their envelope become carbon rich prior to complete envelope loss. For very low initial masses, probably no third dredge-up occurs and the stars never become carbon stars.

(2) Stars from the range of initial masses between about $M = 1.5\,M_\odot$ and about $M = 4\,M_\odot$ increase their carbon abundance over the oxygen abundance after a number of thermal pulses and become carbon rich. They evolve further as carbon stars until their envelope is lost by the stellar wind.

(3) Intermediate mass stars with initial masses between about $M = 4\,M_\odot$ and about $M = 8\,M_\odot$ convert the dredged-up carbon rapidly into ^{14}N via the CN-cycle, since the lower part of their convective envelope overlaps with the upper edge of the H-burning shell. The oxygen, however, is not affected by this process, and for this, the carbon abundance in the envelope of these stars is much less than the oxygen abundance. They do not become carbon stars until most of their envelope is lost, and the convection zone of the remaining envelope no longer overlaps with the H-burning shell. For a short period the stars then also become carbon stars until finally the last portion of their envelope is removed by the stellar wind.

Mechanism of grain growth in stellar winds

The basic process for grain growth is the collision of a species from gas phase with the surface of the grain. If the kinetic energy of gas particle is consumed by excitation of vibrational states of the solid, it is captured into a bound state of the surface oscillator, or adsorbed. At first an adsorbed particle is only weakly bound by van der Waals forces or electrostatic interaction. Since atoms at the grain surface are in permanent vibrations due to thermal excitations, an adsorbed particle excited by these vibrations can hop on the surface performing a random walk. At some point its vibrational energy can exceed the bound energy and it gets desorbed, or it hops into a place with locally higher bound energy, where it is captured and becomes a building block of the solid (e.g, Gail & Sedlmayer 1987, 1987).

Tables for dust production during AGB evolution

Depending on the C/O abundance ratio, the stars produce different dust mixtures in their outflows. Here we are only interested in the dominating dust species, which are formed from the most abundant elements, and so concentrate on the following four types of dust: silicates, carbon, silicon carbide, and iron. The dust masses produced over the whole period of AGB evolution for these dust species was calculated by Ferrarotti & Gail (2006). Magnesium sulphide is also observed to be an abundant

dust species in many C stars (cf. Molster & Waters 2003). The mechanism of formation of MgS in stellar winds was not clear until recently, so that MgS could not be included in modelling of dust condensation in stellar outflows during AGB evolution. In order to enable modeling of magnesium sulphide production in AGB stars and to extend the tables of Ferrarotti & Gail (2006) to include this dust species, we study different mechanisms of MgS formation in Sect. 3.3 explaining its observed high abundance.

The silicate dust is only produced during the oxygen-rich phase of the stellar evolution where the stars spectroscopically appear as M stars. Some minor fractions are also produced during the S star phase where the C/O abundance ratio is close to unity. The silicates are a mixture of olivine- and pyroxene-type amorphous dust and, for part of the stars, also up to about 15% of nearly iron free crystalline forsterite and enstatite is observed to be formed (cf. the review of Molster & Waters 2003). The present work does not distinguish between the two types of amorphous silicate dust since for silicate dust in the interstellar medium it is presently not possible to distinguish by observations of the dust absorption spectrum unambiguously between the two different components (cf. the contradictory results in Chiar & Tielens 2006 and Min et al. 2007, however). In order to calculate the fractions of elements Mg, Si, O, Fe returned by AGB stars as dust grains, the exact composition of silicate is needed. Therefore, we calculate new dust tables with the complete data set showing the separate dust species on finer grids for metallicity and mass, added in Appendix A.

Also, crystalline Mg-silicates are not considered since they are not found in the interstellar medium (Kemper, Vriend & Tielens 2004), possibly because they are rapidly amorphized in the ISM after their ejection by interaction with energetic electrons and ions (cf. Demyk et al. 2004; Jäger et al. 2003).

Carbon and silicon carbide dust are produced by AGB stars during their carbon rich phase of evolution on the AGB where they spectroscopically appear as C stars. Iron dust is included in the model calculation, though it has not yet been unambiguously identified as a major dust component in stellar outflows; only some hints of its existence have been found up to now (e.g. Kemper et al. 2002). This is because no readily identifiable spectroscopic features exist for solid iron. Nevertheless, for reasons of element abundances, it should be an abundantly formed dust species in S stars and C stars, and to some extent also in M stars.

Figure 3.2 shows the calculated dust masses for the four types of dust considered. In the model calculation of Ferrarotti & Gail (2006), olivine- and pyroxene-type dust are treated as separate species, but their production rates are added for the reasons mentioned above.

There is a general tendency for the stars to be a factory either mainly for silicate dust or mainly for carbon dust (cf. Fig. 12 of Ferrarotti & Gail 2006), because most of the dust formed over the total lifetime of a star on the AGB is formed during the very last pulse cycles on the TP-AGB, where mass-loss rates are highest. If the stars are carbon stars during this phase, they mainly produce carbon dust (and SiC); otherwise, they mainly produce silicate dust.

The carbon dust production, shown in Fig. 3.2a, is dominated by stars with initial masses between about 1.5 and $4\,M_\odot$ and does not vary much with initial stellar metallicity, since the carbon required for carbon dust production is synthesised from He by the star itself. Stars with initial masses $M > 4\,M_\odot$ also form some carbon dust, but only small amounts during their very last stage of evolution when hot bottom burning is no longer active. Stars with initial masses $M < 1.5\,M_\odot$ do not form much carbon dust because the total mass returned by them on the AGB is quite small, or because they do not suffer third dredge-up events (for very low initial masses), or there are too few of them.

The production of the other dust species by AGB stars strongly depends on their initial metallicity because the required heavy elements —with the possible exception of Mg— are not fabricated by AGB stars but have to be formed in many preceding stellar generations until their abundances grow to a level where dust formation becomes possible.

Figure 3.2b shows the silicate dust production by AGB stars. The silicate production is efficient for stars from essentially that range of initial masses where they do not become efficient carbon dust producers; i.e., the main contribution comes from stars with initial masses $M < 1.5\,M_\odot$ or $M > 4\,M_\odot$. But also in the mass range in between, where the stars are efficient carbon dust factories, they produce some silicate dust before they become carbon stars. The silicate dust production starts to become efficient only at rather high metallicities because only then are sufficient amounts of Si, Mg, and Fe for silicate formation available in the stellar outflows.

Figure 3.2c shows the production of silicon carbide dust by AGB stars. This is produced by carbon stars, and therefore its production is limited to the same range of initial masses as for carbon production. The lack of available Si, however, also prevents the formation of much SiC in low metallicity stars.

Figure 3.2d shows the production of iron dust by AGB stars. Iron dust formation seems to be efficient in outflows from AGB stars only at rather high metallicities, which are not encountered in the Milky Way at the solar circle, but only close to its centre.

3.2.1 Dust return by single stellar population

The dust production yields can be also presented as dust returned by the single stellar population (SSP). In addition to Fig. 3.2, such representation convey the information about the timescales of dust injection by stars, that is determined by their lifetimes, and distribution of stars over masses in a stellar generation. The SSP introduced earlier in Sect. 2.7.1 is a main component of stellar population synthesis and chemo-dynamical models of galactic evolution (Berczik et al. 2003).

The mass of dust of kind j returned by the SSP of metallicity Z is

$$M_{j,\mathrm{d}}(t) = \int_{M_l'}^{M_{\mathrm{WD}}} \frac{M_{j,\mathrm{ret}}^{\mathrm{d}}(M, Z)}{M_{\mathrm{av}}} \Phi(M)\,dM \,, \tag{3.3}$$
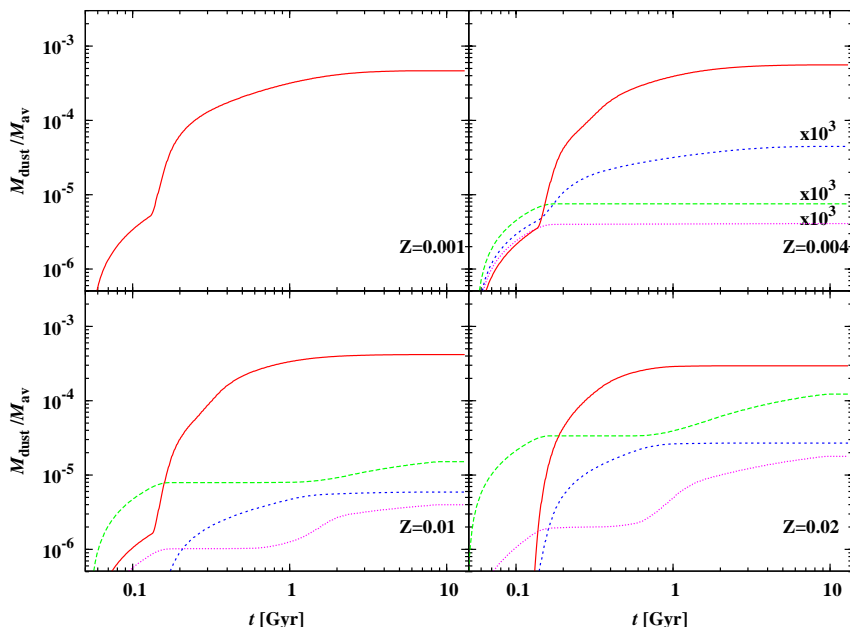
Figure 3.3: Dust mass returned by AGB stars of a single stellar population relatively to SSP total mass as a function of time for metallicities $Z = 0.001$, 0.004, 0.01, and 0.02. The different lines correspond to carbon dust (solid line), SiC (short dashed), silicates (long dashed) and iron dust (dotted). Masses of SiC, silicates and iron dust for $Z = 0.004$ are multiplied by factor of 10^3.

where the integration start from the mass M'_l corresponding to the lifetime $\tau(M'_l, Z) = t$. The quantity Φ is the initial mass function, described in Sect. 2.3.3, M_{av} the average mass of the stars, given by Eq. (2.17).

Figure 3.3 shows the dust return by SSP relatively to SSP mass as a function of time for the metallicities $Z = 0.001$, 0.004, 0.01, and 0.02. The dust content of the SSP is mainly dominated by carbon dust produced during the first Gyrs of evolution. However, for higher metallicities $Z \geq 0.01$ and 0.02 silicate dust dominates the dust mass during the first 150 Myr. For silicates and iron dust Fig. 3.3 basically reflects the bimodal mass distribution of their producers (Fig. 3.2b and d), with the first mode ending at about 150 Myr, that is the lifetime of a star of 4.5 $M_\odot$. Since most stars are born in stellar clusters, that are gradually dissolved on the timescale up to several Gyrs, the grains injected by AGB stars earlier are exposed to an intense radiation field in the dense stellar environment of the cluster, which is an important factor for evaporation and heating of small grains. The second mode of silicate dust injection starts with the final evolutionary phase of stars of ≤ 2.5 $M_\odot$ at $t \geq 1$ Gyr. By this time the radiation field in the cluster is substantially reduced, since more massive bright stars have died, and, also many low and intermediate mass stars have been lost due to tidal interaction. The

probability of survival of the dust grains injected during the second mode is therefore higher than that for dust from massive AGB stars ejected during the first mode. The quantitative estimates of effects of stellar cluster environment on stardust destruction is a separate challenging problem, which has to be considered in close relation to dynamical evolution of the stars in cluster.

Dust production by SSP can be used for analysis of dust return by an instantaneous burst of star formation with no dust destruction. Such short intense star formation events separated by long quiescent periods take place in blue compact dwarf galaxies (Recci 2002). The main sources of dust destruction in the ISM are supernovae shocks as will be discussed in details in Sect. 4.1, which happen within the first 40 Myr after star burst event. Therefore, dust ejected by AGB stars, which have longer lifetimes may survive between the star bursts.

3.2.2 Dust injection rates

The dust-mass injection rate of dust species j into the interstellar medium is given by

$$R_{j,AGB,\mathrm{d}}(t,r) = \int_{M_\mathrm{l}}^{M_\mathrm{WD}} dM \, \Phi(M) \frac{B(t_\mathrm{b},r)}{M_\mathrm{av}} M_{j,\mathrm{ret}}^\mathrm{d}(M, Z_\mathrm{ISM}(t_\mathrm{b},r)), \qquad (3.4)$$

where $B(t,r)$ and $Z_\mathrm{ISM}(t,r)$ are the stellar birthrate and the metallicity of the interstellar medium at instant t and galactocentric radius r, respectively. Both quantities are taken from the model calculation for the evolution of the galactic disk (see Figs. 2.3 and 2.4). The instant t_b is the time of birth of a star ending its life at instant t given by non-linear equation (2.3) that has to be solved numerically.

The metallicity of the stars equals the metallicity Z_ISM of the interstellar medium at their birthtime t_b, which is taken from our model for the Milky Ways evolution (cf. Fig. 2.4). The mass return in the dust species j by AGB stars of different initial masses and metallicities $M_{j,\mathrm{ret}}^\mathrm{d}(M, Z)$ are taken from the tables of Ferrarotti & Gail (2006) discussed above; some additional models have been calculated for the present work. The integration is performed over the initial masses of the stars from the lower limit M_l, here taken to be $1\,\mathrm{M_\odot}$, and the upper limit M_WD up to which stars evolve into White Dwarfs, here taken to be $8\,\mathrm{M_\odot}$.

3.3 MgS formation in stellar winds of carbon stars

This section is based on the results of the paper Zhukovska & Gail 2008.

Magnesium sulphide is a wide-spread dust component in dust forming carbon stars. Since Mg and S are abundant elements, this dust species forms a major component in the dust mixture injected by dying AGB stars to the interstellar medium. Modelling the MgS dust production by AGB stars and its contribution to the interstellar dust requires a knowledge of the production mechanisms at least of the abundant dust species. Since a condensation model for MgS is presently lacking, we try to develop

such a model. We will explain, why we believe that MgS condenses in stellar outflows as a mantle on SiC grains.

The prominent broad emission feature centering around 30 μm is commonly seen in carbon-rich environments, in AGB stars, post-AGB stars and planetary nebulae. It was firstly detected by Forrest et al. (1981) and later attributed to magnesium sulphide by fitting the observed feature with the optical properties of solids measured in the laboratory (Goebel & Moseley 1985; Nuth et al. 1985). In order to allow to include a calculation of the MgS emission feature in model calculations of radiative transfer in circumstellar dust shells, and thus to enable a quantitative comparison between observations and theory, Begemann et al. (1994) determined optical constants of $Mg_xFe_{1-x}S$ $(0.9 \geq x \geq 0)$. They obtained good agreement between the observed emission band profile and the calculated spectrum in the 30 μm region for a radiative transfer model of the circumstellar dust shell of IRC+10216.Nowadays, the identification of MgS as a carrier of this feature seems solid, though other interpretations are occasionally discussed (e.g. Papoular 2000; Grishko et al. 2001; Volk et al. 2002).

A number of observational and theoretical studies of the 30 μm emission from dust enshrouded AGB and post-AGB stars, and from the environment of planetary nebulae appeared since that time (e.g. Omont 1993; Omont et al. 1995; Yamamura et al. 1998; Jiang et al. 1999; Szczerba et al. 1999; Hrivnak et al. 2000; Hony et al. 2002; Volk et al. 2002; Hony & Bouwmann 2004; Lagadek et al. 2006; Zijlstra et al. 2006; Leisenring et al. 2008). Good examples for the emission band can be found in Hony et al. (2002), Volk et al. (2002) for galactic objects and Lagadek et al. (2006) and Zijlstra et al. (2006) for the Magellanic clouds. They all show unequivocally that MgS formation is a common phenomenon for carbon stars on the tip of the AGB.

The formation mechanism of this MgS is not clear. It is already speculated in the first papers by Nuth et al. (1985) and Goebel et al. (1985) that MgS forms via a surface reaction on carbon grains and this scenario was favoured over MgS condensation as a separate dust species. A laboratory investigation on MgS condensation was conducted by Kimura et al. (2005), but this gives no direct insight in the formation process. No further discussion of this problem seems to have appeared in the astrophysical literature so far. In the following we will show that MgS can only be formed in the outflows of stars by precipitating on pre-existing grains and that MgS in all likelihood forms as mantle on the silicon carbide grains formed closer to the star at higher temperature.

3.3.1   Formation of MgS in a stellar wind

In stellar outflows temperature and density variations occur on shorter timescales than particle growth. In this case condensation proceeds far from chemical equilibrium and particle growth has to be treated by reaction kinetics. We consider here the conditions under which MgS condensation may occur in a rapidly expanding stellar outflow.

3. MULTICOMPONENT DUST MODEL

Stationary wind model

The formation of MgS in stellar outflows from AGB stars seems to be associated with late phases of AGB evolution of low and intermediate mass stars, where the mass-loss rate is very high and the stars have lost already most of their hydrogen rich envelope.

At the tip of the AGB, radiation pressure on dust becomes the dominating driving source of the wind. The underlying stars seem all to be variables, either Miras or LPVs. The structure of the outflow is complicated in this case, since there are always several shocks running outwards, which are superposed on the average outflow of stellar material. This is demonstrated by several model calculations of dust forming stellar outflows of pulsating stars (e.g. Bowen 1988; Fleischer et al. 1991; 1992; Feuchtinger et al. 1993; Höfner & Dorfi 1997; Höfner et al. 1998; Winters et al. 1997; 2000; Jeong et al. 2003).

Calculating dust formation rates for multi-component dust mixtures of stars with quite different elemental compositions and widely varying stellar parameters presently seems not to be possible for reasons of computational time requirements if the shock structure of the wind is to be taken into account. For the purpose of calculating the composition of the dust mixture and the amount of dust formed in the outflows of AGB-stars we use a more simple model, which assumes a stationary outflow. If one compares the velocity and density profiles of such stationary winds with published models of dust forming pulsators (e.g. Winters et al. 2000; Jeong et al. 2003), one observes in most cases a strong resemblance of the average velocity and density profiles with that of the stationary models, except that in the pulsation models outwards propagating shocks are superposed on the average flow structure. So we can hope to obtain at least an estimate of the average quantities of dust formed in the outflow if dust formation is calculated for such an average outflow structure. One important consequence of this neglect of the detailed structure of the flow is that we cannot determine self-consistently the mass-loss rate $\dot{M}$. We have to treat this as a free parameter, which has to be fixed in some other way.

Stellar parameters

The central star is assumed to be on the tip of the AGB. Its luminosity then is typically $L_* = 1.5 \times 10^4 \, L_\odot$.

For stars forming MgS in their outflow a rather high metallicity is required since at low metallicities the abundances of Mg and S would be too low for this to be possible. Only a small fraction of the carbon stars in the Small Magellanic Cloud, for instance, seem to form MgS dust (Sloan et al. 2006), while for carbon stars in the Large Magellanic Cloud the formation of MgS seems to be more common (Zijlstra et al. 2006), and in the Milky Way it is quite common for highly evolved carbon stars (e.g. Hony 2002). We note already at this place that according to observations MgS formation

seems to be associated with SiC formation: Stars showing the MgS feature also show the SiC feature, but not all stars showing a SiC feature also show the MgS feature in their spectra (e.g. Zijlstra 2006). In order that low and intermediate mass stars of Pop I (or not much lower) metallicity become carbon stars, their initial masses must be from the mass range between about 1.5 $M_\odot$ and about 4 $M_\odot$.

After massive mass-loss on the AGB the stellar mass is likely to be already substantially reduced and we assume in the model calculation a fixed stellar mass of 1 $M_\odot$. The stellar radiation is approximated by a black body spectrum. The effective temperature (in the inter-pulse phase) is determined from the relation

$$\log T_{\text{eff}} = 0.234 \log M - 0.2 \log L - 0.116 \log \frac{Z}{0.02} + 4.146 \tag{3.5}$$

given by Vassiliadis & Wood (1993) for stars on the AGB. The mass M and luminosity L are in solar units. With the assumed stellar parameters and solar metallicity one finds $T_{\text{eff}} = 2\,250$ K.

The mass-loss rate is estimated from the relation

$$\dot{M} = 2.1 \times 10^{-8} \frac{L}{v_\infty} \tag{3.6}$$

given by Vassiliadis & Wood (1993) for stars in the superwind phase. The luminosity is in units of $L_\odot$, the outflow velocity v_∞ in km s^{-1}, and the mass-loss rate in units of $M_\odot$ yr^{-1}. With the estimated stellar parameters and a typical outflow velocity in the superwind phase of 10 - 15 km s^{-1} one obtains a mass-loss rate of about $\dot{M} = 2 - 3 \times 10^{-5}$ $M_\odot$ yr^{-1} for stars at the end of their AGB evolution. A value of $\dot{M} = 3 \times 10^{-5}$ $M_\odot$ yr^{-1} is used in the model calculations.

The C/O abundance ratio of the outflowing material in any case exceeds unity since MgS is not formed in an oxygen rich environment.

3.3.2 Dust particle growth

The model calculation of condensation in the outflow from a carbon star considers the following dust components: carbon dust, silicon carbide dust, and iron dust. The formation of these dust species is calculated as outlined in Ferrarotti & Gail (2006). Here we add the growth of magnesium sulphide to our model. The dust formation is calculated by solving the equations for dust growth (e.g. Gail 2003)

$$\frac{d a}{d t} = V_0 \, \alpha \, n_{\text{gr}} \sqrt{\frac{kT_{\text{g}}}{2\pi m_{\text{gr}}}} \left\{ 1 - \frac{p_{\text{eq}}(T_{\text{d}})}{n_{\text{gr}} kT_{\text{d}}} \sqrt{\frac{T_{\text{d}}}{T_{\text{g}}}} \right\} \tag{3.7}$$

for all species of interest. Here a is the radius of a dust grain, V_0 the volume of one formula unit of the chemical compound in the solid, α is the growth coefficient, n_{gr} is the particle density of the growth species in the gas phase, m_{gr} its mass, p_{eq} is the partial pressure of the growth species in a state of chemical equilibrium between the condensed phase and the gas phase, and T_{g} and T_{d} are the gas temperature and the internal lattice temperature of the dust, respectively.

61

Table 3.2: Basic data used for calculation of MgS grain growth

Quantity	value	unit
A	56.37	
ϱ_d	2.68	$\mathrm{g\,cm^{-3}}$
V_0	3.51×10^{-23}	$\mathrm{cm^3}$
α	0.2	
ϵ_{Mg}	3.85×10^{-5}	
ϵ_{Si}	3.58×10^{-5}	
ϵ_{S}	1.85×10^{-5}	
ϵ_{d}	10^{-13}	
a_{max}	0.12	μm
v_{th}	1.52×10^4	$\mathrm{cm\,s^{-1}}$

The volume V_0 of one chemical formula unit occupied in the solid is

$$V_0 = \frac{A_d m_H}{\varrho_d}\,, \tag{3.8}$$

where A_d is the atomic weight of the chemical formula unit and ϱ_d the bulk density of the condensate.

The growth equation has to be complemented by an equation for the consumption of the growth species from the gas phase. The details are described in the paper by Ferrarotti & Gail (2006) and are not repeated here.

As rate determining step for the formation of MgS we assume the addition of a H_2S molecule from the gas phase via reaction

$$H_2S \;+\; Mg \longrightarrow MgS(s) \;+\; H_2\,, \tag{3.9}$$

since this is the least abundant of the molecules involved in the reaction. p_{eq} in Eq. (3.7) is calculated from law of mass

$$a_{MgS(s)} p_{H_2} \;=\; p_{H_2S}\, p_{Mg}\, e^{-\Delta G_2/RT}\,, \tag{3.10}$$

with activity $a_{MgS} = 1$. The thermodynamic data for calculating ΔG are taken from JANAF-tables (Chase 1998).

The growth coefficient α, the probability that a collision is followed by a growth step, seems not to be known. For the similar solid MgO with the same structure and similar bonding properties Hashimoto (1990) measured a growth coefficient of about 0.2 and we will use the same value for MgS.

3.3.3   Possible carrier grains

The dust species that may serve as carrier grains for MgS formation need to form dust grains with a size not much smaller than about $a_c = 0.1\,\mu$m because otherwise the condensed fraction of MgS becomes too small if the radius of the cores is smaller than this. This restricts the possibilities, which dust species may serve as substrates of MgS growth, to the most abundant dust species.

The outflowing gas enters the temperature regime below about 650 K favourable for MgS condensation with two major dust species that have grown farther inside in the shell to the required size: SiC grains and carbon grains. From investigations of presolar dust grains it is known that from the many poly-types of SiC only two are formed in circumstellar environments (Daulton et al. 2003): The cubic 3C poly-type (usually denoted as β-SiC) is found in 79.4 % of all observed grains, and the hexagonal 2H poly-type (usually denoted as α-SiC) is found in 2.7 % of all observed grains. In 17.1 % of all grains the material is an intergrowth of these two poly-types.

The lattice structure of the SiC grains in stellar outflows, thus, in most cases is cubic. Magnesium sulphide also has cubic lattice structure. The electronegativity difference (cf. Pauling 1960) of MgS is 1.3 and that of SiC is 0.7. Both compounds therefore show a significant ionic contribution to their bonding. There are obvious similarities of structure and bonding properties of SiC and MgS. On the other hand, no such similarity exists between MgS and solid carbon. This suggests that SiC is much better suited as substrate for MgS precipitation than carbon. We propose therefore that MgS grows on SiC grains.

A possible core grain is any compound that has a lattice structure similar to the MgS crystalline structure and a higher condensation temperature. Among the compounds possibly formed in the stellar outflows CaS also satisfies both conditions. It has a crystal structure, that is the closest to that of MgS and becomes stable at a more than 200 K higher temperature than MgS. The abundance of Ca in a stellar wind, however, is 16 times lower than the Mg abundance, which is not very favourable for its role as core grain for MgS growth. Nevertheless, we will also check this possibility.

3.3.4   Models with core-mantle grains

We performed model calculations of dust formation in stellar outflows according to the wind model described in Sect. 3.3.1 to check the assumption of the core-mantle growth scenario of MgS formation. Grain growth is calculated as described in Sect. 3.3.2.

First we check the model of MgS condensation on tiny seed nuclei. The existence of such seeds of 1 nm is taken for granted and the growth of MgS is calculated. This results in grain sizes of only about $0.02\,\mu$m and a very low fraction of Mg bound in dust, the condensation degree, of about 0.01. The evolution of grain radius and condensation degree for this kind of model are shown in Fig. 3.4 and Fig. 3.6, respectively. The small amount of condensed MgS found in this case is obviously not
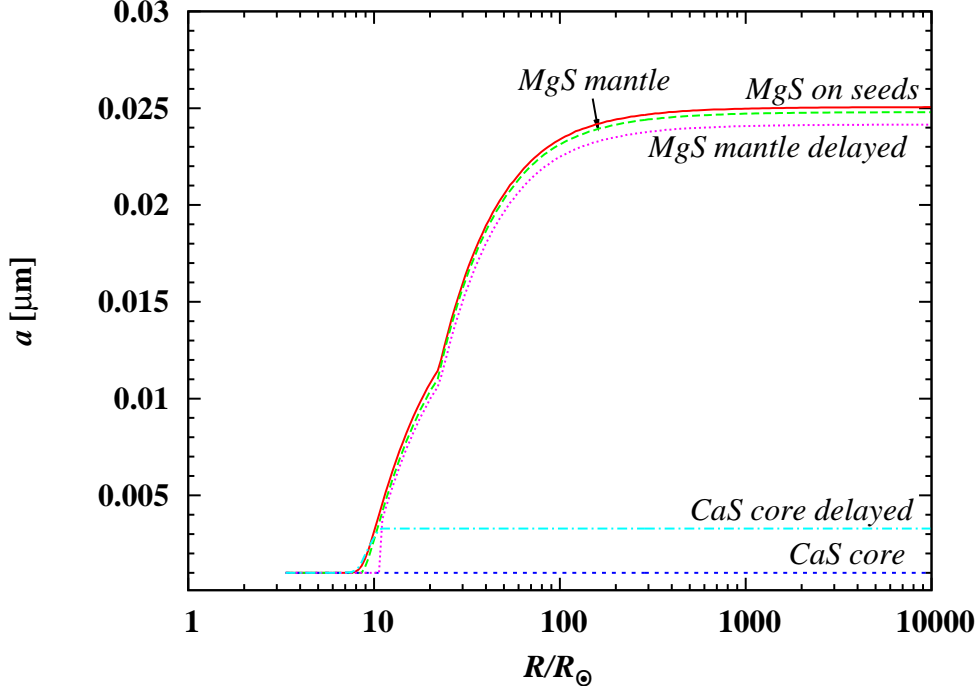
Figure 3.4: Evolution of MgS and CaS grain radius as function of distance from the centre of the star, for MgS formation (i) on seed nuclei of 1 nm size, and (ii) as mantle on a CaS core. Also shown are the results of a model with delayed onset of MgS condensation on CaS core; details are given in the text.

enough to explain the observed 30 μm emission in the spectra of carbon stars, underlining, again, the need for a core-mantle growth mechanism of MgS formation.

Next we check an alternative growth scenario for MgS formation, in which first CaS condenses on seed nuclei by the analogue of reaction (3.9), and then MgS grows as a mantle on this core. The model calculations show that the size of CaS grains is much smaller than the required radius of 0.1 μm. We also tested the case, that MgS condensation is delayed by imposing the additional condition for the growth rate $J_{gr,MgS} \geq 3J_{gr,CaS}$ to gain additional time for CaS core growth in order to get bigger grains. This artificial delay results, indeed, in bigger CaS cores, but also this does not help to increase the final size of the MgS mantle. The results of these calculations of the evolution of the MgS grain radius with distance from the centre of a star for normal and delayed condensation on CaS are also shown in Fig. 3.4. The figure shows that the condensation of MgS on a CaS core results in almost the same grain radius as the growth of MgS on seeds grains. Both these formation mechanisms can not provide the amount of MgS dust that is observed to condense in stellar outflows.

SiC grain growth, however, commences at higher temperature and proceeds faster than CaS growth, so that at the onset of MgS formation the SiC core radius reaches $\propto 0.07\,\mu$m as shown in
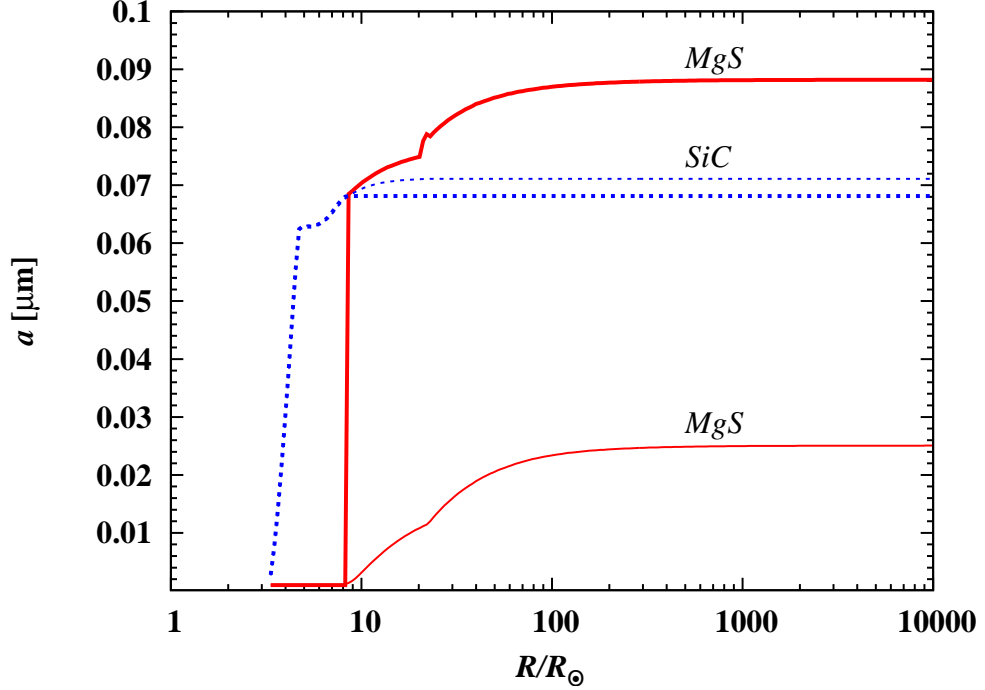
Figure 3.5: Evolution of radius of SiC and MgS grains as predicted (i) by the model for MgS condensation on seed nuclei, and (ii) as mantle on a SiC core (thin and thick lines, respectively).

Fig. 3.5. The results of MgS condensation on tiny seed nuclei are shown in Fig. 3.5 for comparison. The SiC core is big enough to allow the formation of a considerable thickness of the MgS coating, of order 0.02 μm, which results in a final grain size of 0.9 μm. This value is very close to the required grain sizes to explain the shape of the extinction feature in the spectra of carbon stars. We assume in the calculation that SiC grains do not grow anymore as soon as the formation of the MgS mantle begins. Figure 3.5 show that growth of SiC grain with and without termination due to MgS mantle formation does not change the grain size very much. Thus, a model with MgS mantle formation on SiC does not change noticeably the fraction of Si condensed in SiC dust, but results in a much higher value of the degree of condensation of Mg in MgS as compared to the case of growth on seeds. This is illustrated in Fig. 3.6.

A similar test calculations for MgS coating formation on carbon grains also gave sufficient thicknesses of MgS layers. Basically, condensation of MgS on carbon cores cannot be excluded, but from a physical point of view, MgS mantle formation is more likely on a SiC core, since the bond lengths and bonding properties of SiC are similar to that of MgS. Laboratory experiments would be necessary to arrive at a final conclusion about the carriers of MgS mantles.
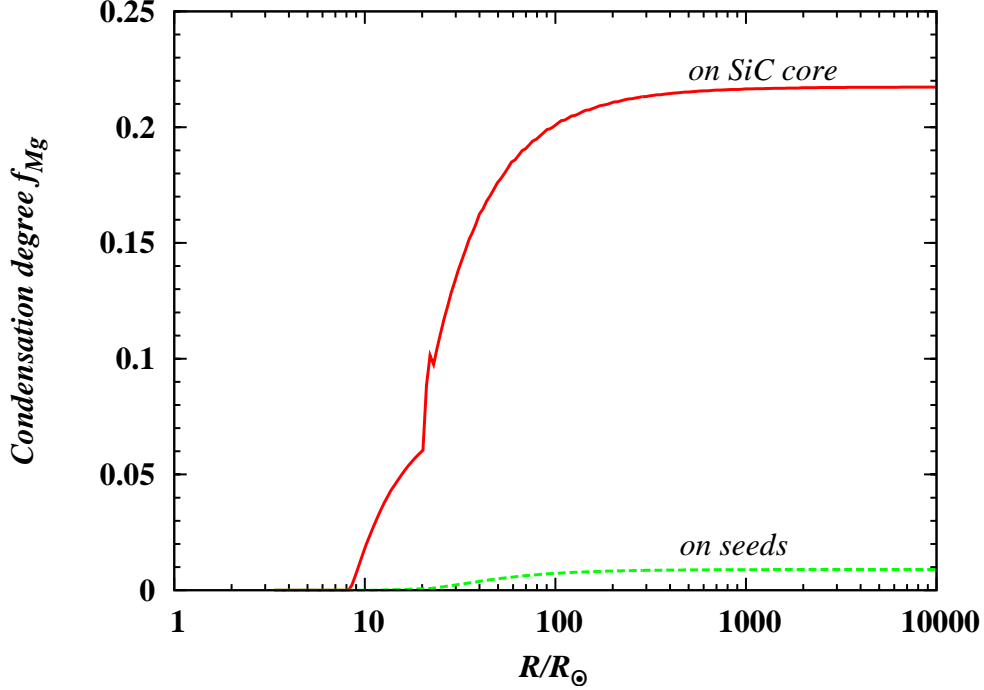
Figure 3.6: Evolution of condensation degree of Mg with distance from the centre of the star for condensation of MgS (i) as mantle on top of a SiC core and (ii) on seed particles (solid and dashed line, respectively).

3.3.5 Optical properties of grains with SiC core and MgS mantle

In order to study the difference of optical properties of grains with coatings of MgS either on a SiC core or on a carbon core we calculate the absorption efficiency C_λ^{abs} (i.e. the ratio of absorption to geometrical cross-section) in the small particle limit (cf. Bohren & Huffman 1983)

$$C_\lambda^{abs} = 4x \operatorname{Im} \frac{\alpha}{4\pi (r_c + r_m)^3} \tag{3.11}$$

with

$$\alpha = 4\pi (r_c + r_m)^3 \frac{(r_c + r_m)^3 (\epsilon_2 - 1)(\epsilon_1 + 2\epsilon_2) + r_c^3 (2\epsilon_2 + 1)(\epsilon_1 - \epsilon_2)}{(r_c + r_m)^3 (\epsilon_2 + 2)(\epsilon_1 + 2\epsilon_2) + r_c^3 (2\epsilon_2 - 2)(\epsilon_1 - \epsilon_2)} . \tag{3.12}$$

Here r_c is the core radius, r_m the thickness of the mantle and ϵ_1 and ϵ_2 are the complex dielectric functions of the core and mantle material, respectively. x is the size parameter $2\pi (r_c + r_m)/\lambda$. The small particle approximation $x \ll 1$ is valid in our case since we are interested in wavelengths from the region from 10 to 40 μm that are much bigger than the size of circumstellar dust particles.

Optical constants for MgS are taken from Begemann et al. (1994) for $Mg_x Fe_{1-x} S$ with $x = 0.9$. For carbon we use data for the BE carbon dust of the evaluation of the data of Colangeli et al. (1993)
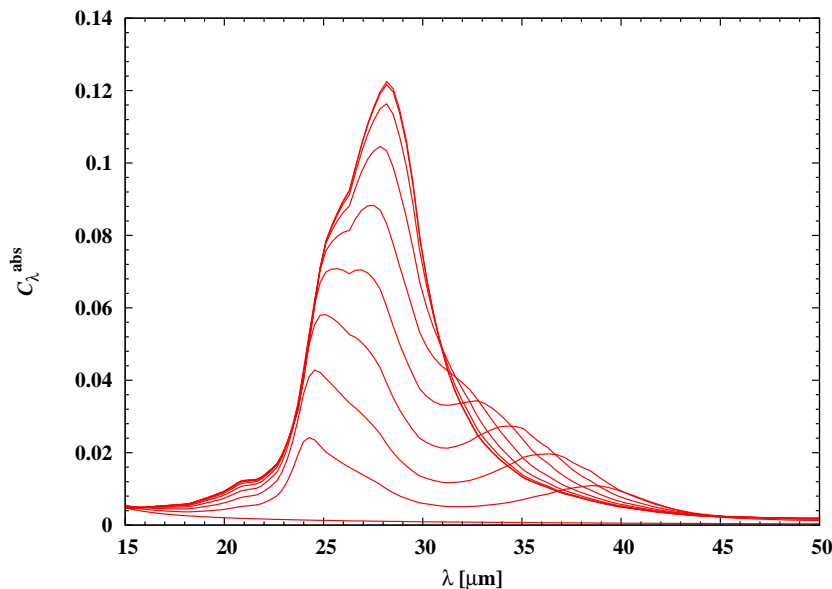
Figure 3.7: Wavelength variation of the absorption efficiency C_λ^{abs} of spherical grains with SiC core of radius r_c coated with MgS mantles of thickness r_m for a total grain radius $r_c + r_m$ of 0.1 μm and for MgS-mantle thickness to total radius ratios from 0 to 1 in steps of 0.1 (from bottom to top).

by Zubko et al. (1996). For SiC we used the data for SiC from Laor & Draine (1993). Extinction efficiencies have been calculated for SiC grains coated with MgS mantles and, for comparison, also for carbon grains with MgS mantles.

Figure 3.7 shows results for grains of total radius $r_c + r_m$ of 0.1 μm and mantle thicknesses between 0 and 0.1 μm, i.e., for grains ranging in composition from pure SiC to pure MgS grains. The results show the rather broad MgS absorption band centred around about 26 μm, which in itself shows some structure. Additionally there appears a secondary peak centred around $\approx$ 33 ... 38 μm for not too big mantle thicknesses. Its position depends on the size ratio of core and mantle. This feature is not present in the extinction efficiencies of MgS or SiC and results from the particular run of the complex dielectric functions of the core and the coating in this wavelength region[1].

Figure 3.8 shows the variation of the extinction coefficient with varying core to mantle size ratios – both for MgS grains with SiC and with carbon core – in a different representation and an extended wavelength region that also covers the 11 μm feature of SiC. The total grain radius $r_c + r_m$, again,

---

[1]It has been checked if this results from a Fröhlich mode in coated particles at a frequency where the denominator in Eq. (3.12) vanishes, cf. the discussion of this effect in Bohren & Huffman (1983), but this seems not to be the case
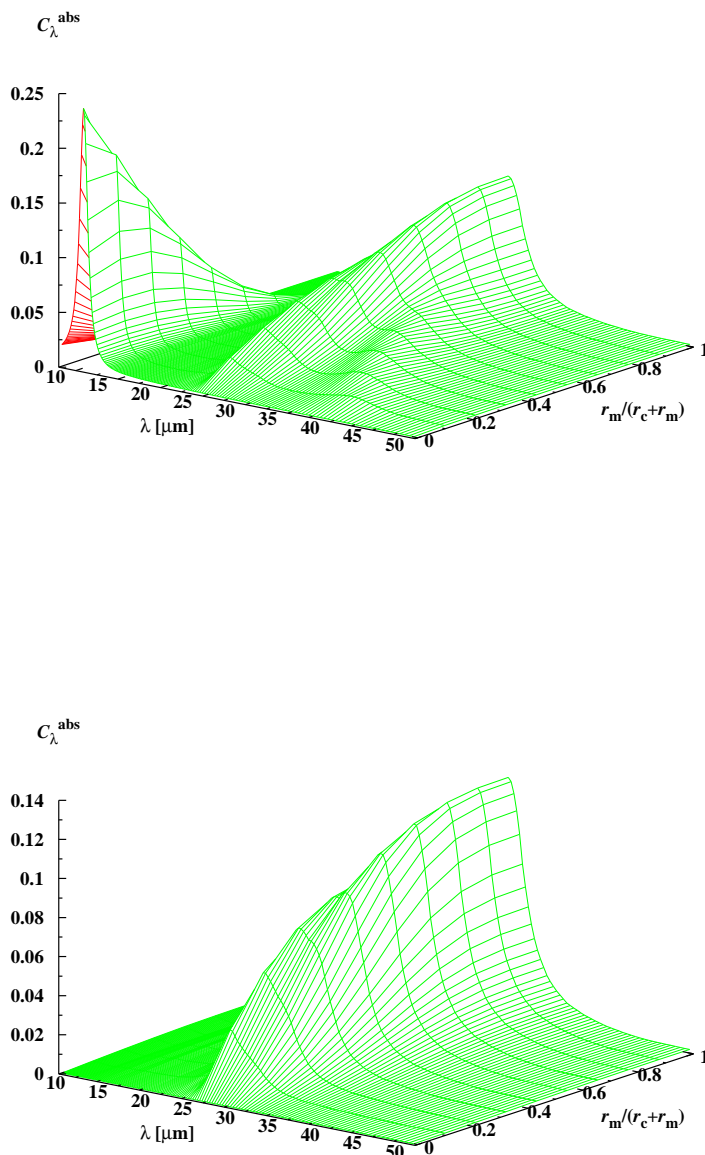
Figure 3.8: Wavelength variation of the absorption efficiency C_λ^{abs} of spherical grains with SiC (top) or carbon (bottom) core and MgS mantle with total radius of 0.1 μm. The MgS mantles range in thickness from zero to unity in steps of 0.05 for the ratio of mantle thickness r_m to total radius $r_c + r_m$, where r_m is the core radius. The extinction properties vary from that of pure SiC or carbon grains to that of pure MgS grains. An extra extinction feature centred on 33 μm for MgS grains with SiC core shows up at moderate mantle thickness. This is missing in case of carbon cores.

is 0.1 μm and the fraction $r_m/(r_c + r_m)$ is varied between 0 and 1. In the upper part of the picture one recognises how the SiC feature disappears and the MgS feature appears as the composition of the grain varies from pure SiC to pure MgS. The extra feature peaking at about 33 ... 38 μm, depending on the mantle thickness, is clearly seen in case of coatings of moderate, but not too small fraction of the total size. For thick coatings the extra feature disappears together with the 11 μm feature from the SiC core. The feature is not very distinct and will probably hardly be detectable in many cases.

The particular feature peaking at about 33 ... 38 μm is missing in the extinction of carbon grains coated with MgS, as can be seen from the lower part of Fig. 3.8, because of the completely different properties of the dielectric function. Therefore this extra feature can be considered as an indicator of a silicon carbide core of MgS grains, if the presence of MgS is indicated by its absorption band around 26 μm. Observationally it was found by Volk et al. (2002) that the so called '30 μm feature' of carbon stars shows in some cases some structure and seems to consist of two overlapping features at 26 μm and 33μm. Our results for the extinction of SiC-core-MgS-mantle grains indicate, that one just sees that the MgS in outflows from carbon stars grows as mantle on silicon carbide cores. If it is not seen this probably does not mean that in this case MgS precipitates on carbon, but merely that the feature is not sufficiently well defined to be unambiguously be detectable.

3.3.6 Concluding remarks

In this paper the mechanism of MgS formation in stellar outflows of AGB stars is studied. From some elementary considerations on the kinetics of MgS condensation we estimate a critical mass-loss rate of about 5×10^{-4} M$_\odot$ yr^{-1} for efficient MgS formation if this would condense as a separate dust species via nucleation and subsequent growth. This value of the mass-loss rate is much higher than any observed mass-loss rate of AGB stars. Within the observed range of mass-loss rates of AGB stars, however, the amount of MgS that can condense on seed particles in stellar winds is much too low to explain the observed strong emission band from MgS in the infrared spectra of many carbon stars.

Our model calculations of MgS formation in stellar outflows show that only MgS growth as mantle atop SiC cores, that condensed before the on-set of MgS formation, results in sufficiently high degrees of condensation of Mg into MgS of the order of $\sim$ 0.2 which are required that MgS may be clearly visible in the infrared spectrum. Condensation of MgS on tiny seed particles would result in a fraction of the Mg condensed in MgS dust of the order of only 0.01. This is much too small to be detectable.

Additionally, we performed calculations of the extinction properties of grains with SiC core and MgS coating of various thicknesses. The presence of a SiC core inside of MgS grains results within some range of core/mantle volume ratios in a secondary peak near 33 ... 35 μm in the broad emission band associated with MgS, that seems to be observed in some spectra of AGB stars. This feature is absent if MgS forms a mantle on carbon grains. We propose this feature as an indicator for the

presence of a silicon carbide core of MgS grains, if the presence of MgS is indicated by its absorption band around $26\,\mu$m.

3.4 Dust production by massive stars

In principle one has four different processes contributing to the dust return by massive stars that finally explode as SNe:

1. Dust formed in the massive cool stellar winds of Red Supergiants, i.e., massive stars on the Red Giant Branch. This is relevant only for stars from the range of initial masses $8 \lesssim M \lesssim 40\,\mathrm{M_\odot}$, since only stars from this mass range enter the Red Giant stage.

2. Dust formed in massive shells of $1 - 10\,\mathrm{M_\odot}$ ejected by repeated giant eruptions during an LBV-phase, such as observed in η Car (cf. Smith & Owocki 2006). This is relevant only for massive stars from the region of initial masses $M \gtrsim 40\,\mathrm{M_\odot}$ which evolve through a LBV phase. Most of the mass ejected by these very massive stars prior to their SN explosion seems to be ejected in a few such events (Smith 2006), which are accompanied by copious dust formation.

3. Dust formed in the outflows from Wolf-Rayet stars.

4. Dust formed in the ejected matter after the final supernova explosion.

The dust grains formed in outflows from Red Supergiants and giant eruptions of very massive stars carry isotopic anomalies resulting from hydrogen burning via the CNO-cycle, while the dust grains formed after a supernova explosion show the very different isotopic signatures from heavy-element synthesis. Both types would be clearly distinguishable, if investigated as presolar grains in the laboratory. Both types should be included as separate types of dust in a model calculation.

3.4.1 Dust formed in pre-supernovae

The dust formed in stellar winds or ejecta prior to the supernova explosion is later subjected to the shock wave from the SN explosion. This shock wave destroys the dust in the swept-up material if the expansion velocity exceeds $150\,\mathrm{km\,s^{-1}}$ (e.g. Jones et al. 1996). For a simple estimation of the importance of this process, we consider the case when the blast wave expands into a medium with constant density. At the end of the adiabatic expansion phase, the radius and the velocity of the shocked region are about (e.g. Shull & Draine 1987)

$$R_{\mathrm{sh}} = 16.2\, E_{51}^{2/7} n_0^{-3/7}\ \mathrm{pc} \tag{3.13}$$

$$V_{\mathrm{sh}} = 331\, E_{51}^{1/14} n_0^{1/7}\ \mathrm{km\,s^{-1}} \,. \tag{3.14}$$

The transition between the Sedov-Taylor expansion and the subsequent pressure-dominated snow-plow phase occurs at

$$t_{ST-PDE} = 1.91 \times 10^4 \, E_{51}^{3/14} n_0^{-4/7} \text{ yr} \,. \tag{3.15}$$

Here E_{51} is the explosion energy in units of 10^{51} erg and n_0 the density of the ambient medium in units of $1 \, \text{cm}^{-3}$. Since the shock velocity drops rapidly in the snowplow phase, the dust destruction occurs mainly up to the end of the adiabatic expansion phase given by Eq. (3.15).

Red Supergiants: First we consider the case of Red Supergiants and let $E_{51} = n_0 = 1$. Typical expansion velocities of stellar winds of supergiants are $v_{\text{exp}} = 20 \, \text{km s}^{-1}$. The wind material requires a time of about $R_{\text{sh}}/v_{\text{exp}} = 790\,000$ yrs to expand to the distance R_{sh}. The shock strength then is sufficient to destroy all dust material ejected during a period of $7.9 \times 10^5 - t_{ST-PDE} \approx 7.7 \times 10^5$ yrs before the SN explosion. This is close to the evolution time on the Red Giant branch (e.g. Schaller et al. 1992). The main period for dust formation of such stars, however, is much shorter. Mass-loss rates of supergiants during the phase where they are enshrouded by massive dust shells are of the order of $10^{-4} - 10^{-3} \, \text{M}_\odot \, \text{yr}^{-1}$ (e.g. van Loon et al. 1999), and this phase can last at most about 10^5 yrs; otherwise, the stellar envelope over the He core would be lost completely by the stellar wind prior to explosion, which is not observed for this mass-range.

Hence, all dust formed by Red Supergiants is expected to be destroyed by the shock wave of the subsequent supernova explosion. Even if some dust survives in some cases, Red Supergiants cannot be important sources for interstellar dust.

Luminous Blue Variables: The expansion velocity of the matter from giant eruptions is somewhat higher than for winds of Red Supergiants (cf. Lamers et al. 2001) and may be as high as $100 \, \text{km s}^{-1}$. Correspondingly, the supernova shock destroys all the dust that was ejected by a giant eruption if the supernova explosion follows within about 2×10^5 yrs after the end of the LBV phase. The LBV phase, however, seems to occur during the first transition from the blue to the red in the Hertzsprung-Russel diagram (Lamers et al. 2001) and is followed by a WR-phase that lasts about $3 \times 10^5 - 10^6$ yrs (Meynet & Maeder 2005). If the star finally explodes, the velocity of the shock from the SN explosion is already too slow to destroy the dust at the instant when it catches up with the ejected LBV shell. Dust formed in giant eruptions could therefore be an important source of interstellar dust. Unfortunately, however, there is presently not enough information on the dust production by these objects to include them in the model calculation and dust production by LBVs, so they cannot be considered in our present model calculation.

Clearly, the real situation is more complex since a supernova explodes into the matter ejected by the stellar winds of the preceding evolutionary stages (cf. Dwarkadas 2006 for a brief discussion), or into the hot bubbles of other supernovae, and the dust ejected by one massive star may be subjected to the SN blast waves of other massive stars from the same stellar cluster. A more detailed investigation of the whole problem is required to determine the survival probability of dust formed by a star prior

to its SN explosion.

Wolf-Rayet stars: these are the massive stars in final evolutionary phase preceding to the SN explosion. They are characterised by strong the mass loss rates of $10^{-5} - 10^{-4}$ $M_\odot$ yr^{-1} resulting from fast dense stellar winds with velocity up to 5000 km s^{-1} (Leitherer et al. 1992). Dust forming Wolf-Rayet stars are rare, with only about 10% of all stars in this evolutionary phase (Marchenko & Moffat 2006), and their lifetime till SN explosion is only 4×10^5 yr (van der Hucht 2003); i.e., most of the dust formed will be destroyed by the subsequent SN explosion. Therefore we neglect their contribution to dust production by massive stars.

3.5 Dust return by supernovae

Unfortunately, it is presently not definitely known which supernovae do form dust and in what quantities. Undoubtedly there is some dust formed by supernovae since presolar dust grains are known that bear the signatures of element synthesis in supernovae. The abundance of X-grains in the population of presolar SiC grains, however, is small compared to mainstream SiC grains (cf. Hoppe et al. 2000; Nittler & Alexander 2003), which are thought to come from AGB stars. Dust formation by supernovae, therefore, seems to be an inefficient process. For supernovae of type Ia, observations even seem to indicate that they do not form dust at all (Borkowski et al. 2006). From the theoretical side also, little is known about dust condensation in SNe; only a few model calculations for dust condensation in supernova ejecta are available (Kozasa et al. 1989; Todini & Ferrara 2001; Nozawa et al. 2003; Schneider et al. 2004), and they are of a very qualitative nature.

Presently there are no reliable models for dust formation in supernovae available on which one can base a modelling of the contribution of supernovae to the interstellar and presolar dust population. Therefore, in the present model calculation we apply the same simplified approach as in Dwek (1998) to account for the contribution of supernovae to the dust production in the Milky Way. The dust return rate is assumed to be given by the total mass return rate of the key element required to form a particular kind of dust[1] times some efficiency factor η. This efficiency factor is simply guessed or is estimated from observational quantities. It is assumed that supernovae of type II produce all types of dust considered here. From theoretical considerations, SN Ia may produce some iron dust, therefore we include iron dust from SN Ia in our model.

We therefore use the following production rates for the dust species

$$R_{\mathrm{sil},l,\mathrm{d}}(t,r) = \eta_{\mathrm{sil,SN\,II}}\, R_{\mathrm{Si,SN\,II}}(t,r)\, \frac{A_{\mathrm{sil}}}{A_{\mathrm{Si}}} \qquad (3.16)$$

---

[1] As key element we usually choose the one of all the elements forming the considered dust species, for which the quantity ϵ/i takes the lowest value. Here ϵ is the abundance of an element by number relative to H, and i is the number of atoms of the element in the chemical formula of the compound. The key element determines the maximum amount of dust material that can be formed for the considered species

Table 3.3: Characteristic quantities and numerical coefficients used for calculating grain formation by the SNe

	silicates	carbon	iron	SiC
$\eta_{\text{SN II}}$	0.001	0.15	0.001	0.0003
$\eta_{\text{SN Ia}}$	0.0	0.0	0.005	0.0
key element	Si	C	Fe	Si
Atomic weight A	172.	12.01	55.85	40.10

$$R_{\text{car},l,\text{d}}(t,r) = \eta_{\text{car,SN II}} R_{\text{C,SN II}}(t,r) \frac{A_{\text{car}}}{A_{\text{C}}} \tag{3.17}$$

$$R_{\text{sic},l,\text{d}}(t,r) = \eta_{\text{sic,SN II}} R_{\text{Si,SN II}}(t,r) \frac{A_{\text{sic}}}{A_{\text{Si}}} \tag{3.18}$$

$$R_{\text{iro},l,\text{d}}(t,r) = \eta_{\text{iro,SN II}} R_{\text{Fe,SN II}}(t,r) \frac{A_{\text{iro}}}{A_{\text{Fe}}}. \tag{3.19}$$

The index l here refers to supernovae of type II, and $R_{\text{Si,SN II}}$ is the rate of mass return to the interstellar medium of element Si by all supernovae of type II, defined by

$$R_{\text{Si,SN II}}(t,r) = \int_{M_{\text{WD}}}^{M_{\text{u}}} dM\, \Phi(M) \frac{B(t_{\text{b}},r)}{M_{\text{av}}} \cdot$$
$$M_{\text{Si,ret}}(M, Z_{\text{ISM}}(t_{\text{b}}, r))\,. \tag{3.20}$$

The quantity $M_{\text{Si,ret}}(M, Z)$ is the Si mass returned by a supernova with initial mass M and metallicity Z. The integration is from the lower limit M_{WD} to the upper limit M_{u}, here taken to be $40\,\text{M}_{\odot}$ since the tables for mass return by supernovae of Woosley & Weaver (1995) and Nomoto et al. (2006) only extend up to this upper mass. The mass return rates for the other elements are defined correspondingly. The quantities A_{sil}, A_{car}, A_{sic}, A_{iro} are the atomic weights of the dust species and A_{Si}, A_{C}, A_{Fe} the atomic weights of the key elements.

For supernovae of type Ia, the dust production rate is

$$R_{\text{iro},l,\text{d}}(t,r) = \eta_{\text{iro,SN Ia}} R_{\text{Fe,SN Ia}}(t,r) \frac{A_{\text{iro}}}{A_{\text{Fe}}}\,, \tag{3.21}$$

where the index l now refers to supernovae of type Ia. The mass return rate for iron is

$$R_{\text{Fe,SN Ia}}(t,r) = M_{\text{Fe,ret}} R_{\text{SN Ia}}(t,r)\,, \tag{3.22}$$

where $R_{\text{SN Ia}}(t,r)$ is the supernova rate of type Ia, which is taken from the galactic evolution model (see Fig. 2.3), and $M_{\text{Fe,ret}}$ is the iron mass returned by supernovae of type Ia and is taken from the tables of Iwamoto (1999).

The quantities $\eta_{\text{sil,SN II}}$, ..., $\eta_{\text{iro,SN Ia}}$ are the efficiencies for conversion of the key elements of the different dust species into dust particles, and they refer to the amount of dust injected into the interstellar medium in relation to the total mass of the key element returned to the interstellar medium. The dust first formed in the expanding SN ejecta is later overrun by the reverse shock and part of it is destroyed again (Dwek 2005; Bianchi & Schneider 2007; Nozawa et al. 2007).The efficiencies η as they are defined here consider the dust destruction by the reverse shock and may therefore be significantly smaller than the efficiency of the initial dust condensation.

So far, only a few attempts have been made to estimate the condensation efficiency in SNe by analysing spectroscopic data, resulting in very different dust yields, from only 5×10^{-4} to 4×10^{-3} for type II SN 1987A (Ercolano et al. 2007) to 0.12 for SN 2003gd (Sugerman et al. 2006). The values of η for different types of SNe are still unknown and have to be guessed somehow. The numerical values chosen in this paper are much lower than the values assumed in Dwek (1998) and are given in Table 3.3. The values for the efficiencies $\eta_{\text{sil,SN II}}$, $\eta_{\text{sic,SN II}}$, and $\eta_{\text{car,SN II}}$ of silicate, SiC, and carbon dust formation in SN II, respectively, are estimated from the abundances of presolar silicate grains from supernovae, of X-type SiC grains, and graphite grains from supernovae. This is discussed in Sect. 5.1.3. The efficiencies $\eta_{\text{iro,SN II}}$ and $\eta_{\text{iro,SN Ia}}$ for iron dust production in SNe of type II and type Ia, respectively, are arbitrarily set to a low non-zero value, but they may well be equal to zero. Tests run without SN Ia dust showed no influence on the amount of iron dust from molecular clouds, since stardust is only important as seed grains for the ISM dust production at an early time.

3.6 Rates of dust injection by stars for the Solar neighborhood

Figure 3.9 shows the variation with time of the dust injection rates from stellar sources into the interstellar medium at the solar circle, as calculated for our model of the evolution of the Milky Way. The dust injection rate in this model is dominated by carbon dust from AGB stars and SNe and by silicate dust from AGB stars, except for the very first period before the first appearance of AGB stars, where dust return from SNe dominates. The SN injection rates are very uncertain, however, since they depend on the efficiencies η, which are only badly known and in this paper are determined from abundance ratios of presolar dust grains from AGB stars and supernovae.

Figure 3.9: Evolution of the dust injection rates at the solar circle from different stellar sources

4

Dust evolution in the ISM

The analysis of astronomical observations indicate strong variations in depletions of dust forming elements, i.e., ratios of element abundances in the gas to the standard abundances, depending on the conditions in the ISM: (1) there is a general trend for observing a much lower gas abundance in cold clouds in comparison with the warm diffuse medium (e.g., Savage & Sembach 1996); (2) the depletions in high-velocity clouds show an anticorrelation with cloud velocity. Another independent evidence of dust evolution in the interstellar medium comes from presolar dust grains in meteorites that indicate a high degree of dust processing in the ISM. There is also evidence of the opposite process, dust growth in molecular, from variation of extinction efficiency due to bigger of grain sizes (Flagey et al. 2006). In the following we describe our approach to modeling the destruction of dust grains and growth in the interstellar medium.

4.1 Dust destruction in the interstellar medium

4.1.1 Dust destruction processes

The processing of dust in the ISM can be divided into two groups:

1. the destruction processes (thermal sputtering, evaporation in high-velocity grain-grain collisions, chemical sputtering) and the growth by accretion that change the total dust mass;

2. the processes modifying the grain size distribution or the phase of the grains, that do not change the mass of dust (shattering in grain-grain collisions, coagulation, amorphisation of crystalline stardust, etc.).

Detailed discussions of dust processing in the ISM can be found in Tielens (2005), for example. Since we do not study the grain size distribution, we are interested in the first group of processes only, i.e., in the destruction processes and the growth processes in the ISM.

4.1.2 Dust destruction in supernovae

The dust destruction mainly occurs in high-velocity SN shocks with velocities about $v_s \geq 100\,\mathrm{km\,s^{-1}}$ (cf. Jones et al. 1996, Seab 1987). The dominant destructive process is inertial sputtering of atoms from grain surface by interaction with impinging energetic ions, mainly He^+. This process works almost exclusively in the warm neutral/ionized phase of the interstellar medium with density of $n_0 \sim 0.25\,\mathrm{cm^{-3}}$ (Seab (1987). This links the dust destruction problem in the ISM closely to the multiphase structure of the ISM. Since we approximate the ISM in our present model by a simple one-phase model, we describe this process in terms of grain lifetimes against destruction by SN remnants $\tau_{j,\mathrm{SNR}}$ (McKee 1989, Dwek 1998). In this approximation the change in surface density of the dust species of kind j per unit time by dust destruction is

$$L_{j,\mathrm{d}} = -\frac{\Sigma_{j,\mathrm{d}}}{\tau_{j,\mathrm{SNR}}} \, . \tag{4.1}$$

We only consider equations for the total element abundances (gas+dust) in the ISM and no separate equations for the gas-phase abundance, therefore the mass return to the gas phase needs no special treatment.

Destruction timescale

Following McKee (1989), we describe the timescale against destruction, i.e., the time needed to return elements locked in dust back to the gas phase, in terms of $m_{j,\mathrm{cleared}}$, the mass of gas, in which the dust species of kind j is completely destroyed by the blast wave of a single supernova remnant. McKee (1989) estimated the average galactic timescale of destruction of dust of kind j:

$$\tau_{j,\mathrm{SNR}} = \frac{M_{\mathrm{ISM}}}{m_{j,\mathrm{cleared}} f_{\mathrm{SN}} R_{\mathrm{SN}}} \, , \tag{4.2}$$

where M_{ISM} is the total ISM mass, R_{SN} is the galactic supernova rate, and f_{SN} is the fraction of single SNe that explode within the galactic plane and destroy dust. McKee (1989) accounted in f_{SN} for the number of massive stars born in stellar clusters that explode in the hot interior of superbubbles, where dust is already swept up by previous supernovae, and stars, which end their life above the galactic gaseous disk. He obtained a fraction of 0.34 for SN II and 0.38 for SN Ia. With the assumption that f_{SN} does not vary in the Galactic disk we define the local timescale of dust destruction as:

$$\tau_{j,\mathrm{SNR}}(r,t) = \frac{\Sigma_{\mathrm{ISM}}(r,t)}{m_{j,\mathrm{cleared}} f_{\mathrm{SNII}} R_{\mathrm{SNII}}(r,t)} \, , \tag{4.3}$$

where dust destruction by SN Ia shocks is neglected, since $R_{\mathrm{SNIa}} \ll R_{\mathrm{SNII}}$ for the whole Galaxy evolution (Fig. 2.3).
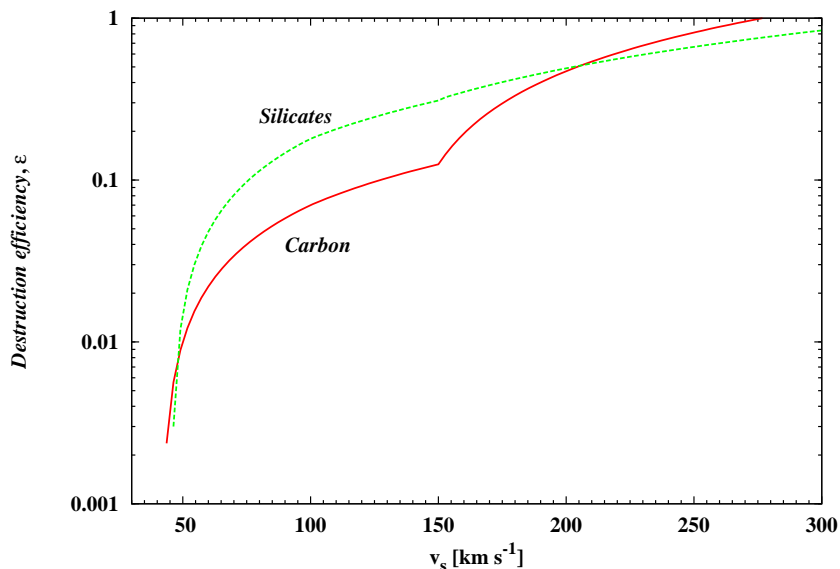
Figure 4.1: Degrees of destruction of carbon and silicate dust as a function of velocity of the shock expanding into a medium with density $n_0 = 0.25$ cm^{-3}. The data are from Jones et al. (1996)

The mass $m_{j,\text{cleared}}$ is primarily determined by the properties of the dust material and the structure of the shock:

$$m_{j,\text{cleared}}(n_0) = \int_{v_0}^{v_f} \epsilon_j(v_s, n_0) \left| \frac{dM_s(v_s, n_0)}{dv_s} \right| dv_s, \qquad (4.4)$$

where v_0 and v_f are the initial and final velocities of the SNR expanding into an ambient medium of density n_0, respectively, $\left| \frac{dM_s(v_s)}{dv_s} \right| dv_s$ is the mass of gas swept up by a shock with velocity in the range of $[v_s, v_s + dv_s]$, ϵ_j is the degree of dust destruction in a SN shock with expansion velocity v_s.

The values of ϵ_j for carbon and silicate dust are taken from the study of dust destruction in SN shocks for SNR expanding into a medium with $n_0 = 0.25$ cm^{-3} by Jones et al. (1994,1996). Unfortunately they did not present the corresponding degrees of destruction for iron and silicon carbide dust, but their results for the sputtered dust mass fraction for different shock velocities for iron and for silicon carbide dust are somewhat higher but similar to carbon dust. We therefore choose for both the same degrees of destruction as for carbon dust.

Figure 4.1 illustrates the dependence of degrees of dust destruction on the velocity of the shock. Although, higher velocity shocks ($v_s \sim 300\,\text{km s}^{-1}$) are more destructive, the net dust destruction is higher for shock with $v_s \sim 100\,\text{km s}^{-1}$ because they sweep more ISM gas. Therefore, for estimating $m_{j,\text{cleared}}$ we are interested only in the stages of the SN evolution until the velocity is decreased to
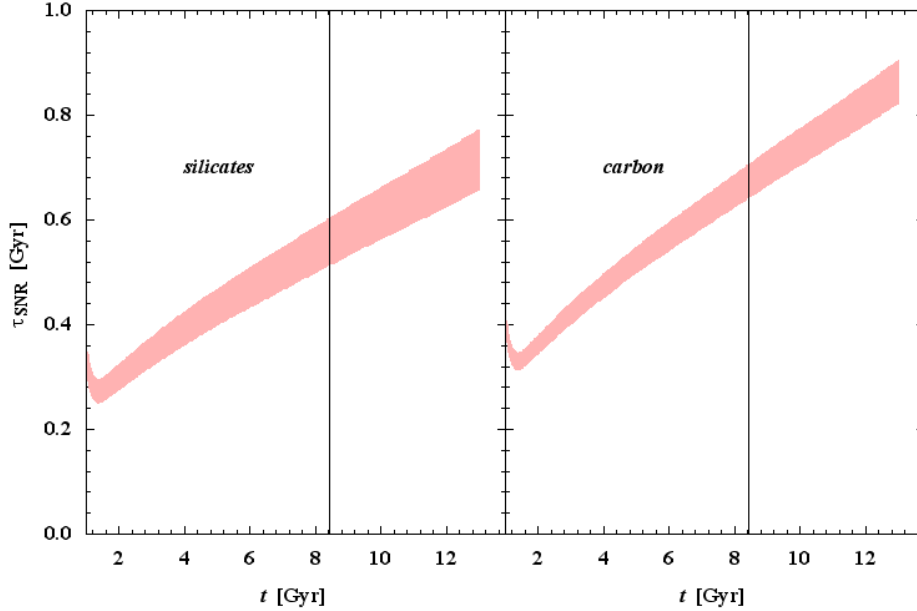
Figure 4.2: Time evolution of the destruction timescales for silicate and carbon dust calculated for the Solar neighborhood model. Shaded areas correspond to values calculated for the observed range of densities n_0 of the warm medium, 0.2-0.5 cm^{-3}(Ferriere 1998).

~ 100 km s^{-1}, which can be taken from analytical solution of SNR evolution. Most of dust destruction occurs in the adiabatic stage described by the Sedov-Teylor expansion (Ostriker & McKee 1989). Eventually, when radiative losses become important, the SNR enters the pressure driven radiative stage described by the analytical solution in Cioffi et al. (1988). We used the formula combining these two stages from Dwek et al. (2007):

$$M_s = 400 E_{51}^{0.86} n_0^{-0.28} \left(\frac{v_s}{v_{\text{PDS}}} \right)^{-\alpha},$$

$$\alpha = \begin{cases} 2, & v > v_{\text{PDS}} \\ 1.28, & v \le v_{\text{PDS}} \end{cases}$$

$$\frac{dM_s}{dv_s} = -\frac{\alpha M_s}{v_s}, \tag{4.5}$$

where E_{51} is the energy of explosion in unit of 10^{51} erg, n_0 the density of the ISM in cm^{-3}, v_{PDS} is the velocity of transition of SNR from adiabatic expansion to the pressure-driven snowplough stage,

80
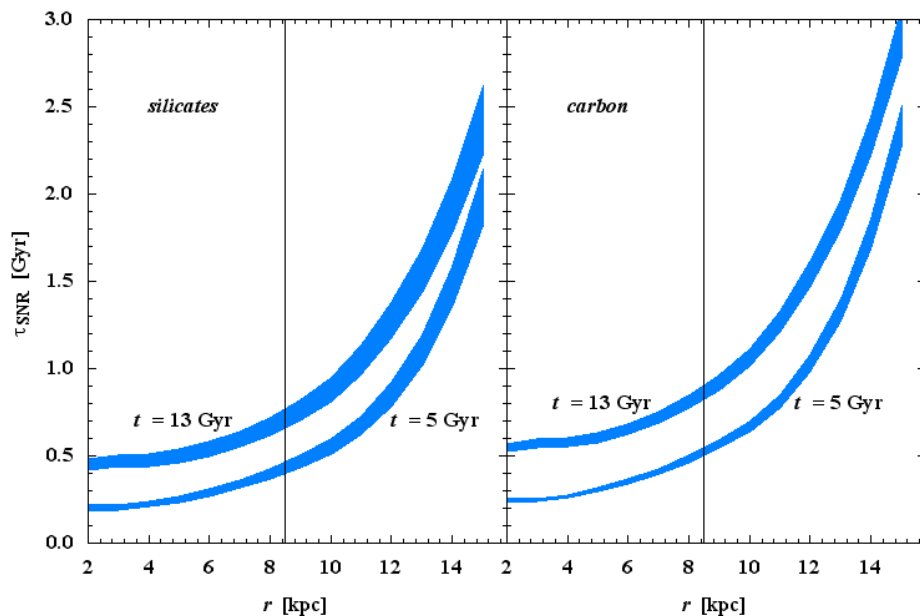
Figure 4.3: Radial variations of the destruction timescales for silicate and carbon dust in the present Milky Way disk as predicted by the model. Shaded areas correspond to the values calculated for the observed range of densities n_0 of the warm medium, 0.2-0.5 cm^{-3} (Ferriere 1998).

given by (Cioffi et al. 1988):

$$v_{\rm PDS} = 413 n_0^{1/7} E_{51}^{1/14} \left(\frac{Z}{Z_\odot} \right)^{-3/14} \tag{4.6}$$

Inserting eqs. (4.5), (4.6) in eq. (4.4) after numerical integration one obtains the ISM mass cleared of carbon and silicate dust as a function of ambient density. However, the data for $\epsilon(j, v_s)$ are available only for a "standard shock" conditions, $n_0 = 0.25$ cm^{-3}. The estimates of ϵ for the medium with lower density give very low values, because the inertial sputtering becomes inefficient in the tenuous medium. Seab (1987) estimated an average galactic life time of dust against destruction by sputtering in the hot phase of $\sim 10^{12}$ yr. Dust destruction efficiency as a function of ISM density for the low-metallicity environment can be found in Nomoto et al. (2006), that also prove negligible dust destruction in SN shocks expanding in hot medium. Although the values ϵ_j are enhanced in the dense cold medium, dust destruction in the clouds is inefficient as a result of much smaller shock velocity v_c, since at pressure equilibrium between hot phase and clouds $n_c v_c^2 = n_h v_h^2$.

In principle, $m_{j,\text{cleared}}$ in eq. (4.3) is the sum of mass cleared of dust by SNR in hot, warm and cold

Table 4.1: Characteristic quantities and numerical coefficients used for calculating grain destruction and grain growth (SiC does not form in the ISM)

	silicates	carbon	iron	SiC
$\tau_{j,\mathrm{SNR}}(r_\odot, t_\mathrm{G})$ [Gyr]	0.7	0.87	0.87	0.87
key element	Si, Fe or Mg	C	Fe	-
Z_{crit}	0.0012	0.004	0.014	-
Atomic weight A	121.41	12.01	55.85	-
bulk density ρ_c [g cm^{-3}]	3.13	2.25	7.86	-

phases, but due to the arguments discussed above the only substantial contribution is from the warm medium (see also McKee 1989). For the density $n_0 = 0.25$ cm^{-3}adopted here as an average density of the warm medium, from eq. (4.4) we obtain $m_{\mathrm{sil,cleared}} = 1590$ for silicates and $m_{\mathrm{car,cleared}} = 1315$ for carbon dust, which are used in eq. (4.3) for τ_{SNR} in our model calculations of dust evolution.

The evolution of the destruction timescales for the carbon and silicate dust in the Solar neighborhood is shown in Fig. 4.2. In order to illustrate that the choice of n_0 does not significantly influence the results, we show the destruction timescales τ_{SNR} for silicate and carbon dust calculated for n_0 from the observed range of 0.2-0.5 cm^{-3}(Ferrière 1998). ϵ_j is assumed to be a constant for this range of densities. For present characteristic timescales of the dust destruction in the Solar neighborhood we obtain the following values, $\tau_{\mathrm{sil,SNR}}(t_\mathrm{G}, r_\odot) = 0.7$ Gyr and $\tau_{\mathrm{car,SNR}}(t_\mathrm{G}, r_\odot) = 0.87$ Gyr, shown in the Table 4.1.

Figure 4.3 demonstrates the radial variations of $\tau_{j,SNR}$ in the present time and at $t = 5$ Gyr calculated for the Galactic disk model described in Sect. 2.3. It shows the lower and upper values of destruction timescales τ_{SNR} for silicate and carbon dust obtained for the observed range of density of warm medium 0.2-0.5 cm^{-3}.

Galactic timescales of destruction

Using eq. (4.2), Jones et al. (1996) estimated the present average destruction timescales for dust in the Milky Way of 0.4 Gyr for silicate and 0.6 Gyr for carbon dust. These short grain lifetimes in comparison with the 2.5 Gyr timescale of dust injection by stars pose a question on the source of dust replenishment in the ISM required to explain the high depletion in the ISM (Seab 1987, McKee 1989, Jones et al. 1996). The problem can only be solved by dust re-accretion in molecular clouds, that will be discussed in the Sec. 4.3. In their estimates Jones et al. (1996) assume the three-phase ISM model regulated by the SNR (McKee & Ostriker 1977), with a volume filling factor of the hot intercloud medium of $0.7 - 0.8$. This model does not account for the magnetic pressure of the ISM and possible

evacuation of the hot gas through chimneys in superbubbles, which substantially reduce the volume filling factor of hot intercloud medium in the disk, to a value of 20% found in Ferrière (1998) or 40% found in MHD simulations by Avilez & Breitschwerdt (2005). Thus, new estimates of average dust destruction timescales involving better treatment of the multiphase structure of the ISM need to be considered in future.

4.2 Evolution of stardust

Stardust is only destroyed in the ISM and does not gain mass by accretion of gas phase material. All material from such grains ejected into the gas phase rapidly mixes with the existing ISM gas-phase material, and the specific isotopic anomalies carried by the stardust material are lost by mixing together eroded material of grains from many different kinds of stellar sources. If such material is later accreted by dust grains in the ISM, it shows no isotopic anomalies. Even it grows as mantle on stardust cores, the differences in isotopic composition between core and mantle survive since dust grains in the ISM are not expected to ever become hot enough (> 1000 K) for long enough periods for solid state diffusion to smooth out isotopic abundance differences between a stardust core and an ISM-grown mantle; hence, any accreted mantle material can be clearly distinguished (if it could be analysed in the laboratory) from cores originating from stellar sources by showing isotopic abundance ratios close to Solar System isotopic abundance ratios, even if the general chemical composition and mineralogical structure of an ISM-grown mantle material should resemble that of a core with a stellar origin. Therefore we treat the dust species from stellar sources in our model as separate dust components and omit the growth term for these species in Eq. (3.1), where only destruction by star formation and SNe are retained. Then change of the surface density $\Sigma_{j,\mathrm{d}}$ of stardust grains of kind j ejected at instant of stellar death t_{d} with time is

$$\frac{\mathrm{d}\Sigma_{j,\mathrm{d}}}{\mathrm{d}t} = -\frac{\Sigma_{j,\mathrm{d}}}{\Sigma_{\mathrm{ISM}}} B - \frac{\Sigma_{j,\mathrm{d}}}{\tau_{j,\mathrm{SNR}}} , \qquad (4.7)$$

here $L_{j,\mathrm{d}}$ is replaced by the dust destruction rate by SNe from Eq. (4.1). The first term can be re-written using the timescale of gas conversion into stars τ_{cyc} from Eq. (2.24) as $\Sigma_{j,\mathrm{d}}/\tau_{\mathrm{cyc}}$. The timescale of dust destruction by SNe $\tau_{j,\mathrm{SNR}}$ is taken from Eq. (4.3). It is always shorter than the destruction due to consumption of dust by the star formation τ_{cyc} along Galactic history as can be seen by comparison of Fig. 4.2 and Fig. 2.24. Introducing the total destruction timescale including both processes

$$\frac{1}{\tau_{j,\mathrm{destr}}} = \frac{1}{\tau_{j,\mathrm{SN}}} + \frac{1}{\tau_{\mathrm{cyc}}} \qquad (4.8)$$

we obtain a simple equation describing the change of the surface density of stardust

$$\frac{\mathrm{d}\Sigma_{j,\mathrm{d}}}{\mathrm{d}t} = -\frac{\Sigma_{j,\mathrm{d}}}{\tau_{j,\mathrm{destr}}} . \qquad (4.9)$$

By integration one obtains the density of dust injected at instant t_d that survives destructive processes at the ISM until instant t

$$\Sigma_{j,d}(r, t, t_d) = \Sigma_{j,d}(r, t_d) \exp(-(t - t_d)/\tau_{j,\text{dest}}) \,. \tag{4.10}$$

Dust production by AGB stars strongly depends on the initial stellar metallicity as described in detail in Sect. 3.2, therefore one expects strong variations in the composition of dust returned by AGB stars in the Galactic disk due to radial metallicity gradient. The second factor determining the dust abundances in the disk is the destruction timescale $\tau_{j,\text{dest}}(r, t)$. It becomes much longer in in the outer regions as seen in Fig. 4.3. Dust grains in the outer regions can survive for much longer time than in the inner disk, and therefore represent a wider range of stellar generations. The interplay between dust destruction, star formation and metallicity dependent dust production determines the present day stardust population in the ISM of the Milky Way. In the following we analyse quantitatively the contribution from different generation of stars to the present day AGB stardust population in the Galactic disk.

4.2.1   Mass-distribution of AGB-stars and their metallicities

The average number of stars per unit of disk surface in mass range $[M, M + dM]$ that die within time interval $[t_d, t_d + \Delta t]$ is

$$\frac{B(t_b, r)\Delta t}{M_{\text{av}}} \, \Phi(M) \, \Delta M \,,$$

where the instant of birth of a star t_b and initial metallicity $Z_{\text{ISM}}(t_b)$ are given by the non-linear equation

$$t_b = t_d - \tau(M, Z_{\text{ISM}}(t_b)) \,, \tag{4.11}$$

which is solved for each $M < M_{\text{WD}}$, $t_d < t$. $\tau(M, Z)$ is the stellar lifetime and $\Phi(M)$ is the IMF described in Sect. 2.3.

The frequency of AGB stars with initial mass M that are observable at instant t_d is obtained by integrating with respect to time over the duration Δt_{AGB} of the dust-forming phase on the AGB

$$f_{\text{AGB}}(M, t_d) = \frac{B(r, t_b)\Delta t_{\text{AGB}}}{M_{\text{av}}} \Phi(M) \,, \tag{4.12}$$

where we assume that B does not vary significantly over the period Δt_{AGB}. Here Δt_{AGB} is, in fact, the duration of the thermally pulsing AGB phase, that lasts typically typically $500\,000$ yr. The values for Δt_{AGB} are taken from stellar evolution formulae (Hurley et al. 2000). For calculating f_{AGB} numerical values for $B(t)$ are provided by the Milky Way model.

By integrating Eq. (4.12) over mass range of low and intermediate mass stars one gets the number density of stars at TP-AGB shown in Fig. 3.1.

4.2.2   Probability of survival of stardust in the ISM

The contribution of the stars of mass M dying at instant t_d to the total production rate of dust of the considered kind j is

$$f_{AGB}(M, t_d)\, R_{j,d}(M, Z)\, \Delta M \,.$$

The quantity $R_{j,d}(M, Z)$ is injection rate of dust of kind j by dying AGB stars of initial mass M and metallicity Z, as discussed in Sect. 3.2.2.

From Eq. (4.10) the fraction $\exp(-(t - t_d)/\tau_{j,\text{dest}})$ of the dust ejected by stars dying at instant t_d survives the destructive processes in the ISM until instant t. The surface mass density of dust of kind j present in the interstellar medium at instance t, returned by stars from the mass interval $[M,\ M + \Delta M]$ during the period $[t_d,\ t_d + \Delta t]$ then is

$$\Sigma_{j,d}(t, t_d, M)\, \Delta M\, \Delta t = e^{-(t-t_d)/\tau_{j,\text{dest}}}\, f_{AGB}(M, t_d)\, R_{j,d}(M, Z)\, \Delta M\, \Delta t \,. \tag{4.13}$$

From this one finds the probability density $P_{j,d}(M, t, t_d)$ that a star of initial mass M dying at instant t_d contributes to the AGB stardust population of type j at instant t

$$P_{j,d}(M, t, t_d) = \frac{\Sigma_{j,d}(t, t_d, M)}{\displaystyle\sum_{j=1}^{j_{max}} \int_{M_l}^{M_{WD}} dM \int_0^t dt'\, \Sigma_{j,d}(t, t', M)} \,. \tag{4.14}$$

The integration over initial stellar masses M is from the lower mass limit M_l, for a star with the lifetime $\tau(M, Z) < t$, to the upper mass-limit M_{WD} of stars becoming AGB-stars, the mass spectrum of AGB stars is taken from Eq. (4.12). The evolution of the stellar birth rate B and of the metallicity Z_{ISM} are taken from the model of the chemical evolution of the Galactic disk for a certain galactocentric radius r. The summation in the denominator is over all considered dust species and results in the total mass of AGB dust survived until instant t, in our case $j_{max} = 4$. The probability density of grain survival $P_{j,d}(M, t, t_d)$ for the first time was introduced in our recent study of dust input from AGB stars to the presolar dust grains at instant of Solar System formation (Gail et al. 2008). In Sect. 5.2.1 we will use the probability density for the analysis of contribution of a star to the total stardust population from AGB stars in the Galactic disk in dependence on initial mass and metallicity.

4.3   Dust growth in the interstellar medium

Dust grains cycle between the cloud and intercloud phase of the ISM on a timescale of $\simeq 3 \times 10^7$ yr due to the destruction of clouds by the star formation feedback (e.g. Draine 1990; Tielens 1998). In the warm intercloud medium grains undergo destruction due to SNe, UV radition, cosmic rays All theoretical calculations of grain lifetimes against destruction by SN shocks agree that they are

much shorter than the ~2 Gyr timescale of dust injection by stars (e.g. Jones et al. 1996; Tielens et al. 2005). This requires an efficient mechanism of replenishment of the dust content of the ISM. Another proof of dust growth in the ISM is that gas abundances in the ISM of major dust-forming elements show strong depletion in comparison to solar abundances (e.g. Savage & Sembach 1996; Jenkins 2004), which correlates with the ISM density. Also, the high dust content observed in some high-redshift objects seems to require dust growth in the interstellar medium (Dwek, Gallino & Jones 2007). The most likely sites of grain growth in the ISM are the dense molecular clouds of the cold phase of the ISM (Draine 1990).

It is known that the density of the ISM is not high enough to allow for the formation of new dust grains, only low temperature accretion of refractory material on pre-existing stellar grains is possible. The mantles accreted in the ISM are likely to be more volatile than stellar dust condensed at high temperature and can be lost more readily during dust cycling between ISM phases. Besides, in dense molecular clouds the accretion will be faster, and grains will probably be formed far from equilibrium, so that one would expect the grain mantles to be amorphous and heterogeneous (Jones 2005). Thus, dust accreted in molecular clouds (the MC-grown dust) has different properties from stardust and is treated in our model as a separate component denoted by an index ISM.

Dust growth in molecular clouds by accretion on existing grains needs to be considered in our model for silicate and carbon dust to explain the high observed depletions of the elements in the ISM (cf. Jenkins 2004 for a recent discussion). The grains that serve as growth centres for accretion of gas-phase material need not necessarily be the stardust particles, though these are needed to serve as initial growth centres for a start-up of the whole process. Also, fragments formed from shattering of MC-grown grains by SN shock waves in the warm component of the ISM may serve as growth centres for accretion of refractory elements in the gas phase if mixed into molecular cloud cores.

An unclear case for growth in the ISM is iron dust, which might be a component of the ISM dust mixture, if not all Fe is used up by the formation of magnesium-iron-silicates. However, metallic iron is probably unstable against oxidation in the ISM (Jones 1990), while, on the other hand, iron oxides do not seem to form a significant species in the ISM dust mixture (Chiar & Tielens 2006). We consider iron in our model calculation as a possible MC-grown dust component since there are observational indications that not all condensed iron always resides in silicates (cf. Cartledge et al. 2006, their Fig. 10).

How the growth process works in detail is not definitely known. For interstellar carbon dust, it may proceed in the way described in Jenniskens et al. (1993) as a multistep process, initiated by deposition of ice mantles, and proceeding via canonisation and polymerisation driven by UV irradiation. Later, Dartois et al. (2005) showed that a hydrogenated amorphous carbon polymer produced in the laboratory via the photolythis of a series of organic molecule precursors at low temperature provides an excellent fit to the diffuse ISM absorption features.

The problem of growth of silicate dust in the ISM has long remained unsolved, because the formation of tetrahedral SiO_4- structures probably requires higher temperatures than the 10-30 K observed in molecular clouds. At these low temperatures, ice mantles are formed on the grain surface, preventing further growth of silicates. This is indirectly confirmed by the observations, which indicate disappearance silicate features and appearence of various solid ice features in the IR spectra from background objects in molecular clouds (Wooden et al 2004). Another possible mechanism Cosmic rays can penetrate dense molecular clouds and effect the structure and composition of teh ices, including the sputtering of icy grain mantles. The solution of the problem is possibly provided by intermittent dissipation of turbulence in molecular clouds (Falgarone et al.2006). The large local release of non-thermal energy in the gas by short bursts of turbulent dissipation has been shown to be able to trigger a specific warm chemistry, which can be traced by the high abundances of CH^+, H_2O, and HCO^+ observed in diffuse gas. It is shown that signatures of warm chemistry survive in the gas more then 10^3yr during chemical and thermal relaxation phases, see Fig. 10 in Falgarone et al. (2006). Such a local change in the gas temperature could provide the mechanism for further silicate growth, if the grain temperature increases enough for ice mantles to evaporate. The latter is defined by equating energy from collisions with warm gas and the emitted infrared energy, and thus depends on infrared absorption coefficients of mantle and core grain material; e.g. it differs noticeably for water and organic ices.

Our preliminary estimates show that the energy released locally by turbulent dissipation in molecular clouds is sufficient to evaporate organic ice mantles from the surface of silicate grains, although detailed calculations of temperatures and residence time in the relaxation phase for grains with different compositions have to be done to make quantitative estimates. This is a separate problem that is important for understanding the physics of dust growth in molecular clouds, and will be studied in further works.

It is assumed in the following that the silicate and carbon dust grains grow as separate species. In molecular clouds the growth of ice mantles certainly does not distinguish between carbon and silicon-bearing gas-phase species, and the ice mantles probably have a mixed chemistry. However, this may not be the case of refractory mantles, with silicate and carbon chemistry, since the spectral features of the dust in the ISM indicate distinct carbon and silicate grains. It is presently not known how it is possible to form either carbon or silicate dust grains in the ISM. Some chemically selective process must be invoked, accordingly to which, for example, C atom will not bond to the surface of a silicate grain and will be removed by some "cleaning" mechanism such as photodesorption or chemisputtering (Draine 1990). Analysis of such possibility with respect to present observations is done in Jones (2004).

4.3.1 Growth of dust grains in molecular clouds

In calculating the growth rates for the dust species, we follow a different procedure, as in Dwek (1998). Some modifications are necessary because (1) we wish to consider specific dust components and not merely the surface density of dust forming elements residing in some not closer specified dust components, and (2) since it is assumed that growth of dust is essentially restricted to molecular clouds (cf. Draine 1990) which relates the dust growth problem, like the dust destruction problem, closely to the multiphase structure of the ISM, which has approximately to be taken into account (for a different type of approach than in this paper see Liffman & Clayton 1989).

It is generally assumed (i) that the growth of dust grains of a specific kind j is governed by some rate determining reaction step, usually by adding of that one of the elements required to form the chemical compound that has the lowest abundance in the gas phase, and (ii) that the rate of adding of all other more abundant elements adapts to the slowest process. The growth is determined in this case by some specific key element and a special atomic or molecular species from the gas phase carrying most or all of this key element, the *growth species*. The key elements for the condensed phases of interest are given in Table 4.1. The equation for the change in the mass m_j of a single grain of species j is

$$\frac{\mathrm{d}m_j}{\mathrm{d}t} = \mathcal{A} A_j m_{\mathrm{AMU}} \frac{\nu_{j,\mathrm{m}}}{\nu_{j,\mathrm{c}}} \alpha_j \nu_{j,\mathrm{th,gr}} n_{j,\mathrm{gr}} \,. \tag{4.15}$$

Here $n_{j,\mathrm{gr}}$ is the particle density of the growth species, $\nu_{j,\mathrm{th,gr}}$ its thermal velocity, α_j the growth coefficient, $\mathcal{A}$ the surface area of the grain, and A_j the atomic weight of one formula unit of the dust material under consideration. Also $\nu_{j,\mathrm{m}}$ and $\nu_{j,\mathrm{c}}$ are the number of atoms of the key element contained in the growth species and in the formula unit of the condensed phase, respectively. Evaporation is neglected since this is not important at the low temperatures in molecular clouds. The change in the mass density ρ_j of the dust particles in a molecular cloud is obtained by multiplying the growth equation of single grains by the number density of grains and the probability distribution of grain radii (assuming spherical grains) and integrating over all grain radii a. One obtains

$$\frac{\mathrm{d}\rho_j}{\mathrm{d}t} = \alpha_j \nu_{j,\mathrm{th,gr}} n_{j,\mathrm{gr}} \frac{3V_{1,j}\langle a^2\rangle}{\langle a^3\rangle} \frac{\nu_{j,\mathrm{m}}}{\nu_{j,\mathrm{c}}} \rho_j \,, \tag{4.16}$$

where $V_{1,j} = A_j m_{\mathrm{AMU}}/\rho_{\mathrm{c}}$ is the volume of one formula unit in the condensed phase, ρ_{c} is the mass density of the condensed phase, and $\langle\ldots\rangle$ denotes averaging with respect to the size distribution of grains. We define the following average grain radius

$$\langle a\rangle_3 = \frac{\langle a^3\rangle}{\langle a^2\rangle} \,. \tag{4.17}$$

For a MRN size distribution (Mathis, Rumpl & Nordsiek 1977), we have for instance

$$\langle a\rangle_3 = \sqrt{a_0 a_1} \approx 0.035\,\mu\mathrm{m} \,, \tag{4.18}$$
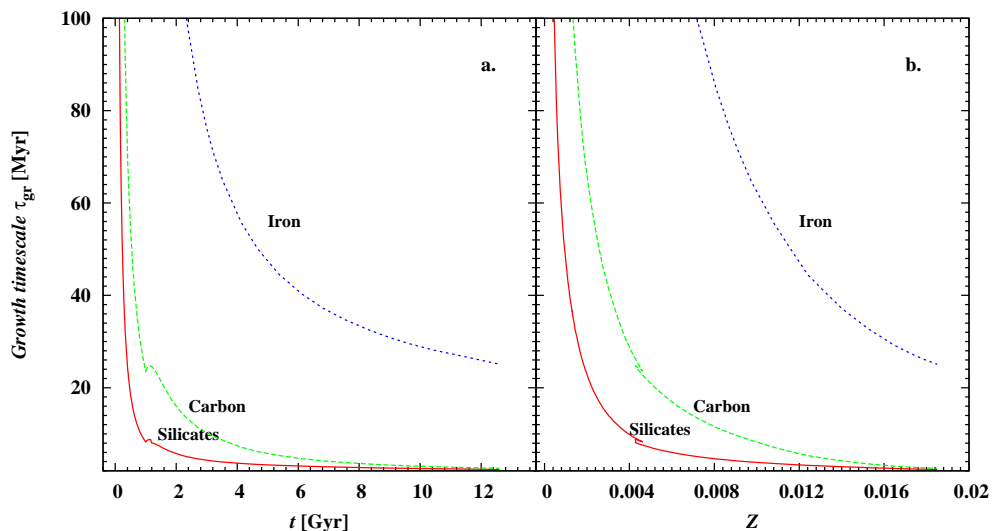
Figure 4.4: Growth timescales for the dust species growing in molecular clouds for the Milky Way model at the solar circle as a function of time (a) and metallicity (b.).

where $a_0 = 0.005\,\mu\text{m}$ and $a_1 = 0.25\,\mu\text{m}$ are the lower and upper limits of the distribution of grain radii, respectively.

The maximum possible particle density of the growth species is

$$n_{j,\text{gr,max}} = \frac{N_\text{H}\epsilon_j}{v_{j,\text{m}}} \,,$$

where N_H is the number density of H nuclei in the molecular cloud (usually equal to $2n_{\text{H}_2}$), and ϵ the element abundance of the key element, possibly lowered by the fraction of this element that is blocked in some unreactive molecular species. Let f denote the fraction of the key element already bound in the dust species under consideration, the *degree of condensation f*. The gas-phase density of the growth species is $(1 - f)\,n_{j,\text{gr,max}}$. Hence we obtain the following equation for the degree of condensation in the molecular cloud

$$\frac{\text{d}f}{\text{d}t} = \frac{1}{\tau_{j,\text{gr}}} f\,(1 - f) \,, \tag{4.19}$$

with

$$\frac{1}{\tau_{j,\text{gr}}} = \alpha_j v_{j,\text{th,gr}} \frac{3V_{1,j}}{\langle a \rangle_3} \frac{\epsilon}{v_{j,\text{c}}} N_\text{H} \,. \tag{4.20}$$

Numerically, we have

$$\tau_{j,\mathrm{gr}} = 46\,\mathrm{Myr} \times \frac{v_{j,\mathrm{c}}\,A_{j,\mathrm{m}}^{0.5}}{A_{j,\mathrm{c}}} \left(\frac{\rho_{\mathrm{c}}}{3\mathrm{g\,cm^{-3}}}\right)\left(\frac{3.5\,10^{-5}}{\epsilon_j}\right)\left(\frac{10^3\,\mathrm{cm^{-3}}}{N_{\mathrm{H}}}\right), \tag{4.21}$$

where $\tau_{j,\mathrm{gr}}$ is evaluated with characteristic values for the physical variables. The temperature of clouds is assumed to be 10 K, and the growth coefficient α at such low temperatures is assumed to be $\alpha = 1$. The characteristic growth time is generally short compared to the lifetime of molecular clouds, except for very low metallicity of the ISM. The density in molecular clouds ranges from 10^2 cm^{-3} to at least 10^5 cm^{-3}. Hirashita (2000) considered the density distribution and mass spectrum of clouds in the Galaxy and concluded that dust growth is determined by the low density molecular clouds with $N_H \sim 10^3$ cm^{-3}. Therefore we adopt this value in our model calculations.

In principle, the average grain radius $\langle a \rangle_3$ depends on the degree of condensation f ($a \propto f^{1/3}$ for compact structures), but we neglect this weak dependence. In this case the equation for f can immediately be integrated with the result

$$f(t) = \frac{f_0 \mathrm{e}^{t/\tau_{\mathrm{gr}}}}{1 - f_0 + f_0 \mathrm{e}^{t/\tau_{\mathrm{gr}}}}. \tag{4.22}$$

Here f_0 is the initial degree of condensation at $t = 0$. For $t \gg \tau_{\mathrm{gr}}$ the degree of condensation approaches $f = 1$.

Dust growth timescales

The growth timescales $\tau_{j,\mathrm{gr}}$ from Eq. (4.21) for the evolution of the disk at the Solar circle are shown in Fig. 4.4. The characteristic quantities for solid materials used in Eq. (4.21) are given in table 4.1. Figure 4.4a demonstrates the time evolution of the growth timescales for silicates, carbon and iron dust. Representation of the growth timescales as a function of metallicity in Fig. 4.4b reveals the metallicity dependence of dust growth process, which is similar for other galactic radii. The figure indicates that dust species can be characterised by some minimum metallicity, after which the timescale quickly decreases, approaching its asymptotic value, the axis of abscissa in this case. It gives a rough estimate of the critical metallicities for dust growth; for our choice of parameters, one has values of 0.0012 for silicates, 0.004 for carbon dust, and 0.014 for iron dust.

4.3.2 Source term for dust production

Molecular clouds form in the interstellar medium by instabilities, mainly during the compression of ISM material in the snowplow phase of SN shocks. They disappear within a rather short time if active star formation starts and winds of massive stars and expanding supernova bubbles disperse the clouds. For the average lifetime of molecular clouds, we take an observationally and theoretically motivated

value of $\approx 1 \times 10^7$ yrs (Leisawitz et al. 1989; Williams & McKee 1997; Matzner 2002; Krumholz & McKee 2006; Blitz et al. 2007). This value for the lifetime is somewhat shorter than used in Tielens (1998) in his model of dust growth in clouds, but seems to be more appropriate for the most massive clouds, which contain nearly all of the ISM mass in clouds. The lifetimes of the clouds equals the characteristic timescale τ_{exch} by which matter is exchanged between clouds and the remaining ISM.

At the instant of cloud formation, the clouds inherit the dust content of the interstellar medium outside of clouds. The dust content of the matter outside of dense clouds is lower than within clouds, since dust destruction processes operate in this material, while in clouds the dust grows by accreting not yet condensed refractory elements. In fact, except if the metallicity of the ISM is very low, the growth timescale is much shorter than the lifetime of the cloud, and the condensation of the refractory elements runs into completion before the cloud disappears.

Let the initial degree of condensation of the key element for some dust species be f_0. If after a period t a cloud is rapidly dispersed, the degree of condensation in the matter returned to the ISM material outside clouds is equal to the value given by Eq. (4.22). The effective dust mass return for species j by a molecular cloud is then

$$M_{j,\mathrm{d,cloud}} = (f(t) - f_0)\, X_{j,max}\, M_{\mathrm{cloud}}\,, \tag{4.23}$$

where

$$X_{j,\mathrm{max}} = \frac{A_j \epsilon}{(1 + 4\epsilon_{\mathrm{He}}) \nu_{j,\mathrm{c}}} \tag{4.24}$$

is the maximum possible mass fraction of the dust species in the material of the molecular cloud and M_{cloud} is the cloud mass. In principle, one has to observe that some fraction of the cloud mass is converted into stars and not converted into other phases of the ISM. Since we describe the effect of dust consumption by star formation within the frame of our approximation by a separate term in Eq. (3.1), this process does not need to be accounted for in Eq. (4.23).

Equation (4.23) has to be multiplied by the probability $P(t)$ that the cloud is destroyed at some instant within the period between t and $t + \mathrm{d}t$,

$$P(t) = \frac{1}{\tau_{\mathrm{exch}}} e^{-t/\tau_{\mathrm{exch}}}\,, \tag{4.25}$$

and integrated over t. Here it is assumed that the cloud destruction occurs at random with a mean lifetime τ_{exch}. Finally, averaging with respect to the mass spectrum of clouds and multiplying with the surface number density of clouds, one obtains for the mass return rate of MC-grown dust per unit time and unit area of the galactic disk

$$G_{j,\mathrm{d}} = \frac{1}{\tau_{\mathrm{exch}}} \left(f_{j,\mathrm{ret}} - f_{j,0} \right) X_{j,\mathrm{max}} \Sigma_{\mathrm{cloud}}\,, \tag{4.26}$$

where Σ_{cloud} is the surface mass density of clouds, and the average degree of condensation on cloud dispersal is

$$f_{j,\text{ret}}(t) = \frac{1}{\tau_{\text{exch}}} \int_0^t dx \, e^{-x/\tau_{\text{exch}}} \frac{f_{j,0}(t-x) e^{x/\tau_{j,\text{gr}}}}{1 - f_{j,0}(t-x)\left(1 - e^{x/\tau_{j,\text{gr}}}\right)}. \tag{4.27}$$

The quantity $G_{j,d}$ is the gain term that has to be used in Eq. (3.1) for the evolution of the MC-grown dust component j.

In principle, the evaluation of this term requires considering a multiphase ISM where molecular clouds form one of the components. Since we wish to consider the simpler model of a one-phase ISM, we have to cast Eq. (4.26) in an appropriate form for this case. In terms of the mass fraction of clouds in the ISM $X_{cloud} = \Sigma_{cloud}/\Sigma_{ISM}$, we have

$$G_{j,d} = \frac{X_{cloud}}{\tau_{\text{exch}}} \left(f_{j,\text{ret}} \Sigma_{j,d,\max} - \tilde{X}_{j,d} \Sigma_{ISM} \right),$$

where

$$\Sigma_{j,d,\max} = \frac{A_j}{\nu_{i,j} A_i} \Sigma_i \tag{4.28}$$

is the maximum possible surface density of dust of kind j if all material from the ISM that can be condensed into this dust species is really condensed, and $\tilde{X}_{j,d}$ is the mass fraction of dust of kind j in that part of the ISM that is not in clouds. Here Σ_i is the surface mass density of the key element for species j in the ISM. For the average mass-fraction of dust in the total ISM, we have

$$X_{j,d} = \tilde{X}_{j,d}(1 - X_{cloud}) + f_{j,\text{ret}} X_{j,d,\max} X_{cloud}, \tag{4.29}$$

which yields

$$\tilde{X}_{j,d} \Sigma_{ISM} = \frac{1}{1 - X_{cloud}} \Sigma_{j,d} - \frac{X_{cloud}}{1 - X_{cloud}} f_{j,\text{ret}} \Sigma_{j,d,\max}.$$

It follows that

$$G_{j,d} = \frac{X_{cloud}}{\tau_{\text{exch}}(1 - X_{cloud})} \left[f_{j,\text{ret}} \Sigma_{j,d,\max} - \Sigma_{j,d} \right]. \tag{4.30}$$

We define the effective exchange time

$$\tau_{\text{exch,eff}} = \tau_{\text{exch}} \frac{1 - X_{cloud}}{X_{cloud}}. \tag{4.31}$$

This is much longer than τ_{exch}, since $X_{cloud} \ll 1$, and reflects the fact that it requires many timescales τ_{exch} to cycle all ISM material through clouds where it is laden with fresh dust. Our final result for the dust production term is

$$G_{j,d} = \frac{1}{\tau_{\text{exch,eff}}} \left[f_{j,\text{ret}} \Sigma_{j,d,\max} - \Sigma_{j,d} \right]. \tag{4.32}$$

This is the appropriate dust production term for MC-grown dust in the approximation of a one-phase ISM model. In this model the mass-fraction X_{cloud} of the ISM in clouds is a free parameter that does not follow from the model calculation but has to be taken from observations. We will use a value of $X_{cloud} = 0.2$ (cf. Tielens 2005), which is appropriate for the ISM at the solar circle.
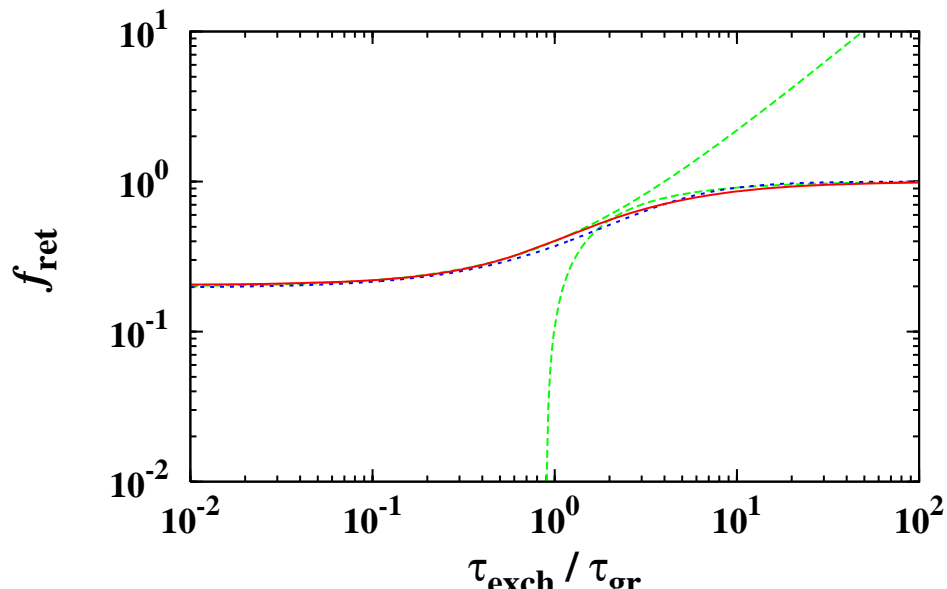
Figure 4.5: Approximation for the variation of the degree of condensation f_{ret} with $\tau_{\text{gr}}/\tau_{\text{exch}}$ for $f_0 = 0.3$. The full line shows the result of a numerical evaluation of the integral (4.27), the dashed lines the two limit cases Eqs. (4.33) and (4.34), and the dotted line the approximation (4.35) (the full and dashed lines nearly coincide).

4.3.3 Limit cases

The degree of condensation $f_{j,\text{ret}}$ in the material returned from clouds at the time of their dispersal essentially depends on the ratio of the growth timescale τ_{gr} to the average cloud lifetime τ_{exch}. If $\tau_{\text{gr}} \gg \tau_{\text{exch}}$ (slow growth at low metallicities) one expects that only small amounts of dust are added to the initial dust content; in the opposite case (rapid growth at normal metallicities), one expects complete condensation in the returned material. This can be confirmed by calculating the lowest order terms of a series expansion of the integral in Eq. (4.27) for the two limiting cases. In the following we assume that $t \gg \max(\tau_{\text{exch}}, \tau_{j,\text{gr}})$ so that the upper limit of integration in Eq. (4.27) can be replaced by ∞ and so $f_{j,0}$ is essentially constant over timescales of the order of $t \gg \max(\tau_{\text{exch}}, \tau_{j,\text{gr}})$.

For slow growth ($\tau_{\text{gr}} \gg \tau_{\text{exch}}$) one introduces t/τ_{exch} as integration variable, expands $\exp\left[\left(\tau_{\text{exch}}/\tau_{\text{gr}}\right) t\right]$ in a series, and integrates term-by-term. The result is in the linear approximation

$$f_{j,\text{ret}} \approx f_0 \left(1 + \frac{\tau_{\text{exch}}}{\tau_{\text{gr}}}\right). \tag{4.33}$$

If this is inserted into Eq. (4.23) one recognises that τ_{exch} cancels out and, thus, the amount of dust produced during the residence time of ISM material in the cloud phase is determined by the details of the growth process.

For rapid growth ($\tau_{\mathrm{exch}} \gg \tau_{\mathrm{gr}}$), one introduces t/τ_{gr} as the integration variable, expands $\exp\left[\,(\tau_{\mathrm{gr}}/\tau_{\mathrm{exch}})\,t\,\right]$ in a series, and integrates term-by-term. The result is in the linear approximation

$$f_{j,\mathrm{ret}} \approx 1 + \frac{1 - f_0}{f_0} \ln(1 - f_0) \frac{\tau_{\mathrm{gr}}}{\tau_{\mathrm{exch}}} \tag{4.34}$$

(note that $\ln(1 - f_0) < 0$). If this is inserted into Eq. (4.23), one finds that the dust production by the clouds is nearly independent of the details of the growth process within the clouds and is (almost) exclusively determined by the cycling frequency of ISM material between the clouds and the other phases of the ISM. The composition of the dust, of course, is determined in this case by the details of growth processes.

The variation in $f_{j,\mathrm{ret}}$ with $\tau_{\mathrm{gr}}/\tau_{\mathrm{exch}}$ in both limit cases for a value of $f_0 = 0.3$ are shown in Fig. 4.5 with the result of a numerical evaluation of the integral (4.27). A rather accurate analytic fit formula for the full range of $\tau_{\mathrm{gr}}/\tau_{\mathrm{exch}}$ values is

$$f_{j,\mathrm{ret}} = \left(\frac{1}{f_{j,0}^2 \left(1 + (\tau_{\mathrm{exch}}/\tau_{\mathrm{gr}})\right)^2} + 1 \right)^{-1/2}. \tag{4.35}$$

The results for other values of f_0 are similar. Only for very small f_0 does the approximation becomes somewhat worse in the transition region $\tau_{\mathrm{gr}}/\tau_{\mathrm{exch}} \approx 1$, but for bigger f_0 it improves. For the purpose of model calculations, it suffices to use the approximation (4.35).

4.4   The individual dust species

Evaluation of the source term Eq. (4.32) for dust requires calculating the growth timescale $\tau_{j,\mathrm{gr}}$, given by Eq. (4.20), $X_{j,\mathrm{max}}$ given by Eq. (4.24), and the degree of condensation $f_{j,\mathrm{ret}}$ in the returned material, which we calculate from the approximation (4.35), for all dust species j which are formed by growth in molecular clouds.

The constants required for calculating these quantities are given in Table 4.1. The growth coefficient is assumed to be $\alpha = 1$ for all cases since, at the low temperatures in dense molecular clouds of about 10 K, even the weak attractive van der Waals forces lead to adsorption. The basic theory for this is discussed, e.g., in Hollenbach & Salpeter (1970), and Watson (1975).

For calculating the average $\langle a \rangle_3$, we use in all cases the approximation Eq. (4.18) following from a MRN-size distribution (Mathis et al. 1977). This is only a crude approximation; but without attempting to calculate grain size distributions, it is hardly possible to fix this quantity with more accuracy.

The initial value $f_{j,0}$ for calculating $f_{j,ret}$ is given by the degree of condensation in that part of the

ISM matter that is not in clouds, i.e., one has

$$f_{j,0} = \frac{\tilde{X}_{j,\mathrm{d}}}{X_{j,\mathrm{max}}} \, . \tag{4.36}$$

Using this and Eq. (4.35) in Eq. (4.29) yields a non-linear equation that has to be solved for $f_{j,0}$. For most purposes it suffices to replace the value of $f_{j,0}$ by the approximation $f_{j,0} \approx X_{j,\mathrm{d}}/X_{j,\mathrm{max}}$ for solving Eq. (4.29) since the difference between $\tilde{X}_{j,\mathrm{d}}$ and $X_{j,\mathrm{d}}$ is not very big.

4.4.1 Silicates

The silicate dust in the ISM accounts for about one half of the total dust mass (e.g. Dwek 2005), but its composition is still a matter of debate. Studies of silicate composition based on interstellar depletions, modelling of extinction curve, and in situ measurements of dust in the local ISM give quite different results, although they all agree that olivine ($[\mathrm{Mg_xFe_{1-x}}]_2\mathrm{SiO_4}$ with $0 < x < 1$) and pyroxene ($\mathrm{Mg_xFe_{1-x}SiO_3}$ with $0 < x < 1$) constitute most mass of the ISM silicates. A number of studies of depletions of Mg, Fe, Si, and O atoms in the interstellar gas phase came to the conclusion that observed depletions indicate an olivine-type stoichiometry of dust in the diffuse ISM (Savage & Sembach 1996, Jones 2000). A recent attempt to fit the silicate features of the interstellar extinction curve (Min et al. 2007) found that the composition of the ISM silicates is consistent with a Mg-rich mixture of olivine and pyroxene with a bigger contribution from pyroxene than from olivine. Fitting of the 9 and 18 μm features of the extinction curve shows that, while the 9 μm feature can be fitted well by olivine dust, the position and peak strength of 18 μm feature is fitted much better with a pyroxene-type stoichiometry (Demyk 1999).

An olivine-pyroxene mixture with a contribution of more pyroxene than olivine is therefore chosen for modelling the ISM silicates in the present paper. As a first approximation we adopt a fixed silicate composition to study silicate dust production by dust growth in molecular clouds. Modelling a variable silicate composition, depending on local growth conditions, is a challenge to be considered in future papers. Let f_{ol} be the (fixed) fraction of the silicate dust that has olivine stoichiometry; the fraction $1 - f_{\mathrm{ol}}$ then has pyroxene stoichiometry. Assuming the same Mg fraction x for both olivine and pyroxene in our model, two parameters determine the silicate properties: f_{ol} and x.

The total efficiency of dust production by molecular clouds does not show a significant dependence on the choice of the parameters f_{ol} and x. Variations of the Mg-fraction x change the total dust mass on the level of 10% at most, but define the silicate-to-iron dust mass ratio. This is due to the fact that for the Mg-rich mixtures that are considered here, Mg is the critical growth species. With decreasing x, less Mg is needed for silicate dust growth, but the total silicate mass increases due to a bigger contribution from the Fe-bearing component, while at the same time less Fe remains for the growth of solid iron. We fix the Mg fraction x to a value of $x = 0.8$ by fitting the present-day silicate-

to-carbon dust mass ratio of the model to its observed value of 0.6, inferred from observations of the infrared emission from the Diffuse Infrared Background Experiment (Dwek et al. 1997).

The olivine fraction f_{ol} is chosen to reproduce the observed Mg/Si ratio in dust using the simple relation for a given olivine-pyroxene mixture:

$$f_{ol} = \frac{A_{Mg}}{x A_{Si}} - 1.$$

(4.37)

Here A_{Mg} and A_{Si} are observed abundances for the elements Si and Mg bound in dust (in particles per million hydrogen atoms, ppm). The ratio A_{Mg}/A_{Si} equals 1.06 or 1.07 for dust in the diffuse ISM, as given by Dwek (2005) or Whittet (2003), respectively, which results in a value of $f_{ol} = 0.32$. Although the A_{Mg}/A_{Si} ratio obviously varies in different ISM phases, we use average dust abundances from the diffuse medium, since this constitutes a significant fraction of the total ISM mass, and only very little is known about the very cold dust in molecular clouds. Test calculations for different A_{Mg}/A_{Si} ratios available from diffuse ISM studies showed no strong influence on dust masses, resulting in 4% change of total dust mass with 10% decrease of A_{Mg}/A_{Si} ratio.

For given silicate composition, the growth species used to calculate the growth timescale, Eq. (4.20), is determined by the abundance of the least abundant species available for dust growth. This is either Si or Mg, and we choose in Eq. (4.20)

$$\epsilon = \begin{cases} \dfrac{\Sigma_{Mg}}{24\Sigma_H} & \text{for } \dfrac{\epsilon_{Mg}}{\nu_{Mg,c}} < \dfrac{\epsilon_{Si}}{\nu_{Si,c}} \\[2em] \dfrac{\Sigma_{Si}}{28\Sigma_H} & \text{for } \dfrac{\epsilon_{Mg}}{\nu_{Mg,c}} < \dfrac{\epsilon_{Si}}{\nu_{Si,c}} \end{cases},$$

(4.38)

where $\nu_{Si,c} = 1$, $\nu_{Mg,c} = 1.06$.

4.4.2 Carbon dust

The formula unit is the C atom, i.e., one has $\nu_{j,c} = 1$. It is assumed that C is present in the gas phase in molecular clouds predominantly as free atoms or in a number of molecules bearing one C atom only and that these serve as growth species. Some fraction f_{CO} of the carbon is blocked in the CO molecule and is not available for carbon growth. The precise fraction cannot be fixed without calculating models for the chemistry of the molecular clouds. Observations indicate a CO abundance in molecular clouds of 20% - 40% of the C abundance (e.g. Irvine et al. 1987; van Dishoek et al. 1993; van Dishoek & Blake 1998). In the calculation we consider the two cases $\xi_{CO} = 0.2$ and $\xi_{CO} = 0.4$. The carbon abundance ϵ in Eqs. (4.20) and (4.24) is calculated as

$$\epsilon = (1 - \xi_{CO}) \frac{\Sigma_C - \Sigma_{C,sic}}{12\Sigma_H},$$

(4.39)
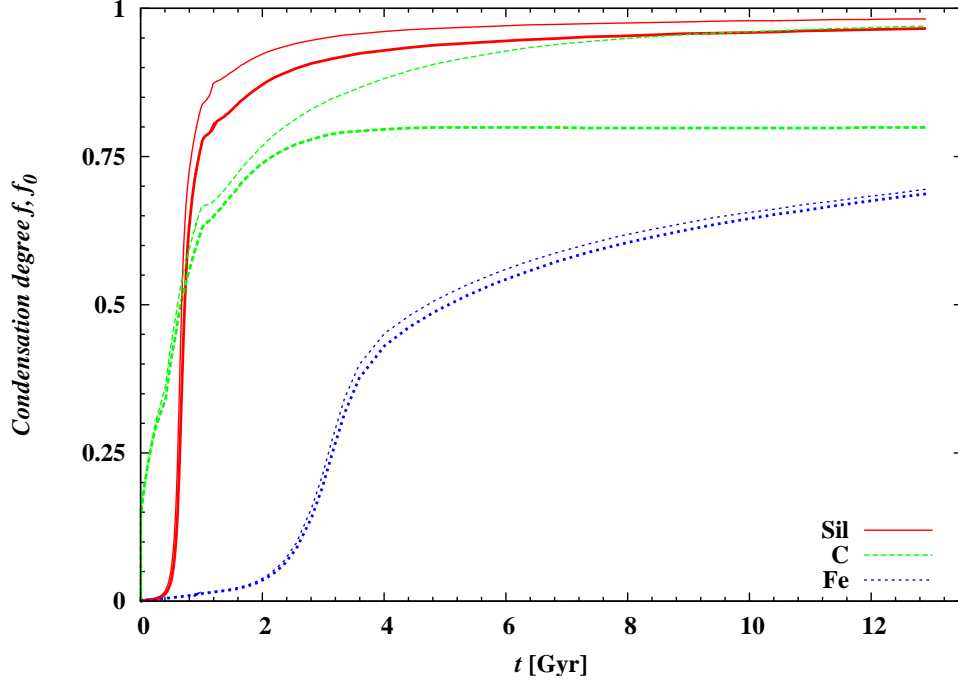
Figure 4.6: Growth of dust in molecular clouds at the solar circle. Thick lines show f, the average degree of condensation of the key elements into dust for the dust species shown at the instant when the molecular clouds are dispersed and their material is mixed with the other phases of the ISM. Thin lines show f_0, the corresponding degree of condensation at the formation time of clouds. One always has $f_0 < f$ since dust grains grow in molecular clouds and are partially destroyed again in the ISM outside of clouds until they enter the next cloud. Growth of iron dust in clouds starts with a significant time delay because of delayed iron production by SN Ia events. The calculation is for $\xi_{CO} = 0.2$; the result for $\xi_{CO} = 0.4$ is not shown because the corresponding curves are almost the sames.

where $\Sigma_{C,sic}$ is the surface density of C bound in silicon carbide dust

$$\Sigma_{C,sic} = \frac{12}{40}\Sigma_{sic} \,. \tag{4.40}$$

4.4.3 Iron dust

The formula unit is the Fe atom, i.e., one has $\nu_{j,c} = 1$. It is assumed that Fe is present in the gas phase as free atoms, which are the growth species in this case. The iron abundance ϵ in Eqs. (4.20) and (4.24) is calculated as

$$\epsilon = \frac{\Sigma_{Fe} - \Sigma_{Fe,sil}}{56\Sigma_{H}} \,, \tag{4.41}$$

where $\Sigma_{Fe,sil}$ is the surface density of Fe bound in silicate dust species.

5

Results of the dust evolution model

5.1 Dust evolution at the Solar circle

5.1.1 Evolution of MC-grown dust

The model for the dust evolution considers silicate dust, carbon dust, and iron dust as species that grow in dense molecular clouds. The corresponding growth timescales τ_{gr} calculated from our Milky Way model at the solar circle are shown in Fig. 4.4.

During the first Gyr of evolution of the galactic disk, the metallicity at the solar circle is low ([Fe/H]$\lesssim -2$, cf. Fig. 2.4) and the characteristic growth timescale of dust in clouds exceeds the average lifetime of dense molecular clouds of about 10 Myr assumed in our model. Only small amounts of dust are added to the dust content of the interstellar matter during its cycling through clouds. This can be seen in Fig. 4.6, which shows the evolution of the initial value $f_{j,0}$ of the degree of condensation of the key elements into dust, defined by Eq. (4.36), for each of the dust species j, and the average final degrees of condensation f_j, calculated according to Eq. (4.35) for the same species, if the clouds are finally dissolved. Both quantities, $f_{j,0}$ and f_j, are calculated during the course of our model calculation for the evolution of the Milky Way at the solar circle. One always has $f_0 < f$ since dust grains grow in molecular clouds and are partially destroyed again in the ISM outside of clouds until they enter the next cloud. Growth of iron dust in clouds starts with a significant time delay because of delayed iron production by SN Ia events.

During the first, about one Gyr the degree of condensation of refractory elements into dust increases only marginally by dust growth in molecular clouds. Therefore, the dust production in the Milky Way is almost completely determined by dust condensation in the ejecta of stars, and the dust content of the ISM is determined during this transient phase by dust injection from stars into the ISM and by dust destruction in the warm phase of the interstellar medium. Obviously the development would be considerably different if one has a strong starburst at early times and metallicity already
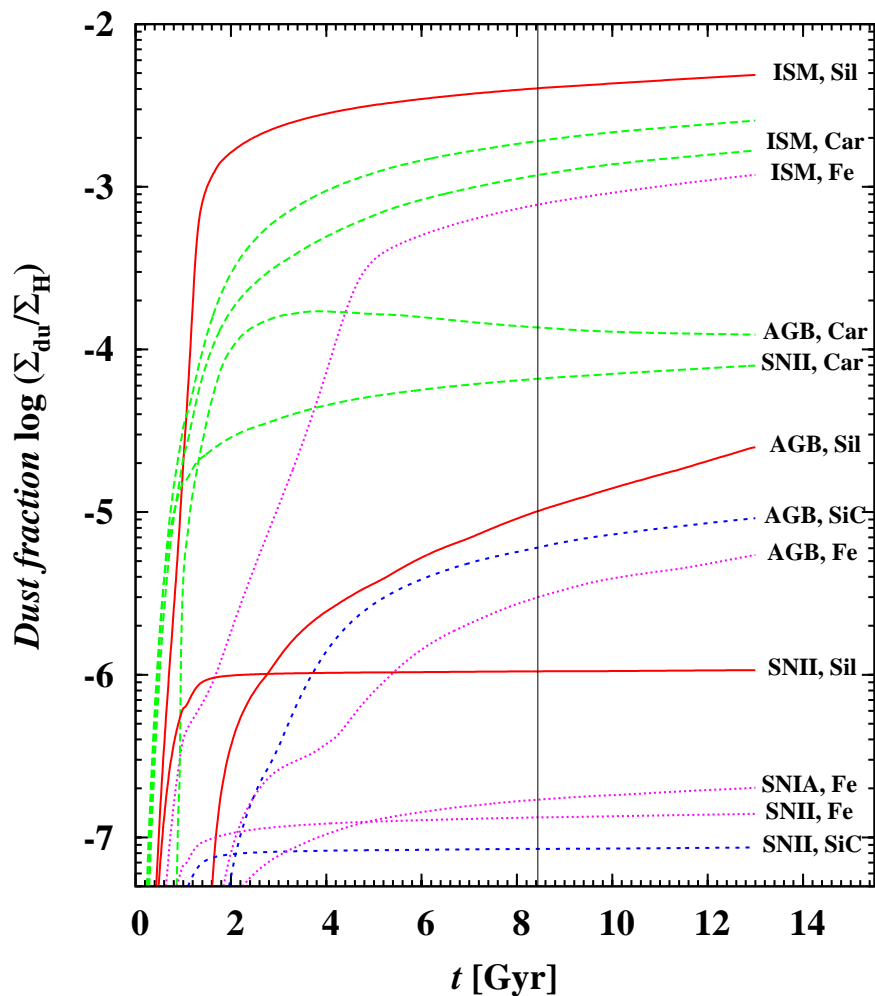
Figure 5.1: Evolution of the dust mass fraction in the interstellar medium of the main interstellar dust components and of the stardust species at the solar circle. For carbon dust two results are shown corresponding to an assumed fraction ξ_{CO} of 0.2 and 0.4 of the carbon in molecular clouds locked in the CO molecule.

becomes high before the first AGB stars appear, but this seems not to have happened in the case of our Milky Way.

Once the metallicity of the ISM has grown to a level of about [Fe/H]= −2, some dust starts to condense during the lifetime of molecular clouds, and their dust content at the instant of their dissolution somewhat exceeds their initial dust content. From this point on molecular clouds start to contribute to dust production in the galaxy.

If the metallicity has climbed after more than 2 Gyrs to a level of about [Fe/H]= −1, the degrees of condensation into dust f_j at cloud dispersal are much higher than the degrees of condensation into dust $f_{j,0}$ at cloud formation; in fact, dust growth almost runs into completion during the lifetime of the clouds. During each cycle step of interstellar matter through clouds, the matter is laden with fresh dust and this dust is mixed into the general ISM at cloud dispersal. The dust content of the ISM then is determined essentially by the equilibrium between dust growth in clouds and dust destruction in the warm phase of the interstellar medium.

The degree of condensation f of carbon into carbon dust does not approach unity (see Fig. 4.6), since it is assumed that 20 to 40% of the carbon in molecular clouds forms CO and then is no longer available for dust condensation.

The iron dust abundance evolves somewhat differently from that of the silicate and carbon dust. The main reason is that most of the Fe is produced in SN Ia explosions and these turn on rather late due to the long lifetime of their low mass precursor stars. We also assumed in our model that SN Ia explosions do not start until the metallicity of the precursor stars has risen to [Fe/H] $\gtrsim$ −1 (see Sect. 2.3.4). A second reason is that it is assumed in our model of dust growth that the silicates grown in clouds contain a certain fraction of iron and the small fraction of iron initially produced by supernovae is then almost completely consumed by the growth of silicates with some iron content. This will change somewhat if the iron content of the silicates is not fixed, as in our present calculation, but will be determined from growth kinetics.

5.1.2 Evolution of dust abundances

Figure 5.1 shows the evolution of the various dust components during the 13 Gyrs of evolution of the galactic disk. The dust components with index 'ISM' are the isotopically normal grains grown in the interstellar medium. Surviving grains from stellar sources are characterised by an index 'AGB' or 'SN' if they are from AGB-stars or from supernova ejecta, respectively. The dust condensed in stellar ejecta (AGB stars, SNe) only has a small abundance in the ISM. The condensation efficiencies of dust in supernovae used for the model calculation are given in Table 4.1.

The results depend on the efficiency of dust production by stars, dust condensation in molecular clouds, and dust destruction rates in the interstellar medium. The dust production by low and intermediate mass stars on the AGB is determined from the table of Ferrarotti & Gail (2006) and the dust

destruction rate from Jones et al. (1996). They are probably not too far from reality. The dust production efficiencies of massive stars are unknown. One has, however, one piece of information: the abundance ratios of the presolar dust grains from AGB stars and SNe. We have varied the supernova dust production efficiencies η in Eqs. (3.16)...(3.19) until the observed abundance ratios for silicate, carbon, and SiC dust from AGB and SNe sources is reproduced. Details are described in Sect. 5.1.3, the resulting efficiencies are listed in Table 4.1. These efficiencies are very low, probably since they also account for a number of destruction effects that prevent dust formed in SNe from escaping into the general ISM.

The dust population of the ISM in this model is dominated by dust grown in molecular clouds except for the very earliest times, where stardust dominates. The model shows that presolar dust grains with their isotopic anomalies revealing the origin of these grains are always a minor component of the interstellar dust. Most of the dust in the ISM has collected nearly all of its material from the interstellar gas phase and is isotopically inconspicuous. If new stars are formed from the ISM containing such a dust mixture, the dust in their protoplanetary accretion disks contains only a tiny fraction of presolar dust grains with isotopic anomalies. This fits well with the recent findings obtained with the nano-SIMS investigations of interplanetary dust grains by Messenger et al. (2003), which show that nearly all of the silicate grains from cometary nuclei, which should be dominated by interstellar grains, are isotopically normal[1]

The population of stardust grains is dominated by grains from AGB stars because of the low efficiency of SN dust production. In our model the AGB dust is dominated by carbon dust; silicate dust and SiC dust are much less abundant. In meteorites presolar carbon dust in the state of graphite is the least abundant of these three components (cf. Nguyen et al. 2007). The discrepancy is certainly due (i) to the different survival properties of different kinds of dust material in the Solar System and the parent bodies of the meteorites, and (ii) the methods of laboratory investigations applied for different dust grains. This frustrates presently any comparison between abundances of different presolar species predicted by the model and observed in meteorites.

One outstanding feature of the abundance evolution of presolar dust grains is the rather late appearance of silicate and SiC as compared to carbon grains. This reflects that AGB stars synthesise the carbon required for soot formation from He and do not have to rely on external sources of heavy elements. In contrast to this, the Si-bearing dust components cannot be formed until enough Si is synthesised in supernova explosions and returned to the ISM, from which subsequent stellar generations inherit the Si required for formation of Si-bearing species. This needs some time and additionally the precursor stars of the main sources of Si-bearing dust, the AGB stars, are rather long-lived low-mass stars (cf. Fig. 3.2). Presolar silicate dust grains in the ISM where a rather new phenomenon at the

---

[1]It is a little puzzling that the STARDUST particles analysed so far mainly seem to be material from the Solar System (see Zolensky et al. 2006; McKeegan et al. 2006)

Table 5.1: SN presolar dust fractions and corresponding derived efficiencies of dust production.

Dust species	Fraction of SN grains	η_j
	0.01	0.00015
Silicates	0.05	0.0005
	0.10	0.001
	0.1	0.04
Carbon	0.3	0.15
	0.5	0.20
SiC	0.01	0.0003

instant of Solar System formation.

The low abundance of silicate stardust may also explain the lack of crystalline silicate dust in the ISM, though a lot of crystalline dust is injected into the interstellar medium by outflows from AGB stars. Even if there were no amorphization processes with energetic electrons and ions (cf. Demyk et al. 2004; Jäger et al. 2003), crystalline silicate dust ($\leq 20\%$ of the silicate dust injected by AGB stars) would be too rare compared to amorphous ISM dust to be observable by its absorption features.

5.1.3 Efficiency of supernova dust production

The dust mass produced in the ejecta of supernovae is not known. Observations indicate that only small amounts of dust condense and that only part of all SNe form dust. With the kind of model for dust evolution in the ISM we have developed, one can try to estimate the efficiency of dust production by supernovae for some dust species. This can be done by comparing the abundance ratios of supernova dust and AGB dust resulting from the model calculation with real observed abundance ratios of presolar dust grains with SN and AGB origin in meteorites. Only silicate, carbon, and SiC dust is presently suited for this, because the required data for presolar dust grains are available only for these dust species. Iron dust has not yet been detected as presolar dust so far, and it is unclear whether it really exists.

Such a comparison depends on some assumptions. The first one is that the production rate of dust by AGB stars is known with significantly better accuracy than the dust production rate of supernovae. The second basic assumption of a comparison between these kinds of data is that the fraction of the dust destroyed between the instant of its incorporation into the just-forming Solar System and the instant of laboratory investigation of presolar dust grains does not depend on the kind of stellar sources where the dust has formed, but only on its chemical composition. One has to assume, in other words, that the basic properties of AGB and SN dust with the same composition,

- its size spectrum,

- its resilience against oxidation, and

- its resilience against treatment by strong acids,

are the same.

Silicon carbide

The observed abundance ratio of X-type SiC grains and 'mainstream' SiC grains in the presolar dust population isolated from meteorites is close to 0.01 (Hoppe et al. 2000). Fitting the efficiency $\eta_{\text{sic,SN II}}$ in Eq. (3.18) such that the calculated abundance ratio for SiC from supernovae of type II and AGB stars agrees with the observed abundance ratio yields $\eta_{\text{sic,SN II}} = 5 \times 10^{-4}$. This ratio seems surprisingly low, but the low abundance of X-type SiC grains already shows that the efficiency of SiC dust formation in supernovae is low. The efficiency $\eta_{\text{sic,SN II}}$ of SiC dust condensation in supernova determined in this way is used for the final model calculation and is the one given in Table 4.1.

The abundance ratio for the SiC grains refers to grain abundances observed after isolating the grains from the meteorite matrix by a rather brutal treatment with oxidising agencies and by strong acids (cf. Amari et al. 1994), but it has been argued by Amari et al. (1994; 1995) that at most a small fraction of the grain material is lost during this procedure. On the other hand, the size distribution of SiC grains in the Murchison meteorite found by Daulton et al. (2003) shows a lack of grains smaller than 0.5 μm diameter, which dominate in circumstellar dust shells (e.g. Jura 1997), i.e., the small grains are already lost in the ISM or in the Solar System. If there were severe systematic differences in the mass fraction of sub-micron sized grains in the size distributions of SiC grains of SN and AGB origin, the abundance ratio derived from isolated SiC grains would be severely misleading, but presently we have no better data.

Silicate dust

The number of silicate grains from stellar sources detected in meteorites and interplanetary dust particles has been small up to now (Nguyen et al. 2007; Messenger et al. 2005). Besides about some 100 silicate grains with isotopic anomalies attributable to an origin from AGB stars only a single grain has been detected with isotopic characteristics pointing unambiguously to an SN origin (Messenger et al. 2005). Recently several more grains have been detected more have been detected that are also of likely SN origin (Nittler et al. 2008, Vollmer et al. 2007, Vollmer et al. 2008). The small numbers do not allow pinning down the abundance ratio of silicate dust from the two possible sources with any reliability. In present work we assume a SN dust fraction of 10% as a working hypothesis. This is somewhat higher than 3% adopted for our first estimates (Zhukovska et al. 2008) taken into
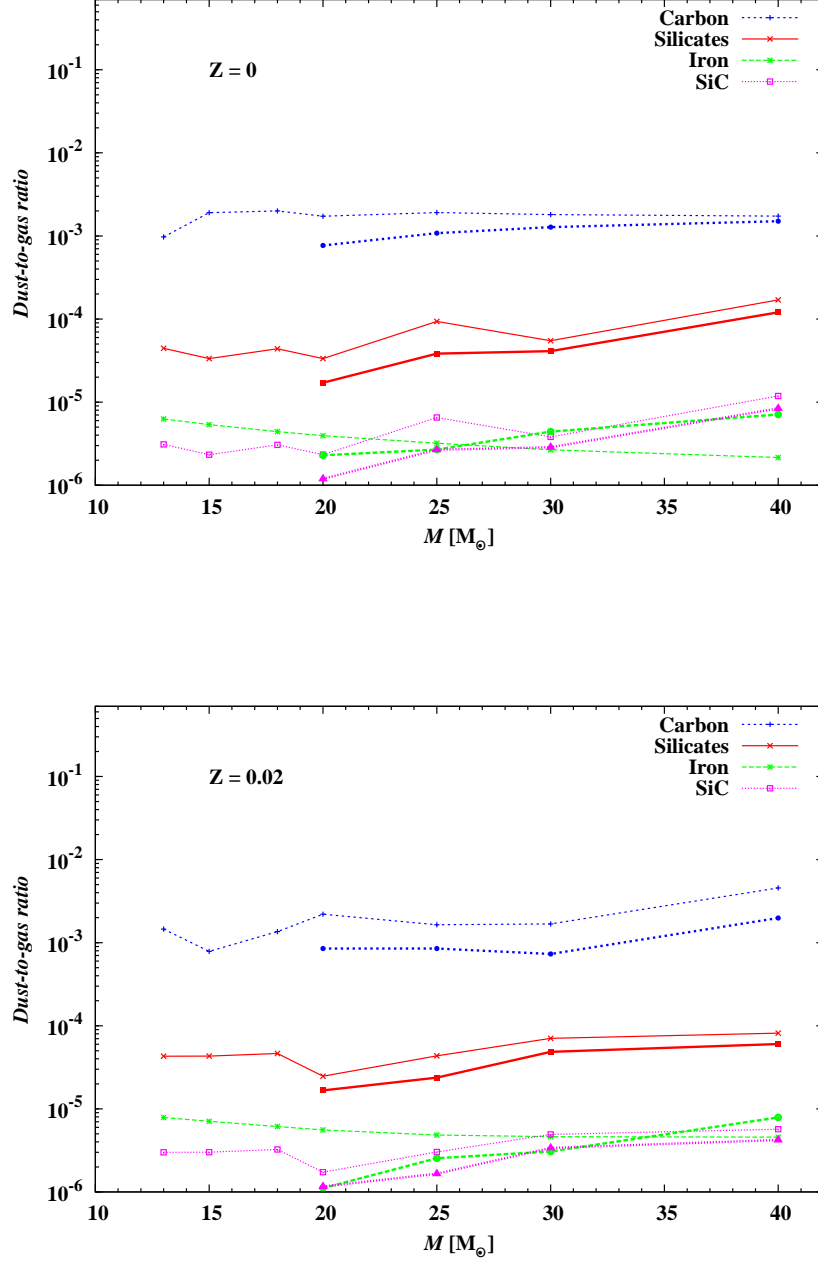
Figure 5.2: Dust-to-gas mass ratio in the ejecta of supernova (thin lines) and hypernovae (thick lines) as a function of initial mass for metallicities $Z = 0$ (top) and $Z = 0.02$ (bottom) as a function of initial mass. The nucleosynthesis yields are from Nomoto (2006).

account recent detections (Nittler et al. 2008, Vollmer et al. 2008). Then we can obtain an efficiency of silicate dust formation in supernovae of $\eta_{\text{sil,SN II}} = 10^{-3}$. This is the value given in Table 4.1. The efficiencies for a somewhat lower abundance ratio, which were obtained in previous work are shown for comparison in Table 5.1.

In contrast to the case of SiC, the silicate grains are detected by scanning techniques from material that has not been prepared by chemical treatment. There is therefore no problem to be expected in the sense that part of the grain population is already destroyed by preparation methods before the particles are investigated.

Carbon dust

The abundance of presolar graphites from supernovae is highly uncertain. Chemically separated graphite fractions were further subdivided into low-density separates KE1 and high-density separates KFA1, KFB1, and KFC1 (Amari et al. 1994). While many – though not all – high-density graphites seem to have an AGB star origin (Croat et al., 2005), low-density graphites are ascribed to supernovae (Hoppe et al. 1995, Amari et al. 1995; Travaglio et al. 1999), particularly inferred from isotope data of the low-density fraction KE3 (Amari et al. 1995b), which is the coarse-grained ($> 2\,\mu$m) subgroup making up 70% of KE1.

If all low-density graphites are from supernovae, this would correspond to a relative abundance of 67% (by weight). However, there is significant uncertainty which fractions of the various density separates do indeed correspond to a specific supernova or AGB star signature, so we adopt an abundance of 50 ± 30 % here (Hoppe, pers. comm.) and calculate 3 different cases for 10%, 30%, and 50% of all graphites coming from supernovae. For the model results shown in the figures, we assumed a mass-fraction of 30%. From this, one derives an efficiency of carbon dust formation in supernovae of $\eta_{\text{car,SN II}} = 0.15$. This is the value given in Table 4.1. This efficiency is much higher than in the two preceding cases and would mean that SNe are mainly sources of carbon dust. Efficiencies for a lower (10%) and higher (50%) abundance ratio are shown in Table 5.1 for comparison.

Presolar graphite grains mainly have size $\gtrsim 1\,\mu$m (e.g. Zinner 1997), while for carbon dust grains in circumstellar dust shells around AGB stars, one knows that they have sizes $\lesssim 0.1\,\mu$m. Only a small fraction of grains from a large-size tail of the size distribution are found in the separates investigated in the laboratory. If the graphite grains formed in SN ejecta had systematically bigger sizes than those formed in AGB-star outflows (there is, however, no indication for this), the supernova graphite dust fraction found in the separates would overestimate the true abundance of graphite grains from supernovae, and our estimated efficiency $\eta_{\text{car,SN II}}$ would be too high.

The high condensation efficiency of carbon dust compared to that of SiC and silicate dust found in this model calculation seems likely since condensation of carbon dust only requires that carbon atoms in the carbon layer have to condense into dust particles, and no complicated mixing processes

of the supernova ejecta between layers with different elemental composition are required, as for the dust species SiC and silicates. The formation of SiC requires that silicon from the layer containing the ashes of O burning and carbon from the layer containing the ashes of He burning are coming into contact without being completely mixed with the material from the thick O shell in between. This kind of incomplete mixing in a turbulent supernova shell is rather unlikely and therefore should only happen for a small fraction of the material.

Dust-to-gas ratio in SN ejecta

For the analysis of the origin of dust in the ISM it is useful to know the dust-to-gas ratio in the material ejected by the SNe into the ISM. In order to get a rough estimate of these dust-to-gas ratios, we simply plot the ratio of the elements returned in the dust form to the total mass ejected in SNe and HNe explosion taken from the nucleosynthesis yields (Nomoto et al. 2006). The resulting dust-to-gas ratios in ejecta are depicted in Fig. 5.2 for carbon, silicates, SiC and iron dust. The dust masses are calculated using the efficiencies condensations given in Table 4.1. As seen in Fig. 5.2 the resulting dust-to-gas ratios is of an order of 5×10^{-3}, solely determined by carbon dust. For comparison, the dust-to-gas ratio in the Large Magellanic Cloud is of 6×10^{-3} (Spitzer 1978).

Need for dust accretion in the ISM

The low efficiency of dust production by supernovae indicated by the rather low abundance of stardust of SN origin compared to stardust from AGB stars means that the supernovae cannot contribute substantially to dust in the ISM, contrary to what is frequently assumed. Therefore it is unavoidable that most of the dust mass observed in the ISM is formed in the ISM itself and not in stars. This has consequences for the dust production in young galaxies with low metallicity, where only supernovae can be sources of stardust. The high dust abundances observed in some high-redshift galaxies cannot, according to our results, result from the first generation of SNe, but already requires additional accretion processes of heavy elements in interstellar clouds. This is in agreement with the recent study of dust evolution in hyperluminous galaxies in the early universe in Dwek, Gallino & Jones (2007), who showed that supernovae can only reproduce high dust content if unrealistically high dust production yields are assumed. Modelling of dust evolution in young starburst galaxies will be treated in a separate paper.

5.1.4 Dust composition

Figure 5.3 shows our model results for the abundance evolution of the main dust-forming elements. Since we assumed a fixed composition of ISM silicates, the ratio between Mg, Si, and O does not change during evolution, but this is not the case for Fe, which is consumed both by silicate and iron

5. RESULTS OF THE DUST EVOLUTION MODEL
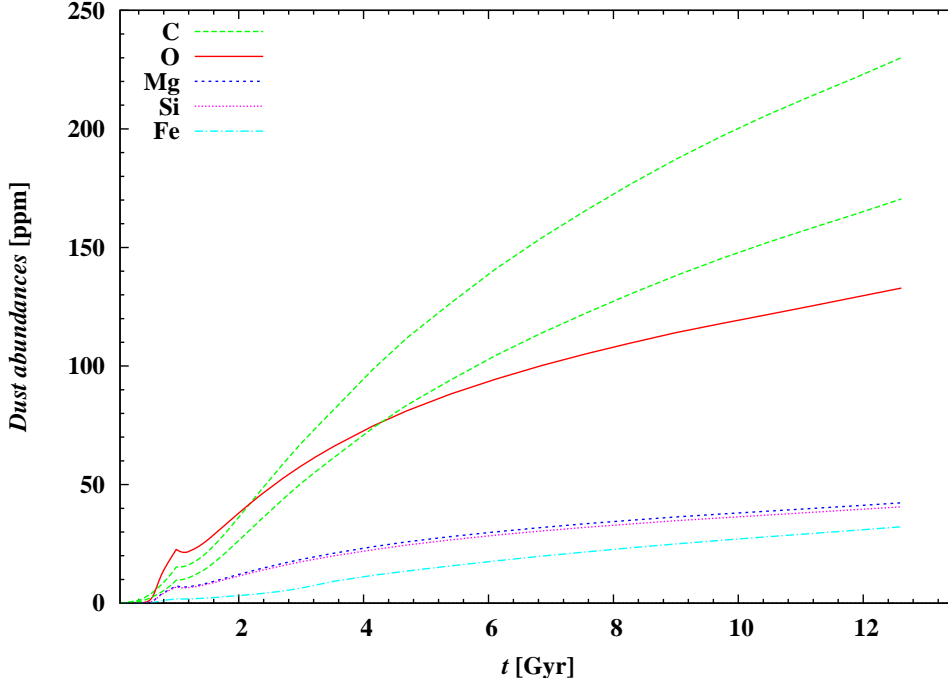
Figure 5.3: Evolution of element abundances in dust per million hydrogen atoms of the main dust-forming elements as predicted by the model calculation. Two lines are shown for carbon. The upper one is for the case that a fraction of $\xi_{CO} = 0.2$ of the carbon is bound in the in-reactive molecule CO, the lower one for the case $\xi_{CO} = 0.4$.

dust-production. In the figure two lines are shown for carbon, corresponding to two different assumed fractions ξ_{CO} of the carbon in molecular clouds tied up in the in-reactive CO molecule. The upper one corresponds to $\xi_{CO} = 0.2$, the lower one to $\xi_{CO} = 0.4$, bracketing typically observed values (e.g. van Dishoek & Blake 1998). A higher value of ξ_{CO} means that less carbon is available for dust formation.

Comparison with existing interstellar dust models

The predicted dust abundances at the present time seems to be consistent with the composition of the local interstellar dust (Kimura et al. 2003b; Frisch 2006; Zubko, Dwek & Arendt 2004). One should make such comparison with caution, since reference abundances (assumed total abundances gas+dust) may differ from those used in the present paper. Frisch (2006) derives the dust composition using the gas-phase abundances from the radiative transfer models of the local interstellar clouds (LIC) that are constrained by observations of ISM both inside and outside of the heliosphere. Our results are quite similar for O, Si, Mg, Fe, except C in carbon dust, which is missing from the LIC, possibly because it does not survive the acceleration mechanism Frisch (2006). At the same time, gas
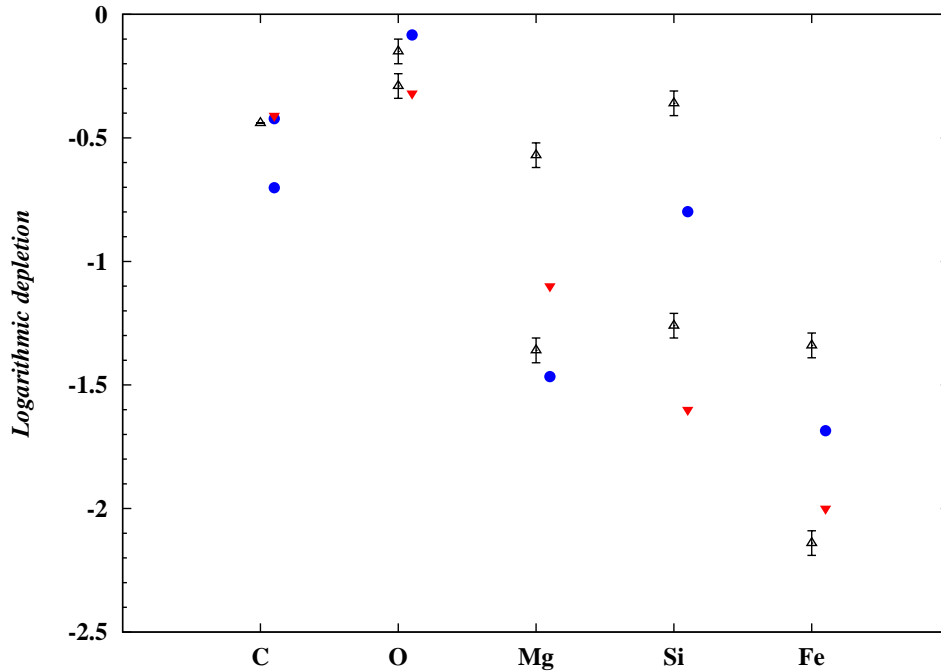
Figure 5.4: Predicted average depletions of main dust-forming elements at the present time are shown with filled circles. Upper and lower points for depletions for carbon calculated with CO mass fraction 0.4 and 0.2 correspondingly. Upper and lower open triangles with error bars represent observed depletions in warm and cold diffuse clouds, respectively, from Welty et al. (1999) for C, Si, Fe and Cartledge et al. (2006) for O and Mg. Filled triangles mark the average depletions in diffuse clouds (see Whittet 2003 and references therein).

absorption measurements in lines of sight through the LIC and in situ dust measurements in Kimura et al. (2003b) indicate the same dust composition of local interstellar clouds as in warm diffuse clouds. In particular our results agree for carbon, iron, and oxygen, and are only about 10 ppm higher for Mg, Si, which is within the accuracy of this kind of models.

The composition of the interstellar dust in the local ISM is also studied in Zubko, Dwek & Arendt (2004) by simultaneous fitting of the interstellar extinction, diffuse IR emission, and abundance constraints. They considered different classes of models composed of silicates, graphite, PAHs, amorphous carbon, and composite particles. The main conclusion was that there is no unique dust model that fits the basic set of observational constraints, since several classes of models give equally good fits. Although a model with composite grains provides a better fit to the extinction and IR emission than a bare-grain model, the probing of interstellar dust models through small angle X-ray scattering favours models with bare silicates and graphite over those with composite particles (Dwek et al. 2004; Smith et al. 2006).

5. RESULTS OF THE DUST EVOLUTION MODEL

Interstellar depletions

The observed gas-phase abundances of elements in diffuse interstellar clouds indicates various degrees of depletions of many of the dust-forming elements relative to their solar abundances. This is explained as resulting from their condensation in interstellar dust. The amount of the dust-forming elements locked up in interstellar dust (shown in Fig. 5.3), however, cannot reliably be derived from observations. The standard procedure is to instead determine gas-phase abundances of the elements and subtract these from some kind of 'standard' cosmic element abundances in order to determine how much of each element is condensed into interstellar dust (cf. Sembach & Savage 1996 for a review). However, to draw conclusions about the dust composition from observed depletion patterns, one needs to make a decision about what set of abundances is used as the reference abundances for the elements. Frequently Solar System abundances, or abundances of nearby F & G stars or of B stars, are adopted (cf. Tables 2.3 and 2.4), resulting in different dust compositions.

A modelling of the chemical evolution of the Galaxy including dust allows study of the evolution of the depletion of the gas abundances by dust condensation and a comparison of the model with presently observed data, since gas and dust abundances are known from calculations. However, a one-phase ISM model reflects properties of the dust averaged over the different ISM phases, so only a qualitative comparison of depletions is possible. One should notice that observed depletions are restricted to diffuse clouds, while molecular clouds are too opaque to be studied in absorption lines.

Our predicted averaged depletions, at the present time and at the solar circle in the ISM, for the 5 main dust-forming elements under consideration (C, O, Mg, Si, and Fe) are shown in Fig. 5.4. For comparison, observed depletions in warm and cold diffuse clouds from Welty et al. (1999) and Cartledge et al. (2006), and average depletions in diffuse clouds (see Whittet 2003) are also shown in the figure. The model calculation reasonably reproduces the observed values, except for a somewhat low calculated degree of depletion of Fe.

The degree of iron depletion cannot be increased by assigning a much longer destruction timescale $\tau_{j,\mathrm{SNR}}$ for iron dust. A model calculation shows that this does not significantly increase the depletion because the lifetime of dust grains is limited in any case by the timescale of dust consumption by star formation, which is about 2.3 Gyr and hence already not really long compared to the lifetime against destruction by shocks. Also a higher than assumed stability of Fe-bearing silicate does not help, since then a higher than observed depletion of Si is to be expected. The main reason for the low degree of depletion in the model seems to be that the fraction of Fe in the gas phase is not completely determined by the destruction of Fe-bearing grains by shocks in the warm phase but to a significant extent also by return of gas-phase Fe by stars, which needs some time until it is cycled into clouds and depleted from the gas phase by dust growth processes. In our model, the degree of depletion of Fe (and this holds in principle for all refractory elements) is limited by the rather long time required for cycling of matter between the ISM matter not in dense clouds and the matter in dense clouds. The
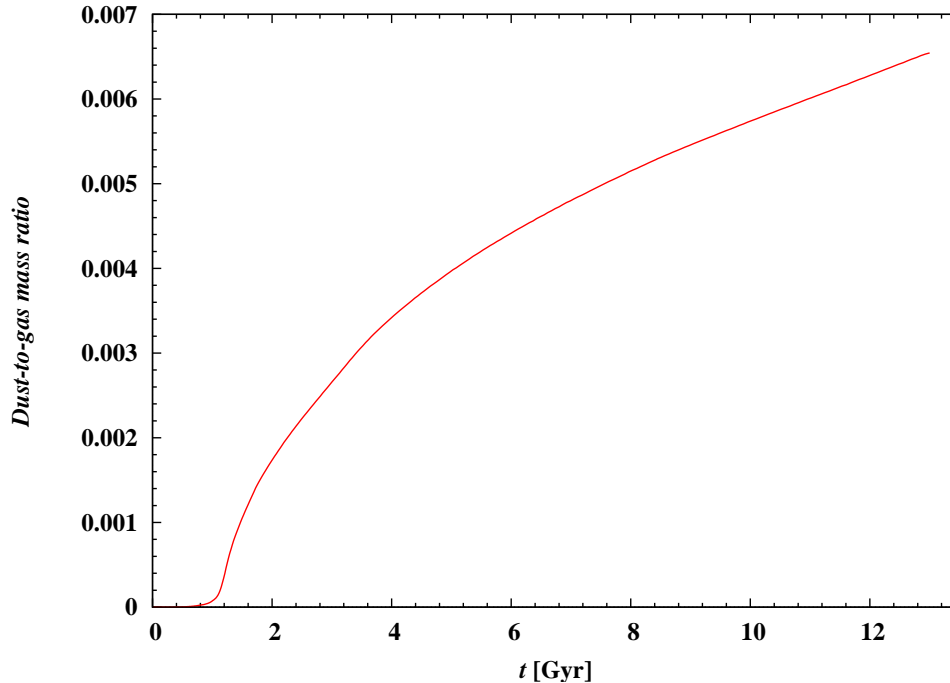
Figure 5.5: Evolution of the dust-to-gas ratio at the solar circle as predicted by the model calculation.

origin of the low degree of depletion of Fe in the model calculation is presently unclear, but probably bears physical significance and may indicate that, for iron, some slow accretion of Fe atoms from the gas phase into dust is also possible in the warm and/or cold phase of the ISM.

5.1.5 Evolution of the dust-to-gas ratio

Figure 5.5 shows the evolution of the dust-to-gas ratio according to the model calculation. The hydrogen gas-to-dust mass ratio is approximately 100 for the diffuse ISM averaged over long lines of sight passing through a number of interstellar clouds (Spitzer 1954). Recent studies of the hydrogen gas-to-dust ratio in the local interstellar cloud (Kimura et al. 2003a) also confirms the canonical value from Spitzer (1954). If one converts this to a ratio of dust mass to total gas mass, one gets a value of 0.007. The value of the dust-to-gas ratio in our model for the present time ISM is close to the average value derived from observations. Our model therefore nicely reproduces the average dust mass fraction of the Milky Way in the solar vicinity.
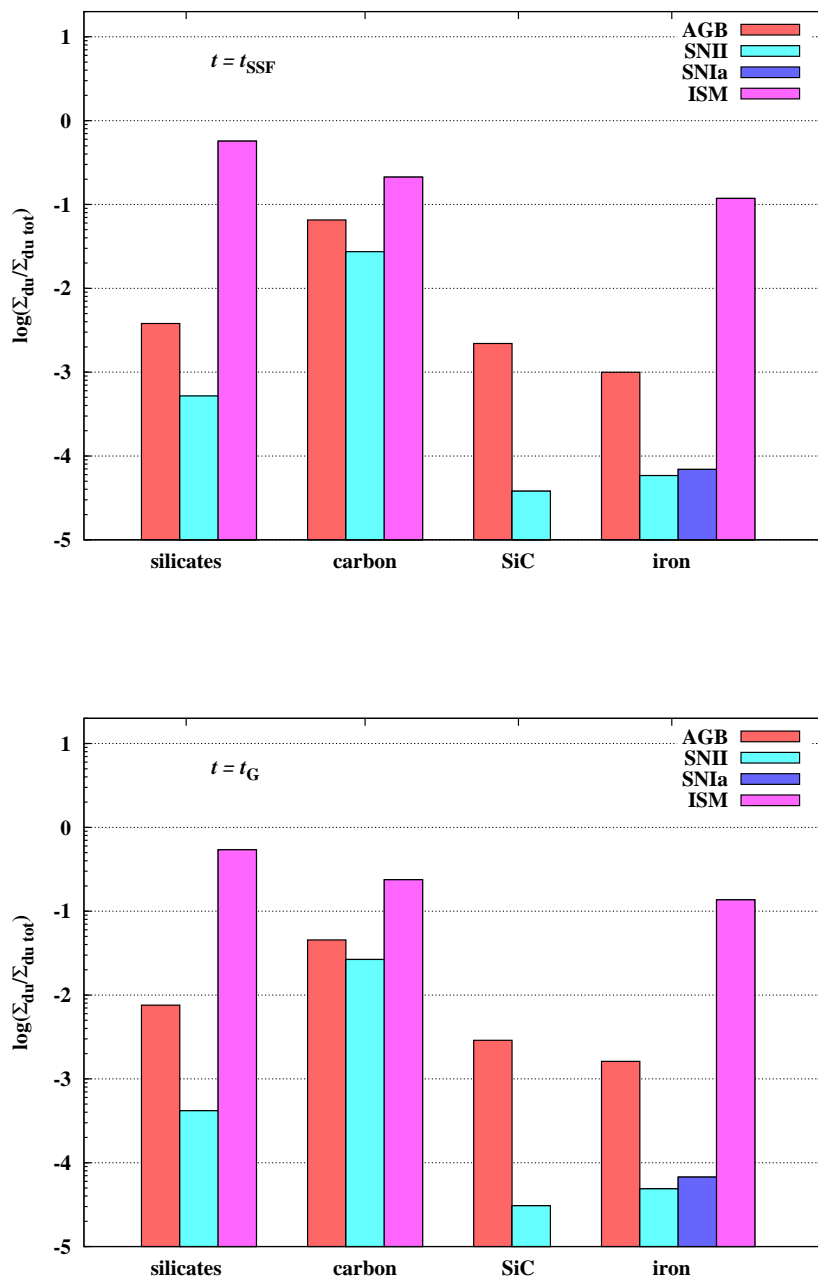
Figure 5.6: Composition of the interstellar mixture of dust species grown in molecular clouds, the MC-grown dust, and dust species from AGB stars and supernovae, the stardust, at the solar circle. *Top:* At the instant of Solar System formation. *Bottom:* For the present solar neighbourhood.

Table 5.2: Surface densities of different dust species at instant of Solar System formation and at the present time as predicted by the model calculation

Dust species	Source	$\Sigma_{j,\mathrm{d}}(t_{\mathrm{SSF}})[\mathrm{M}_\odot \mathrm{pc}^{-2}]$	$\Sigma_{j,\mathrm{d}}(t_{\mathrm{G}})[\mathrm{M}_\odot \mathrm{pc}^{-2}]$
Silicates	AGB	$5.39\cdot10^{-5}$	$1.43\cdot10^{-4}$
	SN II	$2.51\cdot10^{-6}$	$6.10\cdot10^{-6}$
	ISM	$2.76\cdot10^{-2}$	$2.79\cdot10^{-2}$
Carbon	AGB	$7.73\cdot10^{-4}$	$7.04\cdot10^{-4}$
	SN II	$7.86\cdot10^{-5}$	$4.54\cdot10^{-5}$
	ISM	$1.43\cdot10^{-2}$	$1.04\cdot10^{-2}$
Iron	AGB	$1.89\cdot10^{-5}$	$3.11\cdot10^{-5}$
	SN II	$7.72\cdot10^{-7}$	$7.97\cdot10^{-7}$
	SN Ia	$9.83\cdot10^{-7}$	$1.15\cdot10^{-6}$
	ISM	$5.31\cdot10^{-3}$	$6.76\cdot10^{-3}$
SiC	AGB	$3.80\cdot10^{-5}$	$5.23\cdot10^{-5}$
	SN II	$8.21\cdot10^{-7}$	$4.95\cdot10^{-7}$

5.1.6 Dust input into the Solar System

Figure 5.6 shows the composition of the interstellar dust mixture at the instant of Solar System formation and the present-day composition. Numerical values are given in Table 5.2. Both mixtures are not significantly different since the abundances of refractory elements in the ISM have changed only slightly over the past 4.56 Gyr (cf. Fig. 2.6). This dust mixture is clearly dominated by MC-grown dust and contains only a small fraction of stardust. The stardust is dominated by dust grains from AGB stars, meaning dust grains with SN origin form only a minor component.

The dust mixture at time of Solar System formation is the one from which the solid bodies in our planetary system formed. Relics of this dust mixture can be found in the Solar System in two types of objects: matrix material of primitive meteorites and in comets. However, until Solar System bodies formed from the dust component of the matter collapsed from some part of the parent molecular cloud into the protoplanetary accretion disk, the material underwent a number of alteration processes. Even the most primitive material in Solar System bodies is not simply unmodified ISM matter. For this reason meteoritic matrix material is presently not suited to a comparison with the model results, since the alteration processes on the parent bodies are presently not completely understood (cf. McSween et al. 2002). Material from comets is probably more suited; and once more detailed results from the STARDUST mission are available, it may be possible to compare the model predictions for the ISM dust composition entering the protoplanetary accretion disk of the Solar System with observations. Presently most of the analysed particles returned by the STARDUST mission are claimed to be

material from the solar system (Zolensky et al. 2006; McKeegan et al. 2006).

Today one can only state that the dust mixture inherited by the Solar System from its parent molecular cloud and the current ISM dust mixture in the solar neighbourhood predicted by our model calculation are roughly in accord with the dust composition estimated by Pollack et al. (1994) from observations of the extinction properties of the dust material and considerations of element abundances, which is presently held to be the best estimate of the composition of the dust material from which the Solar System formed.

5.2   Dust evolution in the Milky Way disk

As a first application of our model of the dust evolution developed in Sect. 4 we study the evolution of MC-grown dust and dust of stellar origin in the Milky Way disk.

The most important feature of the galactic evolution for the interstellar dust is the different pace of the star formation, which determines the dust destruction rate in the ISM by SNe on one hand, and the dust injection rates by stars on the other hand. In the inner regions of the disk, the elements locked in dust are returned to the ISM faster than those in the outer region due to shorter destruction timescales as illustrated by Fig. 4.3. The whole cycle of elements between dust and gas phase operates on much shorter timescales in the inner galaxy. For the inside-out scenario of the disk formation adopted here, the chemical evolution in the inner regions occurs on much shorter timescales than in the outer disk (Sect. 2.3). In fact, the enrichment of outer regions by heavy elements is delayed due to the star formation threshold of about 7 $M_\odot$ pc^{-2}, below which the star formation proceeds in the suppressed regime (Sect. 2.3.2). For example, the density of the present day Galactic disk drops below the threshold value at $r > 11$ kpc. One consequence of the galactic chemical evolution, crucial for the interstellar dust composition, is the existence of radial metallicity gradients. The dust production by stars and MCs depends on metallicity in different ways, resulting in variations of the dust mixture in the disk during Galactic evolution.

As shown for the Solar neighborhood, the most efficient dust production takes place in dense molecular clouds. The observations show that the molecular hydrogen in the Galactic disk presently has an inhomogeneous distribution characterised by the ring of molecular gas at about 3 kpc$< r <$ 7 kpc with an H$_2$ fraction of about 0.6 (from Dame 1993), presented in Fig. 2.11. We adopt this distribution of molecular hydrogen in the disk for the fraction of molecular clouds $X_{cl}(r)$ needed for the dust production rate by MCs, $G_{j,d}$ in Eq. (4.32). The calculations of dust evolution are performed for the Galactocentric radii from 2 to 16 kpc with 1 kpc steps.

In the following we will present the results of our model calculations of the evolution of MC-grown dust and stardust in the Galactic disk.
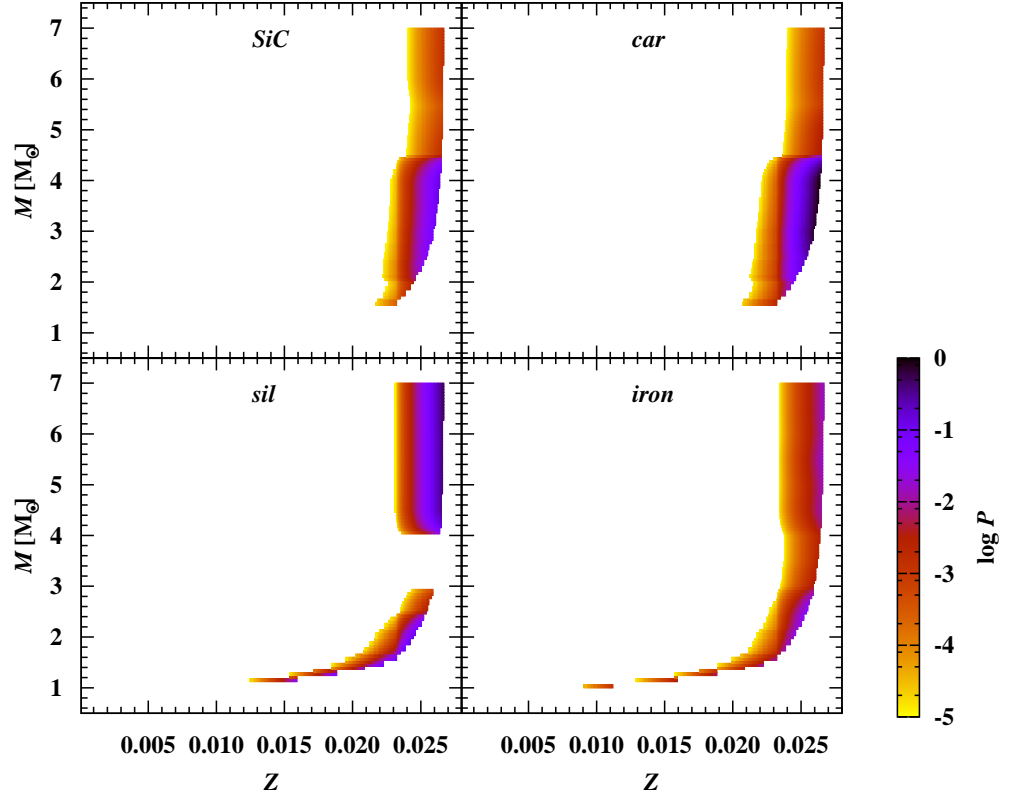
Figure 5.7: Probability density of contribution from AGB stars in dependence on initial stellar mass and metallicity to the present AGB stardust population at $r = 4$ kpc for carbon, iron, SiC and silicate dust. The present day metallicity of the ISM Z_{ISM} is 0.0268.

5.2.1 Contribution of AGB stars to the present day stardust population in Milky Way

As discussed in Sect. 3.2, the composition of dust from AGB stars strongly depends on the initial stellar metallicity. In the following we analyse the contribution of AGB stars in dependence on their mass and metallicity in terms of the probability density introduced in Sect. 4.2. For the analysis of stardust grains in the Galactic disk characterised by the strong metallicity gradient it is more useful to express the probability density in Eq. (4.14) as a function of the initial metallicity of a star $Z_{ISM}(t_b)$, since an instant of death t_d and birth of a star t_b are related through Eq. (4.11).

Results of numerical calculations of the probability density at the present time $t = 13$ Gyr are shown in Fig. 5.7, Fig. 5.8 and Fig. 5.9 for $r = 4$, 8.5 and 14 kpc, respectively. The results are obtained for carbon, silicate, SiC and iron dust using AGB dust production yields from the tables in
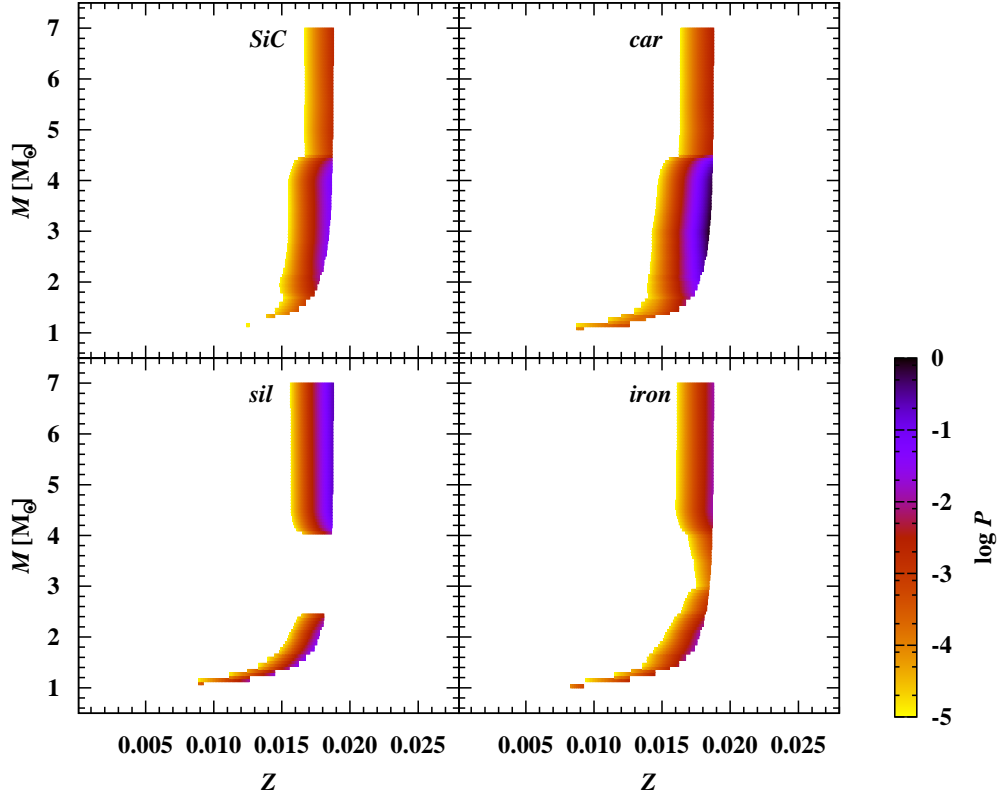
Figure 5.8: The same as in Fig. 5.7 for $r = 8.5$ kpc. The present day metallicities of the ISM is 0.0188.

Appendix A.

The right edge of the diagrams in all figures represents the initial mass and metallicity of stars which die and eject their dust at the present time. The probability density is highest for these stars, because dust from them has not yet undergone destruction processes in the ISM. The shape of the edge is completely determined by the stellar lifetimes $\tau(M, Z)$; the more massive a star, the closer is its metallicity to the present day ISM metallicity because of the shorter lifetimes. Therefore the probability density has an almost vertical right edge in the range of the most massive stars, which approaches to the values of the present day ISM metallicity at each disk radius, $Z = 0.027$, 0.0188 and 0.011 for $r = 4$, 8.5 and 14 kpc, respectively. The lifetimes of these stars are so short in comparison to the timescale of galactic chemical evolution, that the ISM metallicity does not noticeably change during their lifetimes. The tails in the bottom left parts of the diagrams represent the dust input from long living low mass stars formed when the metallicity of the ISM was significantly lower.
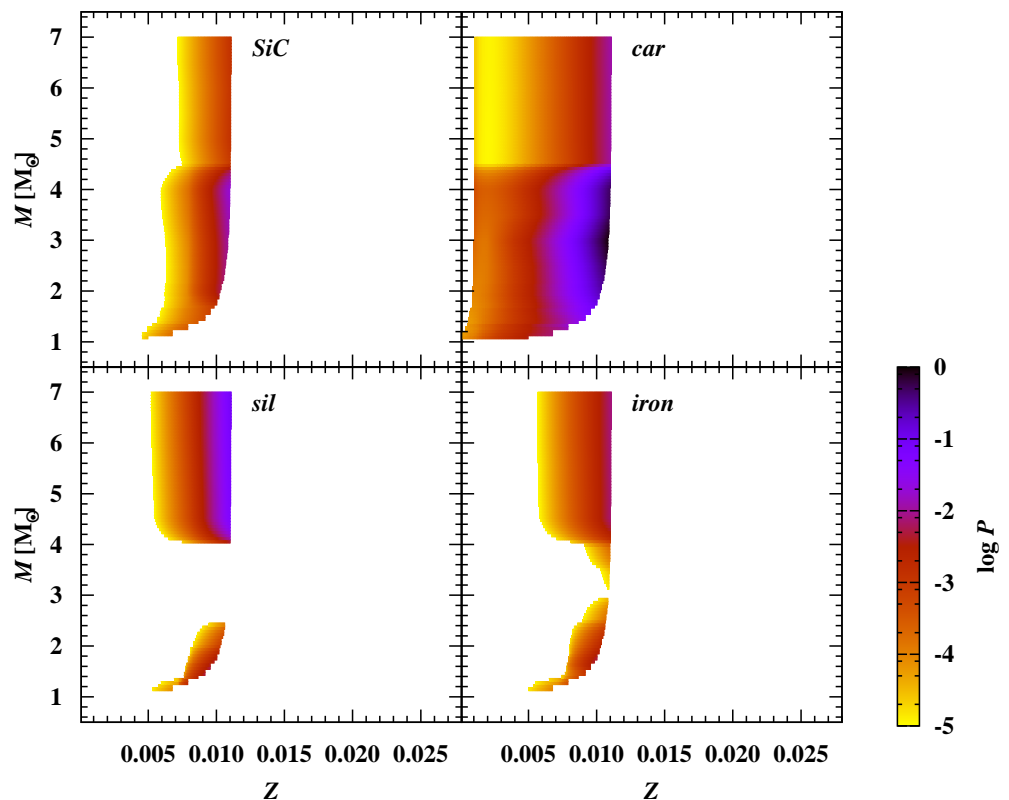
Figure 5.9: The same as in Fig. 5.7 for $r = 14$ kpc. The present day metallicities of the ISM is 0.011.

Although there are two subpopulations of silicate grains from low and intermediate mass stars, the present day AGB silicates are dominated by the grains from massive AGB stars with narrow range of initial metallicities as seen in Fig. 5.7. The gaps between two subpopulations in the probability density distributions appear due to peculiarities of stellar evolution along the AGB explained in Sect. 3.2. Different widths of the diagrams in Fig. 5.7 - 5.9 stem from different dust destruction timescales along the Galactic disk shown in Fig. 4.3. Only dust grains ejected into the ISM within the destruction timescale $\tau_{\text{destr}}(r, t_G)$ from now survive the destruction processes. The corresponding range of birth times and initial metallicities of stars that contribute to the present stardust population is determined by Eq. 4.11. The narrow diagrams for $r = 4$ kpc indicate very efficient dust destruction in the inner Galaxy removing grains ejected in earlier times. The diagrams for the Solar neighbourhood do not much differ from results for $r = 4$ kpc, since the destruction timescales do not vary much in the range of radii $r = 4 - 8.5$ kpc as seen in Fig. 4.3; additionally, this effect is obscured by the less efficient
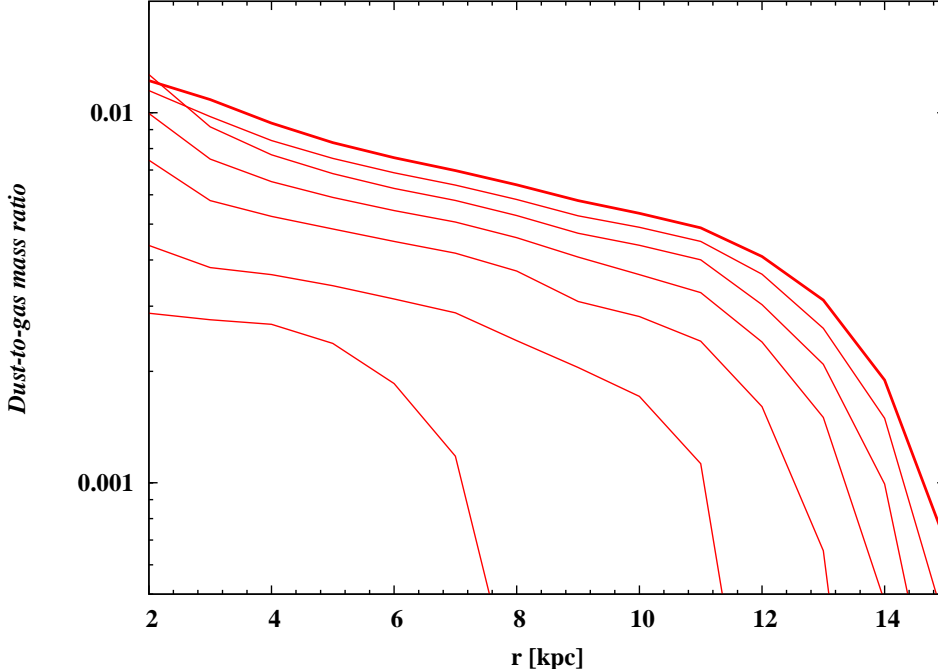
Figure 5.10: Dust-to-gas ratio in the Galactic disk at instants from 1 Gyr to 13 Gyr with 2 Gyr steps (from bottom to top).

dust production at lower metallicity for $r = r_\odot$. In contrast, dust injected at earlier times in the outer disk survives much longer as depicted by broad bands with probability density $P < 0.001$. Therefore, in the outer disk stars from a larger number of generations can contribute to the stardust mixture as illustrated Fig. 5.9. For example, the metallicity of stars contributing to the carbon dust grains at $r = 14$ kpc varies within an order of magnitude.

Composition of dust from AGB stars

The composition of AGB dust changes greatly in the disk from the silicate dominated dust mixture in the inner Galaxy to the carbon dust in the outskirts. At $r = 4$ kpc massive AGB stars formed at supersolar metallicities produce large amounts of silicates, approximately equal to the amounts of carbon dust contributed by stars with $M < 4.2$ M$_\odot$. As discussed in Sect. 3.2 low mass AGB stars of supersolar metallicity also become efficient silicate factories, but due to long lifetimes the stars dieing at the present time were formed at subsolar metallicities, so they produce more carbon dust. Iron is a minor dust component for most of the radii, since its production similarly to the silicates requires supersolar metallicities observed only in the inner Galaxy; in the outer regions it has a negligible contribution to the total stardust mixture of only $10^{-5} - 10^{-4}$. Carbon dust is the dominant dust
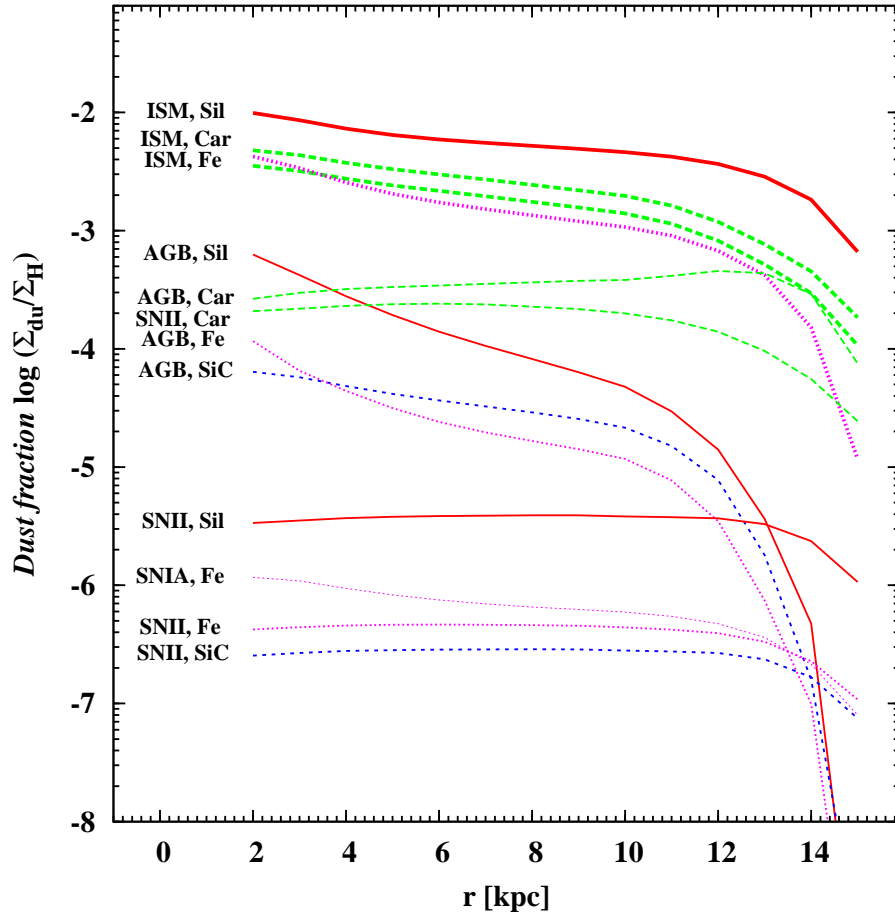
Figure 5.11: Radial profile of the dust mass fraction in the interstellar medium of the main interstellar dust components and of the stardust species in the Galactic disk at present time. All dust species show a radial gradient due to the metallicity dependence of the dust formation process. This effect is most significant for the AGB dust production as explained in Sect. 5.2.3. For carbon dust two results are shown, corresponding to an assumed fraction of 0.2 and 0.4 of the carbon in molecular clouds locked in the CO molecule.

species from AGB stars for $r > 4$ kpc. It is the first dust species injected into the ISM by AGB stars at low metallicities as illustrated in Figure 5.9 showing the first carbon grains from stars with $Z \sim 0.001$ and SiC dust from stars with $Z = 0.005$ for the same minimum probability density of 10^{-5}.

5.2.2 Radial profile of dust-to-gas ratio

Figure 5.10 demonstrates the variation of the dust-to-gas mass ratio in the Galactic disk at instants from 1 to 13 Gyr. Radial profiles of the dust-to-gas ratio for different instants have similar shapes characterised by a flat region ending with a steep decrease that shifts outwards with time. Efficient production of a certain kind of dust by molecular clouds starts when the metallicity exceeds the critical value given in Table 4.1, as can be also seen from Fig. 4.4b. The steep slope marks the region where the metallicity is not high enough for efficient dust production by MCs and the dust content is determined by the stardust. Due to this effect the inner region of the disk reaches a dust-to-gas ratio of 1/20 of the present value in the Solar vicinity within 1 Gyr of evolution, while the outer regions remain dust-free until the metallicity increases to a value enabling dust growth in MCs. The enhancement in the dust-to-gas ratio in the inner disk in Fig. 5.10 is due to the rapid consumption of gas by high star formation rate.

The radial gradient in the dust-to-gas ratio predicted by the model -0.044 ± 0.001 in the Galactocentric distance range 2 - 12 kpc is equivalent with the radial abundance gradients given in Table 2.5. Our result is in a good agreement with the value of $-0.05 \pm 0.03 \, \mathrm{dex \, kpc}^{-1}$ derived from the three-dimensional decomposition of the infrared emission from dust in the Milky Way (Sodroski et al. 1997).

5.2.3 Present day distribution of dust species in the disk

Figure 5.11 shows the radial profiles of densities of MC-grown and stardust grains relative to hydrogen at the present time. One of the main features of the figure are the significant radial gradients in the density profiles of MC-grown dust and AGB stardust, and the almost flat profiles for the SN dust species. This behavior is explained by the following:

1. The present day distribution of AGB stardust in the disk is characterised by a gradual increase of carbon abundance and a rapid decline of the silicate, SiC and iron abundances with the disk radius. These drastic changes in the dust composition originate from the strong dependence of AGB dust production on the metallicity, that varies greatly in the disk due to the Galactic metallicity gradient as seen in Fig. 2.15. In addition to the Z-dependence of AGB dust production, the difference in dust mixture along the Galactic radius is enhanced by the different lifetimes and, correspondingly, initial metallicities of stars ejecting carbon and silicate dust. As discussed in Sect. 4.2, carbon dust production is dominated by the long living low mass AGB stars with
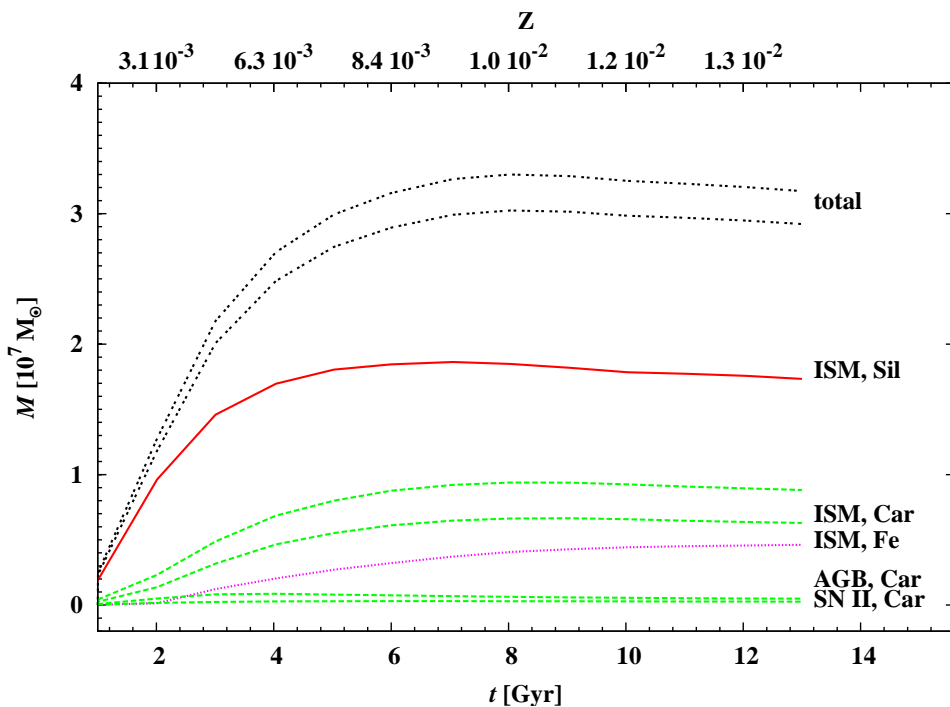
Figure 5.12: Evolution of the total mass of the main dust species integrated over the Galactic disk with time. The upper axis shows the average metallicity of the ISM to indicate the galactic timescale of enrichment with heavy elements. Only the dominating dust species are included constituting > 98% of the total dust: MC-grown silicate, carbon and iron and carbon from SN II and AGB star. For carbon dust two results are shown corresponding to an assumed fraction ξ_{CO} of 0.2 and 0.4 of the carbon in molecular clouds locked in the CO molecule.

$M < 4$ M$_\odot$ formed when the ISM metallicity had lower than the present value. The majority of silicates, in contrast, come from the massive supersolar AGB stars with short lifetimes, thus the dust mixture from these stars is determined by the present high ISM metallicity.

Another factor, influencing the composition of the present day stardust mixture are different destruction rates along disk radius. In the outer Galaxy the destruction timescales are several Gyrs in contrast with 0.6 Gyr at the Solar neighborhood, therefore carbon stardust is accumulated over this time from different stellar generations in the outer Galaxy, while newly ejected silicates are efficiently destroyed in the inner regions.

Condensation of iron dust in stellar winds also requires high initial metallicities, so the conclusions made for the silicates are valid also for iron. At subsolar metallicities in most parts of the disk AGB stars produce only small amount of silicates and iron, that results in the steep decrease of their density profiles seen in Fig. 5.11 at large radii. Like carbon dust, SiC is condensed in the carbon-rich stellar winds. However, in contrast to carbon efficient condensation

of SiC requires abundant Si atoms, therefore it starts at higher metallicities than that of carbon, as seen in Fig. 5.9. At low metallicities in the outer disk SiC abundance rapidly decreasing similarly to silicates and iron.

The contribution of AGB stars to the total dust content also changes along the galactic radius. While in the inner disk AGB stars produce only a minor fraction of the total dust mass, in the outer regions of the disk for $r > 13$ kpc they become exclusively carbon dust factories with production rates comparable to the contribution of carbon dust from MCs.

2. The massive stars exploding as SNe have lifetimes ≤ 40 Myr and therefore their initial metallicity represents the current metallicity of the ISM. Since in the present work we assume that a fixed fraction of refractory material from SNe is condensed in dust, the SN dust profiles follow the radial distribution of dust forming elements produced in SNe. The supernova nucleosynthesis yields generally show very weak dependence on the initial stellar metallicity, because most of the heavy elements are synthesised from H and He in the SN itself, as can be seen in Fig. 2.1. Therefore the distribution of SN dust shows almost no radial dependence in the disk for all dust species, except in the outer disk where the gas density drops bellow the threshold for star formation.

3. The present distribution of MC-grown dust is determined by the present metallicity of the ISM, since the timescales for dust growth in molecular clouds are short in comparison with galactic evolution as soon as the ISM metallicity exceeds the critical values for dust growth (Fig. 4.4b). The minimum required metallicity for dust growth in clouds has the lowest value for silicates, and the highest for iron dust. Therefore, iron dust production is delayed until the ISM is enriched with Fe by SN Ia. Due to this effect iron dust has the steepest decrease in the outer disk with $Z < 0.015$.

As soon as the process of dust production by MCs is established, the composition of interstellar dust, the carbon-to-silicates ratio in particular, does not considerably change during evolution. This has an important consequence for the outer disk: since the chemical evolution proceeds more slowly in this region, the dust content is dominated by the stardust untill the on-set of dust production by MCs.

5.2.4   Global dust properties in the Milky Way

Figure 5.12 presents the evolution of the total dust masses integrated over the disk with time and the average ISM metallicity. Only the dominant species are presented: the MC-grown silicate, carbon, and iron dust, and the carbon from AGB stars and SN II. The mass ratio of the remaining stardust species to the total dust mass constitutes only 0.1% at 1 Gyr of evolution, raising to 10^{-2} at the
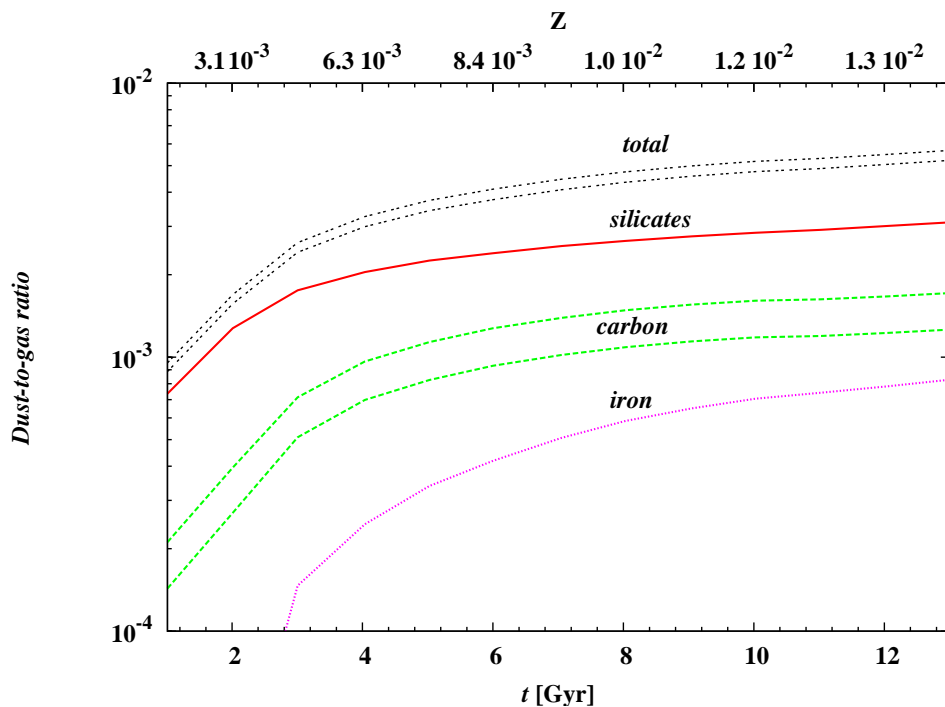
Figure 5.13: Evolution of the dust-to-gas mass ratio integrated over the Galactic disk for total (stars + MC-grown) carbon, iron and silicate dust with time. The upper axis shows the average metallicity of the ISM to indicate the galactic timescale of enrichment with heavy elements. For carbon dust two results are shown corresponding to an assumed fraction ξ_{CO} of 0.2 and 0.4 of the carbon in molecular clouds locked in the CO molecule.

present time. The dust content of the Galaxy is mostly determined by the efficient dust condensation in MCs. Although the carbon dust from SNe and AGB stars dominates locally in outer regions with low metallicities as discussed in previous Section, the overall fraction of this kind of dust is relatively small and globally the interstellar dust remains MC-grown silicates throughout the Galactic evolution, as seen in Fig. 5.12. Iron dust production in the Galaxy is delayed for ~ 1 Gyr relatively to the silicates and carbon due to the longest growth time scales. Also, Figure 5.12 demonstrates that the Galactic ISM is rapidly enriched to the metallicity of 3.1×10^{-3} or $\sim 1/5 \, Z_\odot$. As soon as the molecular clouds start efficient dust production of certain species, its abundance is determined by the quasi-equilibrium between growth and destruction processes and does not notably change in later time. Such equilibrium between dust destruction and formation processes was already noted in Dwek (1998). Since the silicates have the lowest minimal metallicity for the efficient dust condensation in clouds, their mass become approximately constant first. The growth timescale is the longest for the iron dust, therefore the iron dust mass in the Galaxy continues to grow slowly until 10 Gyr.

The evolution of the total dust-to-gas ratio in the Galactic disk is shown in Fig. 5.13 for carbon,

iron and silicate dust. After a steep increase at the early time, the dust-to-gas ratio shows slowly increasing trend with time. Since the dust masses presented in Fig. 5.12 remains approximately constant, this trend results from the gradual consumption of interstellar gas by the star formation. The present day total gas-to-dust ratio of 180 for the Milky Way model is in agreement with the observed value of 190 ± 20 derived for the range of Galactocentric distances 8.5-16 kpc, that consists 80% of the Galactic H I mass (Sodroski et al. 1997). Our result for the Milky Way is very similar to the mean gas-to-dust mass ratio for 14 local spiral galaxies 120 ± 60 (Stevens et al. 2005).

6

Conclusions

In the present work we have developed a model of interstellar dust that, for the first time, follows the complete life-cycle of dust of different origins in the interstellar medium of the Milky Way. It includes also a complete chemical evolution model of the Milky Way disk providing the basis for the dust evolution model.

We construct an open model of the chemical evolution of the Milky Way in which the Galactic disk is gradually built-up by infalling matter from the halo or intergalactic space. The reliability of the model is checked by reproducing the standard set of the observational constraints for the chemical evolution of the Galaxy. We employ the new recently available tables of Nomoto et al. (2006) for the heavy element production by massive stars. With our chemical evolution model it is shown that these data provide a better agreement between the calculated element abundance ratios of the main dust-forming elements (O, Mg, Si, Fe) and observed stellar abundances of main sequence G stars representing the ISM composition than old widely used tables of Woosley & Weaver (1995). In particular the problem with the low Mg abundances with old tables disappears when we employ the new results of Nomoto et al. (2006). A good reproduction of the abundance variations of the dust-forming elements is important if one tries to model the interstellar dust mixture.

Our model for the evolution of the interstellar dust is based on three new elements:

(1) For the dust input to the ISM by low and intermediate mass stars, we extend the results of model calculations of Ferrarotti & Gail (2006), which combine synthetic AGB evolution models with models for circumstellar dust shells that include dust formation in the stellar wind. In the present work we perform additional model calculations to provide a finer mass-metallicity grid and the more detailed information on dust mixture produced by AGB stars in the tables of Ferrarotti & Gail (2006). We also continue the work towards extending these tables to include Magnesium Sulphide, an abundant dust species formed in stellar winds of AGB stars. We study the formation of MgS in outflows from carbon stars and could clarify for the first time the formation condition for this dust species. It is shown that

it forms as a mantle on the surface of SiC grains, which explains its high observed abundance. The new tables allows us to describe consistently for the first time the dependence of dust production by AGB stars on initial stellar masses and metallicities.

(2) The dust production by supernovae (SNe) is described in terms of condensation efficiencies as suggested in Dwek (1998). Over the years, the efforts of the meteoritic science community on studying nucleosynthetic processes in stars by analysing isotopic abundances in presolar dust grains has accumulated a wealth of data. This work provides the abundance ratios of presolar dust grains from SNe and from AGB stars. This allowed us to make the first quantitative estimates of the efficiency of dust production by all SNe by fitting calculated abundance ratios of stardust from AGB stars and SNe in the Solar System to that measured in laboratory in presolar dust grains from meteorites. Applying these estimated efficiencies yields the unexpected result that dust production by massive stars is not important for the evolution of the ISM dust. This may be different at the very beginning of galaxy formation: due to short lifetimes the SNe inject the first grains into the ISM, which provide the surfaces for the condensation of refractory material in molecular clouds at higher metallicities. Accordingly to our estimates SNe produce mainly carbon dust, and not the silicates, in contrary to what was commonly believed. There is only a few observational studies of dust condensation in SNe available, which also indicate very low condensation efficiency in SNe.

(3) We developed for the first time a simple approach to include dust growth in molecular clouds in a model of the evolution of the interstellar dust, which accounts for the multiphase structure of the ISM in an approximate way. Some quantities in the dust growth model, such as the mass fraction of ISM in clouds and lifetime of molecular clouds, still have to be taken from observations, and we only have data for these quantities for the present day Milky Way. This allows us to construct a model for the life cycle of dust in the Milky Way except for its very beginning. Since, however, the distribution of the ISM over the phases is neither temporally nor specially constant, the phase structure in a realistic modelling should be part of the model calculations to be done in future. The results obtained with our dust model are in reasonable accord with observations of interstellar dust: the depletions of refractory elements, present dust abundances and composition, and dust-to-gas ratio averaged over the ISM phases.

With our multicomponent dust model it was for the first time possible to show that dust grown in molecular clouds dominates the interstellar dust population in the Milky Way. The stardust constitutes only a small fraction of the total dust mass. For the Solar neighborhood, the MC-grown dust becomes responsible for most of the dust content already during the first Gyr of evolution, after the ISM metallicity exceeds a minimal value for efficient dust condensation. This has an important consequence for the laboratory studies of presolar dust grains in meteorites and stardust from comets: the majority of dust that formed the Solar System is grown in molecular clouds and therefore does not show any conspicuous isotopic anomalies.

Our model calculations of dust evolution in the Milky Way disk predict strong variations in the dust composition along the Galactic radius. The results are most remarkable for the AGB dust: the dust mixture changes from silicate-dominated in the inner disk to pure carbon dust in the outer regions of the disk. Moreover, carbon dust production by stars becomes comparable with dust condensation in clouds in the outer disk. However, we show that the total dust content in the Milky Way is dominated by carbonaceous dust and silicates grown in molecular clouds across the Galactic history.

For modelling galactic chemical evolution with dust, we have developed a flexible code, which is easily adjustable for other galaxies, spirals, dwarfs, young star bursts as checked by our preliminary tests. It allows the study of the evolution of dust from different sources – SNe, AGB stars and molecular clouds – and therefore can be very useful for modelling of objects where some of these sources are expected to dominate. For dust growth modelling it requires the observed fraction of molecular clouds and estimates of an average cloud lifetime, which can be different from the Milky Way in the other galaxies. By utilizing the subroutines for the stellar evolution from Hurley (2000) we developed a convenient tool for studying the input from stars into the dust content of the ISM.

6.1 Future prospects

Calculation of SEDs from galaxies

The calculations of synthetic spectra enable a direct comparison of model predictions with observed spectra. Our model of dust evolution predicts that, at low metallicities until the on-set of dust condensation in clouds, the interstellar dust content is very low and determined by carbon dust of stellar origin. It changes to silicates as soon as the metallicity is sufficiently high to enable dust growth in MCs. This change in interstellar dust composition can be checked by comparison with observed SEDs of galaxies of different metallicities. We have performed the first step for the galactic spectral synthesis, the calculation of the stellar radiation field in the galactic disk heating the grains. The next step is to solve the radiative transfer problem in the Galactic disk, and this should be an immediate aim.

Modelling of Blue Compact Dwarf galaxies

An interesting application of the multicomponent dust model developed here is the modelling of dust evolution in Blue Compact Dwarf (BCD) galaxies that undergo a starburst event. These objects are extremely deficient in heavy elements. As was shown by our dust evolution modelling, for low metallicities the first dust in the ISM is carbon dust from SNe and AGB stars. The growth of dust in molecular clouds starts when the metallicity approaches the critical value, which is comparable to the typical metallicity in BCDs of $1/3$ $Z_\odot$ (Loose & Thuan 1986). This makes BCDs ideal local

laboratories for studying the first sources of dust in the ISM. Observations indicate that in spite of the low metallicity, even the most metal deficient BCD galaxy known object IZw 18, suffers from dust extinction (cf. Hunt et al. 2003). The active star formation in BCDs followed by the destructive SN explosions allows the study of the dust evolution in the ISM. BCDs show strong variations in dust-to-gas ratios, which are attributed to the variation of dust destruction efficiency or/and mass-loss (e.g., Hirashita, Tajiri & Kamaya 2002). Our model will allow us to verify whether dust injection from SNe and AGB stars alone, with subsequent efficient destruction, is sufficient to describe the amplitude and variations in dust-to-gas ratios of BCDs. An understanding of the sources of dust at low metallicities is particularly important in studies of the distant Universe and the question of the origin of copious amounts of dust in high-redshift galaxies, which remains one of the most puzzling problems yet to solve.

Acknowledgements

Bibliography

Allende Prieto, C., Lambert, D. L., & Asplund, M. 2001, ApJ, 556, L63

Allende Prieto, C., Lambert, D. L., & Asplund, M. 2002, ApJ, 573, L137

Amari, S., Lewis, R. S., & Anders, E. 1994, Geochim. Cosmochim. Acta, 58, 459

Amari, S., Lewis, R. S., & Anders, E. 1995, Geochim. Cosmochim. Acta, 59, 1411

Amari, S., Zinner E., & Anders, E. 1995b, ApJ, 447, L147.

Anders, E., & Grevesse, N. 1989, Geochim. Cosmochim. Acta, 53, 197

Asplund, M., Grevesse, N., & Sauval, A. J. 2005, in Cosmic Abundances as Records of Stellar Evolution and Nucleosynthesis, ASP Conference Series, Vol. 336, ed. T. G. Barnes III, F. N. Bash. (San Francisco: Astronomical Society of the Pacific), p.25

Akerman, C. J., Carigi, L., Nissen, P. E., Pettini, M., & Asplund, M. 2004 A&A, 414, 931

Alibes, A., Labay, J., & Canal, R. 2001, A&A, 370, 1103, 1121

Alongi, M., Bertelli, G., Bressan, A., Chiosi, C., Fagotto, F., Greggio, L., & Nasi, E. 1993, A&AS, 97, 851

Andrievsky, S. M., Kovtyukh, V. V., Luck, R. E., et al. 2002, A&A, 381, 32

Asplund, M., Nordlund, Å., Trampedach, R., Allende Prieto, C., & Stein, R. F. 2000, A&A, 359, 729

Avilez, M. & Breitschwerdt, D. 2005, A&A, 436, 585

Basu, S., Chaplin, W. J., Elsworth, Y., New, R., Serenelli, A. M., & Verner, G. V. 2007, ApJ, 655, 660

Bensby, T., Feltzing, S., Lundström, I., & Ilyin, I. 2005, A&A, 433, 185

Bensby, T., & Feltzing, S. 2006, MNRAS, 367, 1181

Berczik, P., Hensler, G., Theis, C., & Spurzem, R. 2003, Ap&SS, 284, 865

BIBLIOGRAPHY

Bernatowicz, T. J., & Zinner, E. 1997, Astrophysical Implications of the Laboratory Study of Presolar Materials (Woodbury: American Institute of Physics)

Bianchi, S., & Schneider, R. 2007, MNRAS, 378, 973

Blitz, L., Fukui, Y., Kawamura, A., Leroy, A., Mizuno, N., & Rosolowsky, E. 2007, in Prostars and Planets V, ed. B. Reipurth, D. Jewitt, & K. Keil. (Tucson: University of Arizon Press), p. 81

Bohren, C. F., & Huffman, D. R. 1983, Absorption and Scattering of Light by Small Particles. (New York: Wiley & Sons)

Boissier, S., & Prantzos, N. 1999, MNRAS, 307, 857

Boissier, S., Gil de Paz, A., Boselli, A. et al. 2007, ApJS, 173, 524

Borkowski, K. J., Williams, B. J., Reynolds, S. P. and 9 coauthors 2006, ApJ, 642, L141

Bowen, G. H. 1988, ApJ, 329, 299

Braun, R., & Thilker, D. A., 2004, A&A, 417, 421

Begemann, B., Dorschner, J., Henning, T., Mutschke, H., & Thamm, E. 1994, ApJ, 423, L71

Bertelli, G., Bressan, A., Chiosi, C., Fagotto, F., & Nasi, E. 1993, A&AS, 106, 275

Bradley, J. 2003, in Astromineralogy, ed. Th. Henning. Lecture Notes in Physics, 609 , 609, 217

Bressan, A., Fagotto, F., Bertelli, G., & Chiosi, C. 1993, A&AS, 100, 647

Bruzual, G. & Charlot, S. 2003, MNRAS344, 1000

Buser, R., Rong, J., & Karaali, S. 1999, A&A, 348, 98

Cabrera-Lavers, A., Garzon, F., & Hammesley, P.L. 2005, A&A, 433, 173

Caffau, E., Bonifacio, P., Faraggiana, R., Francois, P., Gratton, R. G., & Barbieri, M. 2005, A&A, 441, 533

Cartledge, I. B., Lauroesch, J. T., Meyer, D. M., & Sofia, U. J. 2006, ApJ, 641, 327

Cappellaro, E. & Turatto, M. 1996, in Thermonuclaer Supernovae, ed. P. Luiz-Lapuente, Kluwer Academic Publishers, 74

Cayrel, R., Depagne, E., Spite, M. et al. 2004, A&A, 416, 117

Cescutti, G., Matteucci, F., Frančois, P., & Chiappini, C. 2007, A&A, 462, 943

Chang, R., et al. 1999, A&A, 350, 38

Charbonnel, C., Meynet, G., Maeder, A., Schaller, G., & Schaerer, D. 1993, A&AS, 101, 415

M. W. Chase: NIST-JANAF Thermochemical Tables. 4th edn. Journal of Physical and Chemical

Reference Data, Monograph No. 9 (1998)

Chen, Y. Q., Nissen P. E., Zhao, G., Zhang, H. W., & Benoni, T. 2000, A&AS, 141, 491

Chen, L., Hou, J. L., & Wang, J. J. 2003, ApJ, 125, 1397

Chiappini, C., Matteucci, F., & Gratton, R. 1997, ApJ, 477, 765

Chiar, J. E., & Tielens, A. G. G.M. 2006, ApJ, 637, 774

Cioffi, D., McKee, C., Bertschinger, E. 1988, ApJ, 334, 252

Chiosi, C. 1980, A&A, 83, 206

Colangeli, L., Menella, V., Blanco, A. et al. 1993, ApJ, 418, 435

Croat, T. K., Stadermann, F. J., & Bernatowicz, T. J. 2005, ApJ, 631, 976

Cunha, K., Lambert, D. L. 1994, ApJ, 426, 170

Cunha, K., & Hubeny, I., & Lanz, T. 2006, ApJ, 647, L143

Dame, T.M. 1993, in Back to the Galaxy, AIP Conf. Proc. 278, ed. S. S. Holt & F. Verter, p.267

Daflon, S., & Cunha, K. 2004, ApJ, 617, 1115

Dartois, E., Munoz Caro, G. M., Deboffle, D. 2005, A&A, 432, 895

da Silva, L., Girardy, L., Pasquini, L., Setiawan, J., von der Lühe, O., de Medeiros, J. R., Hatzes, A., Döllinger, M. P., & Weiss, A. 2006, A&A, 458, 609

Daulton, T. L., Bernatowicz, T. J., Lewis, R. S., Messenger, S., Stadermann, F. J., & Amari, S. 2003, Geochim. Cosmochim. Acta, 67, 4743

Deharveng, L., Peña, M., Caplan, J., & Costero, R. 2000, MNRAS, 311, 329

Delahaye, F., & Pinsonneault, M. H. 2006, ApJ, 649, 529

Demyk, K., Jones, A. P., Dartois, E. et al. 1999, A&A, 349, 267

Demyk, K., d'Hendecourt, L., Keroux, H., Jones, A. P., & Borg, J. 2004, A&A, 420, 547

Devriendt, J. E. G., Guiderdoni, B., Sadat, R. 1999, A&A, 350, 381

Dickey, J. M. 1993, in The Minnesota Lectures on the Structure and Dynamics of the Milky Way, ASP Conf. Ser. 39, ed. R. M. Humphreys (San Francisco: Astronomical Society of the Pacific), p. 93

Diel, R., Halloin, H., Kretschmer, K. et al. 2006, Nature, 439, 45

Draine, B.T., & Lee, H.M. 1984, ApJ, 285, 89

Dwarkadas, V. V. 2006, ArXiv Astrophysics e-prints, arXiv:astro-ph/0612665

Dwek, E. 1998, ApJ, 501, 643

Dwek, E. 2005, in The Spectral Energy Distributions of Gas-Rich Galaxies: Confronting Models with Data. AIP Conf. Proc. 761, ed. C. C. Popescu, & R. J. Tuffs. (Melville: American Institute of Physics), p. 103

Dwek, E., Arendt, R. G., Fixsen, D. J. et al. 1997, ApJ, 475, 565

Dwek, E., Galliano, F., & Jones, A. P. 2007, ApJ, 662, 927

Dwek, E., Zubko, V., Arendt, R., & Smith, R. 2004, in Astrophysics of Dust. ASP Conf. Ser. 309, ed. A. Witt, p. 499

Dopita, M. A., & Ryder, S.D. 1994, ApJ, 430, 163

Dorschner, J. 2003, Astromineralogy, 609, 1

Draine, B. 1990, in The Evolution of the Insterstellar Medium, ASP Conf. Proc. 12, ed. L. Blitz (San Francisco: Astronomical Society of the Pacific), p. 193

Edmunds, M. G. 2001, MNRAS, 328, 223

Edvardsson, B., Andersen, J., Gustafsson, B., Lambert, D. L., Nissen, P. E., & Tomkin, J. 1993, A&A, 275, 101

Ercolano, B., Barlow, M. J., & Sugerman, B. E. K. 2007, MNRAS, 375, 753

Falgarone, E., Pineau Des Forêts, G., Hily-Blant, P., & Schilke, P. 2006, A&A, 452, 511

Feldman, U., & Widing, K. G. 2003, Space Sci. Rev., 107, 665

Ferrarotti, A. S., & Gail, H.-P. 2006, A&A, 447, 553

Ferrière, K. M., 1998, ApJ, 503, 700

Feuchtinger, M. U., Dorfi, E. A., & Höfner, S. 1995, A&A, 273, 513

Fioc, M., & Rocca-Volmerange, B. 1997, A&A, 326, 950

Flagey, N., Boulanger, F., Verstraete, L., Miville Deschnes, M. A., Noriega Crespo, A., Reach, W. T., 2006, A&A, 453, 969

Fleischer, A. J., Gauger, A., & Sedlmayr, E. 1991, A&A, 242, L1

Fleischer, A. J., Gauger, A., & Sedlmayr, E. 1992, A&A, 266, 321

Forrest, W. J., Houck, J. R., & McCarthy, J. F. 1981, ApJ, 248, 195

François, P., Matteucci, F., Cayrel, R., Spite, M., Spite, F., & Chiappini, C. 2004, A&A, 421, 613

Freudenreich, H. T. 1998, ApJ, 492, 495

Frisch, P. C. 2006, ArXiv Astrophysics e-prints, arXiv:astro-ph/0603745

Gail H.-P., & Sedlmayr E., 1986, A&A, 166, 225

Gail H.-P., & Sedlmayr E., 1987, A&A, 171, 197

Gail, H.-P. 2003, In Astromineralogy, ed. Th. Hennig. (Heidelberg: Springer), p. 55

Gail, H.-P., Zhukovska, S., Hoppe,P. & Trieloff, M. submitted to ApJ

Gil-Pons, P., & García-Berro, E. 2002, A&A, 396, 589

Gilmore, G., Wyse, R., & Kuijen, K. 1989, in Evolutionary Phenomena in Galaxies, ed. J. Beckman, & B. Pagel (Cambridge: Cambridge University Press), p. 172

Goebel, J. H., & Moseley, S. H., 1985, ApJ, 290, L35

Goswami, A., & Prantzos, N. 2000, A&A, 359, 191

Gratton, R. G., & Sneden, C. 1991, A&A, 241, 501

Grevesse, N., & Sauval, A. J. 1998, Space Sci. Rev., 85, 161

Grishko, V. I., Tereszchuk, K., Duley, W. W., & Bernath, P. 2001, ApJ, 558, L129

Guibert J., Lequeux J., Viallefond F. 1978, A&A, 68, 1

Gummersbach, C. A., Kaufer, D. R., Schafer, D. R., Szeifert, T., & Wolf, B. 1998, A&A, 338, 881

Gusten R., Mezger M. 1983, Vistas Astr. 26, 159

Hachisu, I., Kato, M., & Nomoto, K. 1996, ApJ, 470, L97

Hachisu, I., Kato, M., & Nomoto K. 1999, ApJ, 522, 487

Hashimoto, A. 1990, Nature, 347, 53

Herschel, W. 1785, Phil. Trans., 75, 213

Hirashita, H. 2000, ApJ, 531, 693

Hirashita, H. 2000, PASJ, 52, 585

Helmi, A., Navarro, J. F., Nordström, B., Holmberg, J., Abadi, M. G., & Steinmetz, M. 2006, MNRAS, 365, 1309

Hirashita, H., Tajiri, Y. Y. & Kamaya, H. 2002, A&A, 388, 439

Höfner, S., & Dorfi, E. A. 1997, A&A, 319, 648

Höfner, S., Jørgensen, U. G., Loidl, R., & Aringer, B. 1998, A&A, 340, 497

Hollenbach, D., Salpeter, E. E. 1979, J. Chem. Phys., 53, 79

Holmberg, J., & Flynn, C. 2004, MNRAS, 352, 440

Holmgren, D. E., Brown, P. J. F., Dufton, P. L., & Keenan, F. P. 1990, ApJ, 364, 657

Holweger, H. 2001, in Solar and Galactic Composition. AIP Conf. Proc. 598, ed. R. F. Wimmer-Schweingruber (Melville: American Institute of Physics), 23

Hony, S., Waters, L. B. F. M., & Tielens, A. G. G. M. 2002, A&A,390, 533

Hony, S., & Bouwman, J 2004, A&A, 413, 981

Hoppe, P. 2004, in Astrophysics of Dust, ASP Conf. Ser. Vol 309, ed. A. N. Witt, G. C. Clayton, & B. T. Draine. (San Francisco: Astronomical Society of the Pacific), p. 265

Hoppe, P., Amari, S., Zinner E., & Lewis, R. S. 1995, Geochim. Cosmochim. Acta, 59, 4029

Hoppe, P., Strebel, R., Eberhardt, P., Amari, S., & Lewis, R. S. 2000, Meteoritics and Planetary Science, 35, 1157

Hou, J.L., Prantzos, N., & Boisser, S. 2000, A&A, 362, 921

Hoyle, F., & Wickramasinghe, N.C. 1962, MNRAS, 124, 417

Hoyle, F., & Wickramasinghe, N.C. 1970, Nature, 226, 62

Hrivnak, B. J., Kwok, S., & Kwok, S. 2000, ApJ, 535, 275

Hurley, J. R., Pols, O. R., & Tout, C. A. 2000, MNRAS, 315, 543

Hunt, L.K., Thuan, T.X., & Izotov, Y.I. 2003, ApJ, 588, 281.

Ibukiyama, A. & Arimoto, N. 2002, A&A, 394, 927

Inoue, A. K. 2003, PASJ, 55, 901

Irvine, W. M., Goldsmith, P. F., & Hjalmarson, Å. 1987, in Interstellar Processes, ed. D. J. Hollenbach, H. A. Thronson (Dordrecht: Reidel), 561

Iwamoto, K., Brachwitz, F., Nomoto, K., Kishimoto, N., Umeda, H., Hix, W. R., & Thielemann, F. 1999, ApJS, 125, 439

Jäger, C., Fabian, D., Schrempel, F., Dorschner, J., Henning, T., & Wesch, W. 2003, A&A, 401, 57

Jenkins, E. B. 2004, in Origin and Evolution of the Elements, ed. A. Mc William, & M. Rauch (Cambridge: Cambridge University Press), p. 336

Jenniskens, P., Baratta, G. A., Kouchi, A., de Groot, M. S., Greenberg, J. M., & Strazzulla, G. 1993, A&A, 273, 583

Jeong, K. S., Winters, J. M., Le Bertre, T., & Sedlmayr, E. 2003, A&A, 407, 191

Jiang, B. W., Szczerba, R., & Deguchi, S. 1999, A&A, 344, 918

Jones, A. P. 1990, MNRAS, 245, 331

Jones A. 2004, in Astrophysics of Dust, ASP Conf. Ser. Vol 309, ed. A. N. Witt, G. C. Clayton, & B. T. Draine. (San Francisco: Astronomical Society of the Pacific), p. 347

Jones, A. P. 2005, in The dusty and molecular universe: a prelude to Herschel and ALMA. ESA SP-577, ed. A. Wilson (Noordwijk: ESA), p. 239

Jones, A. P., Tielens, A. G. G. M., Hollenbach, D. J., & McKee, C. F. 1994, ApJ, 433, 797

Jones A. P., Tielens, A. G. G. M., & Hollenbach, D. J. 1996, ApJ, 469, 740

Jones, A. P. 2000, JGR, 105, 10257

Jonsell, K., Edvardsson, B., Gustafsson, B., Magain, P., Nissen, P. E., & Asplund, M. 2005, A&A, 440, 321

Jonsson, P. 2006, MNRAS, 372, 2

Jura, M. 1997, in Astrophysical Implications of the Laboratory Study of Presolar Materials, AIP Conf. Proc. 402, ed. T. J. Bernatowicz, & E. Zinner (Woodbury: American Institute of Physics) p. 379

Jurić, M., Ivezić, Ž., Brooks, A. et al. 2008, ApJ, 673, 864

Karakas, A. I., & Lattanzio, J. C. 2003, Publications of the Astronomical Society of Australia, 20, 279

Kaufer, A., Szeifert, T., Krenzin, R., Baschek, B., & Wolf, B. 1994, A&A, 289, 740

Kemper, F., de Koter, A., Waters, L. F. B. M., Bouwman, J., & Tielens, A. G. G. M. 2002, A&A, 384, 585

Kemper, F., Vriend, W. J., & Tielens, A. G. G. M. 2004, ApJ, 609, 826

Kennicutt, R. C. 1998, ApJ, 498, 541

Kimura, H., Mann, I., & Jessberger, E. K. 2003a, ApJ, 582, 846

Kimura, H., Mann, I., & Jessberger, E. K. 2003b, ApJ, 583, 314

Kimura, Y., Kurumada, M., Tamura, K., Koike, C., Chihara, H., & Kaito, C. 2005, A&A, 442, 507

Kobayashi, C., Umeda, H., Nomoto, K., Tominaga, N., & Ohkubo, T. 2006, ApJ, 653, 1145

Kozasa, T., Hasegawa, H., & Nomoto, K. 1989 ApJ, 344, 325

Kroupa, P. 2002, Science, 295, 82

BIBLIOGRAPHY

Krumholz, M. R., Matzner, C. D., & McKee, C. F. 2006, arXiv:astro-ph/0608471

Lagadec, E., Zijlstra, A. A., Sloan, G. C. and 11 coauthors 2007, MNRAS, 376, 1270

Lamers, H. J. G. L. M., Nota, A., Panagia, N., Smith, L. J., & Langer, N. 2001, ApJ, 551, 764

Laor, A., & Draine, B.T. 1993, ApJ, 402,441

Lattimer, J. M., Schramm, D. N., & Grossman, L. 1978, ApJ, 219, 230

Lejeune, T., Cuisinier, F., & Buser, R. 1997, A&AS, 125, 229

Lejeune, T., Cuisinier, F., & Buser, R. 1998, A&AS, 130, 65

Leisawitz, D., Bash, F. N., & Thaddeus, P. 1989, ApJS, 70, 731

Leisenring, J. M., Markwick-Kemper, F., Sloan, G. C. (2008) Effects on metallicity on the chemical composition of carbon stars (preprint)

Leitherer, C., Robert, C., & Drissen, L. 1992, ApJ, 401, 596

Lemasle, B., François, P., Bono, G. et al 2007, A&A, 467, 283

Li, A. 2005, Journal of Physics Conference Series, 6, 229

Liffman, K., & Clayton, D. D. 1989, ApJ, 340, 853

Lindblad, B. 1935, Nature, 135, 133

Lisenfeld, U., & Ferrara, A. 1998, ApJ, 496, 145

Loose, H. H., & Thuan, T. X. 1986 ApJ, 309, 59

Lyne, A., Manchester, R., Taylor, J., 1985, MNRAS213, 613

Lyubimkov, L. S., Rostopchin, S. I., & Lambert, D. L. 2004, MNRAS, 351, 745

Lyubimkov, L. S., Rostopchin, S. I., Rachkovskaya, T. M., Poklad, D. B., & Lambert, D. L. 2005, MNRAS, 358, 193

Marchenko, S. V., & Moffat, A. F. J. 2006, arXiv:astro-ph/0610531

Mathis, J. S., Rumpl, W., & Nordsieck, K. H. 1977, ApJ, 217, 425

Matteucci, F. 2003, The chemical evolution of the galaxy (Kluwer Academic Publishers)

Matteucci, F., & Greggio, L. 1986, A&A, 154, 279

Matteucci, F., Panagia, N., Pipino, A. & et al. 2006, MNRAS, 372, 265

Matzner, C. D. 2002, ApJ, 566, 302

McKee, O. 1989, in Interstellar Dust, ed. L. J. Allamandola & A.G.G.M. Tielens (Dordrecht:

Kluwer), 431

McKee, O. & Ostriker, J. 1977, ApJ, 218, 148

McKeegan, K. D., Aléon, J., Bradley, J. et al. 2006, Science, 314, 1724

McSween, H. Y., Ghosh, A., Grimm, R. E., Wilson, L., & Young, E. D. 2002, in Asteroids III, ed. W. F. Bottke et al. (Tucson: University of Arizona Press), p. 559

Melendez, J., & Barbuy, B. 2002, ApJ, 575, 474

Mera, D., Chabrier, G., & Schaeffer, R. 1998, A&A, 330, 937

Messenger, S., Keller, L. P., Stadermann, F. J., Walker, R. M., & Zinner, E. 2003, Science, 300, 105

Messenger, S., Keller, L. P., & Lauretta, D. S. 2005, Science, 309, 737

Meynet, G., & Maeder, A. 2005, A&A, 429, 581

Min, M., Waters, L. B. F. M., de Koter, A., Hovenier, J. W., Keller, L. P., & Markwick-Kemper, F. 2007, A&A, 462, 667

Molster, F. J., & Waters, L. B. F. M. 2003, in Astromineralogy, ed. Th. Henning. Lecture Notes in Physics, 609, 121

Morgan, H. L., & Edmunds, M. G. 2003, MNRAS, 343, 427

Nguyen, A. N., Stadermann, F. J., Zinner, E., Stroud, R. M., Alexander, C. M. O., & Nittler, L. R. 2007, ApJ, 656, 1223

Nittler, L. R., & Alexander, C. M. O'D. 2003, Geochim. Cosmochim. Acta, 24, 4961

Nittler, L. R., Alexander, C. M. O., Gallino, R., Hoppe, P., Nguyen, A. N., Stadermann, F. J., & Zinner, E. K. 2008, ApJ, 682, 1450

Nozawa, T., Kozasa, T., & Habe, A. 2006, ApJ, 648, 435

Nozawa, T., Kozasa, T., Umeda, H., Maeda, K., & Nomoto, K. 2003, ApJ, 598, 785

Nomoto, K., Nozomu, T., Umeda, H., Kobayashi, C., & Maeda, K. 2006 Nuclear Physics A, 777, 424

Nordström, B., Andersen, J., Holmberg, J., Jørgensen, B. R., Mayor, M., & Pont, F. 2004, PASA, 21, 129

Nozawa, T., Kozasa, T., Habe, A., Dwek, E., Umeda, H., Tominaga, N., Maeda, K., & Nomoto, K. 2007, arXiv:0706.0383

Nuth, J. A., Moseley, H., Silverberg, R. F., Goebel, J. H., & Moore, W. J. 1985, ApJ, 290, L41

Olling R. P., & Merrifield M. R. 2001, MNRAS, 326, 164

Omont, A. 1993, in Astronomical Infrared Spectroscopy: Future Observational Directions, ASP Conf. Ser., 41, 87

Omont, A., Moseley, S. H, Cox, P. et al. 1995, ApJ, 454, 819

Oort, J.H., & van de Hulst, H.C. 1946, Bull. Astron. Inst. Netherlands, 10, 187

Pagel B., 1997, Nucleosynthesis and Galactic Chemical Evolution (Cambridge: Cambridge University Press)

Palme, H., & Jones, A. 2003, in Treatise on Geochemistry, ed. H. D. Holland, & K. K. Turekian. (Amsterdam: Elsevier), p. 41

Papoular, R. 2000, A&A, 362, L9

Pauling, L. 1960, The Nature of the Chemical Bond and the Structure of Molecules and Crystals, 3rd. Ed. (Cornell University press)

Pollack, J. B., Hollenbach, D. J., Beckwith, S. et al. 1994, ApJ, 421, 615

Pont, F., & Eyer, L. 2004, MNRAS, 351, 487

Portinari, L., Chiosi, C., & Bressan, A. 1998, A&A, 334, 505

Prantzos, N. & Aubert, O., 1995, A&A, 302, 69

Prantzos, N. 2000, New Astronomy Review, 44, 303

Preibisch, T., Brown, A. G. A., Bridges, T., Guenther, E., & Zinnecker, H. 2002, AJ, 124, 404

Ramírez, I., Allende Prieto, C., & Lambert, D. L. 2007, A&A, 465, 271

Rana, N. 1991, ARA&A, 29, 129

Recchi, S., Matteucci, F., D'Ercole, A., & Tosi, M. 2002, A&A, 384, 799

Reddy, B. E., Tomkin, J., Lambert, D. L., & Allende Prieto, C. 2003, MNRAS, 340, 304

Reiteri, C. M., Villata, M., & Navarro, J. F. 1996, A&A, 305, 105

Reddy, B. E., Lambert, D. L., & Allende Prieto, C. 2006, MNRAS, 367, 1329

Rocha-Pinto, H. J., Maciel, W. J., Scalo, J., & Flynn, C. 2000, A&A, 358, 850

Rolleston, W. R. J., Smartt, S. J., Dufton, P. L., & Ryans, R. S. I. 2000, A&A, 363, 537

Savage, B. D., & Sembach, K. R. 1996, ARA&A,34, 279

Scalo, J., & Elmegreen, B. G. 2004, ARA&A, 42, 275

Schaller, G., Schaerer, D., Meynet, G., & Maeder, A. 1992, A&AS, 96, 269

Schaerer, D., Meynet, G., Maeder, A., & Schaller, G. 1993, A&AS, 98, 523

Schneider, R., Ferrara, A., & Salvaterra, R. 2004, MNRAS, 351, 1379

Seab, C. G. 1987, 1987, in Interstellar Processes, ed. D. J. Hollenbach & H. A. Thronson. (Dordrecht: Reidel), p. 134, 491

Shaver, P. A., McGee, R. X., Newton, L. M., Danks, A. C., & Pottasch, S. R. 1983, MNRAS, 204, 53

Shull, J. M., & Draine, B. T. 1987, in Interstellar Processes, ed. D. J. Hollenbach & H. A. Thronson. (Dordrecht: Reidel), 134, p. 283

Silva, L., Granato, G. L., Bressan, A., & Danese, L. 1998, ApJ, 509, 103

Simpson, J. P., Colgan, S. W. J., Rubin, R. H., Erickson, E. F., & Haas, M. R. 1995, ApJ, 444, 721

Sloan, G. C., Kraemer, K. E., Matsuura, M., Wood, P. R., Price, S. D., & Egan, M. P. 2006, ApJ, 645, 1118

Smartt, S. J., & Rolleston, W. R. J. 1997, ApJ, 481, L47

Smith, N. 2006, ArXiv Astrophysics e-prints, arXiv:astro-ph/0609422

Smith, N., & Owocki, S. P. 2006, ApJ, 645, L45

Smith, R. K., Dame, T. M., Costantini, E., & Predehl, P. 2006, ApJ, 648, 452

Sodroski, T. J., Odegard, N., Arendt, R. G., Dwek, E., Weiland, J. L., Hauser, M. G., & Kelsall, T. 1997, ApJ, 480, 173

Sofia, U. J., & Meyer, D. M. 2001, ApJ, 554, L221

Soubiran, C., & Girard, P., 2005 A&A, 438, 139

Spitzer, L., Jr. 1954, ApJ, 120, 1

Spitzer, L. Jr. 1978, Physical Processes in the Interstellar Medium (Wiley, New York)

Stevens, J. A., Amure, M., & Gear, W. K. 2005, MNRAS, 357, 361

Sugerman, B. E. K., Ercolano, B., Barlow, M. et al. 2006, Science, 313, 196

Szczerba, R., Henning, Th., Volk, K., & Kwok, S. 1999, A&A, 345, L39

Talbot, R. J., & Arnett, W. D. 1975, ApJ, 197, 551

Tammann, G., Löffler, W., & Schröder, A. 1994, ApJS, 92, 487

Tielens, A. G. G. M. 1998, ApJ, 499, 267

Tielens, A. G. G. M. 2003, Science, 300, 68

Tielens, A. G. G. M. 2005, The physics and chemistry of the interstellar medium (Cambridge:

Cambridge University Press)

Tielens, A. G. G. M., Waters, L. B. F. M., & Bernatowicz, T. J. 2005, in Chondrites and the Protoplanetary Disk, ASP Conf. 341, eds. A. N. Krot, E. R. D. Scott, & B. Reipurth (San Francisco: Astronomical Society of the Pacific), p. 605

Timmes, F. X., Woosley, S. E., & Weaver, T. A. 1995, ApJS, 98, 617

Tinsley, B. M. 1980, Fund. Cosmic Phys., 5, 287

Todini, P., & Ferrara, A. 2001, MNRAS, 325, 736

Travaglio, C., Gallino, R., Amari, S., Zinner, E., Woosley, S., & Lewis, R. S. 1999, ApJ, 510, 325.

Trumpler, R.J. 1930, PASP, 42, 214

van den Hoek, L. B., & Groenewegen, M. A. T. 1997, A&AS, 123, 305

van der Hucht, K. A. 2003, in A Massive Star Odyssey: From Main Sequence to Supernova, IAU Symp 212, 441

van Dishoeck, E. F., Blake, G. A., Draine, B. T., & Lunine, J. I. 2003, in Protostars and Planets III, eds. E. H. Levy, & J. I. Lunine (Tucson: University of Arizona Press), 163

van Dishoeck, E. F., & Blake, G. A. 1998, ARA&A, 36, 317

van Loon, J. T., Groenewegen, M. A. T., de Koter, A., et al. 1999, A&A, 351, 559

Vassiliadis, E., & Wood, P. R. 1993, ApJ, 413, 641

Vega, O., Clemens, M. S., Bressan, A., Granato, G. L., Silva, L., & Panuzzo, P. 2008, A&A, 484, 631

Venn, K. A., Irwin, M., Shetrone, M. D., Tout, C. A., Hill, V., & Tolstoy, E. 2004, ApJ, 128, 1177

Vilchez, J. M., & Esteban, C. 1996, MNRAS, 280, 720

Volk, K., Kwok, S., Herivnak, B. J., & Szczerba, R. 2002, ApJ, 567, 412

Vollmer, C., Hoppe, P., Brenker, F. E., & Holzapfel, C. 2007, Lunar and Planetary Institute Conference Abstracts, 38, 1262

Vollmer, C., Hoppe, P., & Brenker, F. E. 2008, ApJ, 684, 611

Vorobyov, E. I., & Shchekinov, Y. A. 2006, New Astronomy, 11, 240

Wang, L. 2006, ApJ, 635, L33

Watson, W. D. 1975, in Atomic and Molecular Physics of the Interstellar Matter, Les Houches 1974, eds. R. Balian, P. Encrenaz, & J. Lequex. (Amsterdam: North-Holland Publ. Comp.), p. 177

Weingartner, J.C., & Draine, B.T. 2001, ApJ, 548, 296

Welty, D. E., Hobbs, L.M., Lauroesch, J. T. et al. 1999, ApJS, 124, 465

Westera, P., Lejeune, T., Buser, R., Cuisinier, F., & Bruzual, G. 2002, A&A, 381, 524

Whittet, D., C., B. 2003, Dust in the galactic environment (Institute of Physics Publishing)

Williams, J. P., & McKee, C. F. 1997, ApJ, 476, 166

Winters, J. M., Fleischer, A. J., Le Bertre, T., & Sedlmayr, E. 1997, A&A, 326, 305

Winters, J. M., Le Bertre, T., Jeong, K. S., Helling, C., & Sedlmayr, E. 2000, A&A, 361, 641

Wooden, D. H., Charnley, S. B., Ehrenfreund, P. 2004, In Comets II, 33

Woosley, S. E., & Weaver, T. A. 1995, ApJS, 101, 181

Whelan, J., & Iben Jr., I. 1973, ApJ, 186, 1007

Wyse, R., Silk, J., 1989, ApJ, 339, 700

Yamamura, I., de Jong, T., Justtanont, K., Cami, J., & Waters, L. B. F. M. 1998, Ap&SS, 255, 351

Zijlstra, A. A., Matsuura, M., Wood, P. R. and 13 coauthors 2006, MNRAS, 365, 370, 1961

Zinner, E. 1998, in Astrophysical Implications of the Laboratory Study of Presolar Materials, AIP Conf. Proc. 402, ed. T. J. Bernatowicz, & E. Zinner (Woodbury: American Institute of Physics) p. 3

Zinner, E. 1998, Ann. Rev. Earth & Plan. Sci., 26,147

Zolensky, M. E., Zega, T. J., Yano, H. et al. 2006, Science, 314, 1735

Zhukovska, S.& Gail, H.-P. 2008, A&A, 486, 229

Zhukovska, S., Gail, H.-P., & Trieloff, M. 2008, A&A, 479, 453

Zubko, V. G., Menella, V., Colangeli, L., & Busoletti, E. 1996, MNRAS, 282, 1321

Zubko, V., Dwek, E., & Arendt, R. G. 2004, ApJS, 152, 211

BIBLIOGRAPHY

Appendix A

Dust formation by AGB stars

Table A.1 gives dust masses returned by low and intermediate mass stars separately for all dust species considered in Ferrarotti & Gail (2006). The calculations are done as in that paper, but a finer grid of metallicities and initial masses are used. The initial models at the begin of thermal pulsing not in the model set of the Geneva group are determined by linear interpolation between the available models.

Table A.1: Ejected mass of dust by AGB stars for different chemistries of M-stars, S-stars and C-stars for different initial masses M_* and metallicities Z. All masses are given in Solar mass.

Z = 0.001

M_*	M stars						S stars		C stars		
	forsterite	fayalite	enstatite	ferrosilite	quartz	iron	quartz	iron	SiC	carbon	iron
1.00	0.0	0.0	0.0	0.0	0.0	0.0	0.0	0.0	0.0	0.0	0.0
1.10	0.0	0.0	0.0	0.0	0.0	0.0	0.0	0.0	0.0	$4.124 \cdot 10^{-6}$	0.0
1.20	0.0	0.0	0.0	0.0	0.0	0.0	0.0	0.0	0.0	$3.585 \cdot 10^{-4}$	0.0
1.25	0.0	0.0	0.0	0.0	0.0	0.0	0.0	0.0	0.0	$5.976 \cdot 10^{-4}$	0.0
1.30	0.0	0.0	0.0	0.0	0.0	0.0	0.0	0.0	0.0	$8.878 \cdot 10^{-4}$	0.0
1.40	0.0	0.0	0.0	0.0	0.0	0.0	0.0	0.0	0.0	$1.298 \cdot 10^{-3}$	0.0
1.50	0.0	0.0	0.0	0.0	0.0	0.0	0.0	0.0	0.0	$1.985 \cdot 10^{-3}$	0.0
1.60	0.0	0.0	0.0	0.0	0.0	0.0	0.0	0.0	0.0	$2.520 \cdot 10^{-3}$	0.0
1.70	0.0	0.0	0.0	0.0	0.0	0.0	0.0	0.0	0.0	$3.159 \cdot 10^{-3}$	0.0
1.80	0.0	0.0	0.0	0.0	0.0	0.0	0.0	0.0	$1.122 \cdot 10^{-9}$	$3.827 \cdot 10^{-3}$	0.0
1.90	0.0	0.0	0.0	0.0	0.0	0.0	0.0	0.0	$1.221 \cdot 10^{-9}$	$4.209 \cdot 10^{-3}$	0.0
2.00	0.0	0.0	0.0	0.0	0.0	0.0	0.0	0.0	$1.367 \cdot 10^{-9}$	$4.538 \cdot 10^{-3}$	0.0
2.10	0.0	0.0	0.0	0.0	0.0	0.0	0.0	0.0	$1.483 \cdot 10^{-9}$	$4.799 \cdot 10^{-3}$	0.0
2.20	0.0	0.0	0.0	0.0	0.0	0.0	0.0	0.0	$1.629 \cdot 10^{-9}$	$5.096 \cdot 10^{-3}$	0.0
2.30	0.0	0.0	0.0	0.0	0.0	0.0	0.0	0.0	$1.748 \cdot 10^{-9}$	$5.416 \cdot 10^{-3}$	0.0
2.40	0.0	0.0	0.0	0.0	0.0	0.0	0.0	0.0	$1.895 \cdot 10^{-9}$	$5.687 \cdot 10^{-3}$	0.0
2.50	0.0	0.0	0.0	0.0	0.0	0.0	0.0	0.0	$2.035 \cdot 10^{-9}$	$5.788 \cdot 10^{-3}$	0.0
3.00	0.0	0.0	0.0	0.0	0.0	0.0	0.0	0.0	$3.006 \cdot 10^{-9}$	$6.997 \cdot 10^{-3}$	0.0
3.50	0.0	0.0	0.0	0.0	0.0	0.0	0.0	0.0	$3.842 \cdot 10^{-9}$	$9.751 \cdot 10^{-3}$	0.0
4.00	0.0	0.0	0.0	0.0	0.0	0.0	0.0	0.0	$4.802 \cdot 10^{-9}$	$1.283 \cdot 10^{-2}$	0.0
4.01	0.0	0.0	0.0	0.0	0.0	0.0	0.0	0.0	$4.825 \cdot 10^{-9}$	$1.286 \cdot 10^{-2}$	0.0
4.50	$1.318 \cdot 10^{-9}$	0.0	0.0	0.0	0.0	$1.308 \cdot 10^{-9}$	0.0	0.0	$2.185 \cdot 10^{-9}$	$5.789 \cdot 10^{-4}$	0.0
5.00	$1.744 \cdot 10^{-9}$	0.0	$1.252 \cdot 10^{-9}$	0.0	0.0	$1.699 \cdot 10^{-9}$	0.0	0.0	$2.407 \cdot 10^{-9}$	$5.812 \cdot 10^{-4}$	0.0
5.50	$2.203 \cdot 10^{-9}$	0.0	$1.557 \cdot 10^{-9}$	0.0	0.0	$2.100 \cdot 10^{-9}$	0.0	0.0	$2.454 \cdot 10^{-9}$	$5.903 \cdot 10^{-4}$	0.0
6.00	$2.698 \cdot 10^{-9}$	0.0	$1.875 \cdot 10^{-9}$	0.0	0.0	$2.525 \cdot 10^{-9}$	0.0	0.0	$2.537 \cdot 10^{-9}$	$5.968 \cdot 10^{-4}$	0.0
6.50	$3.234 \cdot 10^{-9}$	0.0	$2.215 \cdot 10^{-9}$	0.0	0.0	$2.981 \cdot 10^{-9}$	0.0	0.0	$2.743 \cdot 10^{-9}$	$6.158 \cdot 10^{-4}$	0.0
7.00	$3.795 \cdot 10^{-9}$	0.0	$2.574 \cdot 10^{-9}$	0.0	0.0	$3.467 \cdot 10^{-9}$	0.0	0.0	$2.904 \cdot 10^{-9}$	$6.266 \cdot 10^{-4}$	0.0

Table A.1 – Continued

M_*	M stars						S stars		C stars		
	forsterite	fayalite	enstatite	ferrosilite	quartz	iron	quartz	iron	SiC	carbon	iron
						$Z = 0.002$					
1.00	0.0	0.0	0.0	0.0	0.0	0.0	0.0	0.0	0.0	0.0	0.0
1.10	0.0	0.0	0.0	0.0	0.0	0.0	0.0	0.0	0.0	$3.101 \cdot 10^{-6}$	0.0
1.20	0.0	0.0	0.0	0.0	0.0	0.0	0.0	0.0	$1.275 \cdot 10^{-9}$	$3.620 \cdot 10^{-4}$	0.0
1.25	0.0	0.0	0.0	0.0	0.0	0.0	0.0	0.0	$1.743 \cdot 10^{-9}$	$4.663 \cdot 10^{-4}$	0.0
1.30	0.0	0.0	0.0	0.0	0.0	0.0	0.0	0.0	$2.822 \cdot 10^{-9}$	$7.462 \cdot 10^{-4}$	0.0
1.40	0.0	0.0	0.0	0.0	0.0	0.0	0.0	0.0	$5.096 \cdot 10^{-9}$	$1.217 \cdot 10^{-3}$	0.0
1.50	0.0	0.0	0.0	0.0	0.0	0.0	$2.527 \cdot 10^{-9}$	0.0	$7.099 \cdot 10^{-9}$	$1.735 \cdot 10^{-3}$	0.0
1.60	0.0	0.0	0.0	0.0	0.0	0.0	0.0	0.0	$8.149 \cdot 10^{-9}$	$2.195 \cdot 10^{-3}$	0.0
1.70	0.0	0.0	0.0	0.0	0.0	0.0	0.0	0.0	$8.617 \cdot 10^{-9}$	$2.632 \cdot 10^{-3}$	0.0
1.80	0.0	0.0	0.0	0.0	0.0	0.0	0.0	0.0	$1.013 \cdot 10^{-8}$	$3.188 \cdot 10^{-3}$	0.0
1.90	0.0	0.0	0.0	0.0	0.0	0.0	0.0	0.0	$1.150 \cdot 10^{-8}$	$3.674 \cdot 10^{-3}$	0.0
2.00	0.0	0.0	0.0	0.0	0.0	0.0	0.0	0.0	$1.318 \cdot 10^{-8}$	$4.047 \cdot 10^{-3}$	0.0
2.10	0.0	0.0	0.0	0.0	0.0	0.0	0.0	0.0	$1.415 \cdot 10^{-8}$	$4.156 \cdot 10^{-3}$	0.0
2.20	0.0	0.0	0.0	0.0	0.0	0.0	0.0	0.0	$1.559 \cdot 10^{-8}$	$4.610 \cdot 10^{-3}$	0.0
2.30	0.0	0.0	0.0	0.0	0.0	0.0	0.0	0.0	$1.704 \cdot 10^{-8}$	$4.674 \cdot 10^{-3}$	0.0
2.40	0.0	0.0	0.0	0.0	0.0	0.0	0.0	0.0	$1.843 \cdot 10^{-8}$	$4.950 \cdot 10^{-3}$	0.0
2.50	0.0	0.0	0.0	0.0	0.0	0.0	0.0	0.0	$2.024 \cdot 10^{-8}$	$5.097 \cdot 10^{-3}$	0.0
3.00	0.0	0.0	0.0	0.0	0.0	0.0	0.0	0.0	$3.049 \cdot 10^{-8}$	$6.147 \cdot 10^{-3}$	0.0
3.50	0.0	0.0	0.0	0.0	0.0	0.0	0.0	0.0	$4.078 \cdot 10^{-8}$	$8.874 \cdot 10^{-3}$	0.0
4.00	0.0	0.0	0.0	0.0	0.0	0.0	0.0	0.0	$5.399 \cdot 10^{-8}$	$1.194 \cdot 10^{-2}$	0.0
4.01	0.0	0.0	0.0	0.0	0.0	0.0	0.0	0.0	$5.429 \cdot 10^{-8}$	$1.200 \cdot 10^{-2}$	0.0
4.50	$7.918 \cdot 10^{-9}$	$3.261 \cdot 10^{-9}$	$5.418 \cdot 10^{-9}$	$1.103 \cdot 10^{-9}$	$1.110 \cdot 10^{-9}$	$9.549 \cdot 10^{-9}$	0.0	0.0	$2.000 \cdot 10^{-8}$	$5.119 \cdot 10^{-4}$	$1.931 \cdot 10^{-9}$
5.00	$1.047 \cdot 10^{-8}$	$4.022 \cdot 10^{-9}$	$7.056 \cdot 10^{-9}$	$1.240 \cdot 10^{-9}$	$1.413 \cdot 10^{-9}$	$1.219 \cdot 10^{-8}$	0.0	0.0	$2.269 \cdot 10^{-8}$	$5.098 \cdot 10^{-4}$	$2.732 \cdot 10^{-9}$
5.50	$1.336 \cdot 10^{-8}$	$4.815 \cdot 10^{-9}$	$8.881 \cdot 10^{-9}$	$1.484 \cdot 10^{-9}$	$1.759 \cdot 10^{-9}$	$1.531 \cdot 10^{-8}$	0.0	0.0	$2.399 \cdot 10^{-8}$	$5.189 \cdot 10^{-4}$	$2.658 \cdot 10^{-9}$
6.00	$1.640 \cdot 10^{-8}$	$5.590 \cdot 10^{-9}$	$1.072 \cdot 10^{-8}$	$1.781 \cdot 10^{-9}$	$2.114 \cdot 10^{-9}$	$1.855 \cdot 10^{-8}$	0.0	0.0	$2.527 \cdot 10^{-8}$	$5.335 \cdot 10^{-4}$	$2.275 \cdot 10^{-9}$
6.50	$1.992 \cdot 10^{-8}$	$6.466 \cdot 10^{-9}$	$1.281 \cdot 10^{-8}$	$2.128 \cdot 10^{-9}$	$2.519 \cdot 10^{-9}$	$2.229 \cdot 10^{-8}$	0.0	0.0	$2.768 \cdot 10^{-8}$	$5.435 \cdot 10^{-4}$	$2.537 \cdot 10^{-9}$
7.00	$2.373 \cdot 10^{-8}$	$7.391 \cdot 10^{-9}$	$1.507 \cdot 10^{-8}$	$2.508 \cdot 10^{-9}$	$2.952 \cdot 10^{-9}$	$2.634 \cdot 10^{-8}$	0.0	0.0	$3.052 \cdot 10^{-8}$	$5.486 \cdot 10^{-4}$	$3.025 \cdot 10^{-9}$

Table A.1 – Continued

M_*	M stars						S stars		SiC	C stars	
	forsterite	fayalite	enstatite	ferrosilite	quartz	iron	quartz	iron		carbon	iron
						$Z = 0.004$					
1.00	0.0	0.0	0.0	0.0	0.0	0.0	0.0	0.0	0.0	0.0	0.0
1.10	0.0	0.0	0.0	0.0	0.0	0.0	0.0	0.0	0.0	$1.486 \cdot 10^{-6}$	0.0
1.20	0.0	0.0	0.0	0.0	0.0	0.0	0.0	0.0	$2.554 \cdot 10^{-8}$	$2.259 \cdot 10^{-4}$	0.0
1.25	0.0	0.0	0.0	0.0	0.0	0.0	0.0	0.0	$7.297 \cdot 10^{-8}$	$5.476 \cdot 10^{-4}$	0.0
1.30	0.0	0.0	0.0	0.0	0.0	0.0	0.0	0.0	$9.196 \cdot 10^{-8}$	$7.373 \cdot 10^{-4}$	0.0
1.40	0.0	0.0	0.0	0.0	0.0	0.0	0.0	0.0	$1.226 \cdot 10^{-7}$	$1.164 \cdot 10^{-3}$	0.0
1.50	0.0	0.0	0.0	0.0	0.0	0.0	0.0	0.0	$1.652 \cdot 10^{-7}$	$1.700 \cdot 10^{-3}$	0.0
1.60	0.0	0.0	0.0	0.0	0.0	0.0	0.0	0.0	$1.949 \cdot 10^{-7}$	$2.442 \cdot 10^{-3}$	0.0
1.70	0.0	0.0	0.0	0.0	0.0	0.0	0.0	0.0	$2.053 \cdot 10^{-7}$	$3.175 \cdot 10^{-3}$	0.0
1.80	0.0	0.0	0.0	0.0	0.0	0.0	0.0	0.0	$2.349 \cdot 10^{-7}$	$4.090 \cdot 10^{-3}$	0.0
1.90	0.0	0.0	0.0	0.0	0.0	0.0	0.0	0.0	$2.587 \cdot 10^{-7}$	$5.151 \cdot 10^{-3}$	0.0
2.00	0.0	0.0	0.0	0.0	0.0	0.0	0.0	0.0	$2.830 \cdot 10^{-7}$	$5.589 \cdot 10^{-3}$	0.0
2.10	0.0	0.0	0.0	0.0	0.0	0.0	0.0	0.0	$2.881 \cdot 10^{-7}$	$6.268 \cdot 10^{-3}$	0.0
2.20	0.0	0.0	0.0	0.0	0.0	0.0	0.0	0.0	$3.391 \cdot 10^{-7}$	$6.850 \cdot 10^{-3}$	0.0
2.30	0.0	0.0	0.0	0.0	0.0	0.0	0.0	0.0	$3.454 \cdot 10^{-7}$	$7.532 \cdot 10^{-3}$	0.0
2.40	0.0	0.0	0.0	0.0	0.0	0.0	0.0	0.0	$3.793 \cdot 10^{-7}$	$7.909 \cdot 10^{-3}$	0.0
2.50	0.0	0.0	0.0	0.0	0.0	0.0	$2.350 \cdot 10^{-8}$	0.0	$3.990 \cdot 10^{-7}$	$8.647 \cdot 10^{-3}$	0.0
3.00	0.0	0.0	0.0	0.0	0.0	0.0	0.0	0.0	$6.012 \cdot 10^{-7}$	$1.429 \cdot 10^{-2}$	$1.095 \cdot 10^{-9}$
3.50	0.0	0.0	0.0	0.0	0.0	0.0	0.0	0.0	$1.128 \cdot 10^{-6}$	$8.011 \cdot 10^{-3}$	$1.799 \cdot 10^{-9}$
4.00	0.0	0.0	0.0	0.0	0.0	0.0	0.0	0.0	$1.595 \cdot 10^{-6}$	$1.063 \cdot 10^{-2}$	$2.083 \cdot 10^{-9}$
4.01	0.0	0.0	0.0	0.0	0.0	0.0	0.0	0.0	$1.605 \cdot 10^{-6}$	$1.068 \cdot 10^{-2}$	$2.087 \cdot 10^{-9}$
4.50	$2.032 \cdot 10^{-7}$	$1.530 \cdot 10^{-7}$	$1.003 \cdot 10^{-7}$	$4.704 \cdot 10^{-8}$	$1.900 \cdot 10^{-8}$	$2.632 \cdot 10^{-7}$	0.0	0.0	$3.989 \cdot 10^{-7}$	$4.100 \cdot 10^{-4}$	$1.686 \cdot 10^{-8}$
5.00	$2.709 \cdot 10^{-7}$	$1.972 \cdot 10^{-7}$	$1.332 \cdot 10^{-7}$	$5.893 \cdot 10^{-8}$	$2.452 \cdot 10^{-8}$	$3.292 \cdot 10^{-7}$	0.0	0.0	$4.525 \cdot 10^{-7}$	$4.018 \cdot 10^{-4}$	$2.418 \cdot 10^{-8}$
5.50	$3.042 \cdot 10^{-7}$	$2.151 \cdot 10^{-7}$	$1.514 \cdot 10^{-7}$	$6.360 \cdot 10^{-8}$	$2.778 \cdot 10^{-8}$	$3.682 \cdot 10^{-7}$	0.0	$2.681 \cdot 10^{-9}$	$5.197 \cdot 10^{-7}$	$4.075 \cdot 10^{-4}$	$3.039 \cdot 10^{-8}$
6.00	$3.462 \cdot 10^{-7}$	$2.398 \cdot 10^{-7}$	$1.742 \cdot 10^{-7}$	$7.091 \cdot 10^{-8}$	$3.200 \cdot 10^{-8}$	$4.256 \cdot 10^{-7}$	0.0	0.0	$5.530 \cdot 10^{-7}$	$4.098 \cdot 10^{-4}$	$2.775 \cdot 10^{-8}$
6.50	$3.944 \cdot 10^{-7}$	$2.700 \cdot 10^{-7}$	$1.983 \cdot 10^{-7}$	$7.935 \cdot 10^{-8}$	$3.657 \cdot 10^{-8}$	$4.867 \cdot 10^{-7}$	0.0	$1.574 \cdot 10^{-9}$	$6.357 \cdot 10^{-7}$	$4.219 \cdot 10^{-4}$	$3.861 \cdot 10^{-8}$
7.00	$4.524 \cdot 10^{-7}$	$3.073 \cdot 10^{-7}$	$2.275 \cdot 10^{-7}$	$9.031 \cdot 10^{-8}$	$4.210 \cdot 10^{-8}$	$5.641 \cdot 10^{-7}$	0.0	$2.388 \cdot 10^{-9}$	$6.819 \cdot 10^{-7}$	$4.251 \cdot 10^{-4}$	$3.691 \cdot 10^{-8}$

Table A.1 – Continued

M_*	M stars						S stars		C stars		
	forsterite	fayalite	enstatite	ferrosilite	quartz	iron	quartz	iron	SiC	carbon	iron
						$Z = 0.008$					
1.00	0.0	0.0	0.0	0.0	0.0	0.0	0.0	0.0	0.0	0.0	0.0
1.10	$1.974 \cdot 10^{-7}$	$1.538 \cdot 10^{-7}$	$1.015 \cdot 10^{-7}$	$4.305 \cdot 10^{-8}$	$1.423 \cdot 10^{-8}$	$1.896 \cdot 10^{-7}$	0.0	0.0	$1.876 \cdot 10^{-8}$	$2.870 \cdot 10^{-7}$	$2.982 \cdot 10^{-8}$
1.20	$1.395 \cdot 10^{-6}$	$1.085 \cdot 10^{-6}$	$7.034 \cdot 10^{-7}$	$3.095 \cdot 10^{-7}$	$1.026 \cdot 10^{-7}$	$1.440 \cdot 10^{-6}$	0.0	0.0	$1.265 \cdot 10^{-6}$	$1.433 \cdot 10^{-4}$	$8.789 \cdot 10^{-7}$
1.25	$7.559 \cdot 10^{-7}$	$6.018 \cdot 10^{-7}$	$3.728 \cdot 10^{-7}$	$1.721 \cdot 10^{-7}$	$5.555 \cdot 10^{-8}$	$6.965 \cdot 10^{-7}$	0.0	$2.697 \cdot 10^{-8}$	$4.326 \cdot 10^{-6}$	$1.766 \cdot 10^{-4}$	$1.651 \cdot 10^{-6}$
1.30	$7.729 \cdot 10^{-7}$	$6.216 \cdot 10^{-7}$	$3.838 \cdot 10^{-7}$	$1.832 \cdot 10^{-7}$	$5.735 \cdot 10^{-8}$	$7.543 \cdot 10^{-7}$	0.0	$2.628 \cdot 10^{-8}$	$5.022 \cdot 10^{-6}$	$4.135 \cdot 10^{-4}$	$6.041 \cdot 10^{-8}$
1.40	$8.243 \cdot 10^{-7}$	$6.744 \cdot 10^{-7}$	$3.963 \cdot 10^{-7}$	$2.028 \cdot 10^{-7}$	$6.196 \cdot 10^{-8}$	$8.762 \cdot 10^{-7}$	0.0	0.0	$5.923 \cdot 10^{-6}$	$6.370 \cdot 10^{-4}$	$6.760 \cdot 10^{-8}$
1.50	0.0	0.0	0.0	0.0	0.0	0.0	0.0	0.0	$7.079 \cdot 10^{-6}$	$8.459 \cdot 10^{-4}$	$4.951 \cdot 10^{-8}$
1.60	0.0	0.0	0.0	0.0	0.0	0.0	0.0	0.0	$8.829 \cdot 10^{-6}$	$1.425 \cdot 10^{-3}$	$3.255 \cdot 10^{-8}$
1.70	0.0	0.0	0.0	0.0	0.0	0.0	0.0	0.0	$1.006 \cdot 10^{-5}$	$2.027 \cdot 10^{-3}$	$1.853 \cdot 10^{-8}$
1.80	0.0	0.0	0.0	0.0	0.0	0.0	0.0	0.0	$1.075 \cdot 10^{-5}$	$2.680 \cdot 10^{-3}$	$1.647 \cdot 10^{-8}$
1.90	0.0	0.0	0.0	0.0	0.0	0.0	0.0	0.0	$1.181 \cdot 10^{-5}$	$3.515 \cdot 10^{-3}$	$1.071 \cdot 10^{-8}$
2.00	0.0	0.0	0.0	0.0	0.0	0.0	0.0	0.0	$1.314 \cdot 10^{-5}$	$4.414 \cdot 10^{-3}$	$1.057 \cdot 10^{-8}$
2.10	0.0	0.0	0.0	0.0	0.0	0.0	0.0	0.0	$1.430 \cdot 10^{-5}$	$5.319 \cdot 10^{-3}$	$9.333 \cdot 10^{-9}$
2.20	0.0	0.0	0.0	0.0	0.0	0.0	0.0	0.0	$1.452 \cdot 10^{-5}$	$5.941 \cdot 10^{-3}$	$9.407 \cdot 10^{-9}$
2.30	0.0	0.0	0.0	0.0	0.0	0.0	0.0	0.0	$1.586 \cdot 10^{-5}$	$6.763 \cdot 10^{-3}$	$9.468 \cdot 10^{-9}$
2.40	0.0	0.0	0.0	0.0	0.0	0.0	0.0	0.0	$1.811 \cdot 10^{-5}$	$7.417 \cdot 10^{-3}$	$9.564 \cdot 10^{-9}$
2.50	0.0	0.0	0.0	0.0	0.0	0.0	0.0	0.0	$1.867 \cdot 10^{-5}$	$8.352 \cdot 10^{-3}$	$9.541 \cdot 10^{-9}$
3.00	0.0	0.0	0.0	0.0	0.0	0.0	0.0	0.0	$2.673 \cdot 10^{-5}$	$1.434 \cdot 10^{-2}$	$9.258 \cdot 10^{-9}$
3.50	0.0	0.0	0.0	0.0	0.0	0.0	0.0	0.0	$4.243 \cdot 10^{-5}$	$6.406 \cdot 10^{-3}$	$2.500 \cdot 10^{-8}$
4.00	0.0	0.0	0.0	0.0	0.0	0.0	0.0	0.0	$5.424 \cdot 10^{-5}$	$8.072 \cdot 10^{-3}$	$2.810 \cdot 10^{-8}$
4.01	0.0	0.0	0.0	0.0	0.0	0.0	0.0	0.0	$5.448 \cdot 10^{-5}$	$8.130 \cdot 10^{-3}$	$2.808 \cdot 10^{-8}$
4.50	$1.108 \cdot 10^{-4}$	$8.666 \cdot 10^{-5}$	$5.988 \cdot 10^{-5}$	$2.551 \cdot 10^{-5}$	$7.295 \cdot 10^{-6}$	$6.689 \cdot 10^{-5}$	0.0	$2.869 \cdot 10^{-7}$	$6.921 \cdot 10^{-6}$	$2.101 \cdot 10^{-4}$	$5.099 \cdot 10^{-7}$
5.00	$1.285 \cdot 10^{-4}$	$9.920 \cdot 10^{-5}$	$7.088 \cdot 10^{-5}$	$2.931 \cdot 10^{-5}$	$8.319 \cdot 10^{-6}$	$7.444 \cdot 10^{-5}$	0.0	0.0	$9.286 \cdot 10^{-6}$	$2.276 \cdot 10^{-4}$	$2.649 \cdot 10^{-6}$
5.50	$1.486 \cdot 10^{-4}$	$1.138 \cdot 10^{-4}$	$8.282 \cdot 10^{-5}$	$3.350 \cdot 10^{-5}$	$9.388 \cdot 10^{-6}$	$8.000 \cdot 10^{-5}$	$1.126 \cdot 10^{-8}$	$1.659 \cdot 10^{-7}$	$8.813 \cdot 10^{-6}$	$2.332 \cdot 10^{-4}$	$8.658 \cdot 10^{-7}$
6.00	$1.699 \cdot 10^{-4}$	$1.288 \cdot 10^{-4}$	$9.651 \cdot 10^{-5}$	$3.808 \cdot 10^{-5}$	$1.056 \cdot 10^{-5}$	$8.725 \cdot 10^{-5}$	0.0	$1.448 \cdot 10^{-7}$	$9.480 \cdot 10^{-6}$	$2.357 \cdot 10^{-4}$	$1.196 \cdot 10^{-6}$
6.50	$1.841 \cdot 10^{-4}$	$1.383 \cdot 10^{-4}$	$1.064 \cdot 10^{-4}$	$4.086 \cdot 10^{-5}$	$1.119 \cdot 10^{-5}$	$8.809 \cdot 10^{-5}$	$1.444 \cdot 10^{-7}$	$2.065 \cdot 10^{-6}$	$1.063 \cdot 10^{-5}$	$2.427 \cdot 10^{-4}$	$1.977 \cdot 10^{-6}$
7.00	$1.983 \cdot 10^{-4}$	$1.477 \cdot 10^{-4}$	$1.168 \cdot 10^{-4}$	$4.377 \cdot 10^{-5}$	$1.180 \cdot 10^{-5}$	$8.890 \cdot 10^{-5}$	$1.679 \cdot 10^{-7}$	$2.906 \cdot 10^{-6}$	$1.062 \cdot 10^{-5}$	$2.441 \cdot 10^{-4}$	$1.354 \cdot 10^{-6}$

Table A.1 – Continued

M_*	M stars						S stars		C stars		
	forsterite	fayalite	enstatite	ferrosilite	quartz	iron	quartz	iron	SiC	carbon	iron
						$Z = 0.015$					
1.00	$4.972 \cdot 10^{-5}$	$3.838 \cdot 10^{-5}$	$2.760 \cdot 10^{-5}$	$1.082 \cdot 10^{-5}$	$3.122 \cdot 10^{-6}$	$2.627 \cdot 10^{-5}$	0.0	0.0	0.0	0.0	0.0
1.10	$7.186 \cdot 10^{-5}$	$5.531 \cdot 10^{-5}$	$4.116 \cdot 10^{-5}$	$1.576 \cdot 10^{-5}$	$4.414 \cdot 10^{-6}$	$3.490 \cdot 10^{-5}$	0.0	0.0	0.0	0.0	0.0
1.20	$7.830 \cdot 10^{-5}$	$6.048 \cdot 10^{-5}$	$4.529 \cdot 10^{-5}$	$1.742 \cdot 10^{-5}$	$4.795 \cdot 10^{-6}$	$3.778 \cdot 10^{-5}$	0.0	0.0	0.0	0.0	0.0
1.25	$8.571 \cdot 10^{-5}$	$6.600 \cdot 10^{-5}$	$5.063 \cdot 10^{-5}$	$1.920 \cdot 10^{-5}$	$5.182 \cdot 10^{-6}$	$3.795 \cdot 10^{-5}$	0.0	0.0	0.0	0.0	0.0
1.30	$1.013 \cdot 10^{-4}$	$7.811 \cdot 10^{-5}$	$6.007 \cdot 10^{-5}$	$2.280 \cdot 10^{-5}$	$6.106 \cdot 10^{-6}$	$4.413 \cdot 10^{-5}$	0.0	0.0	0.0	0.0	0.0
1.40	$1.084 \cdot 10^{-4}$	$8.355 \cdot 10^{-5}$	$6.393 \cdot 10^{-5}$	$2.448 \cdot 10^{-5}$	$6.629 \cdot 10^{-6}$	$5.319 \cdot 10^{-5}$	0.0	0.0	0.0	0.0	0.0
1.50	$1.247 \cdot 10^{-4}$	$9.559 \cdot 10^{-5}$	$7.359 \cdot 10^{-5}$	$2.804 \cdot 10^{-5}$	$7.678 \cdot 10^{-6}$	$6.819 \cdot 10^{-5}$	0.0	0.0	$1.009 \cdot 10^{-5}$	$8.351 \cdot 10^{-5}$	$4.482 \cdot 10^{-7}$
1.60	$1.377 \cdot 10^{-4}$	$1.049 \cdot 10^{-4}$	$8.138 \cdot 10^{-5}$	$3.094 \cdot 10^{-5}$	$8.542 \cdot 10^{-6}$	$8.295 \cdot 10^{-5}$	0.0	0.0	$9.311 \cdot 10^{-7}$	$1.147 \cdot 10^{-5}$	$1.356 \cdot 10^{-6}$
1.70	$6.938 \cdot 10^{-5}$	$3.016 \cdot 10^{-5}$	$8.386 \cdot 10^{-5}$	$1.832 \cdot 10^{-5}$	$1.915 \cdot 10^{-5}$	$2.593 \cdot 10^{-4}$	0.0	0.0	$1.798 \cdot 10^{-5}$	$2.346 \cdot 10^{-4}$	$1.979 \cdot 10^{-7}$
1.80	$1.097 \cdot 10^{-5}$	$8.462 \cdot 10^{-6}$	$7.290 \cdot 10^{-6}$	$2.733 \cdot 10^{-6}$	$6.504 \cdot 10^{-7}$	$4.265 \cdot 10^{-6}$	$1.167 \cdot 10^{-4}$	$3.145 \cdot 10^{-9}$	$5.149 \cdot 10^{-5}$	$4.325 \cdot 10^{-4}$	$5.524 \cdot 10^{-5}$
1.90	$1.130 \cdot 10^{-5}$	$8.715 \cdot 10^{-6}$	$7.354 \cdot 10^{-6}$	$2.783 \cdot 10^{-6}$	$6.754 \cdot 10^{-7}$	$4.843 \cdot 10^{-6}$	0.0	$8.338 \cdot 10^{-7}$	$9.924 \cdot 10^{-5}$	$9.462 \cdot 10^{-4}$	$1.389 \cdot 10^{-5}$
2.00	$1.143 \cdot 10^{-5}$	$8.817 \cdot 10^{-6}$	$7.597 \cdot 10^{-6}$	$2.897 \cdot 10^{-6}$	$6.928 \cdot 10^{-7}$	$5.458 \cdot 10^{-6}$	0.0	0.0	$2.133 \cdot 10^{-4}$	$1.849 \cdot 10^{-3}$	$8.450 \cdot 10^{-5}$
2.10	$8.374 \cdot 10^{-6}$	$6.165 \cdot 10^{-6}$	$6.267 \cdot 10^{-6}$	$2.458 \cdot 10^{-6}$	$6.379 \cdot 10^{-7}$	$6.252 \cdot 10^{-6}$	0.0	0.0	$2.112 \cdot 10^{-4}$	$2.686 \cdot 10^{-3}$	$9.150 \cdot 10^{-6}$
2.20	$6.073 \cdot 10^{-6}$	$3.488 \cdot 10^{-6}$	$5.872 \cdot 10^{-6}$	$1.549 \cdot 10^{-6}$	$1.066 \cdot 10^{-6}$	$1.035 \cdot 10^{-5}$	0.0	0.0	$2.184 \cdot 10^{-4}$	$3.652 \cdot 10^{-3}$	$3.750 \cdot 10^{-6}$
2.30	$2.114 \cdot 10^{-9}$	$2.026 \cdot 10^{-9}$	$1.023 \cdot 10^{-9}$	0.0	0.0	$1.968 \cdot 10^{-9}$	$3.523 \cdot 10^{-5}$	0.0	$2.366 \cdot 10^{-4}$	$4.655 \cdot 10^{-3}$	$2.680 \cdot 10^{-6}$
2.40	$1.208 \cdot 10^{-9}$	$1.048 \cdot 10^{-9}$	$1.113 \cdot 10^{-9}$	0.0	0.0	$2.327 \cdot 10^{-9}$	0.0	0.0	$2.411 \cdot 10^{-4}$	$5.677 \cdot 10^{-3}$	$3.488 \cdot 10^{-6}$
2.50	0.0	0.0	0.0	0.0	0.0	0.0	0.0	0.0	$2.634 \cdot 10^{-4}$	$6.506 \cdot 10^{-3}$	$6.127 \cdot 10^{-6}$
3.00	0.0	0.0	0.0	0.0	0.0	0.0	0.0	0.0	$3.258 \cdot 10^{-4}$	$1.338 \cdot 10^{-2}$	$2.450 \cdot 10^{-7}$
3.50	0.0	0.0	0.0	0.0	0.0	0.0	0.0	0.0	$4.328 \cdot 10^{-4}$	$8.747 \cdot 10^{-3}$	$8.492 \cdot 10^{-7}$
4.00	0.0	0.0	0.0	0.0	0.0	$1.038 \cdot 10^{-9}$	0.0	0.0	$6.015 \cdot 10^{-4}$	$6.385 \cdot 10^{-3}$	$6.446 \cdot 10^{-6}$
4.01	0.0	0.0	0.0	0.0	0.0	$1.029 \cdot 10^{-9}$	0.0	0.0	$6.030 \cdot 10^{-4}$	$6.465 \cdot 10^{-3}$	$6.272 \cdot 10^{-6}$
4.50	$5.104 \cdot 10^{-4}$	$3.923 \cdot 10^{-4}$	$4.112 \cdot 10^{-4}$	$1.467 \cdot 10^{-4}$	$2.628 \cdot 10^{-5}$	$1.141 \cdot 10^{-4}$	0.0	$3.620 \cdot 10^{-5}$	$1.897 \cdot 10^{-5}$	$9.433 \cdot 10^{-5}$	$1.195 \cdot 10^{-5}$
5.00	$5.590 \cdot 10^{-4}$	$4.283 \cdot 10^{-4}$	$4.723 \cdot 10^{-4}$	$1.665 \cdot 10^{-4}$	$2.809 \cdot 10^{-5}$	$1.137 \cdot 10^{-4}$	$3.314 \cdot 10^{-6}$	$9.557 \cdot 10^{-6}$	$2.855 \cdot 10^{-5}$	$8.266 \cdot 10^{-5}$	$1.742 \cdot 10^{-5}$
5.50	$6.023 \cdot 10^{-4}$	$4.596 \cdot 10^{-4}$	$5.356 \cdot 10^{-4}$	$1.866 \cdot 10^{-4}$	$2.972 \cdot 10^{-5}$	$1.163 \cdot 10^{-4}$	0.0	$1.836 \cdot 10^{-5}$	$2.789 \cdot 10^{-5}$	$8.240 \cdot 10^{-5}$	$1.308 \cdot 10^{-5}$
6.00	$6.412 \cdot 10^{-4}$	$4.876 \cdot 10^{-4}$	$5.970 \cdot 10^{-4}$	$2.056 \cdot 10^{-4}$	$3.100 \cdot 10^{-5}$	$1.165 \cdot 10^{-4}$	$8.729 \cdot 10^{-7}$	$9.972 \cdot 10^{-6}$	$2.486 \cdot 10^{-5}$	$7.776 \cdot 10^{-5}$	$1.870 \cdot 10^{-5}$
6.50	$6.759 \cdot 10^{-4}$	$5.126 \cdot 10^{-4}$	$6.566 \cdot 10^{-4}$	$2.238 \cdot 10^{-4}$	$3.206 \cdot 10^{-5}$	$1.159 \cdot 10^{-4}$	$1.395 \cdot 10^{-6}$	$1.288 \cdot 10^{-5}$	$2.694 \cdot 10^{-5}$	$8.094 \cdot 10^{-5}$	$1.715 \cdot 10^{-5}$
7.00	$7.087 \cdot 10^{-4}$	$5.357 \cdot 10^{-4}$	$7.164 \cdot 10^{-4}$	$2.417 \cdot 10^{-4}$	$3.313 \cdot 10^{-5}$	$1.166 \cdot 10^{-4}$	$1.720 \cdot 10^{-6}$	$1.871 \cdot 10^{-5}$	$2.819 \cdot 10^{-5}$	$7.782 \cdot 10^{-5}$	$1.235 \cdot 10^{-5}$

Table A.1 – Continued

M_*	M stars						S stars		SiC	C stars	
	forsterite	fayalite	enstatite	ferrosilite	quartz	iron	quartz	iron		carbon	iron
						$Z = 0.02$					
1.00	$1.416 \cdot 10^{-4}$	$1.103 \cdot 10^{-4}$	$8.849 \cdot 10^{-5}$	$3.324 \cdot 10^{-5}$	$7.925 \cdot 10^{-6}$	$5.077 \cdot 10^{-5}$	0.0	0.0	0.0	0.0	0.0
1.10	$1.740 \cdot 10^{-4}$	$1.358 \cdot 10^{-4}$	$1.092 \cdot 10^{-4}$	$4.139 \cdot 10^{-5}$	$9.785 \cdot 10^{-6}$	$6.522 \cdot 10^{-5}$	0.0	0.0	0.0	0.0	0.0
1.20	$2.194 \cdot 10^{-4}$	$1.712 \cdot 10^{-4}$	$1.411 \cdot 10^{-4}$	$5.292 \cdot 10^{-5}$	$1.209 \cdot 10^{-5}$	$7.449 \cdot 10^{-5}$	0.0	0.0	0.0	0.0	0.0
1.25	$2.532 \cdot 10^{-4}$	$1.979 \cdot 10^{-4}$	$1.624 \cdot 10^{-4}$	$6.118 \cdot 10^{-5}$	$1.400 \cdot 10^{-5}$	$8.641 \cdot 10^{-5}$	0.0	0.0	0.0	0.0	0.0
1.30	$2.396 \cdot 10^{-4}$	$1.875 \cdot 10^{-4}$	$1.554 \cdot 10^{-4}$	$5.855 \cdot 10^{-5}$	$1.318 \cdot 10^{-5}$	$7.955 \cdot 10^{-5}$	0.0	0.0	0.0	0.0	0.0
1.40	$2.788 \cdot 10^{-4}$	$2.178 \cdot 10^{-4}$	$1.849 \cdot 10^{-4}$	$6.915 \cdot 10^{-5}$	$1.517 \cdot 10^{-5}$	$9.015 \cdot 10^{-5}$	0.0	0.0	0.0	0.0	0.0
1.50	$3.214 \cdot 10^{-4}$	$2.523 \cdot 10^{-4}$	$2.115 \cdot 10^{-4}$	$8.031 \cdot 10^{-5}$	$1.770 \cdot 10^{-5}$	$1.144 \cdot 10^{-4}$	0.0	0.0	0.0	0.0	0.0
1.60	$3.297 \cdot 10^{-4}$	$2.584 \cdot 10^{-4}$	$2.198 \cdot 10^{-4}$	$8.282 \cdot 10^{-5}$	$1.802 \cdot 10^{-5}$	$1.093 \cdot 10^{-4}$	$9.297 \cdot 10^{-6}$	$1.678 \cdot 10^{-6}$	0.0	0.0	0.0
1.70	$3.470 \cdot 10^{-4}$	$2.712 \cdot 10^{-4}$	$2.338 \cdot 10^{-4}$	$8.786 \cdot 10^{-5}$	$1.908 \cdot 10^{-5}$	$1.276 \cdot 10^{-4}$	0.0	0.0	$1.673 \cdot 10^{-5}$	$1.200 \cdot 10^{-4}$	$2.483 \cdot 10^{-7}$
1.80	$3.659 \cdot 10^{-4}$	$2.850 \cdot 10^{-4}$	$2.506 \cdot 10^{-4}$	$9.347 \cdot 10^{-5}$	$2.015 \cdot 10^{-5}$	$1.387 \cdot 10^{-4}$	0.0	0.0	$1.897 \cdot 10^{-5}$	$5.696 \cdot 10^{-5}$	$3.038 \cdot 10^{-5}$
1.90	$3.516 \cdot 10^{-4}$	$2.500 \cdot 10^{-4}$	$3.070 \cdot 10^{-4}$	$1.118 \cdot 10^{-4}$	$2.626 \cdot 10^{-5}$	$2.586 \cdot 10^{-4}$	0.0	0.0	$3.244 \cdot 10^{-5}$	$2.813 \cdot 10^{-4}$	$3.029 \cdot 10^{-7}$
2.00	$2.427 \cdot 10^{-4}$	$1.765 \cdot 10^{-4}$	$1.882 \cdot 10^{-4}$	$7.070 \cdot 10^{-5}$	$1.621 \cdot 10^{-5}$	$1.681 \cdot 10^{-4}$	0.0	0.0	$2.934 \cdot 10^{-5}$	$4.076 \cdot 10^{-4}$	$1.361 \cdot 10^{-4}$
2.10	$3.251 \cdot 10^{-5}$	$2.440 \cdot 10^{-5}$	$3.027 \cdot 10^{-5}$	$1.111 \cdot 10^{-5}$	$2.169 \cdot 10^{-6}$	$1.533 \cdot 10^{-5}$	0.0	$7.873 \cdot 10^{-5}$	$2.168 \cdot 10^{-4}$	$8.662 \cdot 10^{-4}$	$2.598 \cdot 10^{-4}$
2.20	$2.498 \cdot 10^{-5}$	$1.978 \cdot 10^{-5}$	$1.888 \cdot 10^{-5}$	$7.149 \cdot 10^{-6}$	$1.366 \cdot 10^{-6}$	$8.374 \cdot 10^{-6}$	$8.014 \cdot 10^{-5}$	$4.558 \cdot 10^{-6}$	$2.580 \cdot 10^{-4}$	$1.393 \cdot 10^{-3}$	$1.314 \cdot 10^{-4}$
2.30	$7.373 \cdot 10^{-6}$	$5.596 \cdot 10^{-6}$	$4.535 \cdot 10^{-6}$	$1.670 \cdot 10^{-6}$	$4.370 \cdot 10^{-7}$	$3.462 \cdot 10^{-6}$	$5.662 \cdot 10^{-5}$	0.0	$3.925 \cdot 10^{-4}$	$2.465 \cdot 10^{-3}$	$9.564 \cdot 10^{-5}$
2.40	$2.238 \cdot 10^{-9}$	$2.086 \cdot 10^{-9}$	$1.169 \cdot 10^{-9}$	0.0	0.0	$1.875 \cdot 10^{-9}$	$2.494 \cdot 10^{-5}$	0.0	$6.101 \cdot 10^{-4}$	$4.675 \cdot 10^{-3}$	$1.478 \cdot 10^{-4}$
2.50	0.0	0.0	0.0	0.0	0.0	0.0	$2.647 \cdot 10^{-5}$	0.0	$6.391 \cdot 10^{-4}$	$5.490 \cdot 10^{-3}$	$3.434 \cdot 10^{-5}$
3.00	0.0	0.0	0.0	0.0	0.0	0.0	0.0	0.0	$7.337 \cdot 10^{-4}$	$1.210 \cdot 10^{-2}$	$2.153 \cdot 10^{-6}$
3.50	0.0	0.0	0.0	0.0	0.0	$1.383 \cdot 10^{-9}$	0.0	0.0	$9.519 \cdot 10^{-4}$	$1.091 \cdot 10^{-2}$	$5.244 \cdot 10^{-6}$
4.00	$1.711 \cdot 10^{-9}$	$1.486 \cdot 10^{-9}$	$1.072 \cdot 10^{-9}$	0.0	0.0	$2.688 \cdot 10^{-9}$	0.0	0.0	$1.218 \cdot 10^{-3}$	$9.796 \cdot 10^{-3}$	$1.685 \cdot 10^{-5}$
4.01	$1.717 \cdot 10^{-9}$	$1.493 \cdot 10^{-9}$	$1.075 \cdot 10^{-9}$	0.0	0.0	$2.674 \cdot 10^{-9}$	0.0	0.0	$1.225 \cdot 10^{-3}$	$9.851 \cdot 10^{-3}$	$1.703 \cdot 10^{-5}$
4.50	$8.636 \cdot 10^{-4}$	$6.707 \cdot 10^{-4}$	$9.145 \cdot 10^{-4}$	$3.179 \cdot 10^{-4}$	$3.820 \cdot 10^{-5}$	$1.205 \cdot 10^{-4}$	$7.352 \cdot 10^{-8}$	$7.790 \cdot 10^{-5}$	$2.049 \cdot 10^{-4}$	$4.291 \cdot 10^{-5}$	$1.323 \cdot 10^{-6}$
5.00	$9.340 \cdot 10^{-4}$	$7.230 \cdot 10^{-4}$	$1.045 \cdot 10^{-3}$	$3.595 \cdot 10^{-4}$	$4.067 \cdot 10^{-5}$	$1.248 \cdot 10^{-4}$	$2.058 \cdot 10^{-7}$	$5.354 \cdot 10^{-5}$	$2.458 \cdot 10^{-5}$	$2.435 \cdot 10^{-5}$	$6.630 \cdot 10^{-6}$
5.50	$9.913 \cdot 10^{-4}$	$7.630 \cdot 10^{-4}$	$1.174 \cdot 10^{-3}$	$3.987 \cdot 10^{-4}$	$4.318 \cdot 10^{-5}$	$1.346 \cdot 10^{-4}$	0.0	$3.654 \cdot 10^{-5}$	$1.960 \cdot 10^{-5}$	$4.102 \cdot 10^{-5}$	$3.937 \cdot 10^{-6}$
6.00	$1.037 \cdot 10^{-3}$	$7.982 \cdot 10^{-4}$	$1.292 \cdot 10^{-3}$	$4.363 \cdot 10^{-4}$	$4.389 \cdot 10^{-5}$	$1.256 \cdot 10^{-4}$	$4.083 \cdot 10^{-6}$	$3.305 \cdot 10^{-5}$	$2.678 \cdot 10^{-5}$	$3.825 \cdot 10^{-5}$	$1.410 \cdot 10^{-5}$
6.50	$1.084 \cdot 10^{-3}$	$8.313 \cdot 10^{-4}$	$1.421 \cdot 10^{-3}$	$4.753 \cdot 10^{-4}$	$4.576 \cdot 10^{-5}$	$1.313 \cdot 10^{-4}$	$2.233 \cdot 10^{-6}$	$2.861 \cdot 10^{-5}$	$2.831 \cdot 10^{-5}$	$3.600 \cdot 10^{-5}$	$1.681 \cdot 10^{-5}$
7.00	$1.123 \cdot 10^{-3}$	$8.611 \cdot 10^{-4}$	$1.544 \cdot 10^{-3}$	$5.135 \cdot 10^{-4}$	$4.679 \cdot 10^{-5}$	$1.285 \cdot 10^{-4}$	$3.430 \cdot 10^{-6}$	$2.150 \cdot 10^{-5}$	$2.761 \cdot 10^{-5}$	$3.458 \cdot 10^{-5}$	$2.929 \cdot 10^{-5}$

Table A.1 – Continued

M_*	M stars						S stars		C stars		
	forsterite	fayalite	enstatite	ferrosilite	quartz	iron	quartz	iron	SiC	carbon	iron
						$Z = 0.03$					
1.00	$4.386 \cdot 10^{-4}$	$3.512 \cdot 10^{-4}$	$2.646 \cdot 10^{-4}$	$1.050 \cdot 10^{-4}$	$2.456 \cdot 10^{-5}$	$1.616 \cdot 10^{-4}$	0.0	0.0	0.0	0.0	0.0
1.10	$5.537 \cdot 10^{-4}$	$4.427 \cdot 10^{-4}$	$3.405 \cdot 10^{-4}$	$1.340 \cdot 10^{-4}$	$3.069 \cdot 10^{-5}$	$1.965 \cdot 10^{-4}$	0.0	0.0	0.0	0.0	0.0
1.20	$6.244 \cdot 10^{-4}$	$5.028 \cdot 10^{-4}$	$3.879 \cdot 10^{-4}$	$1.546 \cdot 10^{-4}$	$3.450 \cdot 10^{-5}$	$2.272 \cdot 10^{-4}$	0.0	0.0	0.0	0.0	0.0
1.25	$6.729 \cdot 10^{-4}$	$5.407 \cdot 10^{-4}$	$4.264 \cdot 10^{-4}$	$1.681 \cdot 10^{-4}$	$3.666 \cdot 10^{-5}$	$2.280 \cdot 10^{-4}$	0.0	0.0	0.0	0.0	0.0
1.30	$7.104 \cdot 10^{-4}$	$5.710 \cdot 10^{-4}$	$4.574 \cdot 10^{-4}$	$1.795 \cdot 10^{-4}$	$3.827 \cdot 10^{-5}$	$2.253 \cdot 10^{-4}$	0.0	0.0	0.0	0.0	0.0
1.40	$8.048 \cdot 10^{-4}$	$6.461 \cdot 10^{-4}$	$5.216 \cdot 10^{-4}$	$2.036 \cdot 10^{-4}$	$4.305 \cdot 10^{-5}$	$2.456 \cdot 10^{-4}$	0.0	0.0	0.0	0.0	0.0
1.50	$8.836 \cdot 10^{-4}$	$7.152 \cdot 10^{-4}$	$5.850 \cdot 10^{-4}$	$2.310 \cdot 10^{-4}$	$4.695 \cdot 10^{-5}$	$2.821 \cdot 10^{-4}$	0.0	0.0	0.0	0.0	0.0
1.60	$8.959 \cdot 10^{-4}$	$7.084 \cdot 10^{-4}$	$6.333 \cdot 10^{-4}$	$2.353 \cdot 10^{-4}$	$5.421 \cdot 10^{-5}$	$3.397 \cdot 10^{-4}$	0.0	0.0	0.0	0.0	0.0
1.70	$9.869 \cdot 10^{-4}$	$7.946 \cdot 10^{-4}$	$6.949 \cdot 10^{-4}$	$2.681 \cdot 10^{-4}$	$5.053 \cdot 10^{-5}$	$2.732 \cdot 10^{-4}$	0.0	0.0	$3.828 \cdot 10^{-6}$	$5.612 \cdot 10^{-5}$	$1.336 \cdot 10^{-8}$
1.80	$1.060 \cdot 10^{-3}$	$8.593 \cdot 10^{-4}$	$7.994 \cdot 10^{-4}$	$3.067 \cdot 10^{-4}$	$5.214 \cdot 10^{-5}$	$2.732 \cdot 10^{-4}$	0.0	0.0	$3.958 \cdot 10^{-5}$	$1.531 \cdot 10^{-4}$	$6.882 \cdot 10^{-6}$
1.90	$1.098 \cdot 10^{-3}$	$8.890 \cdot 10^{-4}$	$8.710 \cdot 10^{-4}$	$3.315 \cdot 10^{-4}$	$5.297 \cdot 10^{-5}$	$2.758 \cdot 10^{-4}$	0.0	0.0	$8.287 \cdot 10^{-5}$	$1.541 \cdot 10^{-4}$	$1.374 \cdot 10^{-4}$
2.00	$1.157 \cdot 10^{-3}$	$9.315 \cdot 10^{-4}$	$9.931 \cdot 10^{-4}$	$3.703 \cdot 10^{-4}$	$5.412 \cdot 10^{-5}$	$3.117 \cdot 10^{-4}$	0.0	0.0	$5.386 \cdot 10^{-5}$	$3.387 \cdot 10^{-4}$	$7.887 \cdot 10^{-7}$
2.10	$1.032 \cdot 10^{-3}$	$7.188 \cdot 10^{-4}$	$1.152 \cdot 10^{-3}$	$3.470 \cdot 10^{-4}$	$8.928 \cdot 10^{-5}$	$7.246 \cdot 10^{-4}$	0.0	0.0	$4.548 \cdot 10^{-5}$	$4.676 \cdot 10^{-4}$	$2.163 \cdot 10^{-7}$
2.20	$8.239 \cdot 10^{-4}$	$6.437 \cdot 10^{-4}$	$7.881 \cdot 10^{-4}$	$2.941 \cdot 10^{-4}$	$4.160 \cdot 10^{-5}$	$2.908 \cdot 10^{-4}$	0.0	$6.207 \cdot 10^{-4}$	$3.795 \cdot 10^{-5}$	$6.144 \cdot 10^{-4}$	$1.149 \cdot 10^{-7}$
2.30	$1.190 \cdot 10^{-4}$	$9.143 \cdot 10^{-5}$	$1.050 \cdot 10^{-4}$	$3.919 \cdot 10^{-5}$	$6.678 \cdot 10^{-6}$	$5.673 \cdot 10^{-5}$	$1.950 \cdot 10^{-3}$	$1.578 \cdot 10^{-8}$	$1.523 \cdot 10^{-4}$	$7.633 \cdot 10^{-4}$	$8.779 \cdot 10^{-4}$
2.40	$4.101 \cdot 10^{-5}$	$3.257 \cdot 10^{-5}$	$4.915 \cdot 10^{-5}$	$1.817 \cdot 10^{-5}$	$2.000 \cdot 10^{-6}$	$1.122 \cdot 10^{-5}$	$1.833 \cdot 10^{-4}$	$5.113 \cdot 10^{-4}$	$3.347 \cdot 10^{-4}$	$1.017 \cdot 10^{-3}$	$1.032 \cdot 10^{-3}$
2.50	$2.804 \cdot 10^{-5}$	$1.425 \cdot 10^{-5}$	$3.954 \cdot 10^{-5}$	$7.333 \cdot 10^{-6}$	$4.294 \cdot 10^{-6}$	$3.770 \cdot 10^{-5}$	0.0	$2.692 \cdot 10^{-5}$	$5.993 \cdot 10^{-4}$	$2.126 \cdot 10^{-3}$	$9.256 \cdot 10^{-4}$
3.00	$1.235 \cdot 10^{-9}$	$1.077 \cdot 10^{-9}$	0.0	0.0	0.0	$1.966 \cdot 10^{-9}$	0.0	$2.250 \cdot 10^{-9}$	$1.847 \cdot 10^{-3}$	$1.087 \cdot 10^{-2}$	$1.026 \cdot 10^{-4}$
3.50	$2.516 \cdot 10^{-9}$	$2.222 \cdot 10^{-9}$	$1.613 \cdot 10^{-9}$	0.0	0.0	$4.438 \cdot 10^{-9}$	0.0	$3.632 \cdot 10^{-9}$	$2.133 \cdot 10^{-3}$	$1.448 \cdot 10^{-2}$	$5.793 \cdot 10^{-5}$
4.00	$3.752 \cdot 10^{-9}$	$3.411 \cdot 10^{-9}$	$2.276 \cdot 10^{-9}$	$1.408 \cdot 10^{-9}$	0.0	$6.132 \cdot 10^{-9}$	0.0	$5.517 \cdot 10^{-9}$	$2.549 \cdot 10^{-3}$	$1.707 \cdot 10^{-2}$	$5.820 \cdot 10^{-5}$
4.01	$3.815 \cdot 10^{-9}$	$3.469 \cdot 10^{-9}$	$2.300 \cdot 10^{-9}$	$1.422 \cdot 10^{-9}$	0.0	$6.122 \cdot 10^{-9}$	0.0	$5.482 \cdot 10^{-9}$	$2.550 \cdot 10^{-3}$	$1.709 \cdot 10^{-2}$	$5.885 \cdot 10^{-5}$
4.50	$1.763 \cdot 10^{-3}$	$1.396 \cdot 10^{-3}$	$2.622 \cdot 10^{-3}$	$8.934 \cdot 10^{-4}$	$6.470 \cdot 10^{-5}$	$1.729 \cdot 10^{-4}$	0.0	0.0	$2.459 \cdot 10^{-5}$	$7.382 \cdot 10^{-5}$	$4.483 \cdot 10^{-6}$
5.00	$1.834 \cdot 10^{-3}$	$1.449 \cdot 10^{-3}$	$2.984 \cdot 10^{-3}$	$1.010 \cdot 10^{-3}$	$6.763 \cdot 10^{-5}$	$1.767 \cdot 10^{-4}$	0.0	0.0	$7.030 \cdot 10^{-6}$	$6.068 \cdot 10^{-5}$	$3.297 \cdot 10^{-7}$
5.50	$1.877 \cdot 10^{-3}$	$1.485 \cdot 10^{-3}$	$3.318 \cdot 10^{-3}$	$1.117 \cdot 10^{-3}$	$6.937 \cdot 10^{-5}$	$1.750 \cdot 10^{-4}$	0.0	$1.354 \cdot 10^{-4}$	0.0	0.0	0.0
6.00	$1.934 \cdot 10^{-3}$	$1.528 \cdot 10^{-3}$	$3.668 \cdot 10^{-3}$	$1.228 \cdot 10^{-3}$	$7.167 \cdot 10^{-5}$	$1.777 \cdot 10^{-4}$	$1.242 \cdot 10^{-5}$	$2.297 \cdot 10^{-5}$	$1.469 \cdot 10^{-5}$	$1.239 \cdot 10^{-5}$	$7.681 \cdot 10^{-6}$
6.50	$1.987 \cdot 10^{-3}$	$1.569 \cdot 10^{-3}$	$4.024 \cdot 10^{-3}$	$1.340 \cdot 10^{-3}$	$7.397 \cdot 10^{-5}$	$1.831 \cdot 10^{-4}$	$7.084 \cdot 10^{-6}$	$1.684 \cdot 10^{-5}$	$1.572 \cdot 10^{-5}$	$1.327 \cdot 10^{-5}$	$4.907 \cdot 10^{-5}$
7.00	$2.028 \cdot 10^{-3}$	$1.600 \cdot 10^{-3}$	$4.381 \cdot 10^{-3}$	$1.452 \cdot 10^{-3}$	$7.638 \cdot 10^{-5}$	$1.905 \cdot 10^{-4}$	$5.351 \cdot 10^{-6}$	$3.804 \cdot 10^{-5}$	$1.579 \cdot 10^{-5}$	$7.799 \cdot 10^{-6}$	$2.605 \cdot 10^{-5}$

Table A.1 – Continued

M_*	M stars						S stars			C stars	
	forsterite	fayalite	enstatite	ferrosilite	quartz	iron	quartz	iron	SiC	carbon	iron
						$Z = 0.04$					
1.00	$7.962 \cdot 10^{-4}$	$6.493 \cdot 10^{-4}$	$4.946 \cdot 10^{-4}$	$1.988 \cdot 10^{-4}$	$4.265 \cdot 10^{-5}$	$2.709 \cdot 10^{-4}$	0.0	0.0	0.0	0.0	0.0
1.10	$1.118 \cdot 10^{-3}$	$9.171 \cdot 10^{-4}$	$6.973 \cdot 10^{-4}$	$2.841 \cdot 10^{-4}$	$5.995 \cdot 10^{-5}$	$3.824 \cdot 10^{-4}$	0.0	0.0	0.0	0.0	0.0
1.20	$1.312 \cdot 10^{-3}$	$1.077 \cdot 10^{-3}$	$8.322 \cdot 10^{-4}$	$3.371 \cdot 10^{-4}$	$6.966 \cdot 10^{-5}$	$4.332 \cdot 10^{-4}$	0.0	0.0	0.0	0.0	0.0
1.25	$1.303 \cdot 10^{-3}$	$1.072 \cdot 10^{-3}$	$8.409 \cdot 10^{-4}$	$3.411 \cdot 10^{-4}$	$6.869 \cdot 10^{-5}$	$4.324 \cdot 10^{-4}$	0.0	0.0	0.0	0.0	0.0
1.30	$1.405 \cdot 10^{-3}$	$1.160 \cdot 10^{-3}$	$9.183 \cdot 10^{-4}$	$3.734 \cdot 10^{-4}$	$7.339 \cdot 10^{-5}$	$4.522 \cdot 10^{-4}$	0.0	0.0	0.0	0.0	0.0
1.40	$1.576 \cdot 10^{-3}$	$1.299 \cdot 10^{-3}$	$1.062 \cdot 10^{-3}$	$4.264 \cdot 10^{-4}$	$8.021 \cdot 10^{-5}$	$4.497 \cdot 10^{-4}$	0.0	0.0	0.0	0.0	0.0
1.50	$1.715 \cdot 10^{-3}$	$1.415 \cdot 10^{-3}$	$1.175 \cdot 10^{-3}$	$4.698 \cdot 10^{-4}$	$8.648 \cdot 10^{-5}$	$4.710 \cdot 10^{-4}$	0.0	0.0	0.0	0.0	0.0
1.60	$1.808 \cdot 10^{-3}$	$1.496 \cdot 10^{-3}$	$1.270 \cdot 10^{-3}$	$5.077 \cdot 10^{-4}$	$9.044 \cdot 10^{-5}$	$5.005 \cdot 10^{-4}$	0.0	0.0	0.0	0.0	0.0
1.70	$2.038 \cdot 10^{-3}$	$1.693 \cdot 10^{-3}$	$1.447 \cdot 10^{-3}$	$5.813 \cdot 10^{-4}$	$1.014 \cdot 10^{-4}$	$5.593 \cdot 10^{-4}$	0.0	0.0	0.0	0.0	0.0
1.80	$2.017 \cdot 10^{-3}$	$1.657 \cdot 10^{-3}$	$1.492 \cdot 10^{-3}$	$5.833 \cdot 10^{-4}$	$9.774 \cdot 10^{-5}$	$4.895 \cdot 10^{-4}$	0.0	0.0	0.0	0.0	0.0
1.90	$2.117 \cdot 10^{-3}$	$1.740 \cdot 10^{-3}$	$1.600 \cdot 10^{-3}$	$6.237 \cdot 10^{-4}$	$1.015 \cdot 10^{-4}$	$4.975 \cdot 10^{-4}$	0.0	0.0	0.0	0.0	0.0
2.00	$2.371 \cdot 10^{-3}$	$1.959 \cdot 10^{-3}$	$1.788 \cdot 10^{-3}$	$7.046 \cdot 10^{-4}$	$1.146 \cdot 10^{-4}$	$5.901 \cdot 10^{-4}$	0.0	0.0	0.0	0.0	0.0
2.10	$2.129 \cdot 10^{-3}$	$1.703 \cdot 10^{-3}$	$1.981 \cdot 10^{-3}$	$7.579 \cdot 10^{-4}$	$1.047 \cdot 10^{-4}$	$5.523 \cdot 10^{-4}$	0.0	0.0	$4.692 \cdot 10^{-5}$	$4.709 \cdot 10^{-4}$	$4.094 \cdot 10^{-7}$
2.20	$1.984 \cdot 10^{-3}$	$1.644 \cdot 10^{-3}$	$2.021 \cdot 10^{-3}$	$7.606 \cdot 10^{-4}$	$8.520 \cdot 10^{-5}$	$4.344 \cdot 10^{-4}$	0.0	$3.409 \cdot 10^{-4}$	$1.256 \cdot 10^{-5}$	$3.706 \cdot 10^{-4}$	$2.403 \cdot 10^{-8}$
2.30	$1.608 \cdot 10^{-3}$	$1.183 \cdot 10^{-3}$	$2.429 \cdot 10^{-3}$	$8.830 \cdot 10^{-4}$	$8.978 \cdot 10^{-5}$	$5.910 \cdot 10^{-4}$	0.0	0.0	$1.390 \cdot 10^{-4}$	$6.324 \cdot 10^{-4}$	$5.151 \cdot 10^{-4}$
2.40	$4.971 \cdot 10^{-4}$	$3.744 \cdot 10^{-4}$	$6.920 \cdot 10^{-4}$	$2.600 \cdot 10^{-4}$	$2.753 \cdot 10^{-5}$	$2.087 \cdot 10^{-4}$	$3.967 \cdot 10^{-3}$	$4.553 \cdot 10^{-8}$	$5.922 \cdot 10^{-5}$	$8.619 \cdot 10^{-4}$	$1.399 \cdot 10^{-3}$
2.50	$5.073 \cdot 10^{-5}$	$3.269 \cdot 10^{-5}$	$1.064 \cdot 10^{-4}$	$3.147 \cdot 10^{-5}$	$3.924 \cdot 10^{-6}$	$3.041 \cdot 10^{-5}$	$1.851 \cdot 10^{-3}$	$2.419 \cdot 10^{-3}$	$2.513 \cdot 10^{-4}$	$7.544 \cdot 10^{-4}$	$3.122 \cdot 10^{-5}$
3.00	$5.884 \cdot 10^{-9}$	$5.412 \cdot 10^{-9}$	$3.584 \cdot 10^{-9}$	$2.293 \cdot 10^{-9}$	0.0	$9.373 \cdot 10^{-9}$	0.0	$2.536 \cdot 10^{-8}$	$2.981 \cdot 10^{-3}$	$9.306 \cdot 10^{-3}$	$2.308 \cdot 10^{-3}$
3.50	$5.893 \cdot 10^{-9}$	$5.374 \cdot 10^{-9}$	$3.850 \cdot 10^{-9}$	$2.458 \cdot 10^{-9}$	0.0	$1.178 \cdot 10^{-8}$	0.0	$1.908 \cdot 10^{-8}$	$3.484 \cdot 10^{-3}$	$1.489 \cdot 10^{-2}$	$4.698 \cdot 10^{-4}$
4.00	$9.763 \cdot 10^{-9}$	$9.002 \cdot 10^{-9}$	$6.214 \cdot 10^{-9}$	$4.020 \cdot 10^{-9}$	$1.484 \cdot 10^{-9}$	$2.010 \cdot 10^{-8}$	0.0	$2.990 \cdot 10^{-8}$	$4.130 \cdot 10^{-3}$	$1.816 \cdot 10^{-2}$	$3.550 \cdot 10^{-4}$
4.01	$9.811 \cdot 10^{-9}$	$9.057 \cdot 10^{-9}$	$6.223 \cdot 10^{-9}$	$4.032 \cdot 10^{-9}$	$1.482 \cdot 10^{-9}$	$2.007 \cdot 10^{-8}$	0.0	$2.968 \cdot 10^{-8}$	$4.115 \cdot 10^{-3}$	$1.786 \cdot 10^{-2}$	$3.624 \cdot 10^{-4}$
4.50	$3.075 \cdot 10^{-3}$	$2.464 \cdot 10^{-3}$	$4.976 \cdot 10^{-3}$	$1.700 \cdot 10^{-3}$	$1.202 \cdot 10^{-4}$	$3.029 \cdot 10^{-4}$	0.0	0.0	$7.947 \cdot 10^{-6}$	$1.619 \cdot 10^{-4}$	$3.310 \cdot 10^{-7}$
5.00	$3.063 \cdot 10^{-3}$	$2.453 \cdot 10^{-3}$	$5.778 \cdot 10^{-3}$	$1.957 \cdot 10^{-3}$	$1.116 \cdot 10^{-4}$	$3.233 \cdot 10^{-4}$	0.0	0.0	0.0	0.0	0.0
5.50	$2.915 \cdot 10^{-3}$	$2.338 \cdot 10^{-3}$	$6.647 \cdot 10^{-3}$	$2.234 \cdot 10^{-3}$	$1.086 \cdot 10^{-4}$	$3.551 \cdot 10^{-4}$	0.0	0.0	$8.865 \cdot 10^{-6}$	$3.758 \cdot 10^{-5}$	$1.632 \cdot 10^{-5}$
6.00	$2.853 \cdot 10^{-3}$	$2.290 \cdot 10^{-3}$	$7.441 \cdot 10^{-3}$	$2.485 \cdot 10^{-3}$	$1.119 \cdot 10^{-4}$	$3.858 \cdot 10^{-4}$	0.0	0.0	$1.748 \cdot 10^{-5}$	$5.776 \cdot 10^{-6}$	$7.898 \cdot 10^{-5}$
6.50	$2.903 \cdot 10^{-3}$	$2.340 \cdot 10^{-3}$	$8.115 \cdot 10^{-3}$	$2.707 \cdot 10^{-3}$	$1.129 \cdot 10^{-4}$	$3.731 \cdot 10^{-4}$	$2.058 \cdot 10^{-5}$	$3.143 \cdot 10^{-5}$	$3.243 \cdot 10^{-6}$	$1.354 \cdot 10^{-5}$	$9.046 \cdot 10^{-6}$
7.00	$2.940 \cdot 10^{-3}$	$2.377 \cdot 10^{-3}$	$8.838 \cdot 10^{-3}$	$2.941 \cdot 10^{-3}$	$1.160 \cdot 10^{-4}$	$3.678 \cdot 10^{-4}$	$1.150 \cdot 10^{-5}$	$9.800 \cdot 10^{-5}$	0.0	0.0	0.0